Design and Optimisation of Terahertz Frequency Photoconductive Antenna Arrays on Optically Transparent Insulating Substrates

Connor Steven Kidd

Submitted in accordance with the requirements for the degree of Doctor of Philosophy

University of Leeds

School of Electronic and Electrical Engineering
Pollard Institute

November 2023

The candidate confirms that the work submitted is his own and that appropriate credit has been given where reference has been made to the work of others.

This thesis is dedicated to my late grandfather Hugh.

Acknowledgements

First and foremost I would like to thank my project supervisor Dr. Joshua Freeman, for the opportunity to continue my studies at the University of Leeds and for the invaluable knowledge, support and guidance he has provided me throughout my project. Without such help it would have been impossible to gain the skills and understanding required to complete this thesis. Secondly, I would like to thank my co-supervisor Prof. Alexander Giles Davies, for his valuable insights and advice that has greatly helped throughout. Not to forget the amazing support provided by the wider THz research supervisory group; Prof. Edmund Linfield, Prof. John Cunningham, Dr. Andrew Burnett and Dr. Paul Dean. The vast pool of wisdom has been of great importance for me to draw upon countless times throughout the project. As well a thank you to Dr. Lianhe Li for the vast amount of superb material you have provided to make all of the devices in this work.

To Dr. Mark Rosamond, a special thanks must be given for the endless support, knowledge and expertise you have offered me throughout my extensive time in the cleanroom. Without him, this project would not have been as successful as it was.

To Dr. Thomas Gill, he took me under his wing in the lab from my first day and somehow was able to put up with the millions of questions I've had over the years. Again without his help it would have been a lot harder than it was. More importantly, he has been a brilliant friend and for this I can not thank him enough.

To the rest of the kids on the fourth floor; Nick, Elly, and Jac, I thank them all for making the hours at work so enjoyable, I do not think that I would have been able to keep sane without them.

To Lu, thank you for the endless support and love you have given to me. You have had to listen to me talk about semiconductor fabrication more than anybody should have to, for that I will be both forever grateful and eternally sorry.

To my parents and family, a heartfelt thanks is in order. Not just for the years of my PhD study but for the years of love, support and guidance you have given. The constant belief in me, even when I did not believe in myself, I will never be able to express how much this means to me.

Finally, to my grandfather Hugh. Thank you for inspiring me to become an engineer and instilling in to me that I can achieve anything I put my mind to.

You were one of the reasons I took this path I'm on and I wish you could have been here to see me get to this stage of completing my PhD.

Abstract

Terahertz (THz) radiation is desirable for many different applications due to the low photon energy exhibited at these wavelengths. With many elementary excitations in materials occurring in this region, the use of THz radiation in non-linear spectroscopy has become a valuable tool for material investigations. Specifically, High-field spectroscopy has been used to probe non-linear effects in solid-state materials, these require intense THz sources which are harder to produce. A promising source is the Photo-Conductive Antennae (PCA), these devices are compact and easily integrated into systems with the ability of electrical modulation and lack of phase matching requirements.

In this thesis a systematic approach has been taken to investigate the effects of device geometry on the emission of THz radiation from PCA devices fabricated from LT-GaAs on optically transparent insulating substrates. Although these devices have been shown to be able to produce high-field THz electric field strengths, no investigations have been undertaken to improve device geometries and improve upon the the generation efficiency. Work on the effects of electrode designs and emitting gap sizes to support higher electrical biasing fields and optical fluences is presented. The results of the investigations led to the fabrication of a large area PCA device capable of producing $\sim$ 200 kV/cm, the largest THz field strengths to date from LT-GaAs PCA devices on sapphire substrates.

Also presented in this work is an investigation of LT-GaAs PCAs operated at an excitation wavelength of 1030 nm. The generation characteristics are compared to that of devices operated at 800 nm. Investigations into the operation of LT-GaAs on sapphire PCA devices using high repetition rate lasers of this wavelength could prove invaluable due to the lack of photoconductive materials currently available.

Publications

Peer-Reviewed Journals

– N. Nilforoushan, **C. Kidd**, A. Fournier, J. Palomo, J. Tignon, S. Dhillon, E. Lhuillier, Lianhe Li, A. G. Davies, E. H. Linfield, J. R. Freeman, and J. Mangeney.
"Efficient THz generation from low-temperature-grown GaAs photoconductive antennas driven by Yb-doped fiber amplifier at 200 kHz repetition rate".
Applied Physics Letters, November 2023, Accepted.
Author Contribution: I designed and fabricated the devices used for this study at the University of Leeds. I tested and analysed the devices at Leeds using the 800 nm wavelength system. I also visited the laboratory at ENS to assist with the testing and analysing the devices with collaborators on the 1030 nm system. I also participated in writing the manuscript.

– T. B. Gill, S. Pavov, **C. Kidd**, P. Dean, A. Burnett, A. Dunn, Li. L, N. Abrosimov, H. -W. Huebers, E. H. Linfield, A. G. Davies, J. R. Freeman.
"2D Time-Domain Spectroscopy for Determination of Energy and Momentum Relaxation Rates of Hydrogen-Like Donor States in Germanium".
ACS Photonics, 2023, Submitted.

Conference Proceedings

- **C. Kidd**, M. C. Rosamond, L. Chen, T. B. Gill, L. H. Li, E. H. Linfield, A. G. Davies, J. R. Freeman.
  "Improving the Efficiency of LT-GaAs Photoconductive Arrays on Optically Transparent Substrates for High Field THz Generation".
  2022 47th International Conference on Infrared, Millimeter and Terahertz Waves (IRMMW-THz), Delft, Netherlands, 2022.

- T. B. Gill, **C. Kidd**, P. Dean, A. D. Burnett, A. Dunn , S. G. Pavlov, N. V. Abrosimov, H. -W. Hübers, E. H. Linfield, A. G. Davies, J. R. Freeman.
  "Ultrafast Two-Dimensional Time-Domain Spectroscopy of Hydrogen-Like Impurity Centers in Germanium".
  2022 47th International Conference on Infrared, Millimeter and Terahertz Waves (IRMMW-THz), Delft, Netherlands, 2022.

- N. Nilforoushan, **C. Kidd**, A. Fournier, S. Dhillon, J. R. Freeman, J. Mangeney.
  "Broadband THz Emission from LT-GaAs Photoconductive Antenna Driven by Yb-Doped Fiber Amplifier at 200 kHz Repetition Rate".
  2023 Conference on Lasers and Electro-Optics Europe & European Quantum Electronics Conference (CLEO/Europe-EQEC), Munich, Germany, 2023.

- T. B. Gill, A. D. Burnett, C. Towler, **C. Kidd**, A. Dunn , L. Li, J. R. Freeman, E. H. Linfield, A. G. Davies, P. Dean
  "Ultrafast Two-Dimensional Time-Domain Spectroscopy of Hydrogen-Like Impurity Centers in Germanium".
  2022 47th International Conference on Infrared, Millimeter and Terahertz Waves (IRMMW-THz), Montreal, QC, Canada, 2023.

- **C. Kidd**, M. C. Rosamond, T. B. Gill, L. H. Li, E. H. Linfield, A. G. Davies, J. R. Freeman.
  "Improved Large Area Photoconductive Antenna Design for High Field THz Generation,".
  48th International Conference on Infrared, Millimeter, and Terahertz Waves (IRMMW-THz), Montreal, QC, Canada, 2023.

Contents

List of Figures

List of Tables

Abbreviations

2D Two Dimensional

ACE Acetone

AlGaAs Aluminium Gallium Arsenide

BCB Benzocyclobutene

BPM Binary Phase Mask

CPA Chirped Pulse Amplification

CW Continuous Wave

DBR Distributed Bragg Reflector

EBL Electron Beam Lithography

ELO Epitaxial Lift-off

EM Electromagnetic

EO Electro-Optic

EOS Electro-Optic Sampling

FE Finite Element

FELs Free Electron Lasers

FFT Fast Fourier Transform

fs Femtosecond

FTIR Fourier Transform Infrared

FWHM Full Width at Half Maximum

GaAs Gallium Arsenide

GaP Gallium Phosphide

HF Hydrofluoric Acid

ICP-RIE Inductively Coupled Plasma - Reactive Ion Etching

IPA Isopropyl alcohol

IR Infrared Radiation

KLM Kerr Lens Mode Locking

LIA Lock-In Amplifier

$LiNbO_3$ Lithium Niobate

LoG LT-GaAs on SI-GaAs

LoQ LT-GaAs on Quartz

LOR Lift off resist

LT-GaAs Low Temperature Grown Gallium Arsenide

ND Neutral Density

Nd:YAG Neodymium Yttrium Aluminum Garnet

OR Optical Rectification

PCA Photo-Conductive Antennae

PCB Printed Circuit Board

PTFE Polytetrafluoroethylene

RF Radio Frequency

SI-GaAs Semi-Insulating Gallium Arsenide

SNR Signal-to-Noise Ratio

TCE Tetrachloroethylene

TDS Time-Domain Spectroscopy

THz Terahertz

THz-TDS Terahertz Time-Domain Spectroscopy

Ti Titanium

Ti:Sapphire Titanium:Sapphire

VRR Vertical Retro-Reflector

Yb Ytterbium

ZnTe Zinc telluride

Chapter 1

Literature Review

1.1 Terahertz Frequency Studies

Terahertz (THz) radiation occupies the space between Infrared Radiation (IR) and Microwaves on the electromagnetic spectrum. The considered frequencies in the so called, now not so accurately named, 'THz gap' range from 0.3 THz to 30 THz. The gap was named thus originally due to the lack of available technology supporting sources, detectors and THz manipulative components that are of a similar level of sophistication and as widely available as the electronic and optical devices that bookend this spectral region [7]. THz radiation is desirable for many different applications due to the low photon energy at these frequencies (4.13 meV at 1 THz), these are important energies for causing elementary excitations in many different materials [8]. THz has potential applications in many different areas including medicine, security and manufacturing. In medicine, THz devices have been used for non-invasive medical imaging and disease tracking (i.e. cancer tracking [9–11]) and medical sensing [12–14]. It is especially suited for this role due to the low interference and non-ionizing characteristics of THz radiation [15], as well as the strong interactions that THz frequencies have with water molecules [16]. Spectral analysis of THz frequency can be used for detection of certain gases within a multi-component mixture, this provides a way to detect marker gases in exhaled breath [17] for non-invasive diagnostics, as well as explosive gases and toxic vapours in the air [18]. In the field of chemistry THz has been used successfully to investigate rotational and vibrational modes in molecular systems [19] and chemical reaction pathways [20]. The continued development of technologies and the increased availability of ultrafast amplified laser systems has allowed for the increased ability to generate higher THz electric field strengths, this in itself has unlocked a wide range of important applications.

1.2 High Field Strength Requirements

The ability to successfully generate high THz field strengths is the motivation that drives the work in this project, due to the potential applications that they unlock. High field strengths are typically classified as those >100 kV/cm [21]. The desire for stronger THz field strengths is to investigate non-linear characteristics of materials in condensed matter systems. With key focus on different non-linear transport mechanisms, non-linear interactions of excitation modes and control of different condensed matter systems. With high fields, the surface of materials can be more readily penetrated and excitations can take place. These effects on materials can be measured and interpreted in different ways. Spectroscopic techniques can be used to measure carrier dynamics in materials [22], non-linear transport mechanisms in materials can be investigated such as impact ionisation and inter-valley scattering [23–25], Bloch oscillations [26, 27], tunnel ionisation of impurity states [28, 29], and Zenner tunneling [30–32]. These are of particular interest to understand material behaviour as electronic devices move towards THz frequencies [33]. Non-linear interactions of excitation modes include ionisation of Rydberg states [34] and inducing Rabi oscillations [35], both phenomenon are of great interest owing to the potential applications they support, such as use in quantum computing [36].

High fields strengths have led to the ability to have coherent control and manipulation of the electronic properties of different matter, such as ferroelectric phases and domain orientations [37–39] as well as the coherent control of charge transport in materials [40, 41]. Dynamic control of intermolecular motions in liquids and gases which would allow for the modification of structure and dynamics of the materials [42].

1.3 Amplified Lasers

With the advancements in the ability to produce tabletop laser sources, utilising the Chirped Pulse Amplification (CPA) technique [43], the ability to achieve high energy fs pulses has become more widely available. CPA is a key technology that has enabled high-field THz table-top sources. This section will explain the theory and operation behind this method.

1.3.1 Laser theory

Electrons sit within discrete orbital shells, these can move around energy levels under influence of external energy to the system. In a laser system there are three main mechanisms that explain photon-electron interactions; absorption, spontaneous emission and stimulated emission [44].

If we consider a two level system, lower level E_1 and higher level E_2, then emission of a photon occurs when an electron drops from E_2 to E_1, this is the principle of photon emission. Electrons can be promoted to E_2 by an external

stimulus; with an incident wave upon the material there is a finite possibility that an electron can be promoted to the higher energy level. The energy for this is provided through the absorption of an incoming photon which has an energy given by:

$$h\nu = E_2 - E_1 \tag{1.1}$$

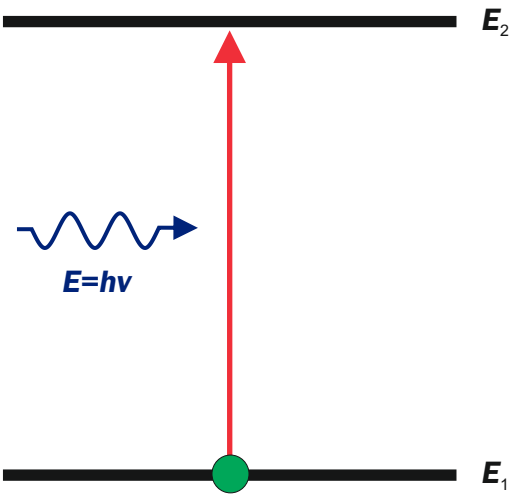

Figure 1.1: Absorption of a photon promoting an electron to a higher energy level in a two-level system

Spontaneous emission can occur when the electron decays to E_1 by itself without any external influence, the emission is not coherent, can be in any direction and can only take place if there is a unoccupied state in E_1. The photon emitted will have a frequency:

$$\nu = \frac{E_2 - E_1}{h} \tag{1.2}$$

At a given time t the number of electrons at an energy level is called the population and is denoted by N. The probability that a photon will emit spontaneously can be quantified by the fact that the rate of decay of the upper energy level ($\frac{dN_2}{dt}$) must proportional to the the population at that level (N_2):

$$\frac{dN_2}{dt} = -AN_2 \tag{1.3}$$

A is the Einstein coefficient or the spontaneous emission rate and is dependent upon the specific transition taking place. The time derivative is negative so the minus sign is to account for that.

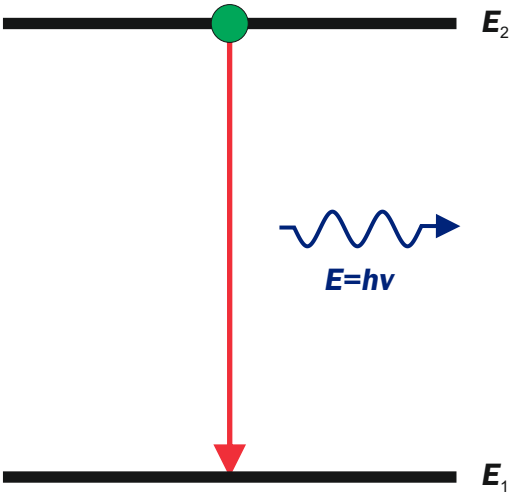

Figure 1.2: Spontaneous emission of a photon due to electron relaxation from a higher energy level in a two-level system

Stimulated emission occurs when a wave with an energy equal to that of the difference between the two energy levels is incident on the material, it can stimulate the electron that is present at E_2 to transition back to E_1. The incident photons electric field couples with that of the electron and forces an oscillation at the same frequency. As the electron transitions it releases the extra energy as a photon of equivalent energy to the incident photon. As the electron if forced by the incoming photon, the emitted photon is in the same direction as that photon, and in phase with it also. This mechanism of emission is the basis for photon amplification as one photon in equals two in phase photons out, see figure 1.3.

Similarly to equation 1.3 the probability that stimulated emission will occur can be written as:

$$\frac{dN_2}{dt} = -W_{21}N_2 \tag{1.4}$$

In this case W_{21} is the rate of stimulated emission and is dependent upon the intensity of the incident wave as well as the particular energy transition.

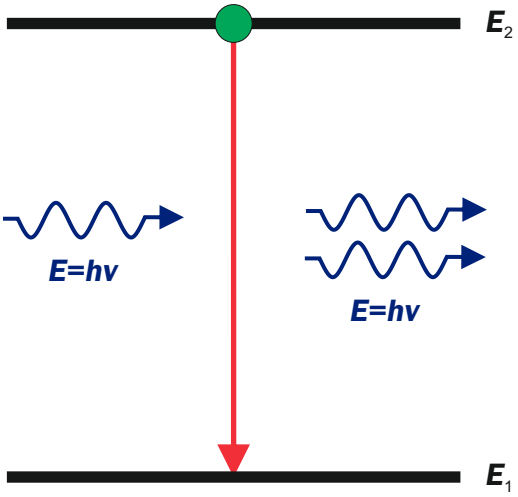

Figure 1.3: stimulated emission of a photon due to a driven oscillation from an incident photon from a higher energy level in a two-level system

LASER is an acronym that stands for Light Amplification by Stimulation of Emitted Radiation, which aptly describes the working mechanics of these devices. It can be seen that from a simple two level system that although we can achieve amplification, the incident photon can only stimulate the emission if it is not absorbed by an electron at E_1. In the two level system the number of absorbed photons will equal the number of stimulated emissions in steady state. Hence it can be seen that in order to produce strong amplification the majority of the electrons need to be at a higher energy level, this is known as a population inversion.

To facilitate a population inversion a three level energy system can be used like that seen in figure 1.4, in which an electron can be optically excited from the ground state E_1 to the top most energy level E_3 this is known as the pumping level. The operation of exciting the electrons is known as pumping and this is performed through absorption of incident photons. Electrons rapidly decay from E_3 to E_2, electrons then accumulate at the energy level E_2 which has a much longer decay time. The longer life state is known as metastable. As the lifetime is much longer a population inversion is achieved at this state as electrons are continually pumped to the E_3 energy level. An electron at E_2 will spontaneously emit a photon, this will cause a stimulated emission of another electron at the same energy level. The process continues as such with each photon stimulating another and this causes an avalanche effect of stimulated emission, All the photons are in phase and emitted in the same direction, and hence the output is a large collection of coherent photons.

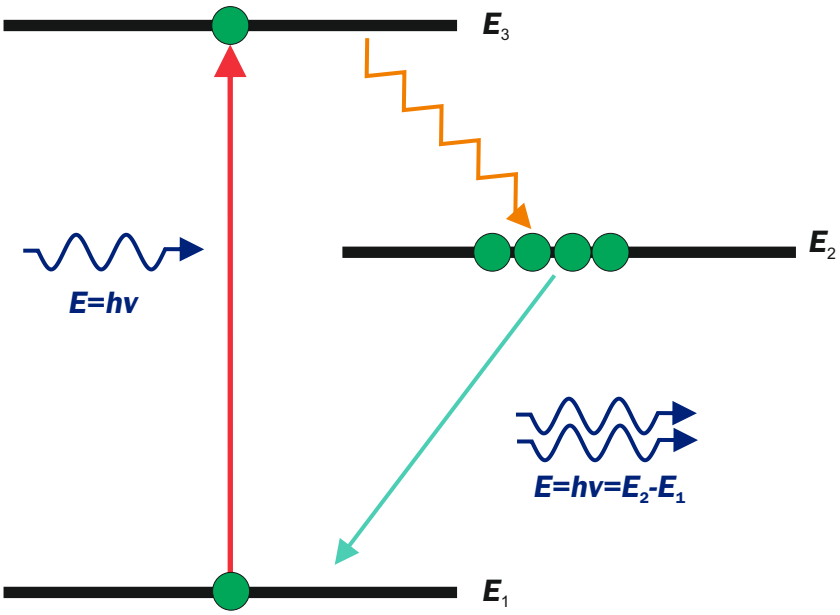

Figure 1.4: Diagram showing how a three-level system achieves a population inversion to create amplified emission. Red arrow indicates the promotion of an electron, orange arrow shows a non-radiative transition to energy level E_2, teal arrows are radiative transitions and dark blue arrows represent photons.

A better approach for achieving a population inversion is by utilising a four level energy system as seen in figure 1.5. In a four level system electrons are pumped from the ground state to a pumping energy level E_4, again electrons decay quickly to a metastable energy level E_3, the key difference in this configuration is that the lasing is between E_3 and an empty electron level E_2 before decaying back to the ground state E_1. In a three level system absorption losses will be compensated by gain until $N_2 = N_1$ after this point electrons promoted will contribute to a population inversion. In a four level system as energy level E_2 is empty from the beginning a population inversion is achieved immediately. [45] [46]

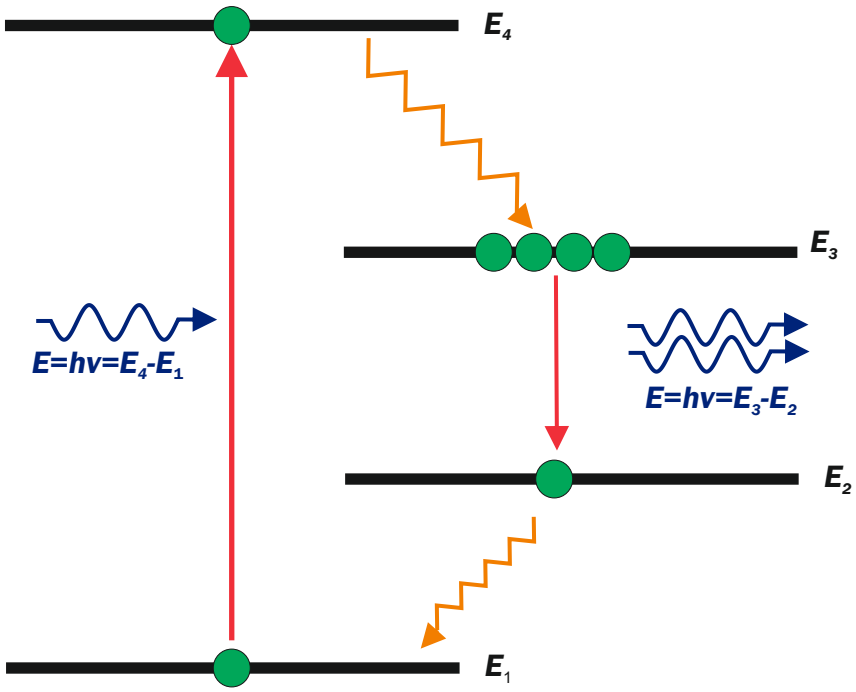

Figure 1.5: Diagram showing how a four-level system achieves a population inversion to create amplified emission.

To increase output power and intensity from the lasing material it is placed between two highly reflective mirrors as shown in figure 1.8. A wave reflected between the two mirrors will pass through the material and stimulate emission from the pumped lasing medium, hence becoming amplified on each pass. One mirror is completely reflective and the other mirror is made to be slightly transparent so that an output can be collected. Oscillation in laser cavity will not begin until the lasing threshold has been reached, this is the point that the gain of the active material overcomes the losses of the laser. It is important to note that the feedback is essential for laser operation, without this it is only an optical amplifier

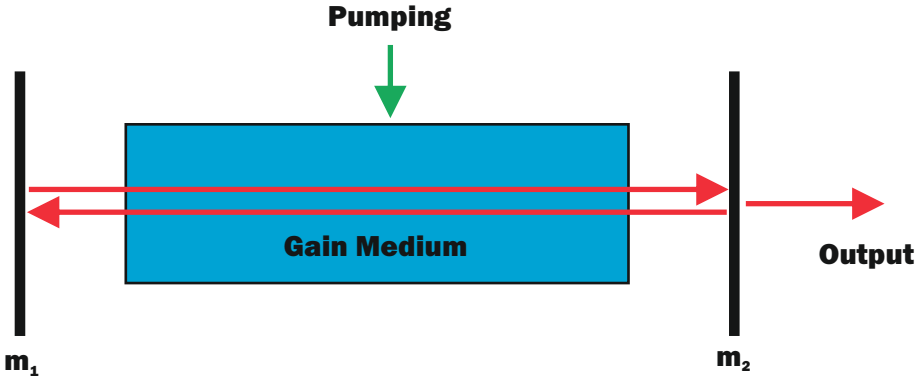

Figure 1.6: A diagram of a simple laser cavity set up, m_1 and m_2 are reflective mirrors with m_2 being partially transmissive

In order to couple the light out of the laser the distance between the mirrors is engineered specifically to set up a standing wave within the laser cavity. The resonator condition which must be fulfilled to set up a constructively interfering wave is given by:

$$l_r = \frac{\lambda N}{2} \tag{1.5}$$

Where N is the mode number [47]. This means that the only wavelength that are multiples of half the cavity length can be supported. The optical cavity can have a infinite number of modes but only wavelengths that fall within laser gain bandwidth will be amplified [48]. This effect can be seen in figure 1.7.

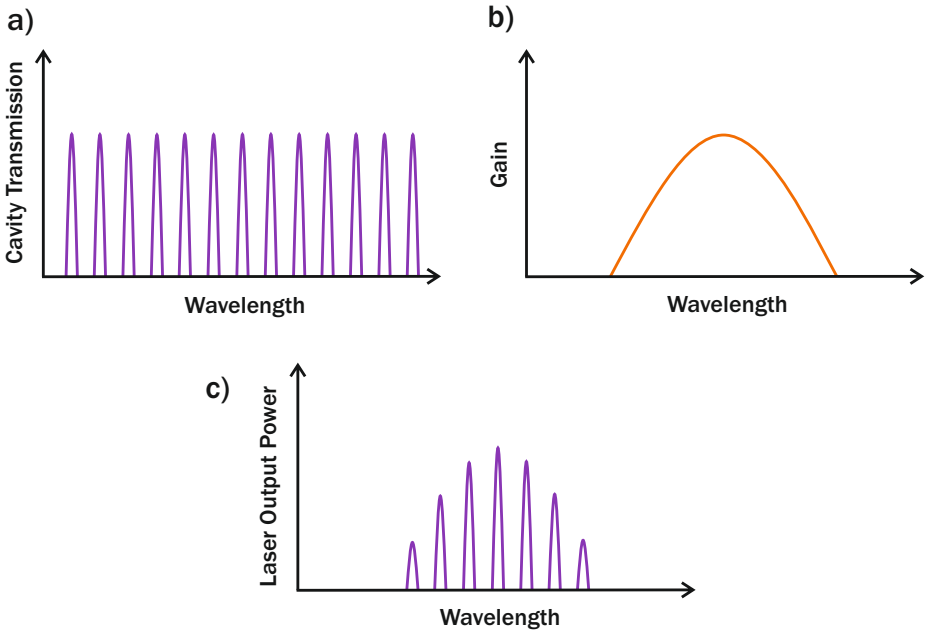

Figure 1.7: a) Shows optical modes set up in the cavity. b) Shows the gain bandwidth of a laser. c) Shows the output wavelengths and powers that can be output by the laser.

The first laser was demonstrated in 1960 [49] using a ruby crystal as the lasing medium stimulated by a flash tube. The ends of the crystal were flat and polished with one of them completely silvered and the other only partially silvered, creating the lasing cavity.

1.3.2 Lasing Materials

From the previous section it can be seen that one of the main components of a laser is the active medium. The active medium is the material that has lasing transitions and therefore is the material that dictates the output frequency. Active mediums can come in many forms including gas: Helium Neon lasers [50] and Carbon Dioxide lasers [51]; dye lasers: Rhodamine lasers [52] and Umbelliferone lasers [53]. Another type of active medium is solid state lasers and are the ones that are used throughout this work.

Solid state lasers are defined mainly as those whose active medium is a transparent host material (oxides like Al_2O_3 and fluorides like $YLiF_4$) that has been doped with transition metal ions (Ti, C, Fe), rare earth metal ions (Ce, Yb, Dy) and actinides (u). The active ions provide the energy levels that are responsible for the lasing transitions and the host material provides physical characteristics that help determine the efficiency of the laser, such as the

thermal conductivity and expansivity. The doped atoms replace atoms in the host material and the arrangement of host atoms around the doped atoms will change the energy levels around it. The material can be engineered to produce different lasing transition and therefore wavelength photons by changing the dopant level in the active medium [54]. Popular solid state lasers are ones based on Neneodymium and Ytterbium crystals including Neodymium Yttrium Aluminum Garnet (Nd:YAG), Nd:YLF (Neneodymium-doped Yttrium Lithium Fluoride) and Yb:YAG (Ytterbium-doped Yttrium Aluminum Garnet). Whilst Neneodymium and Ytterbium laser can achieve high powers due to the longer energy level decay times they can not produce ultrafast laser pulses (within the hundreds of fs range) therefore these are not suited to CPA. For this reason the most common solid state active medium used is Titanium:Sapphire (Ti:Sapphire) as it has a high gain bandwidth and high saturation fluence. This means that peak powers within the Terrawatt and Petawatt region have been achieved [55].

1.3.3 Titanium-Sapphire Laser

Ti:Sapphire solid state laser are fabricated by doping a Sapphire (Al_2O_3) host crystal with Titanium ions (Ti^{+3}). With an output wavelength range from 660 nm to 1180 nm Ti:Sapphire lasers provide the most amount of tuneability of all solid state lasers. The high degree of tuneabillity is due to the fact that the active medium has a large gain bandwidth, caused by the fact that the energy levels have strong interactions with lattice vibrations.

Ti:Sapphire lasers utilise a four-level energy system like that discussed in section 1.3.1. Electrons are pumped from the ground state to the pumping energy level, E_4, efficiently through excitation photons of wavelengths in between 400 nm and 600 nm this means it has good green-blue light absorption with the maximum absorption at 490 nm. From E_4 electrons decay fast through phonon emission to the the upper lasing level, E_3. where the longer life time of around 3.2 μs allows a population inversion to be achieved over the lower lasing level E_2. The lasing transition between E_3 and E_2 produces the coherent emitted photons. The electrons again rapidly decay via phonon emission to the ground state E_1 from E_2 to be available for pumping again.

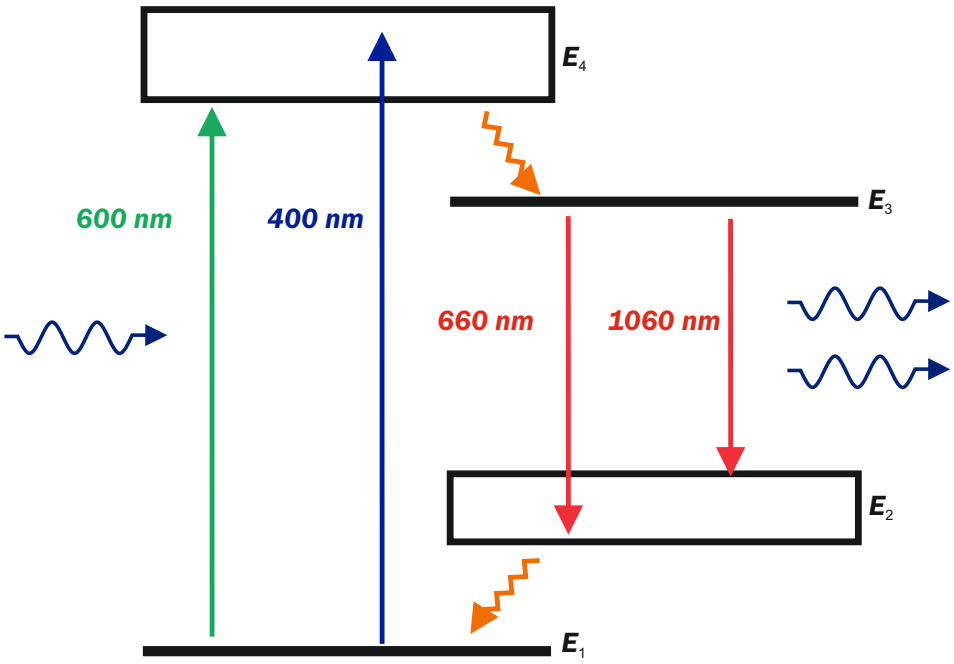

Figure 1.8: A four-level Ti:Sapphire energy level diagram, broad absorption of the blue-green range is shown as well as the broadband emission available.

When absorbing green light the output emission is of a longer wavelength, the red region of the spectrum spectrum. Population inversion when emitting red light is more easily achieved because the lower lasing level for this wavelength is at the top of a multi-vibrational level which is unoccupied due to the fast vibrational decay time. Ti:Sapphire lasers are often used in amplified laser systems as they are ideal for the creation and amplification of fs pulses, explained by the fact they has such a large gain bandwidth. These desirable ultrashort pulses can be obtained through modelocking (explained in 1.5.) [56] [47]

1.4 Q-Switching

The Q factor, also known as the quality factor, of the cavity is a quantity that defines the losses in the cavity. The Q factor is calculated by eq 1.6 where E_s is the stored energy and E_{loss} is the round trip energy losses [46].

$$Q = 2\pi \frac{E_s}{E_{loss}} \tag{1.6}$$

Q-Switching is a method employed in laser engineering to produce an intense short laser pulse. This is achieved through the manipulation of the Q factor to prevent the cavity from oscillating, thus allowing the gain in the cavity to be

altered.

To begin, the cavity losses are kept artificially high, this means that the Q factor of the cavity is kept low. The active material in the cavity is continually pumped during this period increasing the population inversion in the material and hence increasing the gain. During this pumping period the gain reaches a much higher value then would be reached under normal operating conditions. Once the gain is high enough, the Q factor is quickly switched back to a higher value causing oscillations to begin in the cavity again, the round trip losses are heavily outweighed by the round trip gain. As the pulse oscillates it builds up at a rapid rate, depleting the population inversion on a similar timescale, causing then a rapid drop in gain in the cavity to below the round trip loss levels and consequently causing lasing to stop in the cavity (depicted in figure 1.9). The Q factor is then set low and the process begins again. The rapid processes involved allow for intense short pulses of radiation to be emitted. The peak power achieved from a laser in Q switched mode can be up to four times higher then can be generated in the same laser under continuous wave operation.

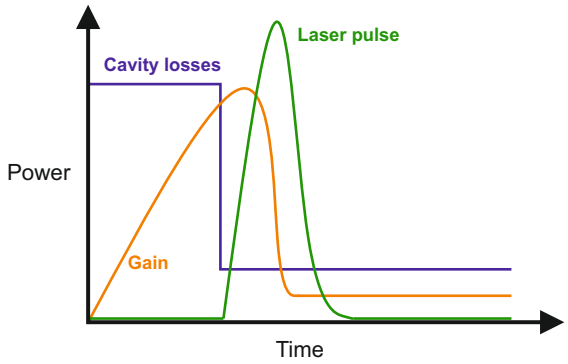

Figure 1.9: The graph shows the changes in the cavity during Q-Switching operation. Losses are kept artificially high until the gain has reached a peak amount, before the Q-factor is switched and losses drop enabling a pulse to be emitted.

There a several different methods utilized to control the Q factor within the cavity, each with their own merits and drawbacks. One of the earliest methods was a simple rotating mirror at one end of the cavity. The mirror is placed on a rotating shaft and controls the Q factor by only allowing oscillations when the mirror aligns with the system and opposite mirror. Whilst being a cost effective and relatively simple method, it suffers from slow switching speeds and mechanical vibrational noise that can cause miss-alignment ultimately leading to unreliability from the system.

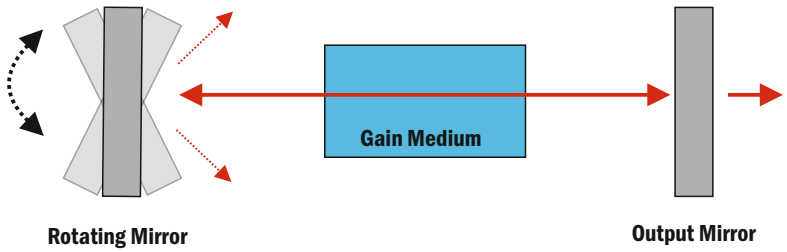

Figure 1.10: An active Q-switching method is using a rotating mirror at one end of the cavity to control the cavity losses during operation.

Another method used is a passive saturable absorber. This is a passive component placed into the laser cavity to control the Q factor by absorbing the radiation keeping the losses high. The active medium is pumped continually building the population inversion until the gain overcomes the losses via absorption and thus oscillations begin within the cavity. The oscillations will completely saturate the passive absorber enabling the pulse to grow rapidly within the cavity leading to an intense pulse. Saturable absorbers are a fairly simple solution, they do not require lots of optical components within the cavity and require no external control. However they do have a myriad of disadvantages such as the need for careful adjustment initially, the inability to sync the laser timing to external equipment, amplitude fluctuations, timing jitters and some saturable absorbers such as organic dye solution as at risk of photo-chemical degradation requiring replacement.

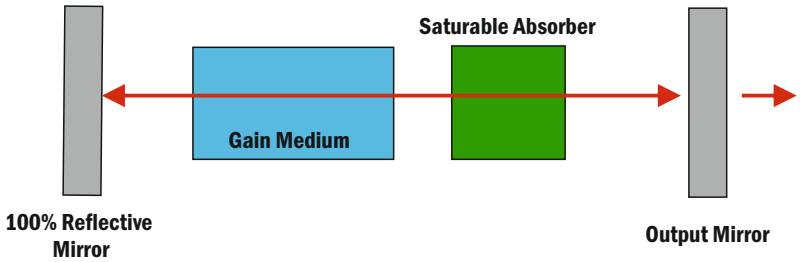

Figure 1.11: A passive Q-switching method where a saturable absorber is placed between one of the reflective mirrors .

Electro-Optic (EO) Q switching involves the use of an EO modulator as the Q factor manipulating unit. The EO modulation unit comprises of an EO crystal which has an induced birefringnece when influenced by an applied electric field, this is known as a Pockels crystal, and another polarising element such as a prism. A voltage can be applied across the EO crystal so that it acts as quarter-wave plate, this means that the radiation circulating the cavity undergoes a 90° polarisation rotation and is then coupled straight out of the cavity after a single

round trip. Turning the voltage off enables the Q factor to become higher and the cavity can enter a low loss mode. This can be done in the opposite configuration where turning on the Pockels crystal can correct for the birefringence of the polarising element and switch the cavity to a high Q factor. This method of Q-switching is capable of the fastest switching times with the most precise timing and stability. However the EO crystal are typically quite expensive and susceptible to laser damage with intense pulses. This method also requires expensive voltage sources that are able to produce fast rise time voltage pulses [57].

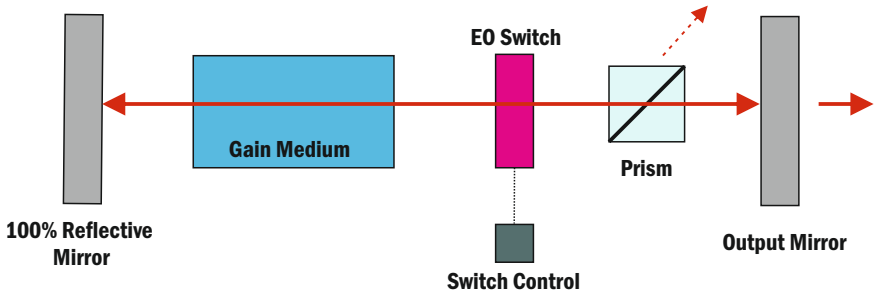

Figure 1.12: Q switching with an EO modulator in the laser cavity consists of turning the EO switch on and off to control the polarisation of the beam. When the switch is set to keep the Q factor low the polarisation induced will cause it to not pass through the prism and keep losses high.

Whilst Q switching has its merits for use in the generation of intense laser pulses it can not be used to achieve ultrashort laser pulses with pulse widths generally in the ns range [58], this becomes an issue when trying to generate broadband THz pulses (discussed further in section 1.8.5).

1.5 Mode Locking

When a laser is used in normal operation, all of the modes in the laser cavity will act independently of each other, that is to say that the amplitude and phase of the modes vary with time. The output field of a laser is a sum of the fields of all of the different modes, meaning the output of a laser operating with multiple modes is that field will also vary in time. The output field will be averaged out to a steady value if there are many modes. [59]

Mode locking refers to the phenomenon of locking of the cavity modes phases, this coherence equates to a pulsed field to be produced [60]. When the maximum intensity of each mode constructively interferes a high intensity pulse is produced with a small pulse width. The pulses produced come as a pulse train which is many pulses at periodic intervals. How many pulses are produced in a given time period is known as the repetition rate of the laser. The repetition rate

is calculated as the time a round trip of the laser cavity takes as only a single pulse is released on each pass, this is calculated as a time:

$$T = \frac{2l}{c} \tag{1.7}$$

Where l is cavity length and c is the speed of light.

One of the key reasons behind the use of mode locking is to produce high intensity short pulses. A higher intensity is produced from mode locking due to the modes combining at the locked phase mode to produce an enhanced output, the peak intensity for a mode locked laser with equal amplitudes is proportional to $N^2 |E_0|^2$ where N is the number of modes and E_0 is the amplitude. This can be compared to the average intensity of a unlocked laser as $N |E_0|^2$. From this it can be seen that in mode locked operation the intensity is increased by a factor of N. [61]

The minimum pulse width that can be obtained for a given lasing medium can be calculated by:

$$\Delta t = \frac{K}{\Delta v} \tag{1.8}$$

Where K is a number that depends of pulse shape and is called the transform-limited pulse and Δv is the gain bandwidth of the lasing material. [62]

There are two main methods of mode locking that are employed; active mode locking and passive mode locking. Each have been shown to be effective at producing mode locked pulsed emission. Active mode locking involves an external influence in the laser cavity to control the mode locking. A modulator (electro-optic, acousto-optic types) optic can be used to synchronously control the cavity losses with the pulse round trip around the cavity. For passive mode locking a saturable absorber can be used within the laser cavity to modulate the losses. The association between saturable coefficient and the saturation in the amplifying material allows a natural modelocking to take place that can take place without any external interference. With passive modelocking the first saturable absorbers that were used were ones made for dye lasers, these were not particularly suitable for solid state lasers, the recovery time and limited bandwidth meant that sub picosecond pulse widths could not be achieved.

The discovery of Kerr lens effect (Kerr Lens Mode Locking (KLM)) has lead to femtosecond pulse widths becoming achievable from solid state lasers. KLM is a technique that uses the Kerr lens effect, which is where a beam can be focused to a higher intensity in the case that the refractive index of the medium it travels through is also intensity dependent. The higher intensities of the beam will be strongly focused whilst the lower intensities will not be focused much. Adding a slit into the beam path will further increase the losses of the weaker intensities. Hence this technique can act as a saturable absorber in the cavity.

One of the key drawbacks of KLM is that the cavity will not inherently enter pulsing mode spontaneously. A strong intensity fluctuation is needed to start the Kerrs lens effect. This can be done by changing the optical path length in the cavity; quickly moving one of the cavity mirrors or rotating an optical slide will achieve this. [62]

1.6 Spitfire Ace PA Laser

The amplified laser system used throughout this project is the Spectra Physics Spitfire Ace PA. This amplified laser system is an 800 nm wavelength regenerative amplified laser. The system consists of four main components; a seed laser, two pump lasers and amplification section. A schematic of the system is presented in figure 1.15.

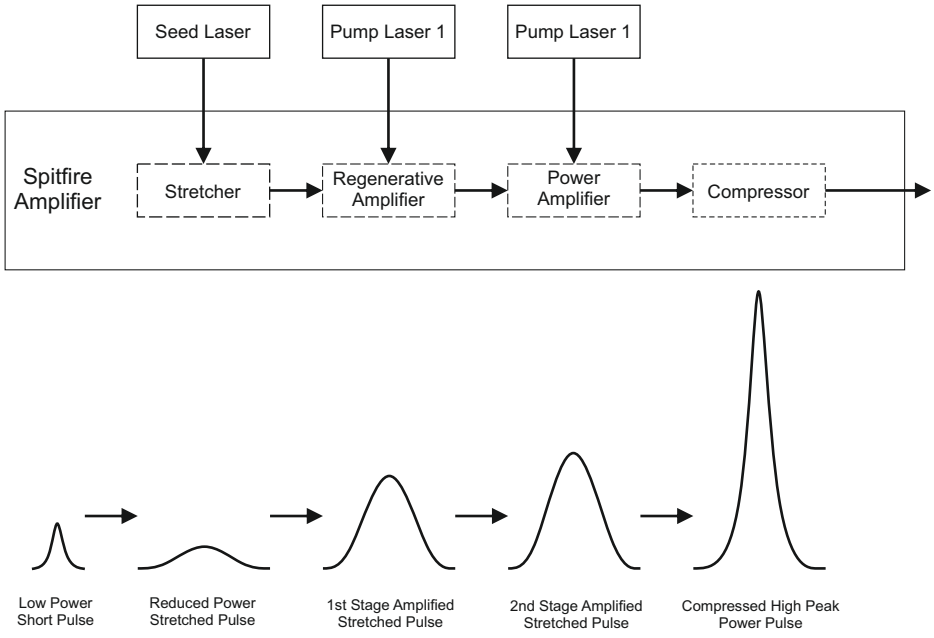

Figure 1.13: Block diagram for the Spitfire Ace PA laser showing the different stages of operation, below shows a representation of how a pulse is stretched, amplified then compressed again. Reproduced from [1]

A Spectra Physics Element is used for seeding purposes, this is a diode pumped Ti:Sapphire oscillator that operates with a central bandwidth of 800 nm. As this is an ultrashort oscillatory system the pulse width is ∼20 fs at a 80 MHz repetition rate. Both pump lasers are Spectra Physics Ascends which are Q-switched Neodymium Yttrium Aluminum Garnet (Nd:YAG) lasers capable

of producing 35 W of output power at a central bandwidth of 527 nm with a 1 kHz repetition rate.

The seed laser produces the initial pulse into the system, it passes into a Faraday isolator that protects the seed laser from any reflected pulses. The Faraday isolator works by polarising the seed pulse twice by 45 degrees so that any reflections are unable to pass through the polarising filter. The next stage is for the pulse to be stretched in time, this is so that the pulse can be amplified safely without the risk of damaging any of the other optics in the amplifying system. To stretch the seed pulse in time it is passed through a Vertical Retro-Reflector (VRR) and a stretch grating that spatially separates the different wavelength. Longer wavelength have to travel further than shorter wavelength and hence become stretched in time. The stretched pulse performs two passes through the stretch grating before being reconstructed and passed through a polarisation rotation periscope and on to the amplification section.

The amplification section consists of two parts, the regenerative amplifier and the power amplifier. Firstly, the seed beam passes into the regenerative amplifier section. This section, seen in figure 1.14, makes use of Pockels cells to manipulate the beam through the amplification crystal. A Pockels cell is an electro-optic device that works on the principal of the Pockels effect. The Pockels effect is found in crystals with a lack of inversion symmetry, when under the influence of an electric field the refractive index of the material can be altered. The change in refractive index has a linear dependence with the strength of the applied electric field strength, hence it can be used as a voltage controlled waveplate [63].

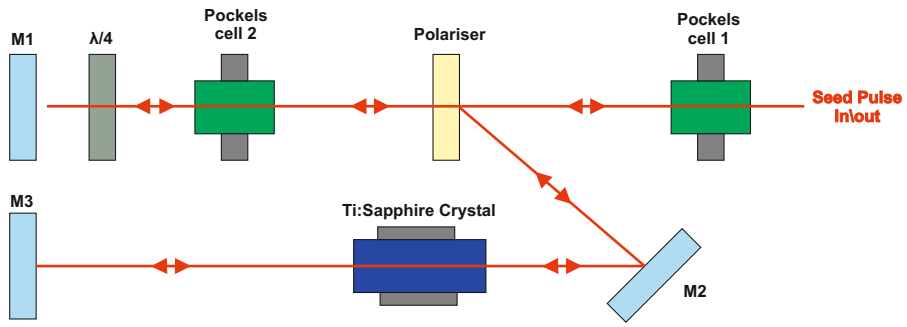

Figure 1.14: Diagram showing the amplification section, the seed beam passes into a 'z' style configuration with use of the Pockels cells to confine it to the cavity for amplification.

If the first cell on the beam passes through to the second cell. If second cell is also on then the beam will be reflected back through the section without any amplification. If the second cell is off then the beam is reflected through a

Ti:Sapphire crystal that is optically pumped by a Q-switched laser. As the beam passes through the crystal it increases in gain and returns to the Pockels cells. If the amplified pulse reaches the second Pockels cell before it is switched on again it is moved towards the power amplifier section, if not then the pulse becomes trapped in this cavity. By careful control of the Pockels cells the number of passes through the crystal can be controlled and therefore the amount of gain the pulse receives can be controlled.

In the power amplifier section the pulse is once more passed through an optically pumped Ti:Sapphire crystal to increase the pulse output energy, only one pass through the crystal happens in this section before the pulse is directed to the final stage of the process, the compressor.

The compressor works in reverse of the stretching grating used at the start of the amplifier system. The pulse's wavelength are split once more, however this time the shorter wavelength are made to travel further and therefore reversing the temporal stretching. At this point the pulse can be adjusted to optimise peak power, by optimising the temporal compression. The pulse reflects back through the compression grating which reverses any stretching effects before being directed out of the system [1, 64].

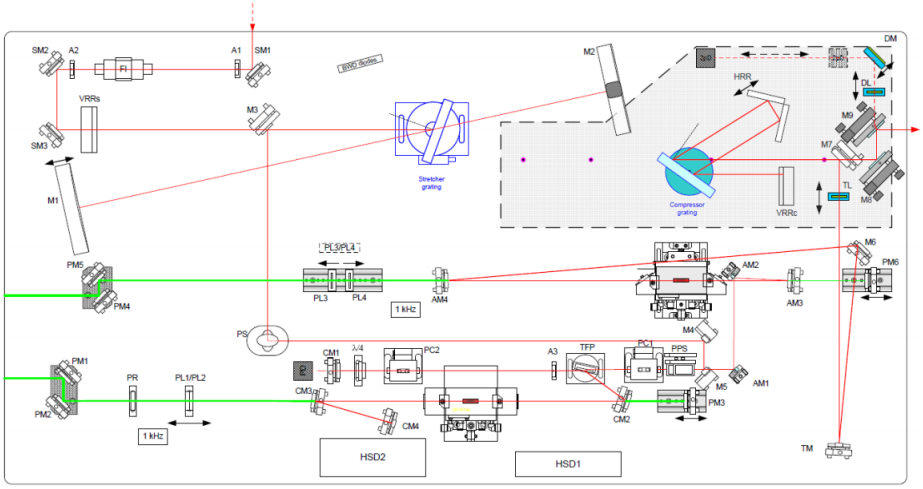

Figure 1.15: Schematic for the Spitfire Ace PA laser. Diagram provided by Spectra-Physics [1]

1.7 High Field Terahertz Sources

This section will be an overview of some of the most common methods of generating high field strength THz sources.

1.7.1 Air Plasma Generation

Air plasma generation is technique that utilises the ionization of a gas as a means of generation of THz radiation. This technique is set apart from others as it uses ambient air or another gas as the generation medium. Whilst air plasma generation is possible using a single wavelength, the highest efficiency and THz field strengths have been achieved utilizing a 2-colour approach. [65]

As with other techniques for THz generation ultrafast laser pulses are required, for this a Ti:Sapphire regenerative amplifier can be used. The 800 nm (ω) output from the laser is focused through a Beta-Barium Borate (BBO) crystal to acquire a second harmonic wave at 400 nm wavelength (2ω). The first and second harmonics interact at the focal point generating an ionised plasma, a third-order nonlinear process takes place at this ionised plasma spot generating intense ultra-broadband THz radiation [66]. Due to the two wavelengths differing phase velocity in air, the phase mismatch (φ) at the focal point depends on the distance between the BBO crystal and the focal point. This has to be adjusted to achieve maximum interaction between the waves to achieve the highest THz field possible [67]:

$$\varphi = \frac{\omega}{c(2n_{2\omega} - n_{\omega})d} \tag{1.9}$$

where n_{ω} and $n_{2\omega}$ are refractive indices for the first and harmonic waves, and d is the distance between the crystal and focal point.

The THz electric field due to the third-order nonlinear process of the two beams mixing in the plasma can be approximated from a four-wave-mixing mechanism approximation [68]:

$$E_{THz} \propto \chi^{(3)} E_{2\omega}(t) E^*_{2\omega}(t) E^*_{2\omega}(t) cos(\varphi) \tag{1.10}$$

Where $\chi^{(3)}$ is the third order susceptibility, E_{ω} and $E_{2\omega}$ are the electric field strengths of the first and second harmonic beams respectively.

THz generation via an air plasma method has been proven to yield field strengths of 1 MV/cm [69] and ultra-broad bandwidths of up to 100 THz [70]. Disadvantages with air plasma generation include the need for intense laser pulses, low optical-to-THz efficiency and the need for very precise alignment to ensure critical focusing is achieved. [65]

1.7.2 Free Electron Lasers

Free Electron Lasers (FELs) are a source of radiation capable to operate over a large range of the electromagnetic spectrum, which makes them highly useful. [71]

The main components of FELs are the electron accelerator, laser cavity and the wiggler (sometimes referred to as the undulator) with the latter two making up the FELs resonator. The wiggler itself is a magnetic array made up of alternating polarised magnet pairs, this creates a periodically transverse magnetic field. A relativistic electron beam is steered into the resonator by a magnetic field and as the electrons travel along the cavity of the resonator the alternating magnetic field forces them to oscillate about the axis of the cavity. This oscillatory motion causes emission of EM radiation [72] this will co-propagate inside the laser cavity with the electron beam. The wiggler field is set so that the interaction between it and the radiation causes the electron beam to become bunched, at a modulated period which matches that of the laser wavelength. This is an important process in order to generate coherent radiation from the laser. As the radiation makes round trips of the cavity it will become amplified from the interaction with the electron oscillations.

The wavelength of the emitted radiation is give by:

$$\lambda = \frac{\lambda_w}{2\gamma^2}[1 + K^2] \tag{1.11}$$

where λ_w is the wiggler magnetic field period, γ is the Lorentz Factor, k is the wiggler parameter given by:

$$K = \frac{eB\lambda_w}{2\pi m_e c} \tag{1.12}$$

Where B is the magnetic field strength, e is the charge of an electron and m_e is the effective mass of an electron. This parameter K is usually chosen to be close to 1 to account for the Doppler shift caused by the induced motion of the electron beam. [8]

Emission across large regions of the EM spectrum is achieved by altering some of the parameters of the device including, the wiggler period, electron beam energy and magnetic field strength. The wiggler period is typically set during construction so the wavelength deciding factors are the electron beam energy and magnetic field strength [72]. FELs are capable of high power generation of THz as they do not suffer from conventional problems attributed to material damages and thermal lensing as the amplifying medium consists of only electrons. The radiated emission from FELs is typically narrowband when compared to that produced by other methods disscused here, and due to the nature of the generation mechanism, the pulse shapes are often complex [73]. The major disadvantage of these devices is the cost of constructing and maintaining the equipment, FELs are in essence small particle accelerators and thus take up a lot of space, and are expensive to run. [8]

1.7.3 Optical Rectification

Optical Rectification (OR) is a high power THz generation technique that is capable of producing broadband pulses. The basis of this technique is to use an EO crystal pumped by a pulsed fs laser source. Popular EO crystals used are Zinc telluride (ZnTe) and Gallium Phosphide (GaP). The way in which these devices work is by making use of the non-linear effects within the crystal. The induced polarisation in the EO crystal is dependent on the polarisation of the radiation that is entering the crystal, more specifically the polarisation will change with the angle of the radiation in relation to the crystal axis.

As the incident radiation is not a constant source but in fact a fs laser pulse, this gives rise to a time dependence in the induced polarisation which follows the envelope of the fs pulse. The induced transient polarisation gives rise to the emitted THz pulse.

An ideal crystal would have zero dispersion and the refractive index of both the THz and the optical pulse would be equal. In this ideal case the emitted THz radiation propagates with the incident fs pulse at the same speed, and the amplitude of the THz pulse would increase linearly with distance. However there is dispersion within the crystal and the incident pulse and the THz pulse will propagate at different speeds. At a certain distance the two waves begin to destructively interfere with each other, meaning over a long distance the amplitude of the THz radiation would be equal to zero. The length at which this happens is known as the walk-off length:

$$l_w = \frac{c\tau_p}{(n_T - n_o)}. \tag{1.13}$$

where τ_p is the femtosecond pulse duration. A long walk-off length is essential for efficient THz generation as well as the EO crystal being sufficiently thinner than the walk-off length [2].

A big problem with OR is with phase matching, in that the optical wave velocity must be closely matched with the THz wave velocity to ensure efficient generation. At present it is only possible to achieve this over a limited spectral range [74].

Inorganic crystals such as ZnTe are relatively stable and phase matching can be achieved at popular excitation wavelengths like 800 nm, however many inorganic crystal have strong phonon-interactions at lower frequencies causing gaps in the emitted bandwidth [75]. Moreover due to low saturation thresholds and smaller nonlinear coefficients THz fields above 0.6 MV/cm have not been achieved [76]. More recently organic crystals like; DAST, BNA and DSTMS, have been shown to produce much larger THz field strengths owing to vastly superior nonlinear coefficients. These organic crystals have been reported as generating THz fields of up to 83 MV/cm [77]. However, organic crystals possess

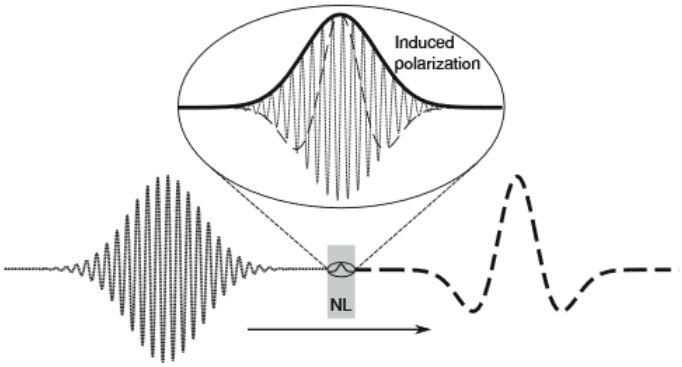

Figure 1.16: OR of a femtosecond pulse. Reproduced from [2]

issues that have held them back from wider application including degradation in ambient atmosphere, low optical damage thresholds and typically small crystal sizes.

Crystals used for generation of THz radiation using the OR technique have shown broadband emission up to 100 THz, but the radiation is strongly suppressed at particular phonon frequencies within the different crystals [78].

Lithium Niobate ($LiNbO_3$) is a popular choice for high field generation due to its large effective nonlinear coefficient and high damage threshold. For crystal used in the OR technique, having a large nonlinear coefficient is desirable to achieve higher field THz generation as the radiated energy is proportional to the square of the value. $LiNbO_3$ presents a difficult phase matching condition due to the large difference between refractive indexes of the pump beam and the THz radiation [75]. A technique utilised to circumvent this issue is to use a tilted-pulse-front approach (seen in figure 1.17) which was first demonstrated in 2003 by Stepanov et al [79]. As the name suggests the exciting pump beam is tilted relative to the phase front using a diffraction grating and lenses, if the tilt angle is selected correctly it allows the generated THz radiation to propagate with the pump pulse front ensuring constructive interference in the $LiNbO_3$. By creating this condition the phase matching conditions are satisfied and THz electric field strengths of up to 1.2 MV/cm have been reported [80]. Issues with this technique however include strong THz absorption above 2 THz at room temperatures, requiring cryogenic cooling to achieve greater bandwidths. Another problem includes the complicated set-up required when compared to other forms of high THz field generation. [81]

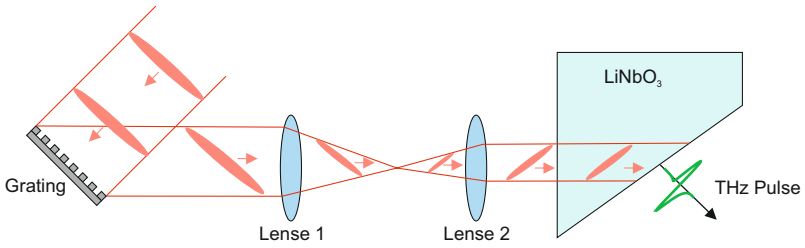

Figure 1.17: Generation of THz radiation in $LiNbO_3$ through the tilted-pulse-front technique. The pulse front is depicted as it changes through the optics in order to propagate with the THz in the crystal.

1.7.4 Spintronic Emitters

A recent development in the field, spintronic emitters offer the first use of ultrafast spin physics for THz radiation. The principle of these devices is the use of the inverse spin Hall effect [82] to create a transient current within the substrate. Devices consist of a heterostructures comprised of both ferromagnetic and nonmagnetic material (see figure 1.18). When the device is pumped with an ultrafast fs laser pulse, spin-polarised electrons are excited in the ferromagnetic layer and will diffuse through to the nonmagnetic layer creating a spin current. A transient current is then generated from the spin current due to the inverse spin Hall effect, giving rise to THz radiation from the nonmagnetic layer of the structure [83]. As this technology is relatively in its infancy there is much work being undertaken into engineering the composition of devices to improve aspects of emission including both the THz bandwidth and amplitudes. This has included study into the effects that thickness of layers in the heterostructure has on generation of radiation [84, 85], the material composition of the device has been studied to investigate the effectiveness of different ferromagnetic and nonmagnetic layers has [86, 87], the dependence of the layer interfaces on the generated emission [88], and work into different heterostructure composition to increase efficiency such as trilayers [86] and repeating multi-layers [89].

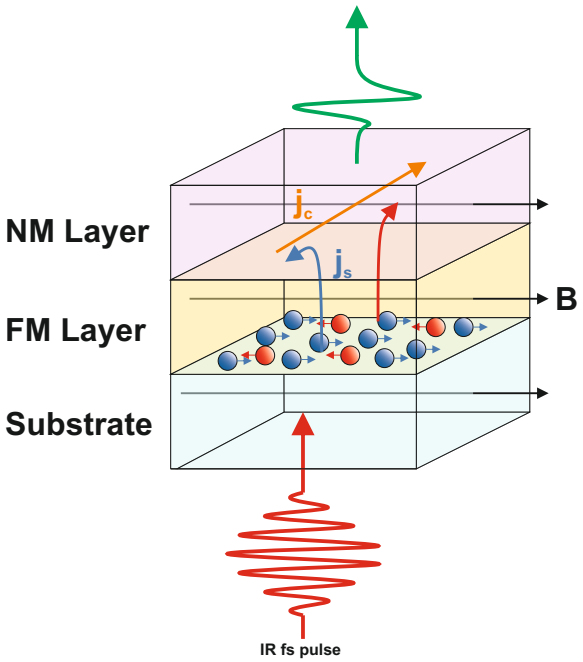

Figure 1.18: The generation technique within a spintronic emitter. A fs pulse excites spin-polarised electrons within the ferromagnetic layer (FM) causing a spin current (j_s) to diffuse through to the nonmagnetic layer. Through the inverse spin hall effect the spin current causes a transient current (j_c) to be set up, from this THz radiation is generated. The THz radiation is perpendicular to the applied magnetic field (B). Figure reproduced from [3]

There is much promise for these devices for spectroscopy with bandwidths of up to 30 THz reported [86]. When the pump excites the material THz is generated in both the forward and backward direction. Field strengths of up to 1.5 MV/cm have been reported [90]. However these devices do have limitations, efficiency is in the same region as generation from nonlinear crystals [86] of around $1e^{-6}$. Engineering the THz emission proves the most challenging aspect of this technology. THz emission is directly controlled by the optical pumping of the device, however modulation of the emission can be achieved through the magnetic field control. These emitters also provide less power for frequencies below 3 THz when compared to other generation techniques [86].

1.8 Photoconductive Emitters

Photoconductive antennas have been a widely adopted source of THz radiation [91–93], much like the name suggests they utilise the photoconductive effect as the underpinning mechanism to enable generation of THz within the device. The operation of these devices can be thought of as that of an optically fast

switch, a pulse from a laser pump source can 'switch' the device on causing electromagnetic radiation to be emitted. The first use of these devices to generate THz radiation extends back 35 years using a simple Hertzian dipole antenna fabricated on radiation damaged Silicon on Sapphire as the active material [94], and since then many different electrode geometries and photoconductive materials have been explored to enhance the generation [95–100].

1.8.0.1 Semiconductors

Understanding the structure of a semiconductor material is important to understanding its electrical properties. When solids are formed, the dense packing of atoms causes their outer orbitals to overlap; this causes the discrete energy levels of the free atoms to broaden into a continuous band of energy levels. Semiconductor materials contain an even number of electrons per atom, which results in the highest-filled energy band being completely filled with electrons. This highest-filled band is known as the valence band, which is separated in energy from the next lowest unoccupied energy band, called the conduction band. The separation between the valence and conduction band is known as the band gap, E_g. In order to achieve electrical conductivity, an energy equal to E_g is needed to excite electrons into the conduction band; this can be achieved through different processes such as absorbing photons or thermal excitation [101].

A key distinction of a semiconductor is that at absolute zero, there is no conduction; however, as temperature increases, a finite number of electrons can be thermally excited into the conduction band, allowing the conduction of electricity. The difference between a semiconductor and an insulator is the size of the band gap, with insulators having much larger band gap energies.

Looking at LT-GaAs in particular it is a Face Centred Cubic lattice structure with a direct bandgap. This means that the maximum energy point of the valence band matches with the minimum energy point of the conduction band at the Brillouin centre 'Γ' (shown in figure 1.19). The two valence bands that meet in the zone centre relate to the heavy and light hole bands. The band gap energy is 1.424 eV at 300 K [102]. Two important features to point out are the shallow defect states and the deep traps. The deep traps are a product of the excess arsenic present during the growth and annealing (explained in 2.2). The arsenic precipitates act as buried Schottky barriers [103] and are the primary electron trapping mechanism. The shallow defects are due to local potential fluctuations induced by the impurities in the lattice.

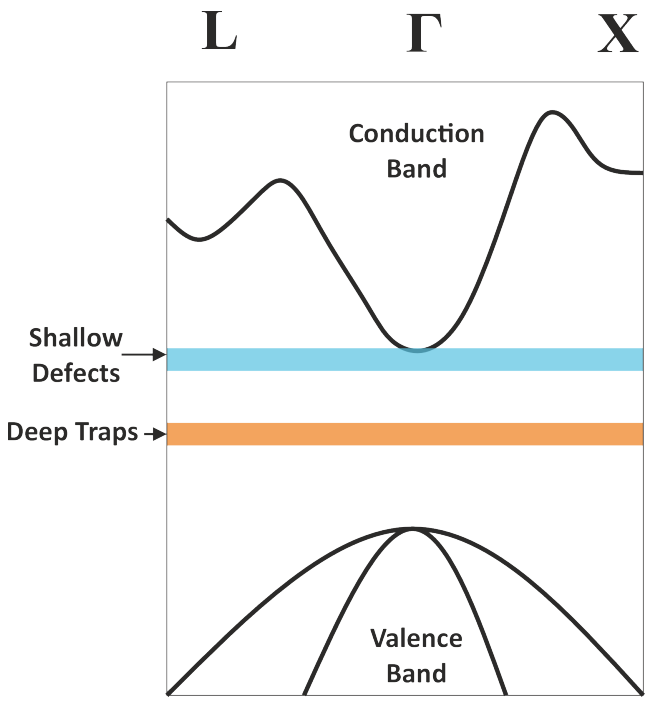

Figure 1.19: The band structure of GaAs showing the direct band gap at the Brillouin centre Γ and the subsidiary minima at X and L. Also depicted are the deep traps and shallow defect states present in LT-GaAs.

1.8.1 Gunn Effect

Under the influence of an applied electric field, 'E', the electrons will begin to drift with a velocity that is related to their mobility 'μ':

$$\mathbf{v}_d = \mu E \tag{1.14}$$

where

$$\mu = -\frac{e\tau}{m_e} \tag{1.15}$$

Hence, it can be assumed that increasing electric field strength will increase the drift velocity of the carriers, and at some point, this velocity will saturate. However, this is not exactly the case in GaAs; the drift velocity increases to a maximum point before decreasing to the saturation value (depicted in figure 1.20 (b)). Looking away from the Brillouin centre in figure 1.19, it can be seen that GaAs has peripheral conduction band minima valleys at both X and L; these are at a higher energy than the minimum at the zone centre. When electrons are excited into the conduction band, they will begin in the valley at the zone centre; here, the effective mass of the electrons is relatively low, and they have a high mobility, 'μ_1'. As electric field strength is increased, at some

point, 'ε_a', the electrons will gain enough energy to transition to the X and L valleys, here the effective mass is higher, and the mobility of the electrons is lower, 'μ_2'. Increasing the electric field strength past ε_a causes more electrons to transition to the higher band valley until ε_b is reached where all electrons have transitioned. The diagrams in figure 1.20 depict this effect. It can be seen that whilst ε is less than ε_a the velocity increases at a steady rate and peaks shortly after ε_a is reached. During the transition phase between ε_a and ε_b, a decrease in velocity occurs with increasing ε. This decreasing velocity region is known as negative differential conductance. Once ε reaches the value ε_b, and all electrons are in the higher valley, the velocity begins to increase again with the increasing field but at a slower rate. This effect is known as the Gunn effect and is exploited in a variety of applications [104–106].

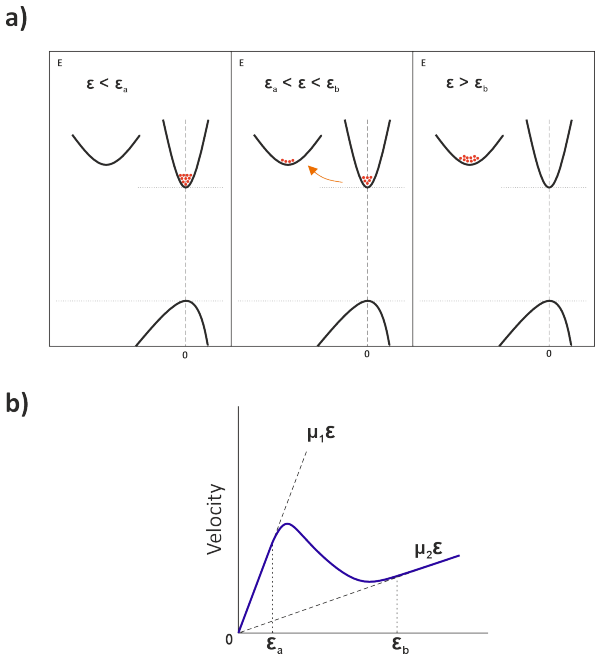

Figure 1.20: Depiction of the Gunn effect in GaAs. a) Shows the transition of electrons from the Γ valley to one of the subsidiary minima with increasing electric field strength. b) the resulting drift velocity of the electrons with increasing electric field strength.

Although the effect can be exploited for benefit, it can also be detrimental in photoconductive devices. In the negative differential conductance region, an increase in bias voltage produces a decrease in photocurrent and, hence, a decrease in the radiated THz field strength. This would restrict the field that can be applied for efficient operation.

1.8.2 Gunn Effect in LT-GaAs

The high-field carrier dynamics of LT-GaAs behaves slightly differently to that of intrinsic GaAs. The nature of the composition of LT-GaAs is explained in detail in section (2.4) and helps to explain the high field transport dynamics. The main difference of note in LT-GaAs is the excess arsenic precipitates that are formed in the material during growth and subsequent annealing. It has already been discussed that the mobility of an electron is dependent on its effective mass. However, another important parameter is the mean free time 'τ' (shown in eq 1.15). Due to the excess arsenic precipitates that are formed within the material, the likelihood of a carrier colliding with an ion in the lattice increases, which reduces the mean free time. It can be seen from eq 1.15 that a decrease in mean free time reduces the mobility and, hence, the drift velocity.

Work by Arifin et al. [107] showed that compared to pure GaAs, the mobility is drastically decreased in LT-GaAs. As the precipitate concentration is increased the mobility decreases due to the increase of scattering associated with this phenomena. They calculated that at a precipitate concentration of 10^{16} $cm^{-}3$ the drift velocity no longer shows a peak and subsequent fall like that seen in intrinsic GaAs. With the reduced mobility, the drift velocity exhibits a relatively linear increase with the increasing field. As discussed, the Gunn effect occurs when the electrons gain sufficient energy to transfer from the Γ valley to one of the subsidiary valleys (X and L). In LT-GaAs, the amount of kinetic energy that an electron can obtain is lower due to the reduced mean free path, and thus, the probability of it being able to transfer is reduced. This means that devices utilising LT-GaAs will be able to operate at electric field strengths above the Gunn threshold exhibited in pure GaAs.

1.8.3 photoconductive Effect

It is known that an external energy is needed to promote an electron to the conduction band of a material. As discussed briefly in section 1.8.0.1, this can be done through the absorption of a photon, and this mechanism gives rise to the increased electrical conductivity in the material. When photons are incident upon the semiconductor material, they can be absorbed if the energy exceeds the bandgap energy. When a photon is absorbed, its energy is transferred to a bound electron in the valence band, allowing a transition across the bandgap; this creates a free electron in the conduction band and an absence of an electron (a hole) in the valence band or in other words an electron-hole pair. This promotion of electrons will increase the free electron density and will hence increase the conductivity of the material [108].

The photocurrent is usually strongest when absorbing photons of energy slightly higher than that of the bandgap [109]. For example, GaAs PCA devices are a popular choice for use with Ti:Sapphire laser systems as the material bandgap is well matched to the lasers' emitted photon energy. Even at the

optimally matched wavelength, materials do not absorb 100 per cent of the photons due to various losses such as surface reflections [102].

1.8.3.1 Urbach Absorption Tail

In a perfect semiconductor, there would be no absorption of any photons that do not possess enough energy to promote an electron to the conduction band, i.e., photon energy smaller than the bandgap energy. Although this is not the case in a real-world scenario, there can be absorption below the bandgap energy. Due to defects and impurities in a semiconductor material's growth, there is a range of photon energies below the bandgap energy that can be absorbed [110].

Due to the disordered nature of some semiconductors, there is a fluctuation of electron energy states from place to place in the lattice; this results in an electron seeing a differing potential at different places in the material. If the disorder is large, then the density of electron states at the band edges develops tails, which will extend into the energy band gap. These localised states will allow for some level absorption below the bandgap energy; the energy range extending into the band gap is known as the Urbach energy [111]. This is reflected in the photon energy vs absorption graph as an exponential decay in the onset of absorption, which is called Urbach tail absorption. The width of the Urbach tail can be calculated from the Urbach energy, E_U [112]:

$$E_U = \frac{E - E_g}{ln(\frac{\alpha(E)}{\alpha_g})} \tag{1.16}$$

where E is the photon energy, $\alpha(E)$ is the absorption coefficient spectra α_g is the value of absorption coefficient at the bandgap energy E_g. A higher value of E_U indicates a higher amount of absorption below the band gap energy.

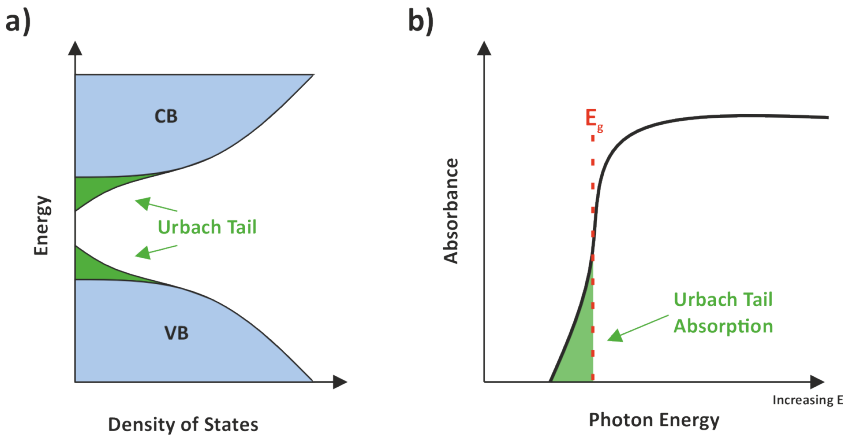

Figure 1.21: a) Urbach tail states extending into the bandgap of the semiconductor due to localised energy states below and above the bandgap edge occurring from defects and impurities in the material. b) The absorption as a function of photon energy showing absorption below the bandgap energy due to the tail states.

1.8.3.2 Absorption coefficient of LT-GaAs

The absorption spectra of LT-GaAs shows the material's behaviour in response to photon energies above and below the bandgap energy. As discussed in section 1.8.3.1, the absorption onset does not begin at the bandgap energy but proceeds it by some amount. The work by Dankowski et.al [113] determined the room temperature absorption spectra for LT-GaAs and the effects of annealing temperature on the absorption coefficient.

It is well established that LT-GaAs contains a large number of deep traps as a byproduct of the excess arsenic forming antisite defects. These defects allow for a broad absorption of energies sub-bandgap. Through annealing, the antisites form precipitates, which reduces the amount of absorption of energies below the bandgap, although it does not completely prevent it. Above annealing temperatures of 430 degrees, the absorption spectra for LT-GaAs begins to return to a similar form of normal temperature-grown GaAs. The sharper rise in absorption for photon energies just below the bandgap is due to the Urbach tail absorption detailed in section 1.8.3.1.

1.8.3.3 Temperature Dependence of GaAs

As discussed in 1.8.0.1, a semiconductor at 0 K has no electrons in the conduction band. However, as the temperature increases, some electrons can be thermally excited into the conduction band. As temperature increases, the number of lattice vibrations also increases; this lattice expansion causes the inter-atomic spacing to increase and, thus, the bandgap energy to decrease. It

is thus important to understand the temperature dependence of the material bandgap to understand the absorption dynamics.

Panish et al. [114] studied the temperature dependence of GaAs and showed that the bandgap energy of GaAs. The bandgap energy from 0 K to 1000 K was measured; from this, it can be seen that the bandgap energy lowers by $\sim$ 500 meV. Although this data was obtained using regular GaAs, the temperature dependence of the bandgap in LT-GaAs should follow this trend.

1.8.4 Basic Operating Principles

The basic operating principles of a PCA device is underpinned by the photoconductive effect (1.8.3). Shown in figure 1.22 is a photoconductive device that consists of a pair of electrodes atop a photoconductive material. The gap width is taken as the separation between the electrodes. The substrate is optically pumped by an ultrafast laser source, with pulse widths typically <200 fs, photons of energy equal to or greater than the material bandgap are absorbed and photogenerated carriers are generated in the material. The illuminated gap is placed under the influence of a biasing field across the electrodes. The biasing field accelerates the carriers in opposite directions, electrons towards the anode and holes towards the cathode, this gives rise to a transient photocurrent in the material. The transient photocarriers give rise to THz radiation which is emitted from the device. There is an array of factors that dictate the nature of the THz generation that is emitted from the PCA. To help explain these factors, we introduce the simple current surge mode (1.8.5).

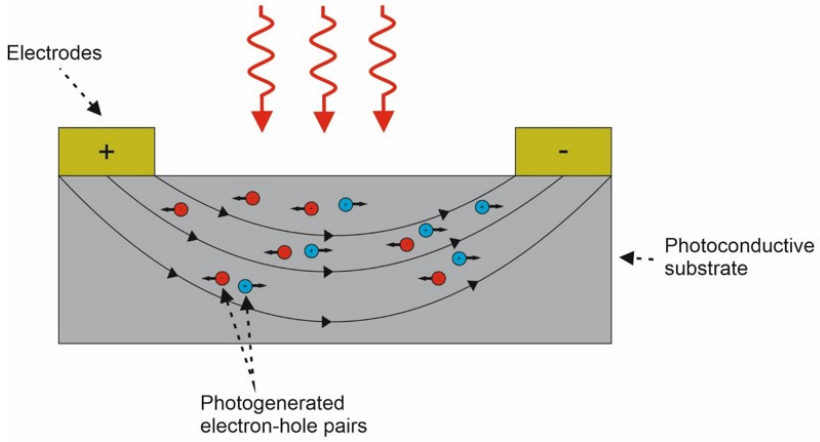

Figure 1.22: Diagram showing carriers being accelerated under the influence of a biasing field within an active photoconductive material.

1.8.5 Current Surge Model

A current surge model can be used to understand the carrier dynamics within a biased photoconductive material. This model is based on a Drude-Lorentz theory of carrier transport in semiconductors. This model is an ideal tool to investigate the effects of material properties on carrier dynamics and, ultimately, THz generation characteristics of the materials. The model is based on a biased semiconductor material optically pumped by an ultrafast femtosecond laser. The model considers different effects within the material that affect the generated current, including electron and hole interactions, dynamic space charge effects, carrier scattering and trapping times. The model mentioned here is adapted from the work seen in [115, 116] and coded in MATLAB by Dr J Freeman. This model specifically looks at LT-GaAs as the active material.

1.8.5.1 Model Assumptions

The model presented by Piao et al. and adapted for use here makes a number of assumptions. Firstly, as the trapping of free carriers into the midgap defect states is much faster than the electron-hole recombination time in the material, this is taken as the carrier lifetime. The model also ignores any non-linear absorption that takes place from mid-gap states, although it is stated that these effects at 800 nm are negligible. A constant momentum scattering time is assumed for all carriers, and a constant effective mass for both holes and electrons is used within the calculations. The model has no variation in space and, as such, does not take into account specific volumes, geometries or distances.

1.8.5.2 Theory of the model

When photons of sufficient energy are incident upon the active material, carriers will be generated at a rate proportional to the density of photons absorbed, $G(t)$. The pump laser is assumed to be a Gaussian pulse; thus, the time dependence of the generation of carriers also takes this shape. The time dependence of the carrier density within the active material can be given by:

$$\frac{dn}{dt} = -\frac{n}{\tau_c} + G(t) \tag{1.17}$$

where n is carrier density, and τ_c is the carrier trapping time. The trapping time is considered the dominant factor in determining carrier lifetime because the free-carrier trapping time is much shorter than the electron-hole recombination time. For this model, the carrier trapping time is treated as the equivalent of the carrier lifetime. The biasing field across the active material will accelerate the carriers at a rate given by the equation:

$$\frac{dv_{e,h}}{dt} = -\frac{v_{e,h}}{\tau_s} + \frac{q_{e,h}}{m^*_{e,h}}E \tag{1.18}$$

where $v_{e,h}$ is the average carrier velocity, $q_{e,h}$ is the effective charge of an electron (hole),τ_s is the momentum relaxation time, $m^*_{e,h}$ is the effective mass

of an electron (hole) and E is the electric field strength at the carrier position. The local field at this point is influenced by screening due to the separation of carriers and is lower than the applied bias:

$$E = E_{bias} - \frac{P_{sc}}{\eta\epsilon} \tag{1.19}$$

where P_{sc} space charge polarisation, η is the geometric factor (equal to 3 for an isotropic dielectric material), and ϵ is the permittivity of the material. Both trapped and free carriers contribute to the screening of the electric field. The time dependence of the polarisation is dependent on the recombination time, τ_r, and the current density contribution of the electron-hole pair, J:

$$\frac{dP_{sc}}{dt} = -\frac{P_{sc}}{\tau_r} + J \tag{1.20}$$

where:

$$J = epv_h - envv_e \tag{1.21}$$

And e is the charge of a proton. This photocurrent change causes the emission of radiation, as is known from Maxwell's equations. Hence the emitted THz radiation in the far-field is given by [117]:

$$E_{THz} \propto \frac{dJ}{dt} \tag{1.22}$$

This equation can be split into two separate components that contribute to the photocurrent:

$$E_{THz} \propto ev\frac{dn}{dt} + en\frac{dv}{dt} \tag{1.23}$$

The first term in equation 1.23 is the contribution from a change in carrier density, and the second term is the contribution arising from the acceleration of carriers under the influence of the bias field. This can be assumed by introducing a relative speed between the electron and hole:

$$v = v_h - v_e \tag{1.24}$$

The models' results show that certain parameters influence the generation of THz radiation more than others. The effects of ultrafast carrier density changes within the material dominate the emission of THz radiation compared to the contribution from carrier acceleration. Changes to the photocarrier density include carrier recombination, trapping of carriers or introducing carriers via laser pumping.

Initial conditions are set according to the chosen material parameters; here, the material chosen was LT-GaAs and resolved over a pre-determined time period; for these simulations, 5 ps was used. A Gaussian distribution function is used to provide an accurate simulation to determine the generation of carriers

from the incident ultrafast optical pump pulse. The resulting dynamics were calculated and plotted.

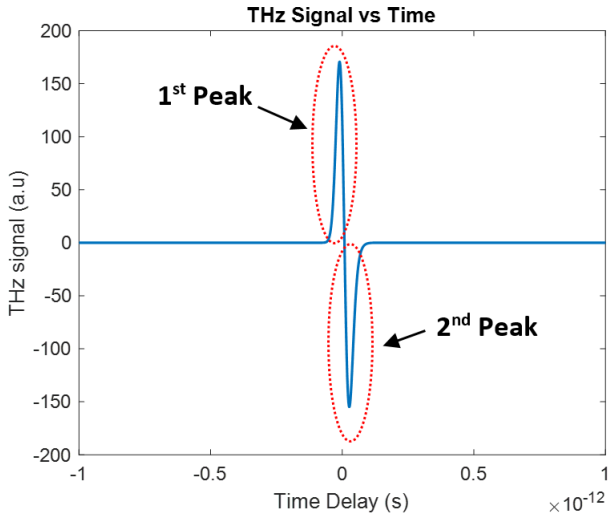

Figure 1.23: An simulated THz pulse, the two main peaks are indicated.

Figure 1.23 shows a simulated THz pulse. The shape of a generated THz pulse can be classified into two main parts. The first part is the positive peak; this part of the pulse is created through the generation and subsequent acceleration of carriers, so the pulse width of the pump beam, the carrier mobility, and the saturation velocity of the active material dictate this. A short pulse width, high mobility and high saturation velocity will ensure the first peak is temporally narrow. The second part of the pulse, the negative peak, is decided by the falling edge of the generated photocurrent [118].

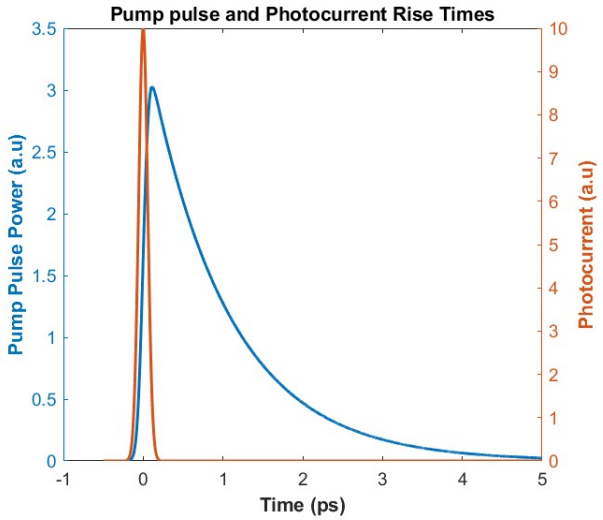

Figure 1.24: The photocurrent rise time in the material can be seen to follow that of the rise time of the excitation pump pulse incident on the material. After the pump pulse peaks, the response of the photocurrent is determined by material parameters.

From the graph in figure 1.24, it can be seen how, initially, the rise time of the photocurrent is proportional to the rise time of the incident pump pulse; the photocurrent continues to rise until the incident pulse peaks. Material characteristics dictate how the photocurrent behaves next, including carrier recombination time, trapping time and carrier lifetime. The effects of increasing carrier lifetime can be seen to increase the width of the photocurrent response, which leads to a reduction in emitted THz bandwidth. In figure 1.25, it can be seen that a longer carrier lifetime can improve the strength of the THz generated pulse; this can be attributed to the fact that shorter carrier lifetimes support much smaller free carrier densities as the carriers are trapped on a shorter timescale. Hence, longer carrier lifetimes lead to larger current densities and THz field intensities [119].

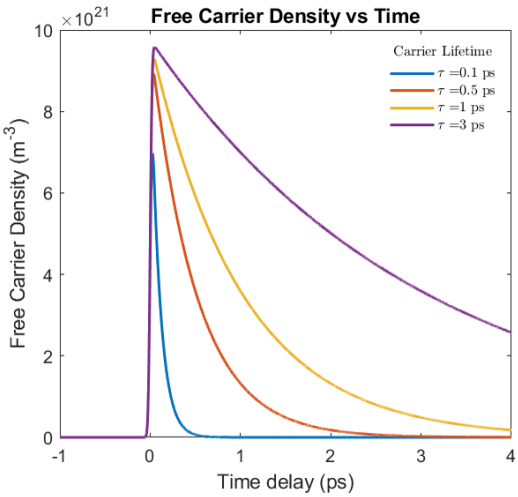

Figure 1.25: Free carrier density changes at different carrier lifetimes. Larger lifetimes lead to higher densities of carriers but much longer relaxation times.

Figure 1.26 shows the effects of increasing lifetimes on the THz pulse shape. Experimentally measured THz pulse shapes will also be strongly affected by dispersion and loss during propagation and the frequency-dependent response function of the detection system. This is explained further in section 1.9.2.

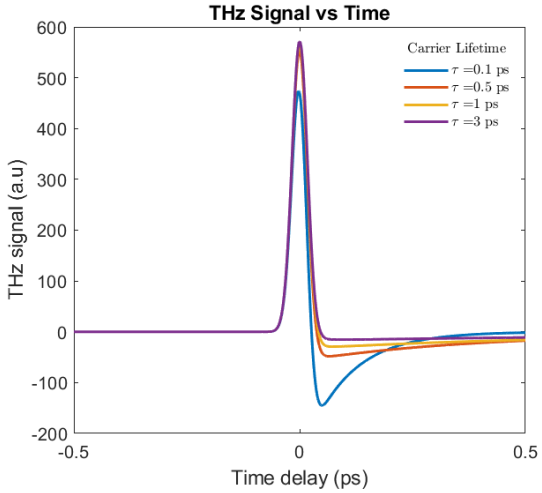

Figure 1.26: Variation of the THz signal in time with differing carrier lifetimes, the move from single cycle to quasi-half-cycle can be seen as carrier lifetime increases.

The graph in figure 1.27 shows the local electric field strengths and space charge polarisation as a function of time for different carrier lifetimes. These graphs show that the local electric field does not deviate significantly from the applied bias at shorter carrier lifetimes. With quicker recombination times, the space charge polarisation is much smaller due to lower carrier densities, which results in reduced screening effects. Longer recombination times cause a more significant space charge polarisation value due to larger separation and thus considerably more screening of the applied bias field and hence weaker local electric field strengths.

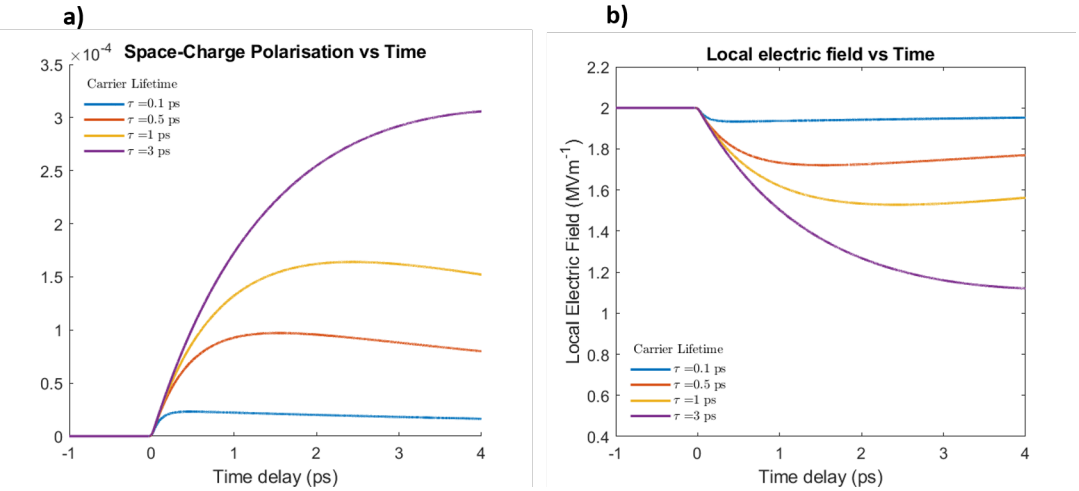

Figure 1.27: Graphs showing the variation of the local electric field strength and space charge polarisation with time at different carrier lifetimes

The current surge model can also be used to investigate the effects of carrier density in the active material and how this will affect the generation characteristics. Figure 1.28 shows the graphs of the local electric field and the THz time domain signal. From the THz time domain signals, it can be seen that as the carrier density increases, the THz pulse begins to oscillate in time. The reason for this oscillation can be explained by looking at the local electric field behaviour; as electrons are initially accelerated in the applied bias field, the polarisation induced by the separation of the charges acts as a restoring force. When the density is high enough, the polarisation reaches a comparable size to the applied field, which is then screened; the electron and hole pair form an oscillator and cause oscillations in the electric field. Over time, the electric field will recover due to the recombination of electrons; hence, the oscillations will settle out and stop.

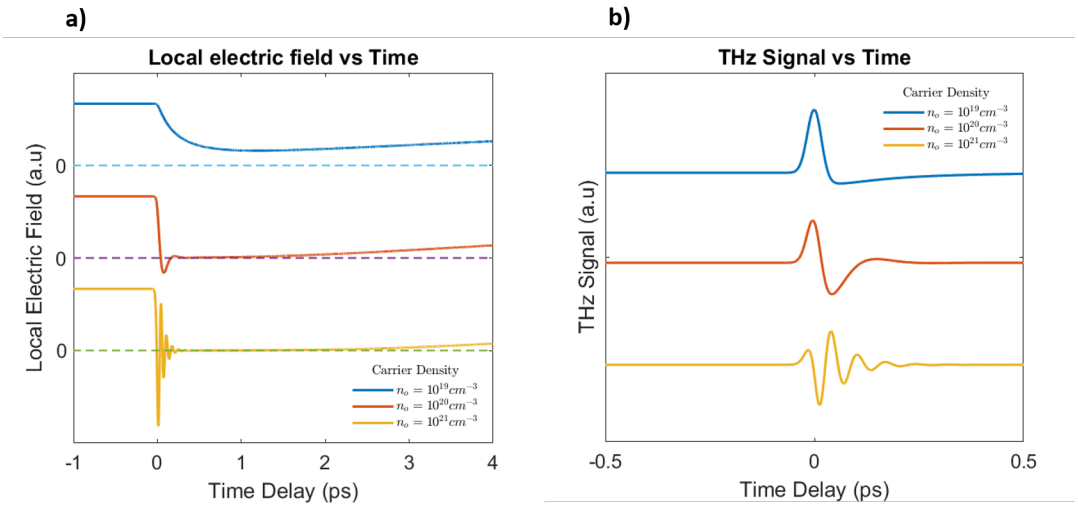

Figure 1.28: Graphs showing the local electric field and THz signal variations with time at different carrier densities

1.8.5.3 Shortcomings of The Model

Although the model shown in this section does provide a good fundamental understanding of the ultrafast carrier mechanisms that are important for THz generation in a PCA device, it makes a number of assumptions and ignores some mechanisms that are important to produce a more realistic model.

The model is based on a one-dimensional Drude-Lorentz model; hence, the simulation does not include any variation over space; this does not allow for modelling any variation of charge density according to depth or width in the material and not being able to account for any effects associated with electrode geometry. A one-dimensional model also means that any scattering occurring is not a completely realistic view of the underlying physics involved. The scattering mechanisms within the semiconductor substrate play a pivotal role in the THz generated during photoexcitation. Thus, a model including as many scattering mechanisms as possible will be a more reliable tool for understanding the full effects material parameters will have. The Drude-Lorentz model uses a single variable to encompass the scattering effects, the momentum relaxation time 'τ_s'. This variable is assumed constant throughout the simulation, which in a real-world scenario is not the case. In materials such as GaAs, the non-parabolicity of the band structure means that there is a chance, under the right circumstances, that the dynamics of the material will change (see the section on Gunn effect); this is not included in the model here and would require the parameters to be changed phenomenologically to provide more accurate simulation. A Drude model only considers that carriers interact with ions in the lattice and do not interact with other carriers; again, this assumption is unreal-

istic. One other shortcoming of this model is that it ignores Poisson's equation; which would lead to a more realistic determination of the electric potential in the system and would improve the understanding of carrier screening of the bias field, which is known to affect PCA devices.

These assumptions mean that care must be taken when using this model to interpret experimental results. However, the model still provides useful insight and a better understanding of the basics of photo-generation of THz emission.

1.8.5.4 Improved Current Surge Models

More complete current surge models have since been developed, which can more accurately model the generation of THz radiation from PCA devices. These models consider more realistic physical phenomena and mechanics and are good tools for more in-depth understanding.

The first of these models was developed by Johnston et al. [120]; this model presents a three-dimensional semi-classical Monte Carlo simulation. The model describes the ultrafast carrier dynamics in GaAs and how THz radiation is generated from a surface depletion field. The model works by dividing the simulation volume into a three-dimensional rectangular mesh to calculate the dynamics of the electrons and holes over small time periods (2 fs), which is much smaller than the scattering time. This allows for the motion of the carriers to be evaluated in each space and time interval.

A set of scattering rate equations is applied to every particle in the simulation to evaluate the scattering phenomena. These equations use a random number generator along with the particle energy and the electron/hole densities in the local simulation space to determine whether the particle will be scattered in the time period; if it is scattered, an angle at which it happens is also calculated. The model considers various scattering mechanisms, including carrier-carrier scattering, polar and non-polar optical-phonon scattering and impurity scattering. Although parabolic band structure is assumed in the simulation, the scattering between Γ and L valleys is included in the calculations to enhance further how realistic the model is.

At the end of each time interval, the individual meshes are updated and used to calculate the electric potential. Solving Poisson's equation on the three-dimensional mesh allows the electric potentials at each point to be calculated. The electric field vector across the material can then be determined using the difference in electric potentials of the rectangular meshes.

This model uses a typical excitation condition attainable from a Ti:Sapphire laser as the means of free carrier injection into the GaAs material. The laser pulse is simulated to have a Gaussian distribution profile in the X and Y directions, whilst the generation in the Z direction is exponentially weighted using the absorption coefficient for GaAs. The initial energy given to the electron-

hole pairs is the difference between the semiconductor bandgap and the photon energy. Over the simulation time period, the net current density vector can be calculated, and thus, the time derivative of this can be used to calculate the THz emission.

The work by Castro-Camus et al. [121] developed the model further to simulate the THz emission from a PCA device. In this model, the same set of equations is used to underpin the ultrafast carrier dynamics except for an extra scattering mechanism, acoustic phonon scattering, which allows the model to provide an accurate tool for analysis of the carrier dynamics and the influence these have on the THz emission.

Further to the model in [120], the boundary conditions of Poisson's equation are set to simulate a specific device gap size device. The two contacts are represented by setting one side of the surface to 0 V and the other to the bias voltage. The inclusions of these in the model allow for a more accurate analysis of how changes in the operation conditions can affect the generation, i.e. the effects of asymmetrical optical pumping are presented.

Castro-Camus et al.'s model was used to simulate the THz radiation emitted by an insulating GaAs photoconductive switch. Their findings gave a detailed understanding of the effects of different parameters on the generation of THz radiation from such a device. It was shown that increasing applied bias voltage caused the generated THz pulse to become shorter; this effect is attributed to an increase of electrons transferring to the L valley, thereby increasing the average effective electron mass and, as a consequence, reducing the mobility. The reduced mobility leads to a shorter THz pulse, which also causes a broadening of the emitted spectrum. The effects of the pump pulse width on generation were also investigated. The results showed that as the pump pulse was increased from 6-120 fs, the temporal width of the THz pulses increased. A THz pulse power dependence on the pump pulse width was also demonstrated; it was found that the power decreased both above and below a pump pulse width of 40 fs. Below 40 fs, the decrease in power was attributed to a broadening of the pump pulses' energy distribution; this meant that the lower energy tail of the pump pulse fell below the material bandgap and hence led to a reduction of the photocurrent. The higher energy tail of the pump pulse causes electrons to be directly injected into the L valley, thus reducing the radiated energy. When the pumps' pulse width was increased above 40 fs, the reduction in emitted power was due to screening of the applied bias. The screening effects within the device were found to be independent of the carrier injection times (for pulse widths $<$ 100 fs), and thus, they are a consequence of the carrier dynamics. Screening of the bias field was shown to be greater across the photoconductive gap but less prevalent at the electrode edges. Photogenerated carriers can exploit this effect nearest the anode to enhance the amplitude and bandwidth of the emitted THz signal.

1.8.6 Photoconductive Material

Many photoconductive materials have been deployed in PCA designs. When designing and fabricating PCA devices capable of THz generation, it is important to use an active material that has specific characteristics that are tailored to the desired application; the following attributes that are discussed are imperative to achieving a device capable of high fields. Quantum efficiency is described in equation 1.25 as the ratio between the radiated THz power and the input power from the incident pulse [122]:

$$\text{Efficiency} = \frac{P_r}{P_s} \tag{1.25}$$

where P_r is radiated power and P_s is the source power supplied by the laser.

High fields require higher efficiencies to obtain better performance from the devices. By choosing a material with a bandgap energy well aligned with the pump lasers' photon energy, the quantum efficiency will be higher, and a more efficient absorption process will take place. Another advantage of bandgap matching is that the photogenerated carriers will be generated at the bottom of the conduction band where the carrier mobility is the highest [117]. Photons of energy much higher than the band gap energy are more susceptible to scattering into the satellite valleys where electron mobility is lower due to higher electron mass at this state [123].

A key material characteristic is having a high mobility, as this dictates the maximum efficiency (η_{max}) that can be achieved as seen in equation 1.26 [117]. A high mobility has been shown to increase the generated photocurrent [124]. However, high mobility has also been attributed to causing earlier saturation and contributing to excess heating within the active material [125, 126].

$$\eta_{max} = \frac{\tau E_b^2}{8\eta_0 F_{sat}} \tag{1.26}$$

Where η_0 is the free impedance, E_b is the applied biasing field, τ is the pulse width of the pump laser, and F_{sat} is the saturation fluence.

A material with a high electrical breakdown field is important as this means that larger biasing fields can be used. This is essential for the generation of high THz electric fields as shown in [118], as the emitted THz is proportional to the biasing field. Large dark resistances are desirable for PCA active material; the dark resistance is quantified as the resistance measured across the material when not in the presence of light, it is important for this to be a high value to ensure that there is a sufficiently small current through the material, this acts to keep excesses heating low during antenna 'off' times. Having a sufficient amount of carriers available to contribute to the photocurrent not only allows

for larger photocurrents to be achieved but also allows for higher optical pump powers to be achieved before saturation occurs. However, there is a compromise needed with carrier density within the active material; having this value too high reduces the dark resistance [127].

Carrier lifetime is an important material characteristic when choosing an active material capable of broadband generation. It is also important to ensure short carrier lifetimes to avoid excess heating in the substrate due to a long photocurrent flowing through the material. The carrier lifetime dominates control of the decay of the photogenerated current in the active material and hence determines the time that the current will flow through the device. From equation 1.22, it can be seen that depending on how fast the photocurrent rises and decays determines the temporal shape as it is directly related to the rate of change of the photocurrent. Again, this can be seen in the current surge model work and how changes to this parameter affect the generation characteristics.

Many different semiconductor compositions can be used as photoconductive materials, such as Gallium Arsenide, Indium Gallium Arsenide, and Gallium Antimonide. Each has its own merits depending on the applications and light source used to photoexcite. The table in 1.1 shows a comparison. In this project, the material extensively used in LT-GaAs due to the excitation compatibility at 800 nm (more in 2.4, a study of this material at 1030 nm is also presented in 5.2.2).

Material	Excitation Wavelength (nm)	Carrier Lifetimes (ps)
LT-GaAs	800	As low as 0.1 [128]
SI-GaAs	800	100 [129]
Ion implanted GaAs such as Cr, O, N	800	Dependent on Ion implanted. ~0.2 [130] for GaAs:As
LT-InGaAs	1000-1550 [131]	0.5 [132]
Au doped Ge	1100-1550	300 [78]
Radiation Damaged Silicon on Sapphire	625	0.6 [133]
GaBiAs	900-1450	1 [134]

Table 1.1: Table showing different photoconductive materials, the optimal excitation wavelength and the carrier lifetimes for each.

1.8.7 Antenna Designs

Since the initial THz PCA emitters designed there has been considerable research into the different electrode geometries, each geometry has advantages and disadvantages when it comes to the radiation generated. Different geometries are shown in figure 1.29, one of the first geometries was the dipole antenna, these consist of typically smaller gap sizes and produce a large bandwidth (reported as high as >60 THz [135]), However due to nature of the design these suffer from earlier saturation points (discussed in detail in section 1.8.8 due to an increase of carrier screening [136]. Pulse duration for a strip line emitter is shorter than that of the dipole, gap sizes are usually much wider meaning that laser focusing is less critical [8]. Bow-tie antennas are more efficient due to the

triangular shape of the electrodes, the sharp points cause higher electric field concentrations which enhances THz generation [137,138] this means that we can get more power when compared to dipole or microstrip antennas, but the output generation provides a narrower bandwidth and lower frequency response [136]. Another electrode structure used is a log-spiral antenna, these are set apart from other design due to the capability to generate circularly polarised THz radiation, this is particularly useful for certain spectroscopic investigations [139].

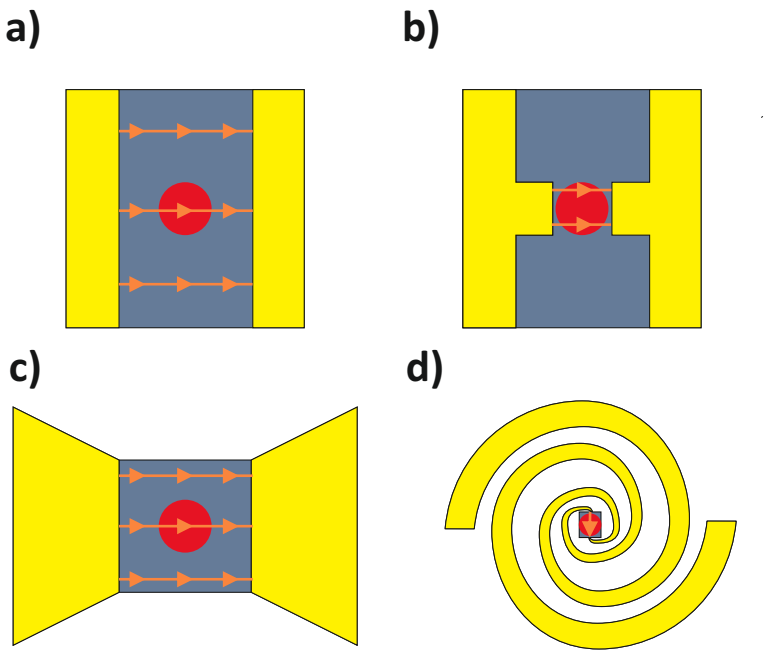

Figure 1.29: Different PCA designs; a) A simple microstrip emitter, b) A Hertzian dipole antenna, C) A bow-tie emitter and D) A log spiral antenna. The orange field lines represent the direction of the biasing field. Typical gap sizes for these designs range from a few microns to 100 microns.

Less traditional designs have been more recently developed that utilise plasmonic structures to enhance the generation of radiation. First reported by Park et al. [140], in this work gold nanostructures were fabricated in the gap between the electrodes of a bow-tie antenna, these nanostructures act to increase the absorption of the optical pump pulse by confining the pulse near the nanostructure antennas. This confinement helps to increase the transient photocurrent and hence the generated THz. Further work has shown that the efficiency can be as high as 7.5 percent [141, 142]. The downside to such a design is the fabrication complexity, due to the nature of the geometry it is very difficult to fabricate over larger areas, as well the saturation point is reached at low optical powers [118].

1.8.8 Optical Saturation

The upper limit of THz radiation that can be generated from PCA devices is governed by key operating parameters and material characteristics. From the simple model in 1.8.5, the terahertz electric field is proportional to both the applied bias and the optical power. However, both of these have an upper limit. As the optical pump power incident on the device is increased, there comes a point where devices will become completely optically saturated, meaning an increase in pump power will cause little to no increase of the generated THz emission. There are several reasons that this is attributed to. One reason is carrier depletion; sufficiently high optical fluence can cause a rapid depletion of carriers [143]. Under no optical excitation, the majority of electrons in the material are bound in the valence band and cannot contribute to any electrical conduction. Under optical excitation, electrons will begin to be promoted to the conduction band through absorption of the incident photons, thus creating a free electron-hole pair. As the intensity of the excitation beam is increased, the number of electron-hole pairs will increase at a rate proportional to the number of absorbed photons. However, only a finite number of electrons in the material can be excited before the valence band is depleted and the conduction band becomes full, i.e., a finite density of states. A sufficiently intense optical pulse can thus deplete the valence band. As the depopulation times of the conduction band are much longer than the pulse duration, no more electrons are made available that can be re-excited. [102].

A significant issue within PCA devices is carrier screening of the applied bias field. This saturation mechanism is brought about by the density of carriers moving inside the device, causing a space charge screening field that results in the applied bias field collapsing [144]. When carriers are separated due to the influence of the biasing field, an internal electric field will be created by the polarisation induced by a separation of space charges, a dipole moment. As mentioned in 1.8.5, the induced local electric field acts as a restoring force and will screen the applied bias field.

Increasing temperature in a device is not desirable, with heat negatively impacting the emitter's efficiency [100]. Increasing substrate temperatures cause a reduction in the mobility of charge carriers and thus leads to lower average photocurrents and smaller efficiency values [145]. Heating can also lead to earlier thermal material breakdown through effects such as thermal runaway. Thermal runaway occurs at the point when the rate of heating exceeds the rate of cooling, causing the temperature in the device to increase rapidly and eventually, material breakdown occurs [146]. Excess heating in a PCA device can be introduced in a few ways; large bias currents can cause joule heating in the substrate, especially when dark resistances are lower. Increased carrier densities are also shown to increase the substrate temperature [126]. At higher carrier densities, the amount of energy absorbed is higher; during carrier relaxation, the excess energy is released into the lattice, thus inducing a material temperature rise. A study into device heating is presented in 5.1.

1.8.9 Photoconductive Antenna Arrays

The desire to generate higher THz field strengths has been discussed in 1.2. This is hard to achieve whilst using small single aperture PCA devices due to the saturation at much lower optical and electrical bias values [125]. Increasing the gap size allows for the saturation point to be increased [147]. However, this in itself brings its own challenge, such as having to use much larger bias voltages to achieve similar equivalent fields. Higher power amplified laser systems are also required to optically saturate large area devices. Increasing bias voltage for larger gap devices has been shown to introduce electrical noise into the generated signals [118].

In order to create devices that are capable of producing higher fields, arrays of PCAs can be used (see figure 1.30). Here, a repeating set of PCA strip line emitters can be fabricated together to create a larger area array of emitting pairs connected to common biasing pads, known as an interdigitated PCA array. Theoretically, each emitting pair can be considered an independent point source, which combines in the far field to achieve a single THz pulse. The advantages of such a design are manyfold; it allows for smaller gap sizes to be used but still keeps the total illuminated area larger; this, in turn, means that smaller biasing voltages can be used to obtain equivalent fields. Larger optical pump powers can be used on larger area devices without reaching optical saturation. As the device area is larger, the optical fluence is smaller per unit area when compared to the same optical power focused onto a smaller area device. In order to saturate the larger area device, a higher power excitation pulse is needed. An advantage of using larger areas is that larger THz powers can be achieved due to more material being available for excitation to take place in. The geometry of an array device allows for a certain level of redundancy to be tolerated, that is to say that single pairs of emitters act somewhat independently of each other, so if a single emitter pair becomes damaged, it will not stop the rest of the device from continued generation. However, the output power will, of course, be reduced. Lower biases mean that operation within safer material regimes is also achievable. This means that the biasing field strength is operated well below the material's electrical breakdown voltage.

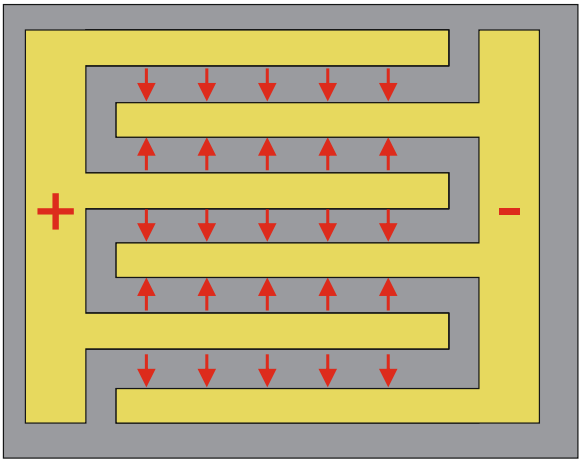

Figure 1.30: An interdigitated PCA array depicting pairs of stripline emitters connected together through two bias pads. The red arrows indicate the opposite electric fields set up in alternate gaps.

A key issue with interdigitated PCA arrays is generation of THz radiation in every gap of the device. Due to the structure of the interdigitated array, adjacent gaps have oppositely polarised electric fields which in turn leads to oppositely polarised THz radiation generated. If the device is fully illuminated by an excitation pulse the THz seen in the far field will be completely cancelled out through destructive interference of the oppositely polarised radiation. One way to avoid this is through the use of a 'shadow mask' [148], depicted in figure 1.31. Typically a shadow mask consists of a metal layer to prevent any optical excitation in alternating gaps. Although this method is effective it reduces the efficiency of the device by removing large active areas of the photoconductive substrate.

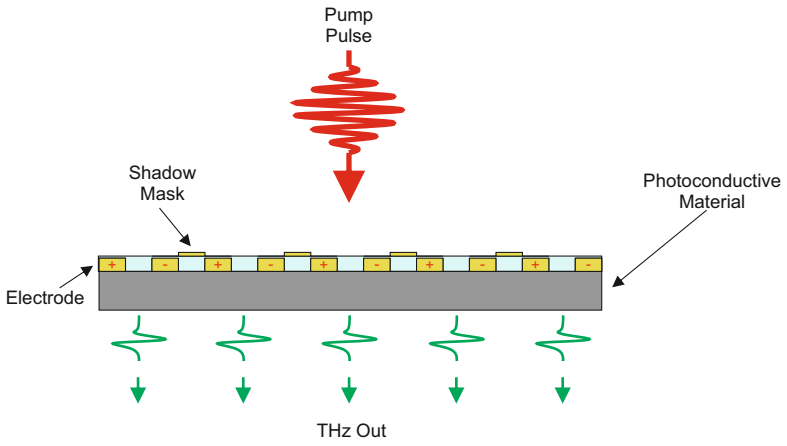

Figure 1.31: An interdigitated PCA array with a shadow mask used to prevent generation of THz in alternate gaps on the device.

1.8.10 Current PCA array research

There is much work being undertaken to improve upon traditionally fabricated interdigitated PCA devices. The following subsections discuss a few areas of research working towards this:

1.8.10.1 Microlens arrays

One of the areas of research with PCA arrays is the use of microlens arrays to increase the efficiency of devices. As discussed, the issue of generating oppositely polarised generation between alternating gaps calls for the need to provide a way of preventing this occurring. A microlens array is a structure that can be coupled to the front of the PCA array and can be used in place of a metallic 'shadow' mask, as it increases the amount of the pump pulse illuminating the active gaps. Work reported by Matthäus et al. [149] used a hexagonal microlens array coupled with an interdigitated PCA array to increase the percentage of excitation pulse reaching the devices active gaps to 75% compared to a calculated 20% achieved in [150]. The microlens array can be engineered such that the excitation IR pulse is focused solely onto the alternating 'active gaps', this is achieved through careful design of the microlens array dimensions. [149, 151]

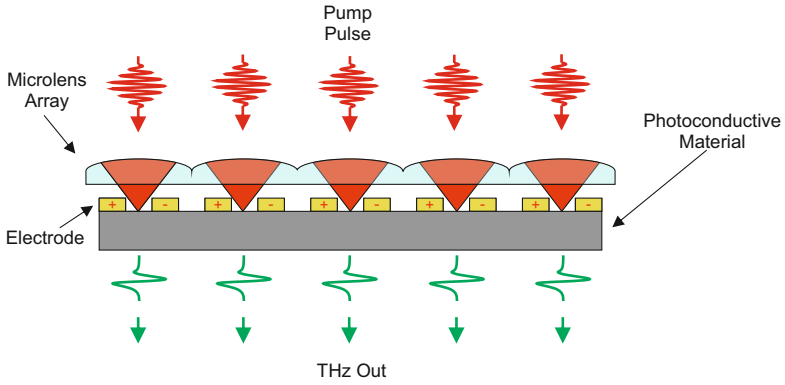

Figure 1.32: A microlens array used with a PCA array to focus the IR excitation pulse onto the alternate gaps. This provides a way to generate THz radiation of the same polarisation.

Whilst there are proven advantages over 'traditionally' designed large area interdigitated PCA arrays, a microlens array is not without considerable disadvantages. One issue with this type of technique is the difficult fabrication technique of creating the microlens array adding considerable complexity to the method. Another problem is the delicate alignment needed with the microlens array to ensure that the excitation pulse is focused on the desired areas of the device. This is especially true for larger area devices adding complexity to the set-up and use.

1.8.10.2 Binary Phase Mask

Binary Phase Mask (BPM)s have been used as another means to improve upon the efficiency of large area interdigitated PCA arrays. Instead of masking the alternate gaps with a shadow mask a BPM can be used to make use of all of the array area that is not covered by electrode structures. The BPM works by fabricating a layer of material, typically quartz, to introduce a change of phase to the IR excitation pulse. The change of phase causes a delay of THz generation from the masked active area thus avoiding any destructive interference with the gaps of opposite polarity. These types of structures have been typically used with large gap sizes (3mm in [152]) that produces quasi-half cycle THz pulses. With the use of a BPM it is possible to achieve a level of control of the temporal profile through the use of both polarity active areas. The figure in 1.33 shows that if the phase shift is designed correctly that the corresponding THz pulse measured in the far-field will resemble a symmetrical pulse. Through varying the thickness of the BPM the amount of interference between oppositely polarised pulses can be altered. Through this method it has been reported an effective doubling of the power radiated from a device, this is to be expected as the number of emitting active areas has doubled. [152]

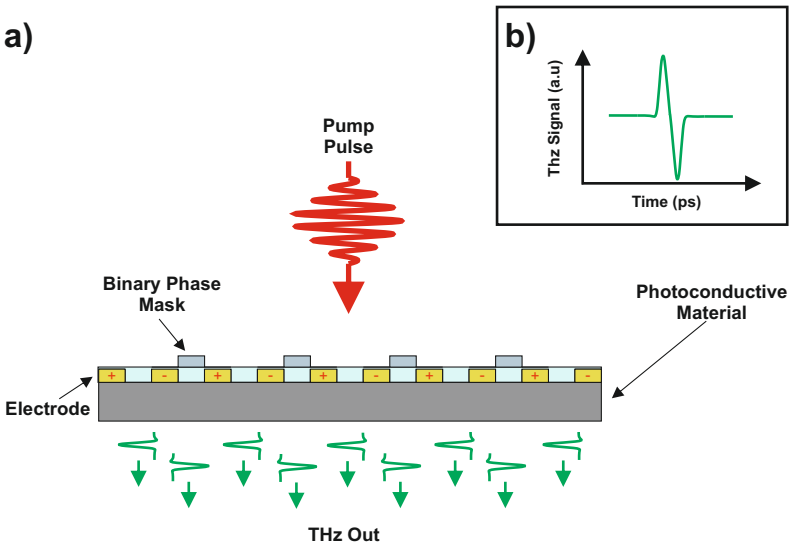

Figure 1.33: A BPM technique causes a delay of excitation in the alternate gaps of the PCA array (a), producing THz generation of opposite polarity that if designed correctly can constructively interfere to create a quasi-full cycle pulse (b).The light blue layer is a dielectric film to fabricate the mask onto.

This method has proven to be effective at increasing the efficiency of a large area interdigitated PCA arrays and consequently the amount of THz radiation generated. This technique is also rather simple and inexpensive to implement and does not add the complexity with alignments that a microlens array would. However one of the major drawbacks is that this technique is only highly effective with the use of relatively large area gaps. When the gap size is reduced the emitted radiation becomes less quasi-half cycle and makes the interference of the oppositely polarised pulses less efficient. There is also a trade-off between bandwidth and high power. By using a thin BPM the delay between the pulses is reduced and the interference results in a pulse of reduced time duration, this shifts the power to a higher bandwidth but reduces the overall power and the opposite effect is present in thicker masks. Large bandwidth are difficult to obtain with this method due to the challenges of performing the phase shift coherently over a broad range of frequencies. [152].

1.8.10.3 Plasmonic Nanostructures

Research into the use of plasmonic structures with PCA devices has shown promising results towards improving the efficiency of THz emission. Initial work reported by Berry et al. [141] showed a drastic increase in efficiency of up to 50 times that of traditional PCA devices fabricated on SI-GaAs. By using a plasmonic nanostructure like that shown in figure 1.35 fabricated on the antenna anode and cathode electrodes allowed for an enhancement of the

IR optical excitation pulse in the area close to them. In this scheme the IR pulse is coupled into the substrate by the plasmonic waves resonating from the nanostructures. As the mobility of electrons is much greater than holes in the material, the pump is focused nearest the anode to achieve the best efficiency. The reason behind the increased efficiency is due to an increase in the amount of electrons that are able to reach the anode electrode and contribute efficiently to the generation of the THz radiation. With an enhancement of the IR pulse near the anode structure the electron transport lengths are reduced and more are able to be swept into the electrodes before recombination with holes can occur. With a grating of plasmonic nanostructures across the length of the device it provides a greater area of the active material in which this mechanism can take place. In this work a proof of concept device was demonstrated.

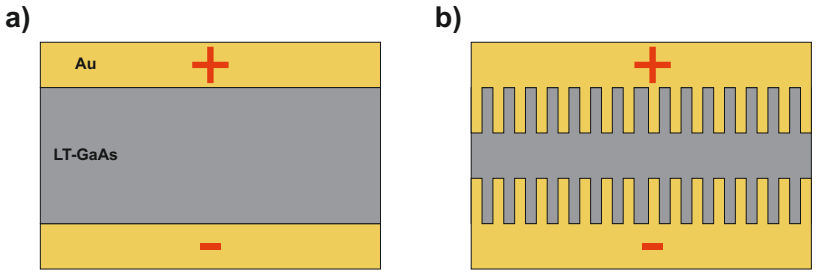

Figure 1.34: a) A normal stripline PCA device. b) A stripline emitter with the plasmonic nanostructure fabricated on both electrodes.

This technique of enhancement was demonstrated in interdigitated PCA arrays by Singh et al. [153]. Here they adopted an asymmetrical plasmonic nanostructure such that alternating active gaps contained it. This method was used as alternative to a 'shadow' mask, here the destructive interference between oppositely polarised THz beams was facilitated. The destructive interference did not cause a net zero emission due to the enhancements produced by the plasmonic nanostructures causing THz emission to still be detected in the far-field.

Further work reported in [154] by Yardimci et.al proposed a new technique to use the plasmonic nanostructure to further increase the efficiency of an interdigitated PCA array. To increase the optical confinement of the IR excitation beam in the active material a nano plasmonic structure was used in conjunction with a Distributed Bragg Reflector (DBR) to create an optical nanocavity. With an optical nanocavity setup almost all of the generated photocarriers are in close proximity to the nanostructures and hence can contribute efficiently to the THz emission. This technique allows for use of materials which might not have as short carrier lifetimes due to the less important role it has in the thermal management of these device.

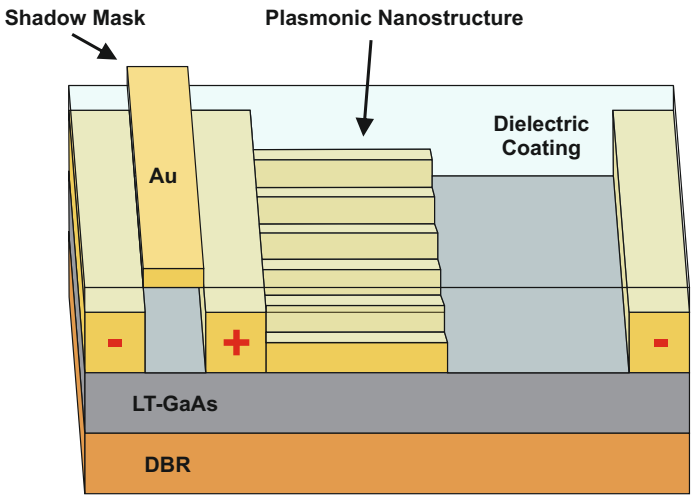

Figure 1.35: The diagram shows a single emitting pair of an interdigitated array with a plasmonic nanostructure. In this case the nanostructure is fabricated only on the anode electrode and the structure is used together with a DBR. A shadow mask is also used to prevent generation in the alternate gaps.

These devices have demonstrated some interesting results and show some promise in increasing the efficiency of THz radiation available from PCA arrays. One of the main disadvantages comes from the more complex fabrication process involved in realising the structures. Patterning plasmonic nanostructures requires the use of Electron Beam Lithography (EBL) due to the small size of the features, EBL is an expensive and relatively slow process compared to standard lithography. Another disadvantage is that due to the nature of the plasmonic nanostructures the enhancement is significantly reduced with higher optical pumping powers, which is due to the increased effects from electron screening causing early saturation. This is also true for increasing the applied bias field strength; as more photogenerated pairs are generated, the bias field is screened earlier due to the large local electric field opposing it. Both of the effects will cause issues moving to pushing to high THz electric field strengths as they will prevent large biases and high optical fluences from being applied.

1.8.11 Current High Power PCA Designs

As THz PCA research develops, achievable THz field strengths have improved. It is essential to analyse the state of the current field of research to see where the devices fabricated within this thesis lay. The highest THz electric field strength produced from a PCA array device using GaAs is $\simeq$ 230 kV/cm; this was produced and presented by Singh et al. [155].

The device in that work is a large area interdigitated array fabricated on SI-GaAs, with an excitation gap width of 10 μm and a total active area of 1 cm^2. The device was illuminated with a 45 fs NIR pulse operating with an 800 nm central frequency provided by a Ti:Sapphire amplified laser system at a 1 kHz repetition rate; the electrical bias applied to the device was 60 kV/cm. The THz pulse power was measured using a calibrated THz power meter and off-axis parabolic mirror to achieve a tight focus (spot size $\sim$ 0.45 mm) and found to be 70 nJ, and this corresponds a peak electric field of $\simeq$ 230 kV/cm.

The current record for LT-GaAs devices fabricated by the group at Leeds University was fabricated by Bacon et al. [91]. They presented a PCA device capable of generating THz electric fields of $\simeq$ 120 kV/cm. The PCA device was fabricated on an LT-GaAs layer transferred onto an insulating substrate (sapphire). This fabrication technique is the basis for the work described in this thesis and can be found in detail in Appendix (A). This device consisted of 200 μm wide excitation gaps and a total active area of 1.8 cm^2. The optical pump was provided by a 40 fs NIR pulse operating with an 800 nm central frequency supplied by a Ti:Sapphire amplified laser system with a 1 kHz repetition rate. The THz electric field was measured by focusing the generated THz pulse down with an off-axis parabolic mirror onto an EO crystal. The field is estimated through EO sampling (see section 1.9.2), and a 150 μm thick GaP crystal is used; a THz electric field was measured as 120 kV/cm. The THz pulse power was measured with a pyroelectric detector and was found to be 113 nJ, and the THz pulse spot size at the focus was $\simeq$ 0.63 mm.

1.8.11.1 Comparison of high powered devices

Comparing this device to the one presented by Bacon et al. [91], some points of interest can be discussed. It can be seen that both devices are capable of producing high field THz generation, with the device fabricated in [155] (SI-GaAs device) producing a field strength 100 kV/cm higher than that of the device in [91] (LT-GaAs device). However, the pulse energy of the Si-GaAs device is $\sim$ 40 nJ smaller than the LT-GaAs; this is due to a tighter focal spot using a shorter length parabolic. The LT-GaAs device has a larger active area than the SI-GaAs device. The saturation fluence of the SI-GaAs device is much smaller than that of the LT-GaAs device; this can be attributed in part to the fact that the LT-GaAs device has a substantially larger excitation gap width. The fabrication process of SI-GaAs is simpler than that of the LT-GaAs device. Still, one advantage of using LT-GaAs is a much higher material electrical breakdown field than SI-GaAs ($\sim$ 300 kV/cm compared to $\sim$ 150 kV/cm). Higher electrical breakdown fields mean that there is the potential that higher biasing fields can placed across the LT-GaAs device. This can be seen as a higher biasing field applied to produce a higher THz pulse, albeit with lower pulse energy, in the SI-GaAs device. The SI-GaAs device can be seen to produce a higher electric field for the respective optical pulse energy, i.e. it has a better optical-to-THz conversion efficiency; this is thought to be because the

broader spectrum emitted from the device leads to a shorter THz pulse width.

1.8.12 Why Choose PCAs Over Other Sources Of High Power?

There are many characteristics that make the use of PCA devices for high field generation of THz radiation highly desirable and why they are chosen over other sources. These devices can be used with a vast range of laser sources to produce both narrowband and broadband generation [156]; many different photoconductive materials can be used to fabricate PCAs. An important feature is attributed to the fact that devices are operated at room temperature, which removes the need for complicated and expensive experimental setups that involve the use of cryogenics. PCAs have greater efficiency than other forms of THz generation based on non-linear optics [156]; this greater efficiency is because PCAs are not governed by the Manley Rowe limit [157]. With PCA devices, there are no phase matching considerations like that seen in 1.7.3; this means that the bandwidth of the emitted radiation is not limited to the frequencies that satisfy phase matching conditions [74]. Relatively low optical powers are required to generate similar emitted field strengths compared to the other forms of high power generation. Air plasma (1.7.1) and free-electron lasers (1.7.2) both require high optical pulse energies to generate high power THz pulses; this value is smaller in PCA THz devices due to greater efficiency. PCA device operation requires the use of a biasing electric field; this grants an additional amount of control over the generated radiation field by being able to attenuate or increase through this biasing voltage. Electrically steerable THz beams can also be realised by controlling the bias voltage [99]. Electrical control of the polarisation is achievable with these devices [123, 158], which make it possible to obtain anisotropic properties and material excitations that were previously not possible [159]. Having electrical control of the polarisation allows for much faster modulation of the THz radiation than is achievable by systems based on mechanically rotating components [160].

1.9 Detectors

In section 1.1 it was stated that one of the reasons that the so called 'THz gap' originated initially was due to a lack of available detectors. Whilst this has improved greatly over the past 30 years there are still fewer detectors available than that seen at other frequencies. There are a few different detector technologies that can be drawn upon for such a set-up as described here, the key parameter being that both phase and amplitude information needs to be obtainable, hence a detector that exclusively measures power is unsuitable. The leaves several appropriate options; one is using a PCA device in the detection space whilst the other is Electro-Optic (EO) detection.

1.9.1 PCA Detectors

The operational theory behind PCA devices, when operated as detectors, is conceptually similar to that of the generation scheme. A fs pulse generates electron-hole pairs in the semiconductor material, which are then accelerated under the influence of an incident THz electric field. This movement generates a net current across the gap of the device that is proportional to the convolution of the THz pulse electric field and detector response; from this, the information of the THz pulse can be determined. The recapture time is a key parameter of this detector; a small recapture time is essential to be able to detect over a large bandwidth. When the current is produced across the gap, it is amplified and converted into a voltage, which is then recovered by a lock-in amplifier. As the sampling beam used in this system is from an amplified system, it is unsuitable for use. The amplified laser system has a low repetition rate of 1 kHz, so multiple measurements can not be taken of the small photocurrent generated in the detector. For a higher Signal-to-Noise Ratio (SNR), EO detection is used to measure the THz fields through this thesis.

1.9.2 Electro-Optical Sampling

Electro-Optic Sampling (EOS) can be used as a means to detect THz radiation in both Continuous Wave (CW) and ultra-short single-cycle pulse generation schemes. The operation of this technique is theoretically similar to that used for generation in an EO crystal described in (ref optical rectification). The difference when an EO crystal is used for detection is that the THz radiation is focused onto the crystal. This will induce the polarisation change, which can be detected through a change in a NIR sampling beam [161].

In linear optics, the relationship between polarisation and the electric field is given by:

$$P = \epsilon_0 \chi \varepsilon. \tag{1.27}$$

where P is induced polarisation, ϵ_0 is permittivity of free space, χ is electrical susceptibility and ε is the electric field. When a non-linear optical element is used, the equation that describes the induced polarisation becomes a series of increasing order terms:

$$P = P^{(1)} + P^{(2)} + P^{(3)} + ...P^{(n)}. \tag{1.28}$$

When considering EOS, the second order term is used:

$$P_i^{(2)} = \epsilon_0 \sum_{j,k=x,y,z} \chi_{ijk}^{(2)} \varepsilon_j \varepsilon_k. \tag{1.29}$$

where i,j and k are representative of the Cartesian crystal coordinates x,y and z. The ε_j and ε_k represent the electric fields of the optical fs pulse and the THz pulse respectively. The second-order non-linear susceptibility tensor $\chi_{ijk}^{(}2)$

solves the polarisation in multiple dimensions. The tensor contains 27 elements; however, for most crystals, this can be reduced to 18 elements due to zero value elements [2].

The quasi-static electric field is applied to the EO crystal by the THz pulse ε_j in an EOS detection scheme. It induces a polarisation change in the NIR pulse. The induced polarisation is proportional to the product of the electric field components of the THz pulse ε_j and the NIR pulse ε_k. For detection, the electric field of the NIR pulse is kept constant. Hence, the polarisation change induced becomes proportional to the magnitude of the THz pulse.

The magnitude of the induced effect depends on the angle at which the pulses hit the crystal; the largest magnitude of induced polarisation and, therefore, the largest signal is achieved when the pulses propagate along the crystal axis with the highest electro-optic coefficient. The induced polarisation is orthogonal to the pulses' propagation direction, which causes a field-induced birefringence in the crystal. The NIR sampling beam begins as a linearly polarised pulse before it passes through the crystal; once it goes through the crystal, the field-induced birefringence causes the pulse to become slightly elliptically polarised. The magnitude of the ellipticity of the polarisation is dependent on the strength of the quasi-static field of the THz pulse. Without the presence of the THz pulse, the polarisation of the NIR pulse will stay linear; this is depicted in figure 1.36.

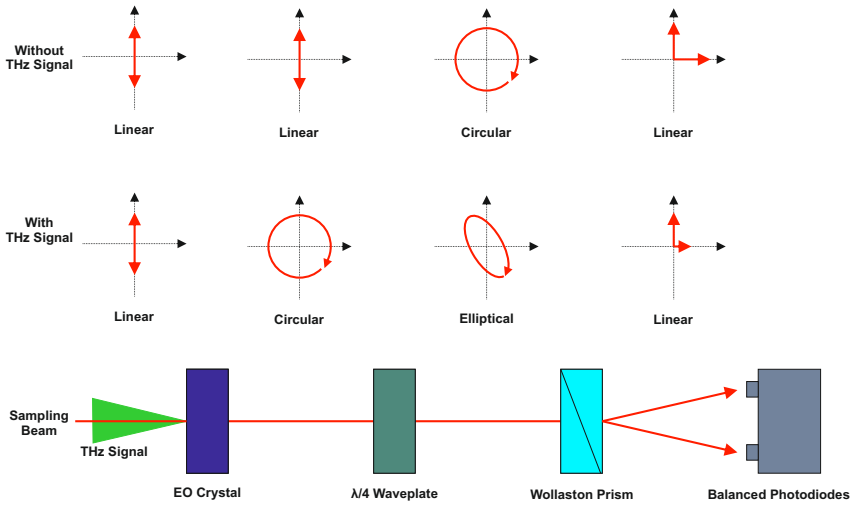

Figure 1.36: The EO detection setup showing how the THz influences the polarisation during detection, both cases of how the polarisation altered with and without a THz beam are shown. Note that the effect on the polarisation is heavily exaggerated to highlight the effect.

In an ideal scenario, the NIR pulse and the generated THz radiation would propagate at equal speeds through the detection crystal. However, the reality is

that there will be some dispersion in the crystal medium, and this results in a difference in propagation velocities between the two beams. At a certain point, they will destructively interfere. The length at which this occurs is known as the coherence length, L_c, defined as:

$$L_c(\omega_{THz}) = \frac{c}{\omega_{THz} \left| \eta_o - \eta_T \right|} \tag{1.30}$$

where η_o and η_T is the effective refractive indexes of the EO crystal at NIR and THz frequencies respectively. This shows that the coherence length is a frequency-dependent value. EO crystals need to be thinner to allow higher frequency THz detection, but this is a problem due to the loss of detection sensitivity. Thus, there must be a trade-off between the bandwidth and the detection sensitivity [162]. Two crystals used in this thesis are a 1 mm thick ZnTe crystal with an effective bandwidth of $\sim$3 THz, and a 150 μm thick GaP crystal which has a much larger effective bandwidth of $\sim$6 THz.

Once the sampling NIR beam has passed through the crystal and undergone a change in polarisation, it can be processed to find the strength of the THz electric field. The NIR pulse is passed through a quarter-wave plate, which causes the beam into an X and Y component; if the polarisation is elliptical, these components will not be equal. The pulse finally passes through a Wollaston prism that spatially separates the X and Y components. The intensity of the separated beams is detected by balanced photodiodes, which measure the difference between the two components.

The NIR sampling pulse is an order of magnitude shorter in time than the THz pulse. Therefore, the induced polarisation change in the pulse is proportional to the instantaneous value of the THz field at the point the two pulses overlap. By delaying the sampling pulse incrementally, the THz pulse can be sampled in full [161].

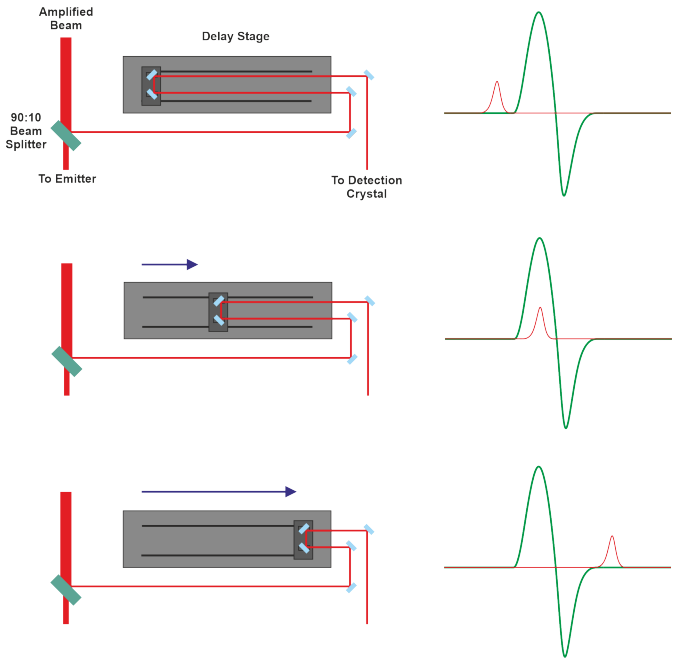

Figure 1.37: The the stage moving causes a delay to the sampling beam; by moving this through a range of times, sampling of each section of the THz beam is achievable

1.10 Electric Field Measurements

The motivation to produce devices capable of generating high electric field strengths was discussed in section 1.2. In order to characterise this quantity, a reliable method of measuring must be established. Two options can be used for this: one is a direct calculation via electro-optic sampling, and the other is to use a power measurement and spot-size measurement to estimate the field strength.

1.10.0.1 EOS Electric Field Measurement

The detected voltage on the photodiodes 'V_p' is used with equation 1.31 to calculate the generated THz electric field strength. [2]

$$E_{THz} = \frac{V_p \cdot \lambda \cdot LIF}{V_o \cdot 2\pi \cdot L \cdot \eta_o^3 \cdot T_c \cdot D_R \cdot d_{41}} \tag{1.31}$$

Where λ is the wavelength of the sampling beam, V_o is the photodiode response with no THz signal present, L is the crystal thickness, η_o is the refractive index of the crystal at the sampling beam frequency, d_{41} is the EO coefficient

of the detection crystal and D_R is the response of the crystal. T_c is the transmission of the THz pulse at the air-crystal interface, given by:

$$T_c = \frac{2}{1+\eta_T} \tag{1.32}$$

where η_T is the refractive index of the crystal at THz frequencies. LIF is to account for the lock-in amplifier detected signal; it is the first Fourier component of the detected square wave:

$$LIF = \frac{\pi}{2\sqrt{2}sin(\pi D)} \tag{1.33}$$

D is the duty cycle of the detected signal. The values for the crystal used within this thesis can be seen in table 1.2.

Crystal	L	d_{41}	D_R	η_o	η_T
GaP	150×10^{-6}	0.97×10^{-12}	0.9	3.57	3.34
ZnTe	1×10^{-3}	4×10^{-12}	0.72	2.85	3.12

Table 1.2: The two different EO crystals used throughout this work and their associated values.

A 200 μm gap 18 x 18 mm PCA array at a bias voltage of 20 kV/cm ($\sim$400 V) was measured using the optical set-up discussed in this thesis. Using a 150 μm thick GaP detection crystal, the electric field strength was estimated to be $\sim$120 kV/cm (this is the device reported in [91]). The measured THz time domain signal is shown in figure 1.38.

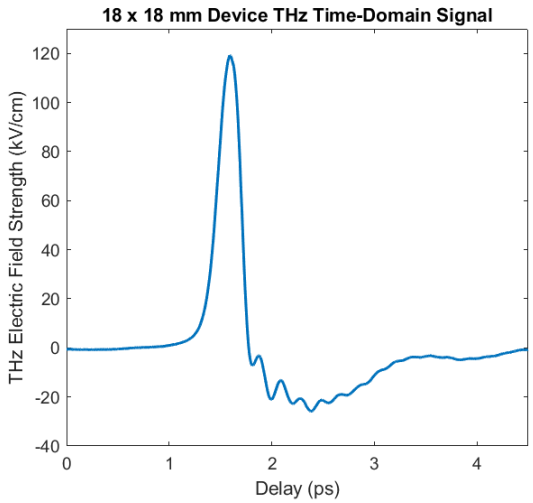

Figure 1.38: THz time domain signal of an 18x18 mm PCA device. The peak THz field strength measured is 120 kV/cm, using a 150 μm GaP crystal for EO detection. This field was achieved using an electrical bias of 20 kV/cm and an optical excitation energy of 0.66 mJ.

1.10.0.2 Pulse Energy Measurements

One method of obtaining the electric field strength of the THz pulses generated is to obtain the pulse power and convert it to a field measurement. A power measurement can be obtained using a calibrated pyroelectric power meter. A pyroelectric meter utilises the pyroelectric effect seen in some materials because the polarisation of the material has a temperature dependence. When radiation is incident upon the material's surface, the heat-induced will cause a polarisation change of a size determined by the pyroelectric coefficient of the material and the temperature change. This change in polarisation is detected as a change in output voltage [163].

As this heating change is typically small and the power meter is sensitive to other sources of heating present, the measurement is taken over a set period to allow for averaging. Further, average power measurements are taken with the device on and off to obtain more accurate readings.

To estimate the electric field strength, the power measurement is used with the spot size of the pulse [164]:

$$E_{THz} = \sqrt{\frac{4W}{c\epsilon_0 d^2 \pi t}} \tag{1.34}$$

where W is The THz pulse energy, d is the measured pulse spot size, and t is the pulse duration.

1.10.0.3 Spot Size Measurements

An accurate spot size measurement with a pulse energy measurement is required to obtain the THz electric field strength. In order to determine the spot size, a knife edge measurement can be performed; this is carried out through a systematic sweep through the spot using a sharp edge to block each part of the beam in turn. A time domain signal is acquired at each knife position, and the peak signal is extracted. To obtain a two-dimensional spot size value, the knife edge is swept first through the x-axis; the knife edge is then rotated 90◦ and swept through the y-axis. The knife edge is moved in the z-axis through the focus to obtain a three-dimensional spot size, repeating the same x- and y-axis movements.

The spot size can be obtained through signal processing from the obtained peak values. The pulse has a Gaussian-type power distribution. Therefore, the values can be fitted to the integration of the Gaussian function (the error function). The fitted graph can then be used to determine the spot size using the following equation [165]:

$$d = 0.7803 \times |\text{Knife}_{90\%} - \text{Knife}_{10\%}| \tag{1.35}$$

Where $\text{Knife}_{90\%}$ and $\text{Knife}_{10\%}$ are the knife position values taken where the peak signal is at 90 and 10 % respectively, it is important to note that using the peak signal value gives the spot size across all the frequencies generated from the broadband source.

1.10.0.4 EOS Validity

The EOS detection scheme was cross-checked with a power and spot size measurement in order to obtain the accuracy of the THz electric field strength measurements. The test in this subsection was performed by Dr Thomas Gill [164] using a 200 μm gap 18 x 18 mm PCA array at (the device reported in [91]) a bias voltage of 20 kV/cm ($\sim$400 V).

The power measurements were taken with a pyroelectric detector (OPHIR RM9-THz) placed in the detection space (see figure 3.2). The power is averaged over a few minutes to achieve a more reliable reading; this is performed with the device, both biased and unbiased, allowing any background noise to be subtracted from the measurement. The average power is then taken as the average biased power subtracted by the average unbiased power. The measured power of the device was calculated as 113 nJ.

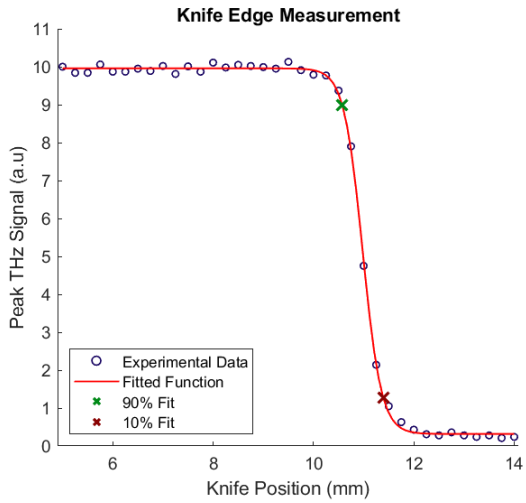

Figure 1.39: Knife edge measurement data plotted with the fitted error function. The 90% and 10% points of the THz signal are used to calculate the THz spot size (shown in 1.35), this results in a spot size of 640 μm.

Next, the THz spot size was determined through knife-edge measurements as described in 1.10.0.3. A knife edge measurement for the 18x18 mm PCA device can be seen with the fitted error function in figure 1.39. The graph in figure 1.40 shows the THz spot size measured for multiple knife-edge measurements as the z-axis position of the knife is moved through the focus of the beam; this gives a minimum spot size of 640 $\pm$ 35 μm. The THz electric field strength can now be estimated using eq 1.34 along with the spot size and power measurement values. The electric field calculated is $\sim$120 kV/cm; this value is in good agreement with the value obtained through EOS. From these calculations, the validity of the EOS detection is demonstrated.

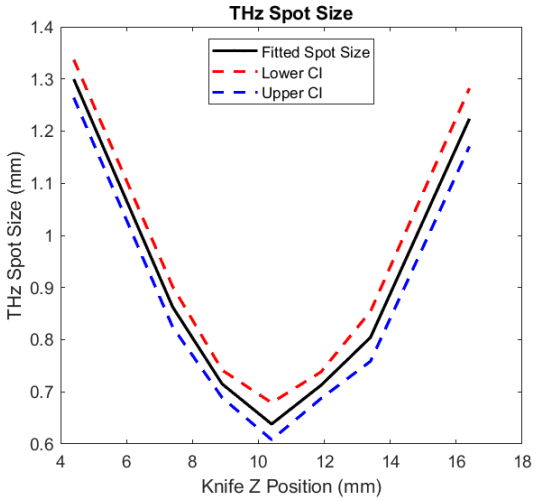

Figure 1.40: Spot size measurements obtained as a function of the knifes' z-axis position. The spot sizes are obtained through the error function fitting of the measured peak THz values.

1.11 Spectroscopy

One of the driving factors for the improvement of PCA devices is the desire to utilise the high fields THz fields they are capable of producing for spectroscopic investigations. Terahertz Time-Domain Spectroscopy (THz-TDS) is a widely used technique for material identification and characterisation. In this version of TDS, THz radiation is employed to penetrate and probe materials. The resultant radiation that passes through can be detected, and the material information can be extracted. The advantage of THz-TDS is that the collected radiation contains both phase and amplitude information of the probed materials' effect on the radiated THz pulse. The key applications of high field strength THz pulses and the material information that can be investigated have been discussed in 1.2.

With THz-TDS, a few different set-ups can be used to perform investigations, each with slightly different methods of probing and gathering material information. An in-depth discussion of these methods is beyond this project's scope; however, due to the influence these methods have on PCA designs, some noteworthy methods are briefly discussed. These main methods to note are two-dimensional THz-TDS, which is used to examine the ultrafast non-linear response of materials.

With 2D THz-TDS, an initial pump pulse excites the target material, and at a set delay time, a secondary pump pulse follows and causes a secondary excitement of the material. At each stage, the detected THz signal is measured and

recorded. In order to determine the system's non-linear response, each combination of the pulses incident on the sample must be captured. By comparing the collected pulse information, it is possible to obtain material characteristics and behaviour. The following equation is used to determine the non-linear signal:

$$E_{NL}(t,\tau) = E_{AB}(t,\tau) - E_A(t) - E_B(t,\tau) \tag{1.36}$$

where E_{AB} is the signal when both excitation pulses on the sample together, E_A is the signal for just the initial pulse exciting the sample, E_B is the signal when just the second pulse is exciting the sample. This gives the non-linear signal as both a function of the time delay 'τ' between pulses A and B, as well as the time delay of the sampling pulse 't'. By adjusting τ and t, the full 2D-time domain non-linear signal is to be acquired.

Another noteworthy THz-TDS method, that is a similar set-up to the one used to characterise PCA devices, is one-dimensional THz-TDS. This method is less complicated to implement by design than the previously mentioned method, it utilises a singular beam line to excite the material and then the information from this interaction can be investigated.

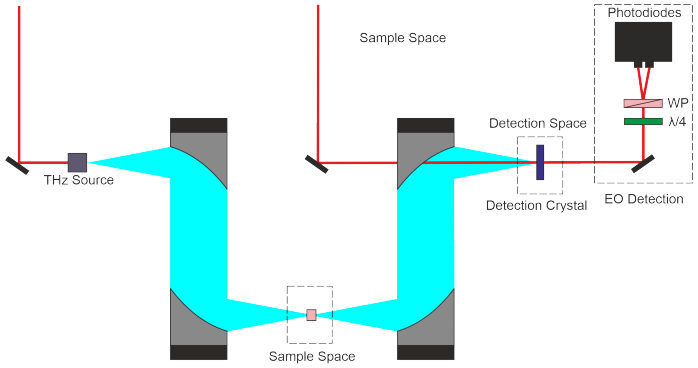

Figure 1.41: A typical 1D THz-TDS set-up, here the THz pulse is generated from a source before interacting with the sample, the beam line is the only source of THz radiation in the system.

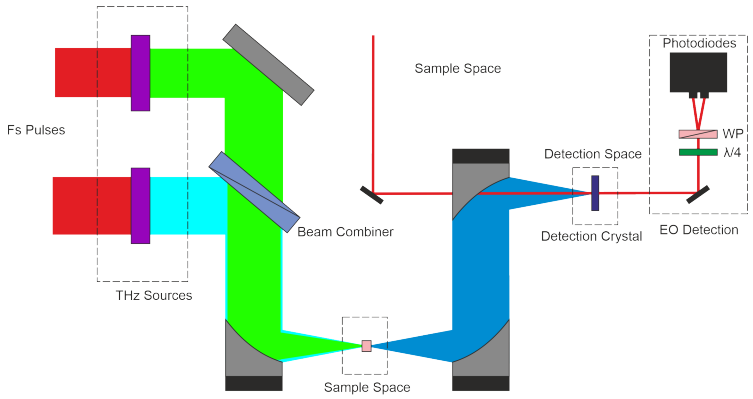

Figure 1.42: The 2D THz-TDS set-up is similar to that of the 1D set-up, however it can be seen that there is two THz sources here to create both a pump and a probe beam. Using the configuration depicted here, the sources generate THz radiation from a fs source. These beams propagate co linearly towards the sample.

Chapter 2

Fabrication

This chapter will outline the fabrication processes used for producing PCA emitters on sapphire substrates. There will be a discussion on the benefits of transferring LT-GaAs to a sapphire substrate using an Epitaxial Lift-off (ELO) technique over other methods. A focus on the improvements made to the fabrication process and the reasons for these are also included in this chapter.

2.1 LT-GaAs

LT-GaAs differs from traditionally grown GaAs by the temperature it is epitaxially grown at; careful control of this temperature results in arsenic-rich sites in the crystal. This allows the growth of high-quality crystals with substantially reduced carrier lifetimes [166]. LT-GaAs is typically grown at temperatures of 200-300 °C; this lower temperature and the excess arsenic lead to lattice deformations in the GaAs layers. The deformations occur in the form of arsenic antisite defects, with these forming a donor miniband near the centre of the bandgap. The lower the temperature, the larger the lattice deformation, and the concentration of arsenic antisite defects increases as the growth temperature decreases [167]. The decrease in carrier lifetime is attributed to the rapid trapping of conduction band electrons into the newly created midgap state [128].

LT-GaAs has many characteristics that are highly desirable for THz frequency capable PCA device including carrier lifetimes reportedly as short as 100 fs [128] ensuring broadband THz generation, and high break down fields of 300 kV/cm. High breakdown fields result from reduced electron mobilities of 200 cm^2/Vs [168, 169] leading to reduced ohmic heating [170].

Potential saturation problems arise due to the accumulation of charges in the defect energy states. With the electron-hole recombination time being several orders of magnitude larger than the trapping time [128], charges are quickly trapped into the defect energy states but do not recombine as fast, leading to

the accumulation of charges. Also, the midgap states formed by the large density of arsenic antisite defects cause hopping conduction, leading to substrate resistances as low as tens of ohms [171]. These issues can be resolved by annealing the material at high temperatures [172]. All of the LT-GaAs used within this project were epitaxially grown at the University of Leeds, with wafer compositions typically taking the form seen in figure 2.1

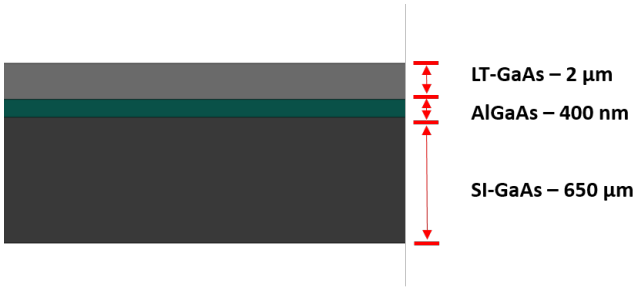

Figure 2.1: A typical LT-GaAs wafer composition, the three distinct layers are the bulk SI-GaAs and the LT-GaAs layer separated by a thin etch stop layer composed of AlGaAs. Not to scale

2.2 Annealing LT-GaAs

A post-growth high temperature annealing of the LT-GaAs wafer causes the arsenic antisite defects to form metal precipitates [167]; these become the primary trapping sites. The metal precipitates act as buried Schottky barriers in the GaAs material, and the overlapping As/GaAs depletion regions lead to a rise in the device resistance. The saturation effects are overcome due to the large density of states formed in the As precipitates.

The temperature at which the material is annealed plays a crucial role in the materials' behaviour post-anneal. Increasing the annealing temperature increases the size of the As precipitates and increases their distribution in the GaAs material, resulting in higher resistance [173]. Higher annealing temperatures, however, have an intrinsic drawback as they increase carrier lifetimes. Therefore, a compromise is required to achieve acceptable carrier lifetimes and sufficiently high resistance values. Temperatures typically used are between 500-600 °C for 10-15 minutes; this allows enough time for the As point defects to form the precipitates. As the temperature increases, the amount of point defects decreases as they migrate to form precipitates. Around 550 °C, it has been shown that the As point defects are essentially eliminated with all contributing to precipitates. At an annealing temperature between 500-600 °C, the resistance is increased 5-fold. [128].

2.3 LT-GaAs on Optically Transparent Substrates

Extensive engineering of the device's active material has been undertaken to improve PCA device performance.

One way to improve device performance is by removing a thin film epitaxially grown active layer from a bulk substrate and transferring it onto a more desired one, known as a lot technique. This technique is advantageous as it allows for the use of substrates which are not well lattice-matched to the epitaxial layer. Poor lattice-matching means the two materials would be difficult to fabricate through heteroepitaxial growth. This method was first demonstrated by Yablonovitch et al. [174], where an epitaxially grown layer of AlGaAs was removed and transferred from the bulk GaAs substrate to an arbitrary substrate. The process involved covering the epitaxially grown layer in wax and then releasing the layer from the substrate by etching a sacrificial AlAs (Aluminium Arsenide) layer. The thin film layer can then be transferred to a substrate through vdw bonding.

Cunningham et al. [175] were the first in the group to use an ELO technique to fabricate on-chip THz spectroscopy frequency band-stop filters for applications in sensing and detection. In this work, thin film LT-GaAs was transferred onto an organic dielectric (Benzocyclobutene (BCB) discussed further in appendix A). Etching the transferred LT-GaAs layer allows for photoconductive switches to be defined at any desired location on the device. Similar work has been undertaken to transfer LT-GaAs, utilising the ELO technique in [174], onto different substrates [176, 177].

Building on the work mentioned above, Bacon et al. [4,91,162] used the ELO technique to transfer an LT-GaAs layer onto an optically transparent substrate, first quartz and later sapphire to fabricate PCA devices. This work has been shown to lead to an increase in device performance.

Typically, thin epitaxial layers of LT-GaAs are grown onto thick bulk substrate SI-GaAs. PCA emitters historically have been fabricated directly on a Semi-Insulating Gallium Arsenide (SI-GaAs) substrate (these are known as LT-GaAs on SI-GaAs (LoG) emitters) with the electrode structures patterned directly onto the top of the LT-GaAs. However, it has been shown that by removing the LT-GaAs from the bulk SI-GaAs substrate, the output performance of the device can be increased; these are the LT-GaAs on Quartz (LoQ) devices.

Transferring the LT-GaAs from the bulk improves the device's thermal properties. SI-GaAs has a relatively low thermal conductivity (~ 0.6 $\mathrm{Wm^{-1}K^{-1}}$ [178]), and therefore, the ability to transfer heat is not as efficient. Transferring to a substrate with a higher thermal conductivity value will, therefore, increase the ability of the device to dissipate heat. Another advantage of transferring the epitaxial layer to a different substrate is that it removes the parasitic current

channel in the device's SI-GaAs bulk. This parasitic current is due to the difference in carrier lifetimes in the two materials, meaning that the current flows in the SI-GaAs after the carriers in the LT-GaAs have recombined. Excess joule heating is no longer generated with no parasitic channel, leading to higher output powers and increased device breakdown voltages (material breakdown due to excessive heating) due to an increased dark resistance value. By removing the bulk substrate, no carrier generation occurs in the substrate, as there is no photon absorption in the quartz. Another consequence of the ELO process is it allows through substrate illumination to occur; this method allows for the THz to propagate freely from the device.

Quartz has a high electrical resistivity compared to SI-GaAs, has very low losses and is optically transparent to 800 nm light. It has a low refractive index in the THz region of approximately 2 [179], whereas SI-GaAs has a refractive index value of 3.5 [180]; this means that less of the emitted THz radiation is directed back into the device and omits the need of a hemispherical lens to collect radiation. The graph in figure 2.2 shows that LoQ devices emit peak fields as high as 8 times that of equivalent LoG devices [4].

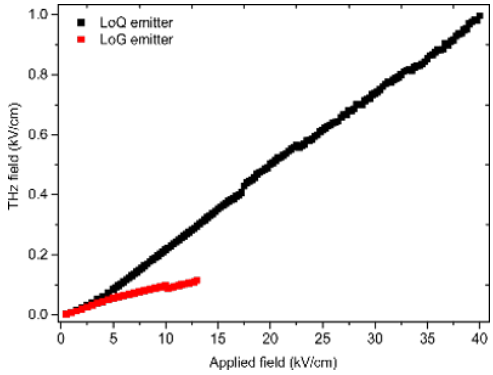

Figure 2.2: Graph comparing the peak-to-peak value of THz field produced from both devices at different optical powers [4]

However, fabrication complications arise with the use of quartz due to the thermal expansion coefficient miss-match between itself and LT-GaAs; this leads to often long bonding times and unreliable bonds, which is detrimental to the fabrication process. For this reason, sapphire was replaced by quartz. Whilst still being optically transparent to 800nm light, it has a slightly higher refractive index in the THz region of 3 [179]. Still, the thermal expansion coefficient is a closer match to that of LT-GaAs, resulting in more reliable bonds. Sapphire has a thermal conductivity value of ~ 30 $\mathrm{Wm^{-1}K^{-1}}$ [181], so provides a high level of thermal dissipation. Further, a thin layer of BCB is used to ensure an even and reliable bond. The BCB acts as an adhesive layer between the LT-GaAs and the sapphire layer (see appendix A).

Material	Thermal Expansion Coefficient ($10^{-6}K^{-1}$)
LT-GaAs	6.0 [182]
Sapphire	7.0 [183]
Quartz	0.55 [184]

Table 2.1: A comparison of the thermal expansion coefficient for the three materials. The large thermal mismatch between quartz and LT-GaAs can be seen.

2.4 LT-GaAs Basic Fabrication Process

As mentioned in 2.3, the basic fabrication method was developed by Bacon et al., and the results of early devices can be found in [91, 162]. However, this process suffered from low yield. An in-depth description of this process can be found in the Appendix A. This section will discuss the improvements made to the basic process throughout this project.

The following briefly summarises the basic fabrication process first presented in [4]. This process was the starting point for the fabrication of devices before the improvements were made. The diagram in figure 2.3 depicts the fabrication steps.

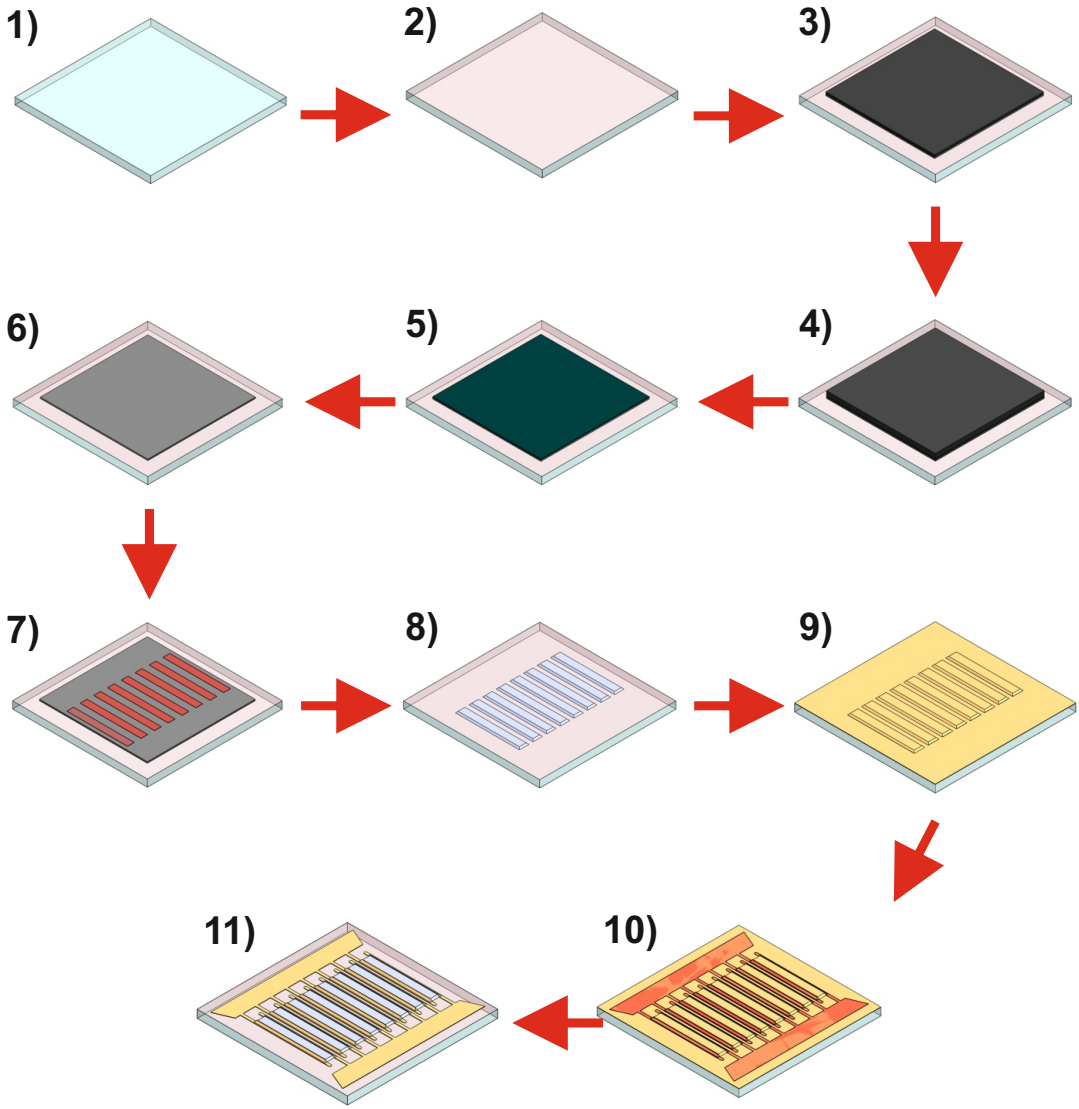

Figure 2.3: A depiction of the steps of the basic fabrication process, (1) The starting wafer, (2) An BCB layer is applied, (3) The LT-GaAs wafer is bonded to the sapphire substrate, (4) The substrate is thinned, (5) A citric etch is used to remove the remaining SI-GaAs, (6) Etch stop removal to complete the ELO process, (7) Photoresist bars are patterned on, (8) LT-GaAs bars are etched, (9) Gold is evaporated onto the device, (10) The electrode structure is patterned onto the device, (11) The unwanted metal is removed via an etch to finish the device.

2.4.1 Steps

1. The sapphire substrate and LT-GaAs wafer are cleaned to ensure a strong and even bond is achieved between the layers.

2. A spin on polymer called Benzocyclobutene (BCB) is applied to the sapphire substrate. BCB is a polymer-based resin used as an adhesive layer to ensure a reliable bond between the LT-GaAs and sapphire layers. A target layer thickness between 400-500 nm ensures a strong bond with as little interference to the radiation introduced as possible (the thermal characteristics of BCB are discussed in section 5.1).

3. To achieve the ELO process the LT-GaAs layer must be bonded to the sapphire substrate. The LT-GaAs wafer is inverted and placed in the centre of the sapphire substrate in the chamber of a wafer bonder. The wafer is bonded at a force of 500 Ncm^2 and a temperature of 250 °C for 1 hour. The chamber temperatures cure the BCB and secure the two wafers.

4. To leave only the LT-GaAs layer, the bulk SI-GaAs must be removed. This is achieved through a two-step process. Firstly, the majority (≈ 620 μm) of the material is removed through mechanical lapping; this relatively aggressive method introduces a high-stress level to the device. To ensure that the LT-GaAs layer is not damaged, the final $\simeq 28$ μm is removed through a second process using a wet etch.

5. The final 30 μm is removed using a citric etch (5:1-$C_6H_8O_7$:H_2O_2). This process is a lot more selective, and coupled with using the AlGaAs etch stop, the remaining SI-GaAs is removed.

6. The final step of the ELO process is removing the etch stop; this is achieved using a buffered Hydrofluoric Acid (HF) solution.

7. An etch mask is patterned onto the LT-GaAs layer to be able to define the individual emitting strips of the device.

8. The bars are etched using a wet etch solution (comprising of H_2O:H_2O_2:H_2SO_4 in a ratio 250:8:1). The diluted ratio is used to produce sloped sidewalls of the LT-GaAs bar to ensure the electrodes can be interfaced properly.

9. To fabricate the electrode structures, a metal layer is sputtered onto the device first. Sputtering ensures that the metal coats the sidewalls of the device well and achieves good electrical contact. An initial 20 nm titanium layer is deposited before applying a thicker 200 nm gold layer.

10. To define the gold structure, a photoresist mask is used to cover the areas in which the gold is to remain.

11. A potassium iodide etch is used to remove the unwanted gold, and a final HF etch is used to remove the titanium.

2.4.2 Mounting

The finished device must be packaged for testing. The device's resistance in the absence of the optical pump (the 'dark' resistance) is probed. The resistance value varies depending on the device gap size. However, all devices are expected to be within the MΩ range. Low resistances will lead to increased dark currents flowing through the device and excess heating. Measuring the resistance at this point also allows any shorts to be found; if any are detected, re-masking and etching can be performed to rectify.

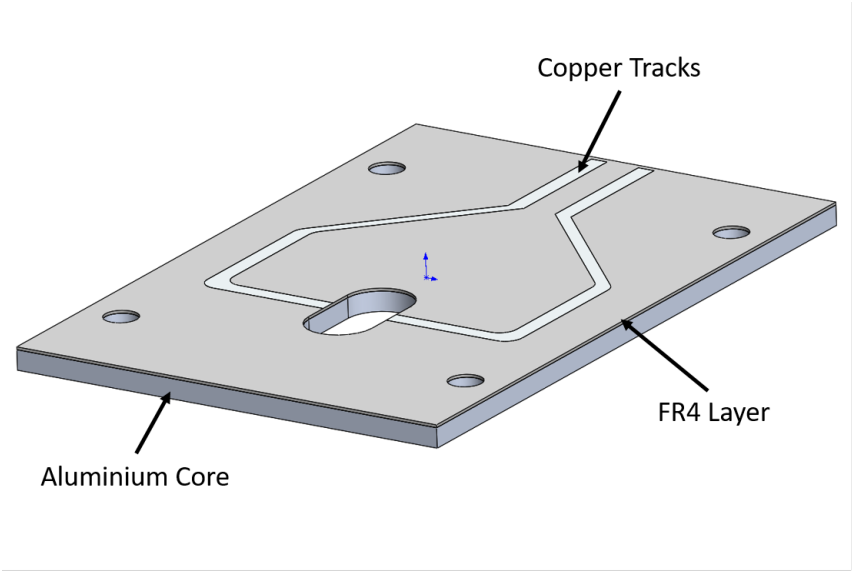

Figure 2.4: Structural layout of the PCBs used for mounting PCA devices. The FR4 acts as the top insulator on top of the aluminium core.

The devices are mounted on custom Printed Circuit Board (PCB); the diagram in figure 2.4 shows the board's composition. The PCB is an aluminium core with an insulating top layer of material called FR4, a flame-retardant glass-reinforced epoxy resin laminate material. The copper tracks provide an electrical connection between the device and the SMA connector. The hole size in the board is drilled to match the device's active LT-GaAs area. The PCA is connected to the board's copper tracks via their gold contact pads; a silver conductive paint can be used to hold the devices to the board and serve as the electrical connection. Larger devices require a two-part silver epoxy to connect fly wires to the board due to the silver paint's inability to support the increased device weight. Before the SMA connector is soldered to the board, a small strip of Kapton tape is used to isolate the connector from the board's aluminium core electrically, avoiding any grounding issues.

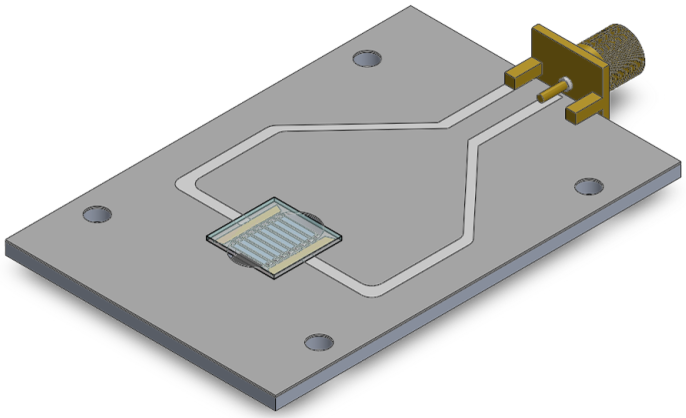

Figure 2.5: The device mounted with the backside pointing out from the board

2.5 Fabrication Improvements

The fabrication process is difficult and requires high levels of precision. For this reason, the yield of working devices is low. Throughout the project, improvements to the fabrication process have been implemented to ensure a higher yield of successful devices.

2.5.1 Fabrication issues

Whilst the existing process presented by Bacon et al. [91] does yield working devices, certain issues arise from it. These issues have led to device design and operation limitations.

One of the major issues found with the existing process was the citric etching process, causing a high percentage of device loss. During the bulk SI-GaAs removal, it was found that the LT-GaAs layer was being attacked and etched simultaneously. This is an undesirable circumstance, especially because the layer thickness is considerably thinner than the remaining bulk SI-GaAs, ultimately causing the LT-GaAs to etch fully. When the edges of the LT-GaAs layer etch, it causes the wafer to fracture, and large pieces detach from the sapphire substrate. As can be expected, this is not a salvageable issue and, in all cases, led to the failed devices.

Another issue arising from the fabrication process was found during device testing. The LT-GaAs bars have rough sidewall profiles; this was adjudged to cause a lack of continuity in the gold electrode layer, which is thought to lead

to lower breakdown applied electrical biases.

With the investigations of device structures, it was seen that the process was limited to producing large gap sizes of >50 μm and large electrode widths of >50 μm. With the existing fabrication process, the electrodes are added to devices via an etch-down approach. However, issues with this method arise when trying to move to smaller electrode widths. The etch rate of the gold etch solution becomes difficult to predict when the widths were smaller, meaning that anything below 50 μm was not feasible to fabricate in this way; in all cases where this was attempted, it resulted in over-etching of the gold, giving inconsistent and non-reproducible features and in some cases complete removal of the gold.

2.5.2 Bulk Etch Preparation

Protecting the LT-GaAs active layer while removing the remaining bulk SI-GaAs material is an important step in the fabrication process. Originally from the process in section 2.4.1 2, a photoresist barrier is applied to the edges of the semiconductor layer with a fine-tip cotton bud to protect the active material. This method, whilst, if done correctly, will protect the LT-GaAs during etching, is relatively time-consuming and hard to do so accurately. A thick photoresist, AZ4562, is used to ensure that the layer barrier thickness is sufficient to cover the LT-GaAs layer. To apply the photoresist accurately, it must be ensured that the LT-GaAs layer is covered but that there is no overlap onto the SI-GaAs surface as this prevents it from etching. With the combined thickness of both these layers at this point being around 30 μm, achieving a high percentage of LT-GaAs coverage without greatly overlapping the SI-GaAs also is difficult.

A new method for protecting the active was developed to improve the yield of devices undergoing successful bulk SI-GaAs removal and the time it takes to process devices. The new method still uses a photoresist as the means of protection; however, by spin coating the entire device and uncovering only the SI-GaAs surface, the LT-GaAs layer is protected well.

To apply the protective layer, a negative photoresist is chosen, Ma-N440. A negative photoresist means that the exposed photoresist is not dissolvable in the developer solution, whereas the unexposed photoresist is. By using a negative photoresist, the optically transparent sapphire substrate can be exploited to expose the resist through the backside of the device; this then uses the LT-GaAs as a natural mask to prevent the exposure of the photoresist on top of the SI-GaAs.

The photoresist is applied in two layers; the reason for this is to provide a sufficiently thick layer to cover the device. The first layer is spun at a lower speed to ensure a thicker layer, and the second layer is spun faster to create a slightly thinner top layer. The first layer is statically dispensed on the device

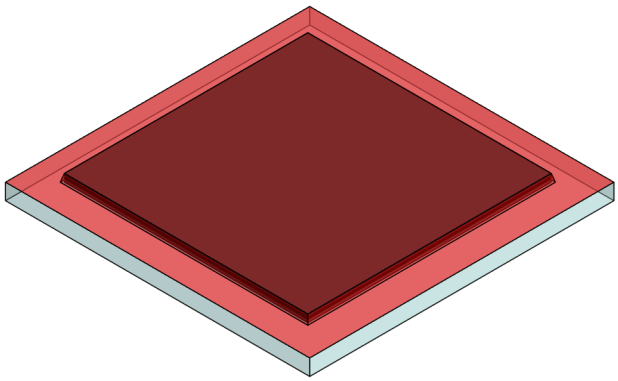

Figure 2.6: The completely covered device before exposing the AZ4562 resist.

surface and spin-coated at 3000 rpm for 60 seconds; the device is then baked for 5 minutes at 100 °C. The longer bake time is purposefully used to deform the shape of the photoresist; longer bake times partially destroy the photochemicals, which increases the exposure time and increases the adhesion to the device. The longer bake times produce a slight overlap of the resist with the SI-GaAs edges when developed. The second layer of resist is applied in the same way as the first but at a spin speed of 6000 rpm. Again, the device is baked for a longer time of 10 minutes at 100 °C to deform the resist and ensure good adhesion to the first layer.

To expose the photoresist, a UV IR mask aligner provides a flood exposure. The device is placed upside down on the exposure stage and then exposed with a relatively high dose of 2400 mJ/cm^2; as mentioned beforehand, this is due to the longer bake times. The device is placed into the developer Ma-D 331, a sodium hydroxide-based solution, for around 5 minutes to clear the unexposed photoresist. The technique of application for the protective layer is the cause for the longer development time as the resist is adhered well to the surface of the device. The slight resist overlap with the edge of the SI-GaAs wafer edge ensures that the underlying LT-GaAs is still protected when the wafer starts etching.

This new method solved the problems with this step of the process, with 100% of the devices fabricated with this method successfully undergoing the substrate removal.

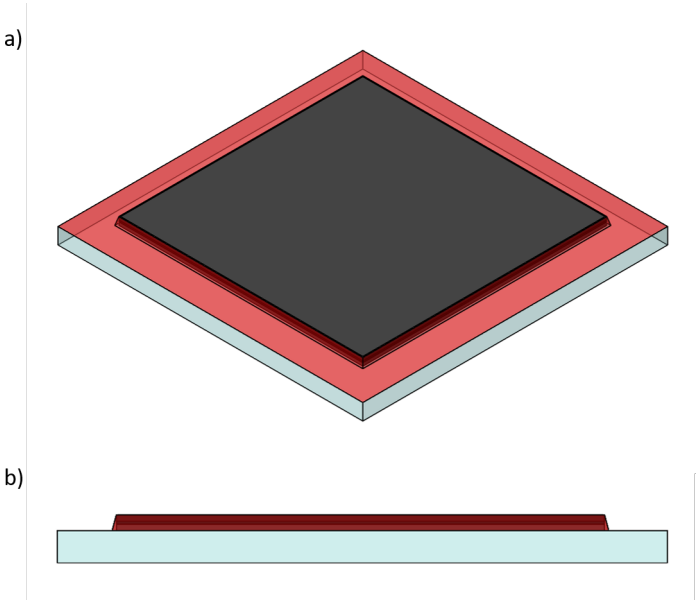

Figure 2.7: a) Once the resist is photoexposed and developed, the SI-GaAs surface is exposed, while the rest of the device remains covered with resist. b) A side view showing how the resist protects the bottom LT-GaAs layer by flowing up the sidewall.

2.5.3 LT-GaAs Etching

Problems appeared during device testing, with them exhibiting earlier than expected electrical breakdowns. One of the reasons theorised for this was a poor continuity of the electrode gold layer due to a rough sidewall profile. The ratio of constituent etch chemicals outlined in section A.0.4 defines the sidewall profile of the LT-GaAs bars; with a smaller ratio of water to hydrogen peroxide and sulfuric acid, the etch is quite aggressive, leaving pits and dents in the sidewall. Different ratios were tested to find an improved ratio to improve the sidewall profile. A test pattern (seen in figure 2.8 was created with differing LT-GaAs bar sizes to investigate the etch capabilities.

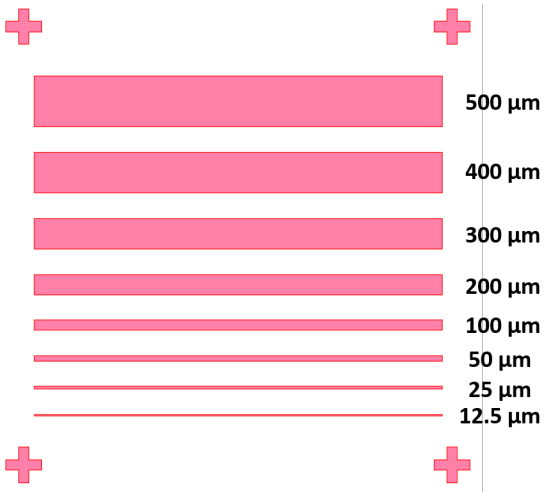

Figure 2.8: The etch test pattern design. The designs consist of different width bars ranging from 500 μm down to 12.5 μm.

Three different etch ratios were investigated, each with a different water concentration and maintaining constant sulfuric acid and hydrogen peroxide concentrations. The ratios of constitute chemicals were ; 250:8:1, 800:8:1, and 1000:8:1 of H_2O:H_2O_2:H_2So_4. A single 1x1 cm piece of LT-GaAs on SI-GaAs wafer was used. For simplicity, the wafer did not undergo the ELO process, and instead, the designs were patterned straight onto the LT-GaAs.

The Scanning Electron Microscope (SEM) images in 2.9 show the LT-GaAs bars created by each etch. The profile produced by the strongest etch (250 parts water) is as expected, with rough sidewalls and many pits and dents. Measuring the features post etch showed an undercut on the bar width dimensions; hence, the design accuracy is also somewhat lost with this ratio. The 800 part water etch ratio yielded better results; there is still some pitting and dents on the sidewall and some small undercutting of the bar dimensions. The weakest etch (1000 parts water) provided the best looking sidewall profiles from the testing; the sidewalls are virtually free of pitting and visible roughness. There is also no visible undercut of the bars due to the weaker etch being less aggressive.

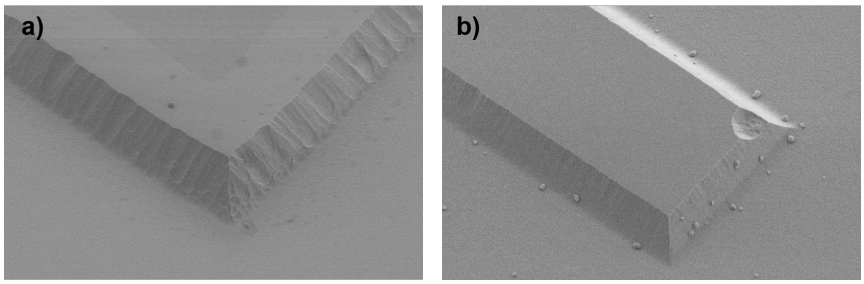

Figure 2.9: SEM images of the etched bars. (a) The strongest etch can be seen to aggressively attack the sidewalls, leaving rough surfaces. (b) The weakest etchant produces much smoother sidewalls due to the slower etch rate.

A by-product of a weaker etch is a much steeper sidewall pitch, which limits the size of the bar that can be produced. For the weaker etch, the sidewall slope length is 20 μm; this left only the 50 μm width bar as the smallest feature on the test device.

From these tests, the etch ratio was adapted to 1000:8:1 of H_2O:H_2O_2:H_2So_4. The sidewalls support better electrode continuity, and the weaker etch allows for greater repeatability with the devices.

2.5.4 Electrode Deposition

Experimenting with the electrode widths (see 4.2) became a point of interest to improve device efficiency. This required asymmetrical electrode geometries; some designs became much smaller than previously fabricated. The problem with fabricating smaller electrode widths using a gold etch method became apparent with features below 50 μm in width. It was found that for most cases smaller features were over etched, with really small features (>20 μm) being etched through due to an unreliable etch rate. The reason for the unreliable etch rate is due to the acceleration of the rate once the etchant becomes exposed to the underlying titanium layer. Therefore, a new method must be developed to achieve the desired features.

Using a photolithography and lift-off technique, it is possible to fabricate smaller features. This technique was not considered when the original fabrication method was devised owing to worries that the photoresist would not adhere well to the BCB, rendering it an unviable option. After preliminary testing of some simple structures patterned directly on a BCB layer, it was apparent that these suspected issues were not prevalent, meaning that this method could be used. Previously, sputtering was the deposition technique chosen as it provides good sidewall coverage. However, it can not be used in conjunction with a lift-off technique as the angled coverage is not compatible; removing the unwanted gold after deposition without damaging the device would be impossible. For the aforementioned reasons, thermal evaporation was selected for electrode deposi-

tion. This is still a suitable method for producing good sidewall coverage, as there are no protruding features to cause shadowing.

The electrode patterning step takes place after defining the LT-GaAs bars. The process is similar to the one in A.0.5 except a Lift off resist (LOR) layer is applied to ensure a clean lift-off. The LOR, LOR7B, is spin-coated onto the device at 3000 rpm for 40 seconds and baked on the hot plate at 165 °C for 5 minutes. The photoresist, S1813, is spin-coated onto the device at 3000 rpm for 40 seconds before being baked at 115 °C for 1 minute. A direct write laser completes the photoresist patterning, although the dose and defocus values change to 130 and -1 respectively, to account for the LOR layer now present. The device is developed in MF-319 for 1 minute and then rinsed in DI-H_2O to stop the development process. The device must be checked under the microscope to ensure that the LOR has been fully developed and cleared from unwanted areas; this can be seen as a slight undercut of the top photoresist layer. If the LOR is not removed fully, then the metal will be stopped from adhering to the device surface; over-development causes channels where LOR is completely removed, which can lead to photoresist de-lamination. The devices are ashed in the plasma asher at 50 percent power for 2 minutes to remove any delaminated or residual photoresist.

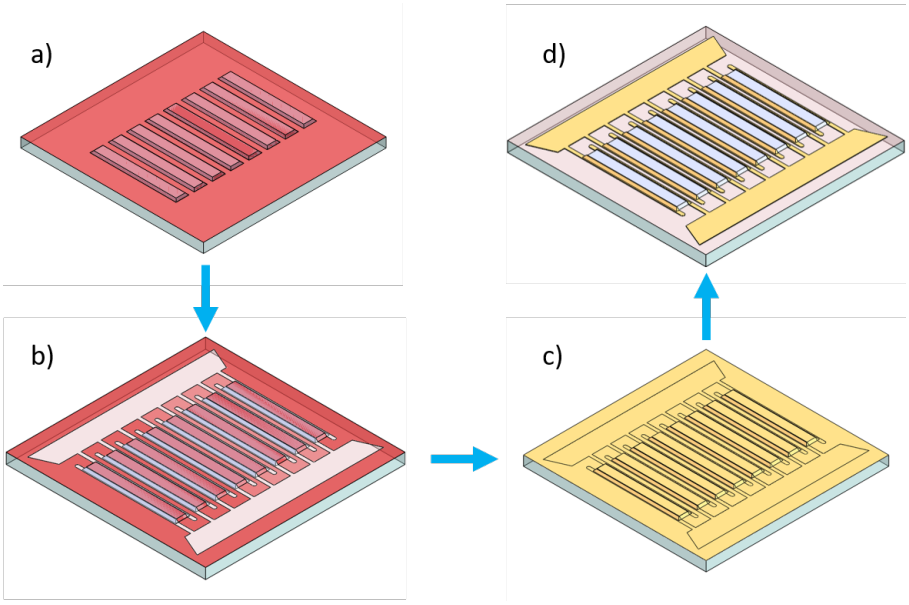

Figure 2.10: An overview of the new electrode fabrication steps. a) A photoresist layer covers the device b) The electrode mask is patterned onto the surface c) A Gold layer is evaporated onto the entire device d) After lift-off, the electrode pattern is left defined on the device.

An E-beam evaporator is chosen for thermally evaporating the electrode materials as it provides a high level of precision when evaporating layers. Evaporation must be performed under a high vacuum to ensure a high-quality film free from impurities. A high vacuum will improve the mean free path of the vaporised material from the metal source and allow the material to travel directly to the target substrate without reacting with any other particles [185]. Not achieving a high vacuum can lead to non-uniform or discontinuous films, as vaporised molecules from the source material can collide with undesired particles in the chamber. Therefore, the evaporation chamber is pumped down to a high vacuum of $1 \times 10^{-}6$ mBar. First, a 5 nm Ti layer is deposited again to aid the adhesion of the gold layer. The source is then changed, and a thicker 200 nm layer of gold is deposited. Devices are placed into a positive photoresist stripper, SVC-14, heated to 60 °C on a hotplate. The photoresist stripper is left to work on the device until all unwanted metal is removed. This occasionally requires a gentle agitation in an ultrasonic bath at 20 percent power; this aids in removing the LOR layer underneath. This technique has allowed for electrode widths down to 5 um to be fabricated successfully.

2.5.5 Small Gap Fabrication

The new etch ratio provides reproducible results with good sidewall profiles. However, the sidewall length is 20 μm in length, meaning that the filling factor is limited when moving to small gaps devices (<50 μm). To maximise the packing factor, the periodicity of the electrode pairs must be reduced. A new method for defining the LT-GaAs bars was developed to achieve this.

To reduce electrode pair periodicity, the etched bar sidewall length needed to be reduced. The solution was to use a fast etch which is much more aggressive and provides near-vertical sidewalls. A by-product of this method is that it no longer allows for the electrodes to be fabricated to roll up the sidewalls of the LT-GaAs bars. This resulted in a complete restructuring of the fabrication steps. The electrodes are patterned and deposited on top of the un-etched LT-GaAs layer before the bars are defined.

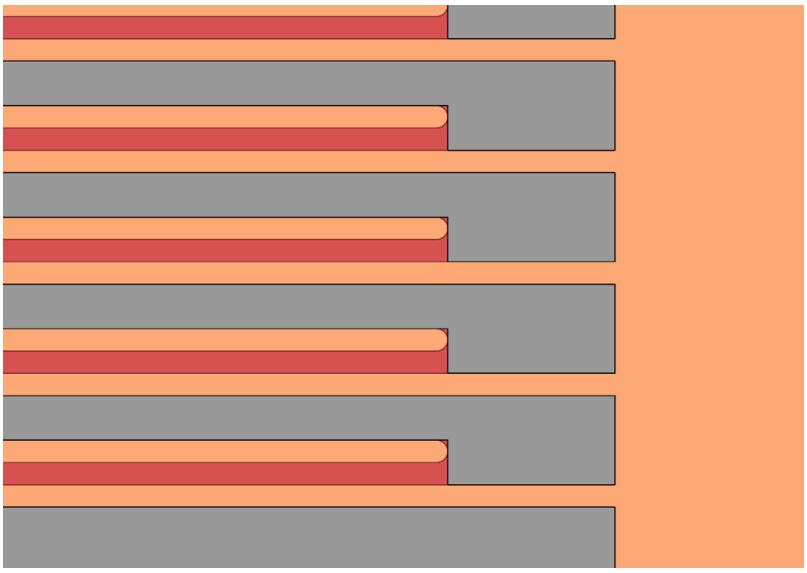

Figure 2.11: A close up section of an array with the etch mask patterned on. The red coloured photoresist protects the LT-GaAs between the electrode pairs and the entire electrode structure.

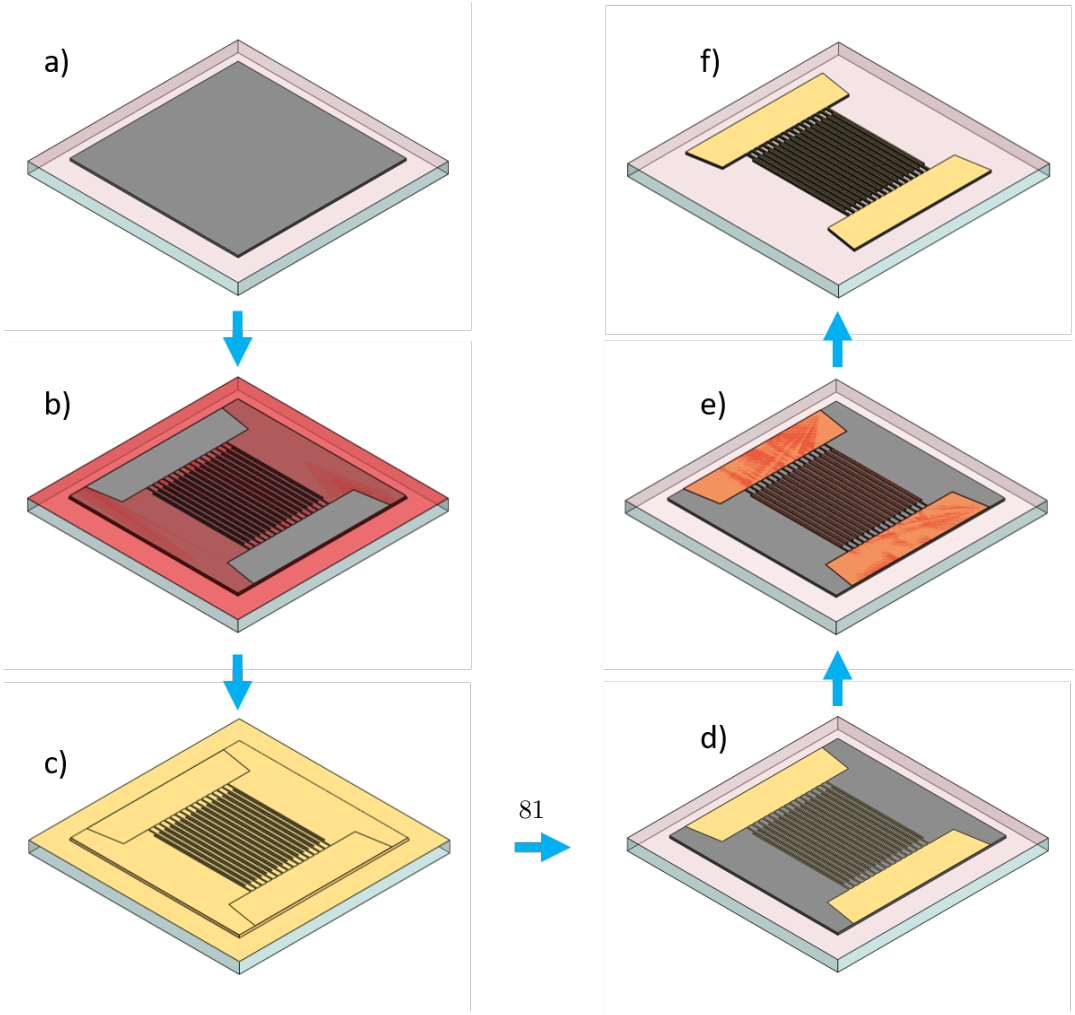

Figure 2.12: Once the device is exposed and developed, the SI-GaAs surface is

After the ELO fabrication steps are completed and the LT-GaAs layer is exposed, the electrodes can be patterned and deposited. The electrodes are realised in the same method as outlined in section 2.5.4; once the lift-off process is completed, the device can be masked ready for the LT-GaAs etching step. As with most of the masking in the fabrication process, S1813 is statically dispensed and spin-coated onto the device at 3000 rpm for 40 seconds before being baked at 115 °C for 1 minute. The design of the etch mask seen in 2.12 e) shows that the amount of LT-GaAs removed is much less as the entire device sits atop the active layer. The etch mask is patterned onto the device using a direct write laser, the dose and defocus of 130 and -1 respectively, before being developed in the standard solution of 4:1 H_2O:MF-319 until clear. A plasma ash is again used to remove all unwanted photoresist.

To etch the LT-GaAs bars, the etch solution consists of H_2O:H_2O_2:H_2SO_4 in the ratio 40:8:1. The etch is very aggressive providing an etch rate of 500 nm/min; it is clear to see when the LT-GaAs has etched due to the optically transparent substrate. It is imperative that the device is not left too long as it will over-etch, leading to loss of the electrode structures. The results in 4.5 demonstrate the fabrication capabilities this method provides.

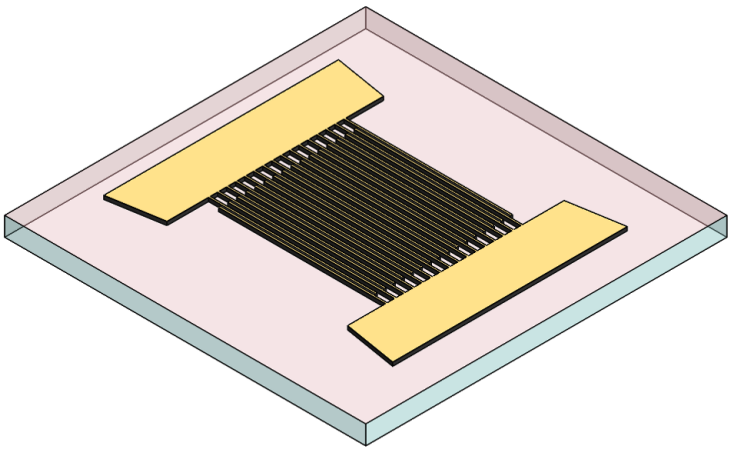

Figure 2.13: The entirety of the finished small gap device sits atop the LT-GaAs material.

2.6 Conclusion

In conclusion, the initial process for fabricating PCA devices using an ELO technique was presented. A number of issues arising from the initial fabrication were discussed, and the current limitations on device design and fabrication were highlighted. Several improvements to the fabrication were also presented, increasing the yield and fabrication times for the devices. A new method for protecting the LT-GaAs layer during the bulk SI-GaAs etch was developed, which ensured that the LT-GaAs layer was prevented from being exposed to the etchant solution and subsequent device failure. A study on the LT-GaAs etchant ratios was conducted to find an optimum ratio that provided LT-GaAs bars with an improved sidewall profile and repeatable sidewall lengths. In order to fabricate smaller electrode geometries, a new method for electrode deposition was employed; this provided the ability to fabricate <50 μm electrode features. An E-beam thermal deposition was used to increase the design accuracy of the electrode geometries. Finally, a new technique for fabricating small gap PCA devices was developed, allowing a greater range of device designs to be used. The new technique involved completely restructuring the fabrication process, moving to fabricating the electrode structures on top of the device and then using a fast wet etch to remove unwanted LT-GaAs.

Chapter 3

Characterisation Methods

This chapter will discuss the characterisation set-up and the system variations used throughout this project to characterise fabricated devices. A discussion of the difference between the setups is presented here, as well as comparisons with alternative methods.

3.1 Emitter Characterisation

The two main components of the testing set-up are the optical and instrument set-ups. The optical set-up comprises the optical components used to facilitate the generation and detection of THz radiation. Then there is the array of control electronics employed to ensure accurate capture of device information and provide biasing for PCA devices. Both parts are of equal importance.

3.1.1 Optical Set-Up

The set-up used for testing devices is similar to that which would be used for 1D-THz-TDS and can be seen in figures 3.1 and 3.2. A Spitfire ACE PA provides the excitation pulse (discussed in 1.6, and the pump line is attenuated using Neutral Density (ND) filters, with this providing a range of adjustability to the optical power available. The fs pump beam excites the PCA device, causing the emission of THz radiation. This radiation propagates into free space, following the path of the incident IR pump beam. Due to the pump beam having such a high peak power, a Polytetrafluoroethylene (PTFE) filter blocks the pump beam after excitation to prevent it from damaging the photodiodes. As this set-up is designed for THz-TDS, a set of parabolic mirrors directs the generated radiation to the detection area. The THz radiation is generated in a collimated beam before being focused down to a sample area; during device characterisation, this area is void of any materials. The radiation is collimated again before being focused onto the detection crystal in the detection space. The sampling line originates from the main fs beam line earlier in the system using

a 90:10 per cent beam splitter. This line passes through a hole in the center of the final parabolic to ensure a collinear arrival at the EO crystal, providing maximum overlap with the focused THz spot. The altered sampling beam then goes through the detection optics mentioned above. The main experimental arrangement discussed here is within a purge box, ensuring a low humidity atmosphere (<10% humidity).

3.1.1.1 Testing Set-up versions

Throughout the project, the optical layout of the experimental arrangement underwent slight variations, the main one being a change from generating in a collimated beam to generating in a focused beam. The optical layout discussed in 3.1.1 is the main basis for the set-up used for testing, with the changes being how and where the pump beam excites the PCA.

The first optical layout generates THz using a collimated fs pump beam. When the pump beam leaves the amplifier, the beam diameter is roughly 8 mm, measured as Full Width at Half Maximum (FWHM). The pump beam is expanded using a reflective beam expansion method to a width of 32 mm; this consists of a reflective telescope and a 2-inch beam expander. Expanding the beam to this diameter pre-excitation of the PCA has a dual purpose: it firstly allows for the use of larger devices, and secondly, it accounts for any intensity variations of the excitation pulse, ensuring the centre of smaller devices are not saturated before the outer edges. This set-up can be seen in figure 3.1.

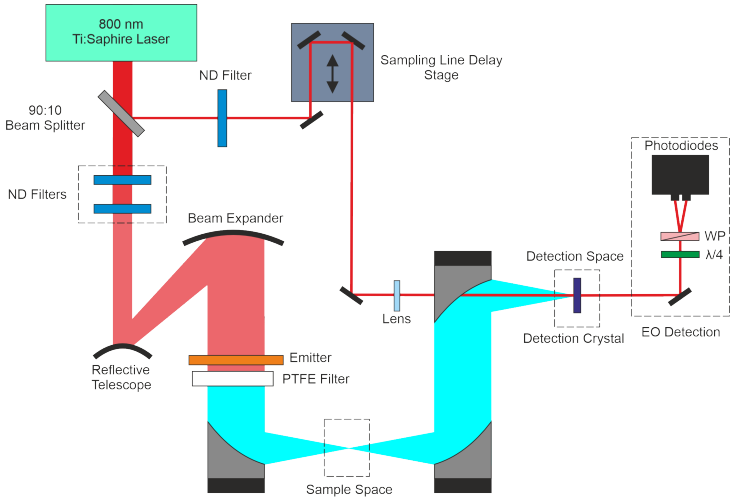

Figure 3.1: Optical diagram of the testing set-up with the emitter in the collimated beam.

The second optical set-up seen in figure 3.2 shows that THz generation takes

place in a focused fs beam. The reason for this is to improve the detected signal, by generating in a focused beam it ensures the resulting generated THz beam will fill the collecting parabolic. The advantage of a fully filled parabolic is that the focus of the THz pulse will be much smaller in the detection space. This can be explained in terms of Gaussian beam theory. A Gaussian beam has an intensity profile that follows an ideal Gaussian distribution. This is to say that the intensity profile is radially symmetrical about the centre of the beam and decreases as the distance from the centre increases. The beam waist 'ω_O' is taken as the point at which the intensity drops to $1/e^2$ (13.5%) of the peak value at the centre of the beam. A collimated Gaussian pulse is one in which the beam radius does not vary significantly over the distance it propagates [57]. When a collimated Gaussian beam is focused by an optical element, the spot size achievable at the focus is given by [186]:

$$2\omega_0 = \frac{4M^2\lambda f}{\pi D} \tag{3.1}$$

where M is the beam quality parameter, λ is wavelength, f is the parabolic mirror focal length and D is the beam diameter before focusing. The tighter the focus, the higher the field strength. There are drawbacks to this method; it is hard to align well and thus is susceptible to larger beam deformities, which negatively impact the spot size. Also, with a focused generation scheme, there is no longer any compensation for intensity variations in the fs pump beam.

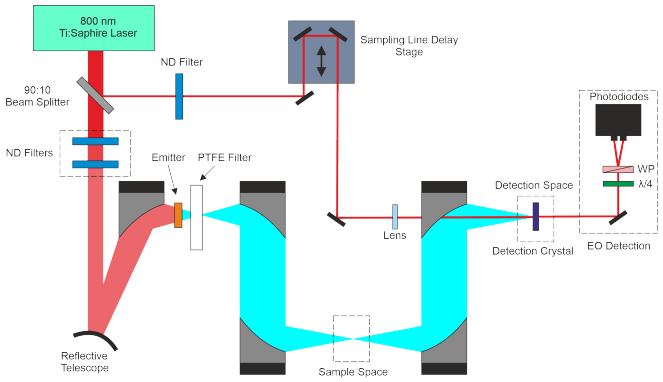

Figure 3.2: Optical diagram of the testing set-up with the emitter in the focused beam. This ensures that the excitation beam will fill the entirety of the device. The THz spot sizes at the sample and detection space is $\simeq$ 640 $\pm$35 μm

3.1.2 Instrument Set-Up

The instrument set-up plays a vital role within the testing set-up; a block diagram of the instruments involved can be seen in figure 3.3. A boxcar averager and Lock-In Amplifier (LIA) is used for data acquisition to improve the SNR.

The reference for the LIA is set to match that of the frequency at which the PCA bias is modulated. A 1 kHz master reference signal is provided by the spitfire laser, which is synchronised with the pulse output. A signal generator (Agilent 33500B) is triggered from the master reference, producing a 125 Hz signal used to gate the pulse generator (DEI PVX-4150). The PCA emitter electrical bias is supplied by a high-voltage DC power supply (Keithley 2410) connected to the pulse generator's input. The pulse generator creates a square wave voltage signal by chopping the DC voltage supply; this square wave provides the bias voltage for the PCA.

On the detection side, a pair of balanced photodiodes (Newport Nirvana 2007) are used for the EO detection (as described in 1.9.2), the output of which is connected to the boxcar averager (SRS SR250). The signal from the photodiodes is a very low-duty cycle signal, with a repetition rate of 1kHz and an electrical pulse duration of 3 μs; this adds a large amount of noise to the signal; in order to improve the signal, the boxcar averager can be used. The 1kHz master signal triggers the boxcar amplifier. Once triggered, there is a controllable delay time and window width. The signal is averaged over this window and then sent to the lockin for further processing. This removes any noise from the photodiodes when no signal is expected. The LIA receives the signal from the boxcar output and is 'locked' into the modulation frequency of the PCA being 125 Hz; this means that the LIA works on an 8 pulse train with 4 'on' and 4 'off' pulses, to suppress the noise further. Finally, the signal is acquired from the LIA and recorded using a Labview program running on a PC.

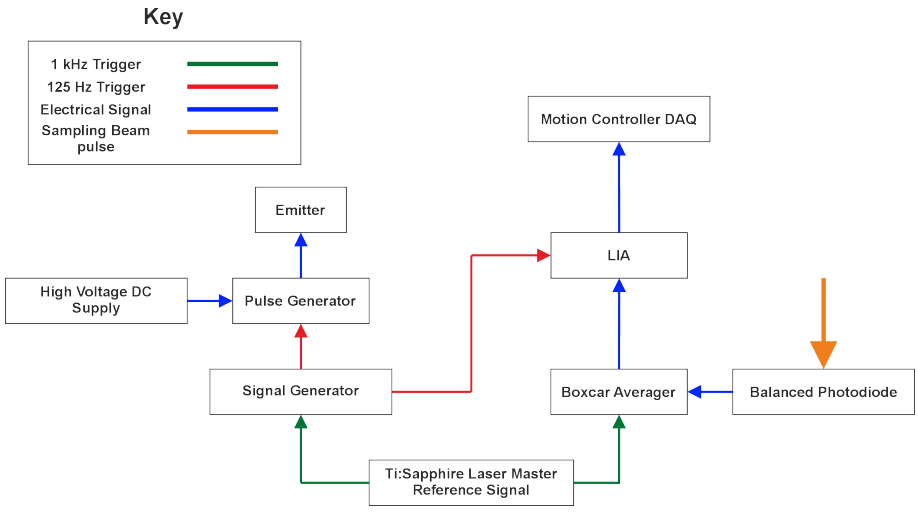

Figure 3.3: The block diagram shows the instrument control set-up, the main signal of note is the master 1 kHz reference from the amplifier as this provides the synchronisation for the rest of the instrumentation.

3.1.3 Reflections

Reflections are a significant problem during spectroscopy scans. The resolution of the frequency domain information is proportional to the scanned time range of the time domain signal. Thus, reflections determine the length of time the sample can be scanned without introducing oscillations in the frequency domain. This limiting of the time scans reduces the overall resolution of the scan and the information obtained from each experiment. Also, reflections of the THz pulse may interfere with 2D spectroscopy measurements; this can occur if reflected pulses interact with the sample fast enough after the initial excitations to re-excite the sample and give false results.

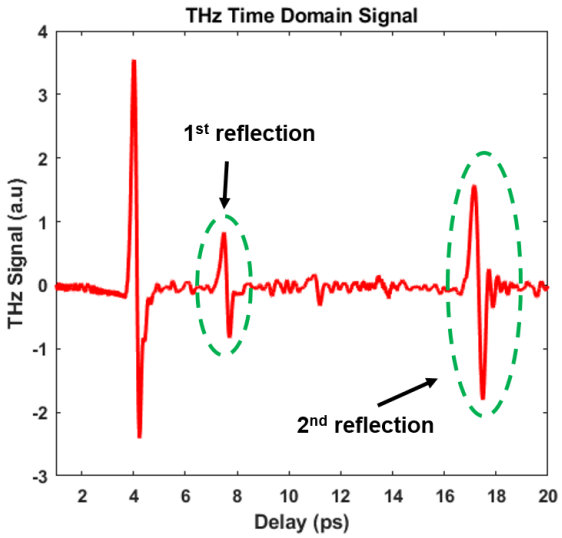

Figure 3.4: The time domain signal of a 5 μm gap array measured with a 150 μm thick GaP crystal. The main pulse can be seen as the first and largest pulse followed by two reflections. The 1st reflection is from the detection crystal and the 2nd comes from the substrate.

There are a few different places that reflections in the system may come from. One of the main sources of THz reflections is from the substrate of the PCA emitter. Another area of the set-up that reflections come from is the EO crystal. Reflections can also occur from the sample being experimented on. In each of these cases, the reflections result from the mismatch between the refractive indexes of air and the materials. The delay between the main THz pulse and the reflections can be estimated using the equation:

$$t = \frac{2nL}{c} \tag{3.2}$$

where n is the material's refractive index, and L is the length of the material. Using this equation, the origin of the reflections in figure 3.1.3 can be determined. The main pulse is seen at $\simeq$ 4 ps. The reflection from the GaP detection crystal will have a time delay of $\simeq$3 ps (using n=3.3 at 1 THz and L=150 μm). The reflection from the sapphire substrate will be delayed from the main pulse by $\simeq$13 ps (using n=3 at 1 THz and L=650 μm). Therefore, the first reflection originates from the detection crystal, and the second comes from the substrate.

There are different ways to improve the reflection issue, mostly by pushing the reflections back in time to delay them. Delaying the reflections allows for longer scans, improving the scans' resolution. This can be done in the emitter by using a thicker substrate, as this would delay the reflection in time. In the EO crystal, increasing the thickness would also push the reflections back in time. However, this presents its own problems mentioned in section 1.9.2.

3.2 Characterisation

There are some key characterisation experiments that are performed for each device; the two main tests are designed to determine the relationships the generated THz signal has with bias voltage and optical pump power.

3.2.1 Optical Characterisation

The pump power is swept through a range of values to characterise the THz emission as a function of the optical excitation pulse incident on a device. The optical pump power is set, and a scan is taken to acquire the time domain THz pulse generated. The peak THz signal value can be extracted from this. These scans are repeated for each new optical pump power and are used to build an accurate picture of the optical behaviour. Throughout each optical sweep, the bias voltage is kept consistent; the bias can be changed for a new set of sweeps depending on the information required. It is important to obtain this information as it indicates how the excitation power affects the emission. The device will begin to saturate at a certain optical power, as discussed in 1.8.8; this point is critical to ensure that it is not exceeded when operated.

The pump laser line is attenuated by 2 sets of ND filter wheels, allowing for 36 variations of the optical power available to excite devices. Each individual filter must be chosen to be of a similar thickness and as thin as possible to ensure as little beam broadening as possible. The graph shown in figure 3.5 shows the behaviour of a PCA device with changing optical power; from this, two distinct operational modes can be observed. The peak THz field increases linearly at low optical pump powers. This is the first operational regime, referred to as the linear regime. The second regime is present at higher optical pump powers. As

the power increases, the device begins to saturate, and a linear increase is no longer observed; instead, an exponential decay can be seen. There will come a point when the device becomes completely saturated, and there will be no increase in THz field for increasing optical power. The saturation occurs for several reasons, all discussed in 1.8.8. During measurements, it is important to ensure that the device behaviour is observed carefully as the optical power is increased; this is because the risk of damage becomes greater when the device enters the saturation regime. Operating a device in the saturation regime for experimental work is preferred due to the increased protection against power fluctuations of the pump laser. However, increasing the pump power whilst the device is completely saturated leads to an increase in device heating and, in some cases, complete breakdown of the device.

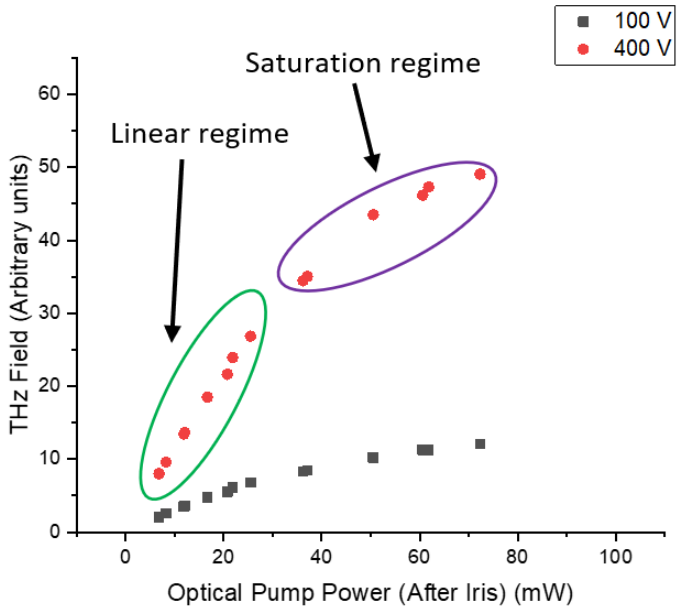

Figure 3.5: An optical characterisation graph for a PCA device, the linear and saturation regimes are depicted. The device is a 5x5 mm active area array.

3.2.2 Bias Field Dependence Characterisation

Testing the electrical behaviour of a device is an important step during the characterisation process that is required to fully understand how the device operates. When electrical behaviour is spoken of here, it refers to the relationship between the biasing voltage and the peak THz signal obtained. To characterise the electrical behaviour, the biasing voltage is firstly started at a fairly low value before being incrementally increased to a bias voltage deemed "safe"; ini-

tially, this biasing field was 20 kV/cm due to the breakdown in air value ($\sim$ 30 kV/cm), this is discussed further in 4.3. During the voltage sweeps, the optical pump power is kept the same to ensure that the only influencing factor is the biasing field. As with the optical characterisation, sweeps may be repeated at different optical powers to observe the behaviour under different regimes. At each bias value, a time domain scan of the THz generated pulse is collected, and from this, the peak THz signal is extracted. The graph in figure 3.6 shows the electrical behaviour of a device (same device shown in figure 3.5); it can be seen from this that the peak THz signal increases linearly with increasing bias values. The linear relationship is a key indicator of how good a PCA design is; the equation describes the linear relationship:

$$E_{THz} \propto E_{Bias} \frac{\delta n}{\delta t} \tag{3.3}$$

This shows that the THz field increases proportionally with the biasing field. Any sub-linear behaviour is an indication of the electrical saturation of a device.

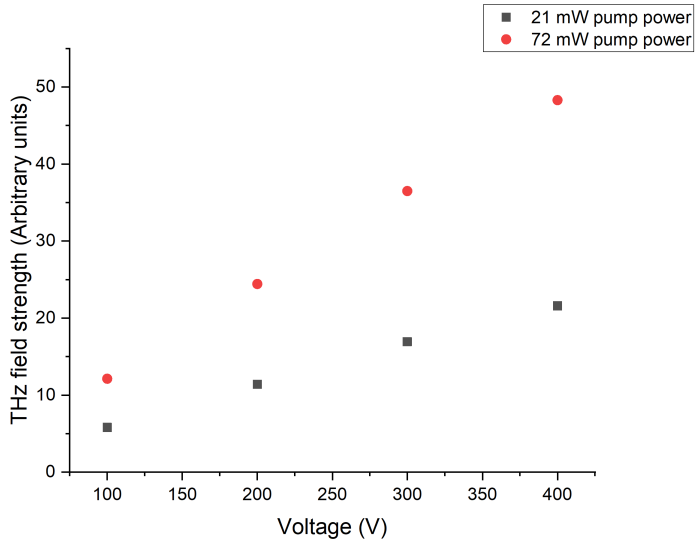

Figure 3.6: An electrical characterisation graph for a PCA device, the linear trend can be seen. The device is a 5x5 mm active area array the same as figure 3.5. As the device is optically excited in a collimated beam the optical power values can be adjusted. This is done by using an iris set to the size of the device active area and taking a power meter measurement.

During characterisation, it is important to note that selected bias voltages are chosen as a function of device gap size. In essence electric field across each

emitting pair is given by:

$$E_{Bias} = \frac{V_{Bias}}{D_{Gap}} \tag{3.4}$$

Where D_{Gap} is the emitting gap width and V_{bias} is the applied voltage. The optical pump power chosen for electrical testing is one that sits within the saturation regime and one within the linear regime, this allows for a greater understanding of electrical operation in both states of device operation.

3.3 Repeatability of Experiments

In order to be able to understand and interpret any trends within the experimental data measured in chapter 4, the repeatability of experiments must be considered. For experiments performed within this work, there are three areas that could potentially introduce areas of unreliability. These areas are as follows: pump laser variations over the course of days, pump laser variations pulse-to-pulse and device fabrication variations.

The Ti:Sapphire amplified laser system used for excitation requires a stable ambient room temperature to minimise laser instability. This is because temperature changes in the room can cause the beam's pointing to change slightly. However, this change is more in the order of days than pulse-to-pulse, with a day-to-day power variation of <5%. To minimise the effects of this type of variation and increase the reliability of the measurements, directly compared devices are measured one after another on the same day of testing.

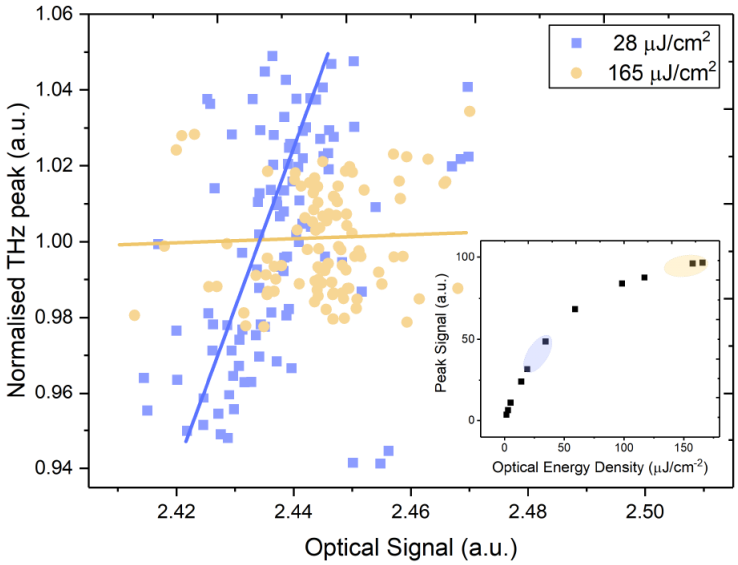

Figure 3.7: THz peak field vs excitation beam power for 100 repeats of a PCA device operated in the saturation and linear regime (highlighted in the inset). The standard deviation is 3% and 1.4% in the linear and saturation regimes respectively.

The pulse-to-pulse-laser variations cause another area of variation that could affect the reliability of the results. This is explained as the power variation between pulse trains common within low repetition rate laser systems. For this laser system, the pulse-to-pulse variation was investigated by Dr David Bacon [91]. A bias PCA emitter was tested in both the linear and the saturation regimes of optical pumping. The peak THz signal was plotted, and the standard deviation was acquired to determine the variation over 100 repeated THz time domain scans. Figure (3.7) shows that the standard deviation of the peak THz signal obtained from the device operated in the linear and saturated regime is around 3 % and 1 % respectively.

Finally, device variations could make determining trends in experimental results difficult. Device variations occur during the fabrication of individual devices. There are many steps to the fabrication process, and there is a possibility of introducing small variations at each step. This could cause two nominally identical devices not to generate identical THz radiation. To minimise as many device variations as possible, each device that forms a comparative study was fabricated simultaneously on a single chip and separated before mounting (4.1.1).

3.4 Conclusion

In this chapter, different device characterisation methods are discussed. The different optical set-ups used throughout this project were presented; these were the two main optical layouts used to characterise devices: a collimated generation and a focus-through generation scheme, with the advantages and disadvantages discussed. The testing instruments set-up was shown, and a detailed block diagram showing how the electrical equipment is interfaced to obtain accurate measurements was provided. The methods used for characterising PCA devices were explained in detail, and examples of the typical trends that are looked for when testing devices were presented. A discussion on the repeatability of experiments explained the variations that can be introduced into device measurements. The main introduction of results variations is from the excitation laser system, both pulses-to-pulse and day-to-day, as well as device-to-device variations introduced during fabrication. It was shown that the variations pulse-to-pulse did not, on average, exceed 3 %, and day-to-day variations of the laser power were less than 5 %.

Chapter 4

Device Geometry

Throughout this project, numerous studies have been undertaken to improve the device geometry of interdigitated PCA array devices, one aim being to increase the strength of the THz THz electric field generated. The work presented in this chapter will outline each of the studies conducted and present the findings. Each study was used to investigate different device geometries and the effects these have on the device characteristics.

4.1 Triangular Electrodes

Some of the earlier fabricated devices showed signs of electrical weakness when biasing voltages were increased; it is theorised that the current densities flowing in the electrode structures are the issue. It is desirable to be able to fabricate devices that support higher current densities as it prevents earlier device failure. Support of larger current densities would lead to an increase in THz radiation. This is seen in equation 1.22 in 1.8.5.

When the bias voltage was increased, the electrical weakness observed was manifested at so-called 'weak' points in the electrode structure; in the cases seen, the electrodes underwent electrical failure, rendering the electrode pair on the array no longer operational. The weak point is where the electrode leaves the LT-GaAs bar and connects to the biasing pad, seen in figure 4.1. When higher biases and larger optical pumps are applied to a device, the current density flowing through the electrodes will be higher. The point where this current would be the highest is located in the area of the electrode connecting the biasing pad and the LT-GaAs. The device seen in figure 4.7 indicates the weak points of the device.

Another reason device failure could have been seen in the device is due to dielectric breakdown. High biasing fields can cause dielectric breakdown if the fields exceed certain values. The important dielectric breakdown values with these devices are air ($\simeq$30 kV/cm), LT-GaAs ($\simeq$300 kV/cm) and BCB

(5.3 MV/cm []). Thus, a dielectric breakdown of air is likely to occur before the breakdown of the other materials. However, the area that this would be expected would be across the dark gap due to the reduced distance compared to the active gap. For this reason, it was theorised that it was the aforementioned current density issue.

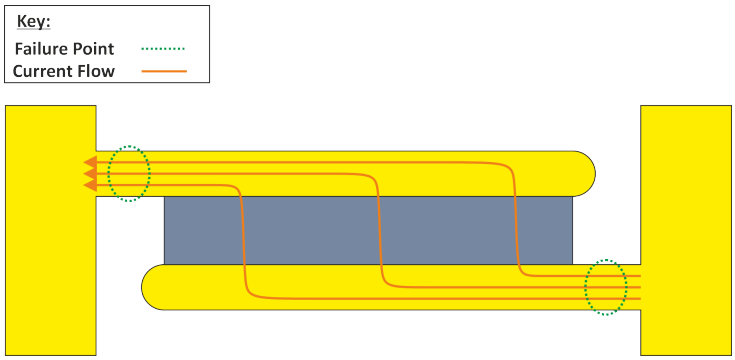

Figure 4.1: The diagram shows a simple interdigitated electrode PCA structure with the suspected weak points highlighted at the point where the electrode arms connect to the biasing pads.

4.1.1 Designs

A new electrode design approach was tested to prevent this type of failure. If the theory is correct and a large current density causes failure in the electrode fingers via overheating/melting, then changing the electrode shape to compensate for the weak point should allow higher currents to be applied without causing damage. Increasing the amount of current that the electrode can handle at the weak point can be done by increasing the width of the electrode at this point; this allows for the concentration of the current to be spread over a larger area.

The new electrode structure design can be seen in figure 4.2. The electrode fingers have been altered from a rectangular shape to a more triangular design. The triangular shape was chosen for this design as it increases the electrode finger width in the targeted area without changing the overall layout of the design greatly; this allows for the packing factor to be kept the same. As with the rectangular style electrode fingers the ends of the triangular electrodes are also rounded as this prevents any fringing effects and field concentrations caused by a sharp point.

Multiple designs were created to investigate the effect of the electrode geometry on the THz generation and the biasing capabilities. Table 4.1 lists the different designs created; the main difference for each is the pitch of the electrode geometries, i.e. the electrode finger width at the suspected weak point

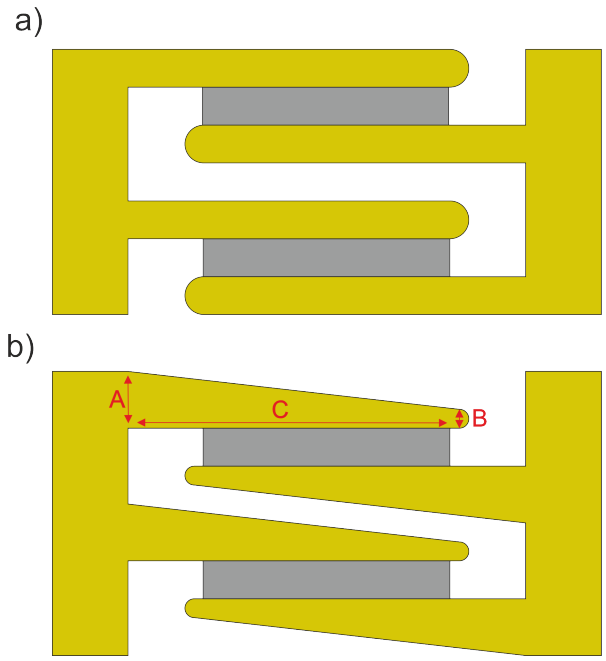

Figure 4.2: A comparison of the two different electrode geometries. a) Shows the rectangular geometry, b) shows the proposed triangular geometry.

and the width at the end of the electrode.

Design	Gap size	A	B	C
1	150	140	20	5500
2	150	120	40	5500
3	150	100	60	5500
4	150	70	70	5500

Table 4.1: The different electrode geometries dimensions for the triangular designs 1-3, the design 4 is the control device adopting the rectangular electrode geometry.

All devices are fabricated from a single piece of LT-GaAs to ensure that the testing produces fair and comparable results. The designs were adapted to fit onto the single piece of LT-GaAs bonded to the sapphire substrate, allowing every device to undergo an identical fabrication process. The CAD design in figure 4.3 shows the designs used for this investigation; the active area of each device is 1.4 x 4.6 mm. Note that the active areas were chosen to ensure equal sizes for each device from the material available.

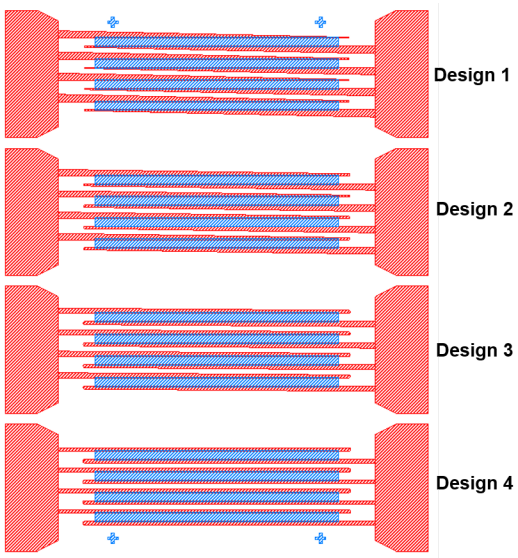

Figure 4.3: The CAD design used to pattern device geometries onto a single piece of LT-GaAs. From the top down it is device 1 to 4. All devices consist of 4 pairs with a 150 μm gap size.

Once the devices were made, two different post-fabrication processes were tried. Due to the risk of damaging devices during post-fabrication, dicing was not performed initially. A new PCB was designed to support the mounting of all four devices so that operation can be switched between each one. However, this new approach proved unusable for the reasons mentioned in the following section. Thus, post-fabrication dicing was performed. With devices diced, they can be mounted via the usual method described in 2.4.2.

It is also important to note that two different sets of the designs shown in 4.1 were fabricated. However, due to complications with the fabrication, only four of the eight devices were successful. These are devices with designs 1,2, and 4 fabricated on the first chip (set 1), and then from the second chip (set 2), only one device based on design 4 worked.

4.1.2 Results

To fully characterise each device, it is important to keep the testing set-up the same throughout; this includes ensuring that each device is tested in one session. Operating the tests in such a way ensures that the results are comparable due to the negation of variation in laser power day by day. Devices in this section were optically excited in a collimated beam with a diameter of 2 cm.

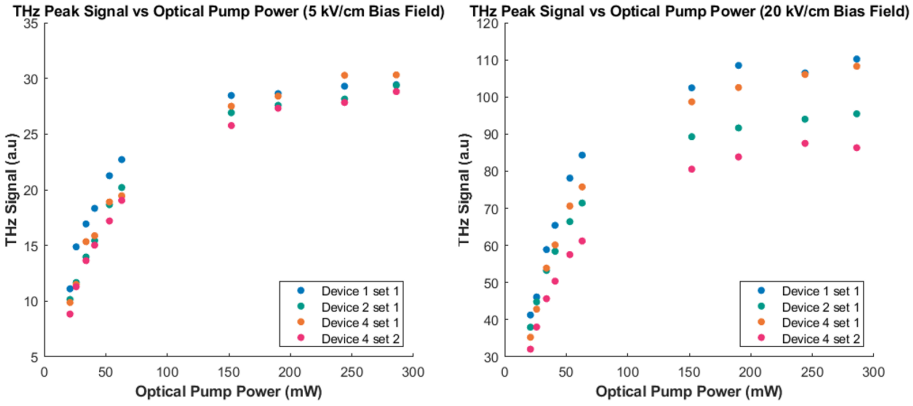

Figure 4.4: THz signal as a function of optical pump power for the four different test devices, testing was performed at two different electrical biasing field strengths 5 kV/cm (left) and 20 kV/cm (right).

The graph in 4.4 shows a comparison between the optical performance for the four different designs, characterised at two different biasing fields: 5 kV/cm and 20 kV/cm. It can be seen that under the influence of the lower biasing field, all devices generate similar THz radiation; from the theorised operation, this is what would be expected for these devices. The generation from the devices should be similar, as the active area is identical for all four devices. At lower bias voltages, there is not believed to be an issue with the current density damaging the electrodes, with all electrode structures able to support the operation of the devices.

Comparing the results at the higher applied field of 20 kV/cm, there appears to be an enhancement of the generated THz radiation as electrode width increases. This enhancement could be due to the near anode effect, explained and tested below, which is seen to have reduced effectiveness as the width is decreased. This does not seem to be the case for a conventional electrode design (rectangular) like device 4, as it can be seen that the device generates the same amount of radiation that device 1 is capable of. Due to the failure of the other devices in this set, direct comparisons between sets 1 and 2 cannot be drawn as they were fabricated separately. Therefore, this cannot be taken fully into account. Here, it can be seen that the regular electrode device operates similarly to device 1. Theoretically, this makes sense at lower bias voltages as the gap size is the same for both, and the fluence is the same. Analysing the results with respect to the potential errors that can be introduced to the results (as discussed in 3.3), the accuracy of the trends seen can be determined. As the devices are tested in succession on the same day, the laser power variation considered is the pulse-to-pulse measurements. The average pulse-to-pulse variation seen in results is only around 3%, so this would not explain the large difference between the two nominally identical devices seen in figure 4.4 where

the devices were operated at a higher biasing field. However, this does show that device-to-device variation appears to be more prevalent under higher device stress (i.e. at the higher biasing fields); this is why direct comparisons between the different device sets not fabricated together can not be drawn.

The peak THz signal as a function of the applied bias strength for the devices at two different optical excitation powers is shown in figure 4.5. It can be seen that in both cases, at the lower biasing strengths, the peak emission is similar for all devices; this, however, changes as the biasing field is increased. At both the higher and lower optical excitation power, the rate at which the field increases can be seen to follow a steeper rise for the larger-width triangular electrodes (device 1) and a shallower gradient for device 2. Again following the same trend exhibited with increasing optical powers, it can be seen that device 4 from set 1 shows an increase that is slightly shallower than device 1 and produces THz peak signals just below the values of it also.

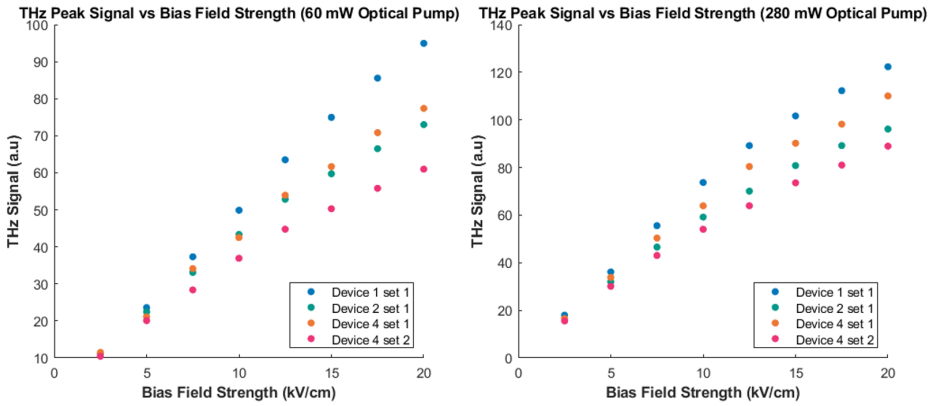

Figure 4.5: THz signal as a function of electrical biasing field strength for the four different test devices, tested at two different optical pump powers; 60mW (left) and 220 mW (right)

Two devices are shown here to assess how robust the devices are (device 1 and device 4). These devices were illuminated using an optical power of 42 mW, and the electric bias increased linearly until each device showed signs of failure. The devices are considered to have started to fail when the radiated emission drops significantly, as this is a key sign of damage or complete device failure in some cases. It can be seen from figure 4.6 that both devices increase roughly linearly with increased bias until the point that they failed. Both devices increased beyond the point of normal bias operation (20 kV/cm) by a considerable amount, to almost x3.5 that value to 70 kV/cm for device 4 and 67.5 kV/cm for device 1. The triangular electrode device was able to operate at the highest bias of the two, but no significant improvement was seen from the triangular

designs. The value of bias operation for both these devices is considered highly impressive compared to any previous devices tested; for reference, the largest device fabricated with this ELO technique to date [91] started to show signs of damage at 25 kV/cm biasing field. The image in figure 4.7 shows a stereoscope image of one of the devices after undergoing failure. The images show the failure points on the device, which appear to be similar; it is shown that there is damage between the bias pad connecting the arms of the electrodes and the tips of the other electrodes. This damage is believed to result from shorting across the dark gap (the etched gap between emitting pairs), which is attributed to the bias voltage, not the current. A similar observation was made with the triangular electrode device.

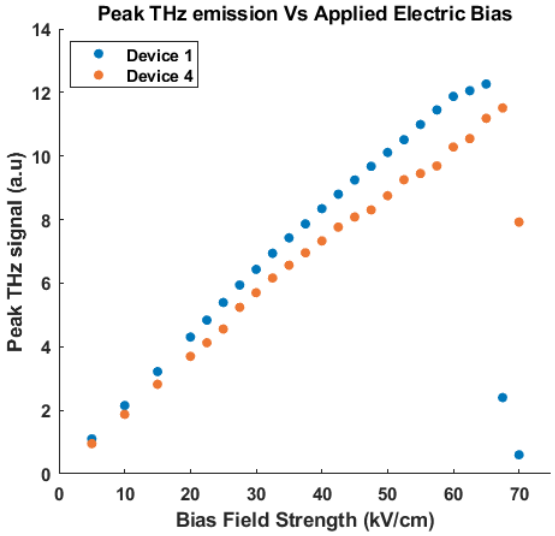

Figure 4.6: A comparison of the peak emitted THz signal as a function of applied bias strength for device 1 and device 4. It can be seen that both increase towards a bias field strength of 70 kV/cm before damage was sustained.

This test concludes that the issues that were seen previously, showing the failure points of each device, were not found to be a problem with either of these devices. A minor improvement was seen; however, there is no clear benefit to using a triangular geometry over the current rectangular designs. For this reason, it was decided that future devices would continue to use the rectangular geometry.

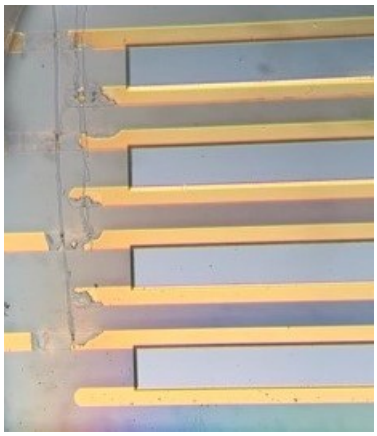

Figure 4.7: Device PCA device showing the failure point on the rectangular electrode device. It can be seen that the damage occurred between the tips of one set of electrodes and the connecting arms of the other. This is indicative of shorting across the gap.

4.1.2.1 Single Chip Testing

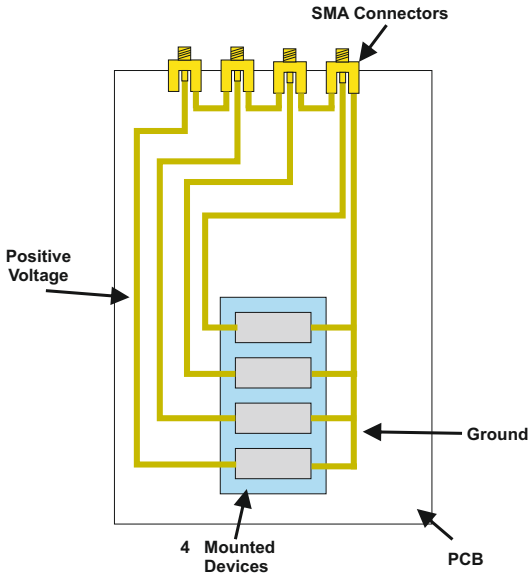

Figure 4.8: A schematic showing how the 4 devices on a single chip were mounted and tested. A specially designed PCB that allows all 4 devices to be independently biased. All devices share a common ground connected through the SMA connectors.

As discussed above, initially, the devices were not diced post-fabrication to avoid damaging devices, and these were mounted to custom PCB for testing. As above, devices A, B, C, and D correspond to the electrode designs of 1,2,3, and 4 seen in 4.1. The results for the single chip produced some results that were not as expected; ignoring the antenna geometry initially, it was expected that the performance from equal active area devices under the same bias and optical fluence would produce similar THz emission. The real difference was expected at increased electric biasing fields, hoping for increased operation into higher biases. From the optical sweep plot, seen in 4.9, of all devices operated at a biasing field of 5 kV/cm, it can be seen that the devices exhibit a trend of decreasing performance from the largest triangular width device A to device D, whilst the decreasing performance could conceivably be an artefact of the electrode design the difference of signal of x2.5 times of C and D compared to A was not expected.

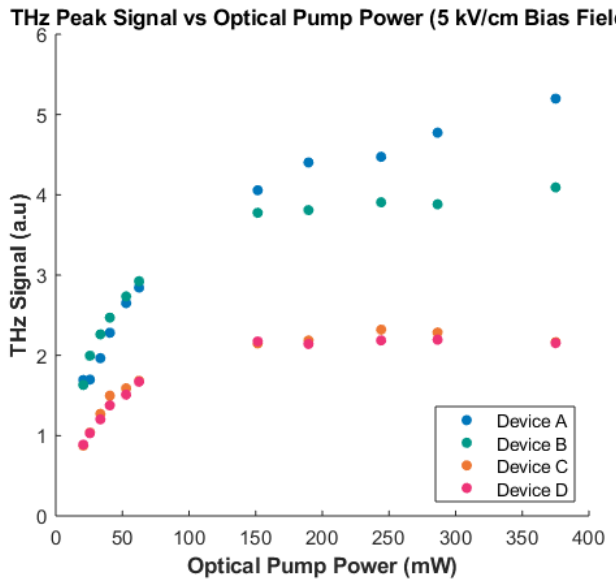

Figure 4.9: THz signal as a function of optical pump power for the four different test devices on one chip, an electrical biasing field of 5 kV/cm was applied to all devices.

Even at low optical powers, there is a clear difference between the THz signals of devices A and B and devices C and D. This difference could not be explained by any device-to-device error, as the devices were fabricated simultaneously on a single chip. The pulse-to-pulse variation would also not explain the difference as the variation between peak THz signals is larger than 3 %; hence, the difference must be caused by a different mechanism. This turned out to be an issue with the device mounting method. It can be clearly seen when

compared to the operation of the diced devices in figure 4.4. When the devices were diced and mounted separately, their operation was more closely matched, especially at the lower optical powers. The erroneous results are theorised to have arisen from a capacitance issue between the devices; this could have been from the ground passing through each SMA connector or coupling between the devices on the board through the ground connection. To avoid any further issues, it was decided to perform the post-fabrication dicing and single device mounting as described in 2.4.2 and tested above.

4.2 Anode Width

Another area for improvement is the near-anode enhancement effect. This is where the anode electrode can be engineered to enhance THz generation from the area closest to it. This effect has been demonstrated before with single stripline emitter pairs fabricated on LT-GaAs on SI-GaAs, seen in [187]. In that work, it was shown that increasing the anode width produced an increase in the THz emission generated. However, this has never been tested with a LT-GaAs on sapphire device like the ones fabricated in this project, nor with gap sizes as large as the ones tested here.

The potential advantages of adopting this method with these devices are two-fold; firstly, there is the added enhancement of the THz field, which provides increased emission from each optical excitation pulse. Secondly, by finding the optimum electrode widths, the device's layout can be optimised to allow for the best packing factor, ensuring the most efficient use of the device's active area.

It was discussed in the 1.8.5 the contributions that electrons have on the emitted THz radiation. As the electron mobility in GaAs is much higher than the mobility of the holes, the electrons are considered the major contributor to the emitted radiation. Along with carrier dynamics and direct emission from the semiconductor substrate, there will be a contribution to the emission due to the current that propagates in the electrodes. Photoexcited carriers generated near the electrode cause an impulsive THz field due to their motion. The local dipole can excite resonant modes in the electrode structure due to the near-field coupling of the local dipole and the resonant modes' electrical near-field, with the strength of this coupling dependent on the spatial and spectral overlap of the two [188]. The THz emission from the electrode is influenced by the change in mode structure; these can be thought of as plasmonic excitements at the semiconductor-metal interface. The surge current that is induced in the electrode by the plasmonic excitation is dependent on the propagation length in the electrode; this is equivalent to the width of the electrode in this case. Hence, by changing the width of the electrode, the THz emission can be altered. This effect, previously studied in [187], has shown that the THz electric field will increase linearly for electrode widths much smaller than the wavelength emitted.

Device Number	Anode Width (μm)	Cathode Width (μm)	Gap Size (μm)	Number of Pairs	Packing Factor
1	40	10	50	18	45.69 %
2	30	10	50	18	45.69 %
3	20	10	50	18	45.69 %
4	10	10	50	18	45.69 %

Table 4.2: The dimensions of the test devices from test set A, the cathode width is kept consistent with the anode width varying. Each device contains 18 generating pairs, ensuring packing factor is identical for each.

4.2.1 Designs

As mentioned in the previous section, this enhancement effect is most prominent for anode widths that are much smaller than the emitted wavelength. Therefore, the gap size of the emitter is important. The size of the electrode gap defines the amount of biasing voltage required to achieve the required biasing electric field; this, in turn, directly affects the electrode's size. With smaller electrodes, a smaller current flows through it, and we can scale it to fit the size of the emitting gap width. Hence, the smallest gap size supported by the current fabrication method was selected, this being 50 μm.

Increasing the electrode width will increase the periodicity of the emitting pairs, thus reducing the packing factor. Finding an optimal ratio of the anode width enhancement to the packing factor will lead to an increase in efficiency from the fabricated devices.

Two different sets of test devices were designed and fabricated to carry out the investigation. As with the previous study in 4.1, each set of 4 devices are fabricated from a single piece of LT-GaAs and separated post-processing to ensure identical fabrication conditions. The dimensions of test set A are shown in table 4.2; this test set varies the anode widths of each device without increasing the number of electrode emitting pairs. This test set allows the anode enhancement effect to be investigated independently of any other device geometry variations. The second group of devices, test set B, are displayed in table 4.3. Again, the same anode width designs are used here; however, each device is purposefully designed to maximise the packing factor. From this set of test devices, it is hoped to understand to what extent an enhancement of the anode improves the THz generation capabilities of these devices when compared to maximising the packing factor.

Device Number	Anode Width (μm)	Cathode Width (μm)	Gap Size (μm)	Number of Pairs	Packing Factor
1	40	10	50	18	45.69 %
2	30	10	50	20	50.76 %
3	20	10	50	22	55.84 %
4	10	10	50	25	63.45 %

Table 4.3: The dimensions of the test devices from test set B, each generating electrode pair keeps the dimensions outlaid in test. Each device contains a varying amount of generating pairs, ensuring packing factor is maximised for each device.

4.2.2 Results

The results in figure 4.10 show a comparison of the THz signal generated from the four different device designs at differing optical pump powers. These devices are composed of identical active areas to ensure that the effects of the anode enhancement effect could be isolated from any other device enhancements. It can be seen that there is a clear trend of the generated THz signal with anode width. It can be seen that as the anode width decreases, the emitted peak THz signal is decreased; this is the result that was to be expected from the literature. The maximum radiation emitted is when the anode width is 50 μm. There is then a drop in signal when the anode is at 30 μm width, and subsequent drops for 20 and 10 μm respectively. The emission performance from the 10 and 20 μm devices is much lower than the two larger anode-width devices, which can be seen as roughly the same. As discussed above, it was seen that the near-anode enhancement effect produced only a linear effect for anode widths that were much smaller than the emitted wavelength.

The results plotted in 4.11 show the anode enhancement test devices with the bias reversed across the electrodes; this means, in effect, that the devices are operated in a widened cathode configuration (see figure 4.12) whilst the anode width is kept constant. This allows for an investigation into the effect that a widened cathode width has on the THz generated. It can be seen from 4.11 that the devices generate a similar THz signal. This indicates that the cathode width does not play a significant role in the generation of THz radiation. This result is expected and can be explained by the carrier dynamics in the active material. As mentioned in the current surge model section 1.8.5, the electron mobility is much higher than that of the holes in GaAs; hence, the electrons are considered the majority carrier. Therefore, the anode width has a larger impact on the generated THz signal. This is due to the greater electron density change at the anode-semiconductor interface compared to a smaller hole density change at the cathode-semiconductor interface [189]. It is to be noted that the results for device 4 have been omitted; the results for these devices were considered invalid due to a laser drifting issue and became damaged before being re-tested.

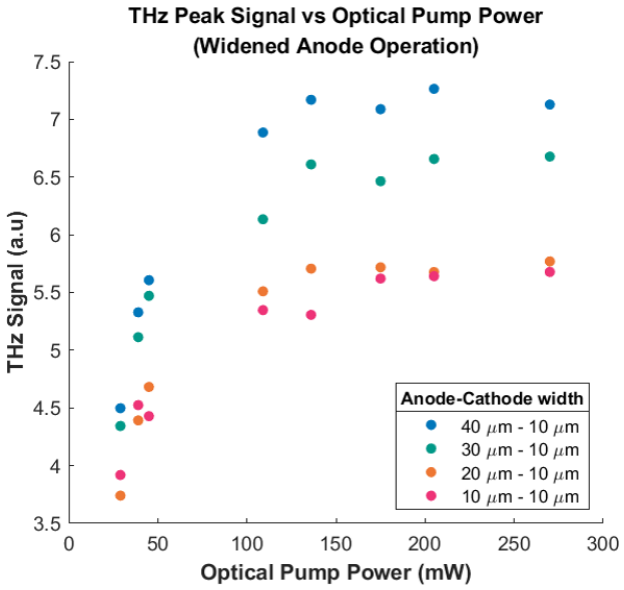

Figure 4.10: THz signal as a function of electrical bias field strength, for the different devices of test set A. The changing anode widths were used to investigate the effects of width on the generated emission.

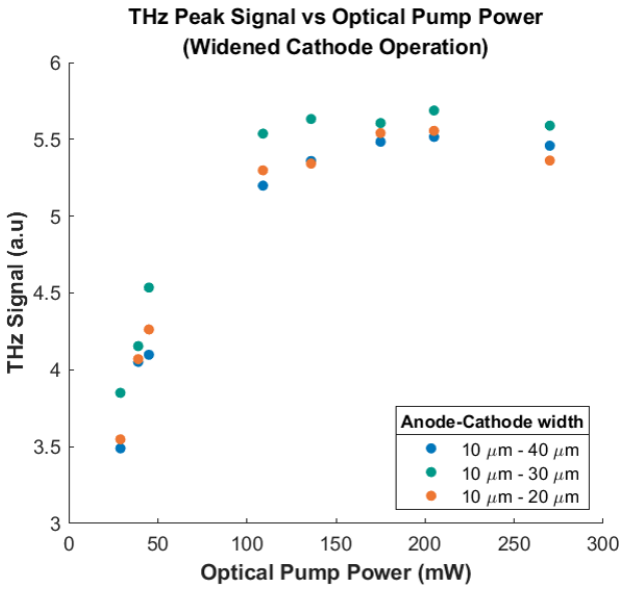

Figure 4.11: THz signal as a function of electrical bias field strength, for the different devices of test set A. The anode width is kept the same whilst the cathode width is varied. This confirms that the width of this cathode matters little with regards to the generation of THz radiation.

The enhancement resulting from an increased anode width can be seen further from the results plotted in 4.13. Each plot compares the peak THz signal as a function of optical pump power for each device with the positive bias applied to the designed 'anode' and the designed 'cathode'. The widest anode device has the largest difference between the two operating modes, producing the largest anode enhancement. This difference in peak signal decreases with decreasing anode width; as the anode width decreases to the point that it is double that of the cathode, the difference in peak signal is quite small with only a slight enhancement of the THz field. This trend is consistent with the expected response and the analysis of the results with respect to any errors that could arise from the testing. As all devices were fabricated simultaneously, the device-to-device error would be small. The difference in peak THz signals between each of the devices is outside of the 3% error that pulse-to-pulse variations in the beam power can introduce.

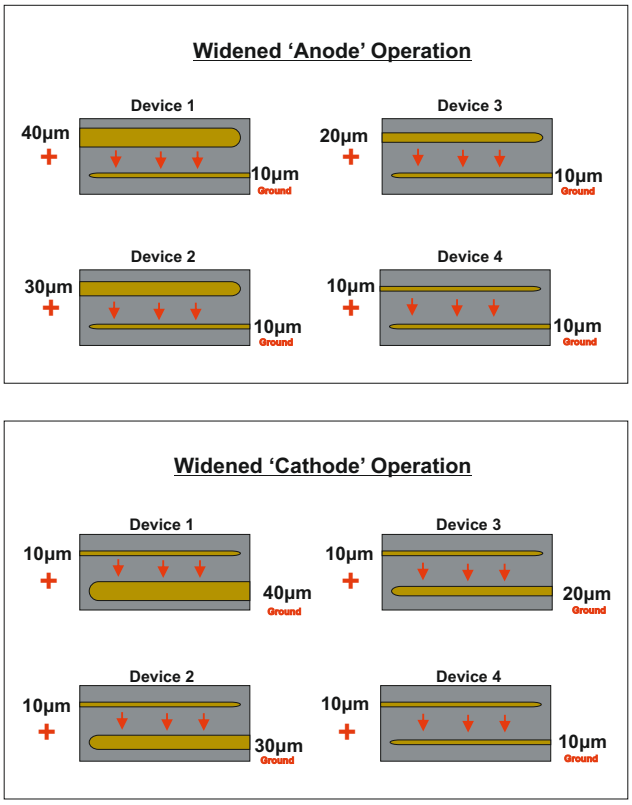

Figure 4.12: Diagrams showing the two operated states of the devices, the top four devices depict the widened anode operation and the bottom is the case when the devices are operated with a widened cathode operation. The red arrows indicate the direction of the electric field.

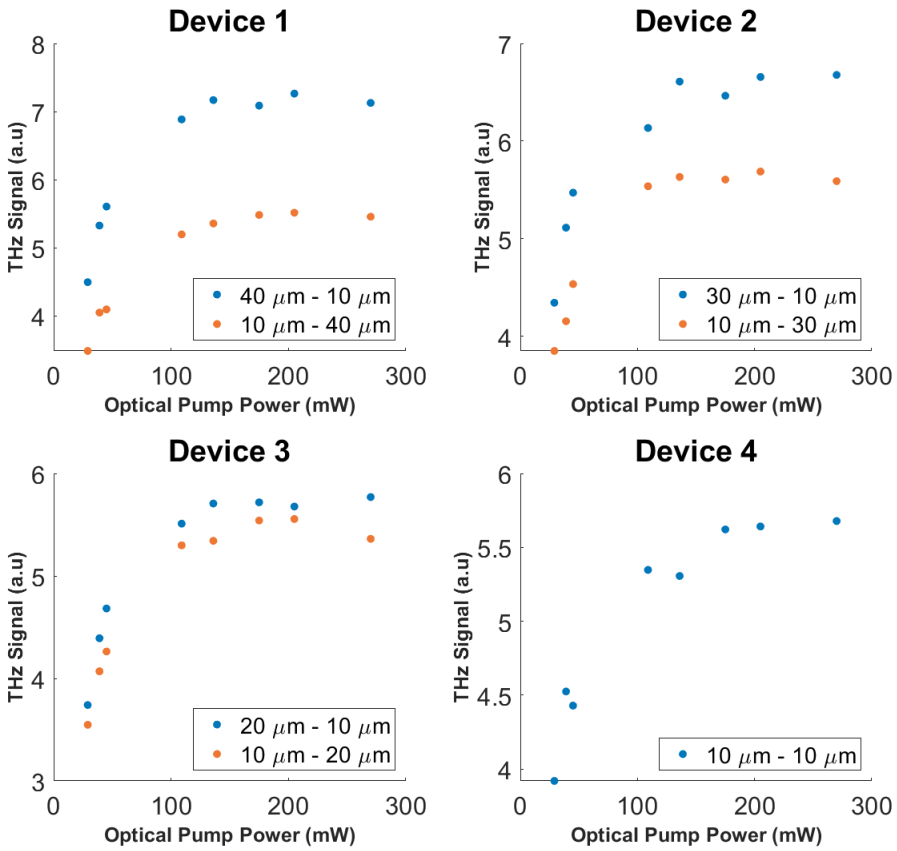

Figure 4.13: THz signal as a function of electrical bias field strength, for the different devices. Each graph shows a comparison of the generated emission as the device is operated with the anode or the cathode as the positive electrode.

The graph in 4.14 shows a comparison of the peak THz signals generated at different optical pump powers for the four different 'maximum active area' test devices. It is shown that the device with the equal anode and cathode widths generates the highest peak THz signal; this device has the highest packing factor of all devices at 63 per cent. A clear correlation can be determined from the data set that the peak THz signal of a device decreases with the packing factor; the largest anode width device generates the lowest peak signal. By decreasing the anode width of the device, the number of generating pairs in the array can be increased, thus increasing the packing factor. It is apparent from these results that the additional THz radiation generated from the increased active area is greater than the enhancement provided by the increased anode width.

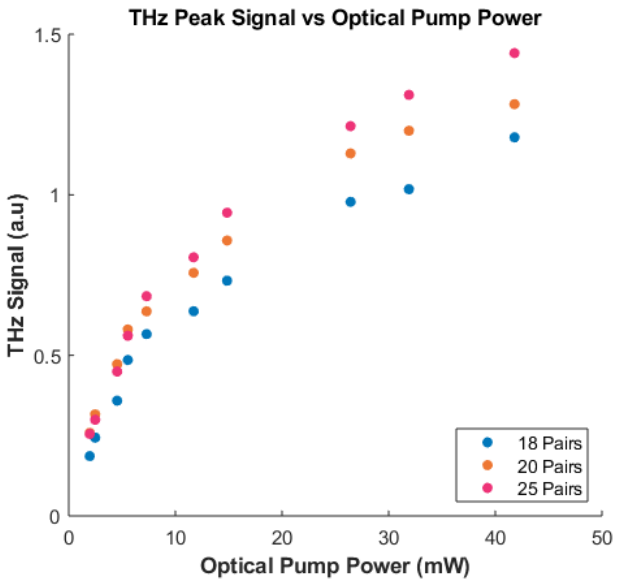

Figure 4.14: THz signal as a function of electrical bias field strength, for the different devices of test set A. The graph indicates that maximising the amount of photoconductive area on the device has a greater effect on the generated THz field.

The results from this study show that there is a clear enhancement to the radiated THz field as the anode width increases, but this is not a dominant effect when compared to a maximised surface area. A greater near-anode effect enhancement of the THz field may be seen if the device gap size and electrodes are smaller. For smaller active areas, enhancing the anode width to increase the generation capabilities may prove beneficial to maximise efficiency if the active area is limited or fixed. However, the anode enhancement effect is a non-dominant effect compared to the generation provided by increased active area; thus, prioritising maximising active area during device design is important. Further study would be needed into the effectiveness of anode enhancement on gaps less than 50 μm to reveal systematic trends.

4.3 Gap Size

It is theorised that by using smaller gap sizes, the device should support much larger equivalent biasing fields, increasing the generated peak THz field strength. The reason for this is that for smaller gaps, the amount of bias required to cause electric ionisation of the air is increased, which is desirable as an electric breakdown in the air is one of the major causes of device failure. Paschens's law is used to determine the minimum field strength needed to cause the electric breakdown of a particular gas, and this law states that for smaller gap sizes with constant pressure, the biasing field required to cause breakdown is increased [190, 191]. To date, the most powerful device fabricated utilising the method outlined in this project uses large gap sizes of 200 μm [91]. With such large gap sizes, the biasing field applied is kept to a maximum value of 20 kV/cm; this is deemed the 'safe' operating voltage found from previous testing. An advantage of using smaller gaps is that the biasing voltages needed to create equivalent fields are reduced significantly; this facilitates the use of less sophisticated and less expensive lower-voltage power supplies.

4.3.1 Methodology

Three different devices were designed with varying gap sizes to investigate the effects of smaller gap sizes on the amount of bias that can be supported. As with the other devices described in this chapter, these were fabricated concurrently using a singular bonded wafer of LT-GaAs on sapphire before being diced during post-processing. With the developments in the fabrication method (2.5.3), specifically the wet etch chemistry, the smallest gap size obtainable is 50 μm. Fabricating smaller gap devices requires a different process, described in 2.5.5. Due to this, 50 μm will be the smallest gap size designed and tested. The designs can be seen in 4.4.

Device Number	Gap Size (μm)	Anode Width (μm)	Cathode Width (μm)	Pairs	Packing Factor
1	200	70	70	4	44 %
2	100	35	35	9	50 %
3	50	17.5	17.5	18	50 %

Table 4.4: The dimensions for the devices in the gap size study, the gap sizes are 200,100 and 50 μm. Table also indicates the packing factor of each device.

To test the operation, each device had an equivalent biasing field applied before a time domain scan was captured. The biasing fields were firstly applied at 2.5 kV/cm before being increased in steps of 2.5 kV/cm until device breakdown occurred. The devices were all optically characterised through the method detailed in 3.2.1 to find the saturation point; this was then chosen as the point to operate the device for bias testing. With this investigation, the comparison between absolute values of the generated THz electric fields is not considered a dominating factor, with the maximum biasing field that can be applied to the device before breakdown as the value of merit.

4.3.2 Results

The bias operation of the three different gap size devices can be seen plotted in 4.15, it shows the THz generated at increasing bias strengths of each device compared with one another. It can be seen that the THz radiation generated does not deviate significantly between each device; as the gap size decreases to 50 μm, the generated THz radiation can be observed to be reduced when compared to the other two widths fabricated. As mentioned before, the geometry of each device was designed to provide an accurate comparison of the gap size operation and the effects of such changes; the active area of each device was kept at roughly the same size. It can be seen that a decreasing gap width is not detrimental to the generation capabilities of a device; this indicates that the width of the generating gap can be reduced without reducing the maximum field achievable by a device, holding to the fact that the active area of the entire device remains near enough unchanged. It is clear to see, however, that the bias field strength that each device can withstand before mechanical (or electrical) breakdown occurs is not equivalent for each device, with a clear trend emerging. As the gap width decreases, the strength of the biasing field that the device is able to withstand increases as expected. As the THz signal is similar at each bias point for each device, this confirms that the gap size can be decreased without impacting the generation significantly, withstanding that the total active area remains roughly the same. As the active area is kept similar for each device, this would not explain the difference in the amount of bias that can be applied; hence, it confirms that it is the smaller gap sizes and dark gap widths that are responsible for an increase in bias field that the device can support. The 50 μm gap operated up until an applied bias of 60 kV/cm, compared to the larger 200 μm, which became damaged above 30 kV/cm. The smaller gap was able to handle twice the applied field strength.

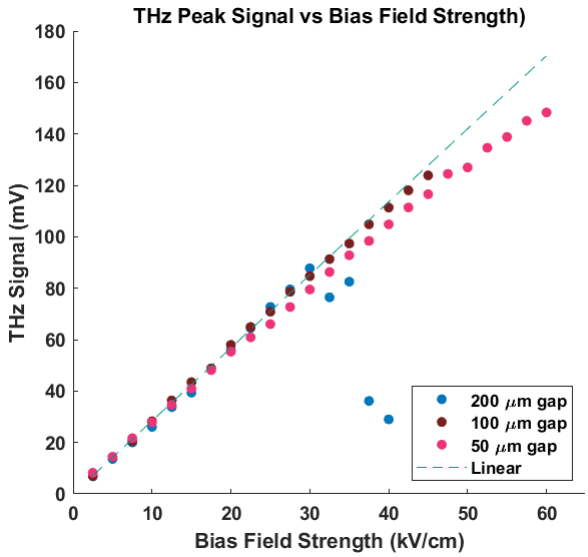

Figure 4.15: Peak THz signal as a function of electrical bias field strength, for the 3 different gap size devices. It can be seen by using a smaller gap device, it is possible to apply a larger biasing field and increase the the amount of THz radiation generated. Note that the 200 μm gap device became damaged at a bias of 30 kV/cm and continued to operate until complete breakdown at 40 kV/cm. A linear fit is plotted to show the deviation of the THz peak values from ideal behaviour.

The deviation of each device from ideal linear operation can be seen in figure 4.15, from equation 3.3 in section 3.2.2 it can be seen in the ideal case the peak THz signal should increase linearly with field strength. Devices with gap sizes of 200 μm and 100 μm operate with near linearity, and the 50 μm device is slightly sub-linear; these results suggest that there is no saturation occurring from electrical biasing fields of the two larger gap sizes, but there are signs at higher biases the 50 μm gap does exhibit slight saturation. One of the issues with moving to smaller gap sizes is the problems that can occur from earlier device saturation, which limits the operating capabilities of the devices [125].

A motivation behind a move to smaller gaps is that it removes the need for large power supplies, as smaller gaps require smaller voltages to achieve equivalent biasing field strengths. The results from the comparison study show that the equivalent biasing field strengths of the smaller gaps still provide similar levels of peak THz radiation. The peak signals achieved at 100 V for a 200 μm gap can be achieved using 25 V when the gap sizes are reduced to 50 μm.

The time domain plot in figure 4.16 shows each device's time-resolved THz pulses. As the gap size decreases, the negative 'tail' of the THz pulse increases.

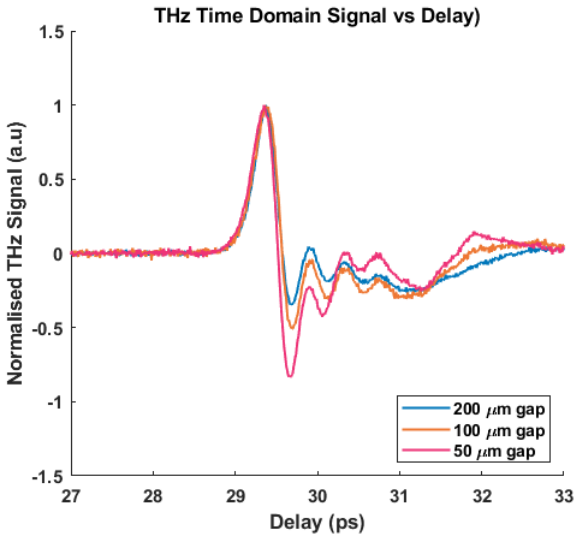

Figure 4.16: THz pulse shape shown for the 3 different gap size devices, taken at equivalent bias strengths of 20 kV/cm and optical pump power of 286 mW. It can be seen as the gap size reduces the negative peak of the pulse gains in strength. The THz signal values have been normalised for comparison.

This result is of interest; it can be seen in the time domain pulse of the 200 μm gap device that the negative portion of the pulse is almost non-existent; the reason for this is not fully understood. One of the potential reasons for this observed phenomenon is related to the geometry of the array structure. The time domain pulses in 4.18 show both a 100 μm gap bowtie device compared to the 100 μm array device; it can be seen that despite the array device consisting of the same gap size that there is a significant difference between the negative peaks produced by the respective devices. This result suggests that rather than being an issue with the gap size of the array device causing the asymmetrical peak, the array structure causes it. As mentioned in section 1.8.9, each generating pair of electrodes and consequent LT-GaAs active area acts as an independent point source generating radiation between the gap, the resultant THz generation seen in the far-field is, therefore, a coherent superposition of the individual point sources. The array structure of individual point sources provides a grating effect depending on the gap size of the array; hence, the emitter pairs' period will dictate the effect's strength. Later on in this chapter, this effect will be discussed further.

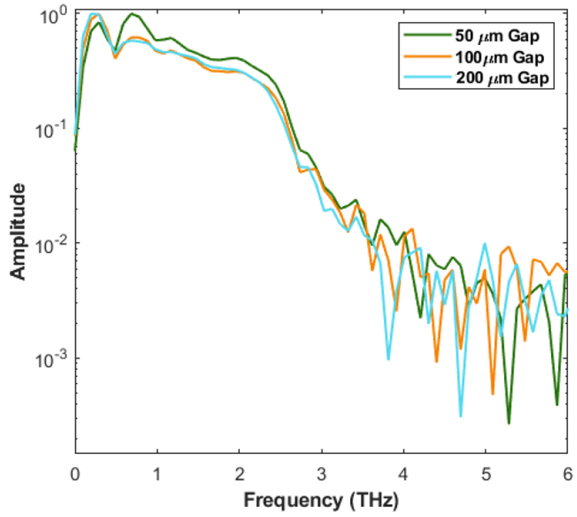

Figure 4.17: The bandwidth of the three devices plotted from the time domain pulse signals recorded above. The smallest gap device has its peak amplitude at higher frequency then the other devices. Signal amplitude is shown in normalised values for direct comparison. These were obtained using a 1 mm ZnTe detection crystal.

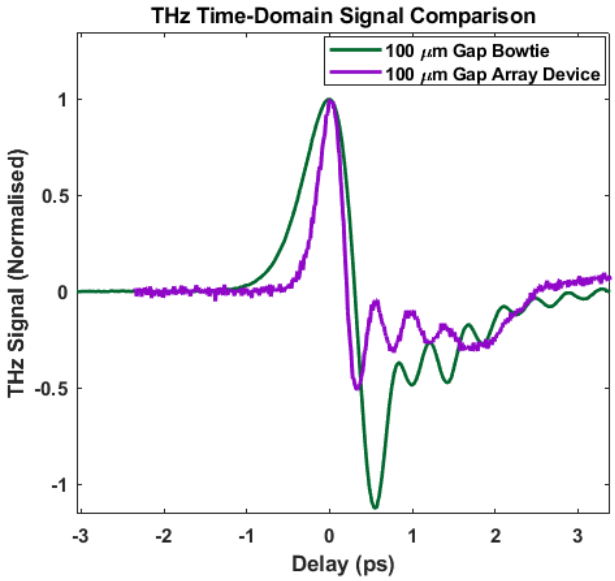

Figure 4.18: TDS pulses taken from a 100 μm gap bowtie PCA and the 100 μm gap PCA from this study. Both 100 μm devices were biased with 20 kV/cm biasing fields. The differing pulse shapes are clear to see. The difference in pulse widths is due to the different excitation pulse widths each device was pumped with (40 fs for the array device and 100 fs for the bowtie device).

4.4 Large Area Emitter

A key aim for this project is to improve the peak THz field strength obtainable for PCA devices fabricated on sapphire substrates. While improvements to the electrode designs described above will contribute to this, large area devices are required to maximise emission and achieve the highest peak fields.

4.4.1 Methodology

To fabricate a device capable of generating high THz fields, it is essential that the device supports high biasing fields to maximise the generation capabilities. Another important factor deduced from the investigations conducted in this chapter is that the packing factor should be kept as high as possible. This information was collated, and the designs for a large area PCA device were created to incorporate the optimised features that have been tested.

The design seen in 4.19 shows the features mentioned above all incorporated. Fabrication becomes significantly harder to complete for devices with large active areas; this leads to a lower yield of successfully completed devices. The device has an 18x18 mm active area; the full design geometry can be seen in table 4.5. The packing factor is relatively low; this is due to the length of the sloped sidewalls being 20 μm, which means to maintain a sufficient dark gap, the period of the emitting pairs must be reduced.

Device Active area (mm)	Gap Size (μm)	Anode Width (μm)	Cathode Width (μm)	Number of Pairs	Packing Factor
18 x 18	50	40	20	140	38.9%

Table 4.5: The dimensions for the large area PCA, these features were designed according to results learnt from preliminary studies on smaller test devices. The cathode width in this case was determined by the pitch of the LT-GaAs sidewall bars, this being 20 μm.

4.4.1.1 Fabrication Challenges

One of the challenges that has seen a lack of implementation and use of large area devices is the complexities that are introduced during the fabrication stage. Increasing the device area size decreases the tolerance for errors in all aspects of the fabrication process, leading to lower yields.

During the fabrication of this device, one of the main issues encountered arose from the wafer bonding process; obtaining a strong, level bond across the entirety of the increased surface area proved difficult. This has been attributed to either the bonding plate levelling or the applied bonding force. Compared to small area devices like those discussed earlier in this chapter, a large area device requires a higher degree of plate levelling accuracy due to its higher percentage of contact with the bonding plates. If the bonding plate levelling is insufficient,

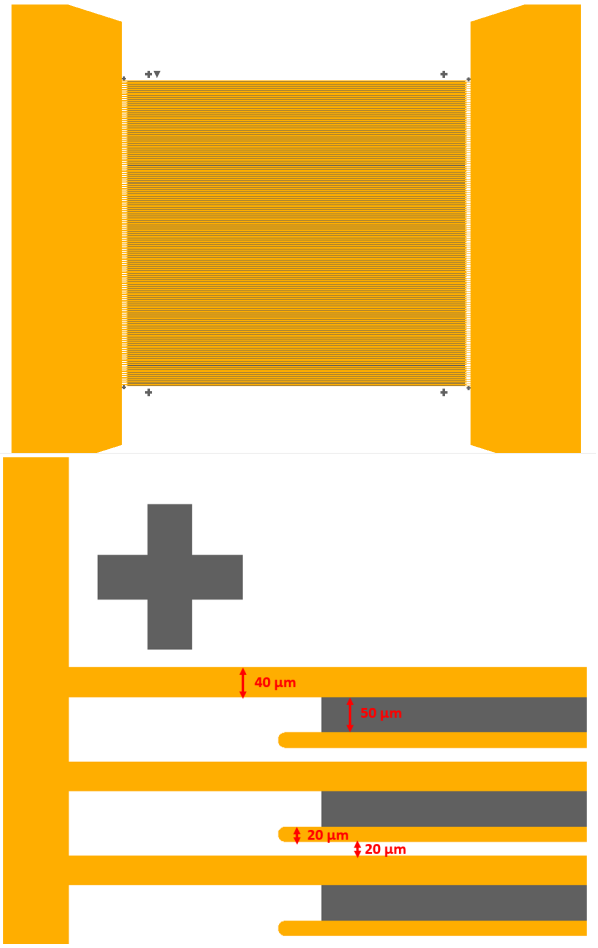

Figure 4.19: The CAD design for the large area design, these were created as two masks one for creating the LT-GaAs bars (grey) and the other to pattern the electrode structure (gold). The full design is seen in the top image and the bottom is a small exert showing specific geometry of the pair and an alignment cross.

the device will fail to receive an equal bonding force in areas below the initial contact point. Problems are also believed to have originated from the use of insufficiently high bonding forces. A standardised bonding force of 500 N/cm^2 was used to fabricate previous smaller devices. However, when this was used for the large area devices, it yielded only a partial bond.

Due to a shortage of LT-GaAs wafers available for fabricating large area devices, only two attempts were made to produce this design. During the fabrication, there were issues with both device bonding attempts, the first using

the standardised bonding force stated in A.0.2 and the second using a force of 750 N/cm^2. On both bonding occasions the wafers were not bonding correctly, with one of the wafer edges not bonded to the sapphire substrate. To correct for this, attempts were made to apply additional BCB to the device edge to try and secure the bond and remove the gaps.

Another issue that can be encountered is an uneven BCB layer. Instead of an even layer of BCB, deformities in the form of ridges can form in the layer. This is a direct result of correcting for uneven bonding; an uneven BCB layer causes issues for patterning electrodes. A correction can be made by using an oxygen Inductively Coupled Plasma - Reactive Ion Etching (ICP-RIE) etch; this completely removes the exposed BCB. Although this solved the issue for patterning, this caused a 'step' between the substrate and LT-GaAs bars, shown in figure 4.20. The BCB step can cause further issues with the device performance, however, as discussed in the following section.

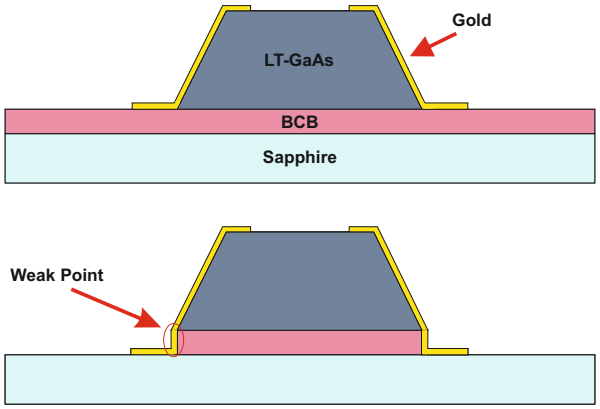

Figure 4.20: The issue that occurs from etching the BCB creating a step up to the LT-GaAs bars. The top image shows how the device should be with a full BCB layer and the lower image shows the case with it removed creating the potential issue.

Due to the fabrication challenges, only one of the two starting devices fabricated successfully made it through the entire process. This device was mounted on the specially designed PCB and then tested.

4.4.2 Results

The peak THz field as a function of applied bias for the large area PCA at two different optical pump powers can be seen in figure 4.21

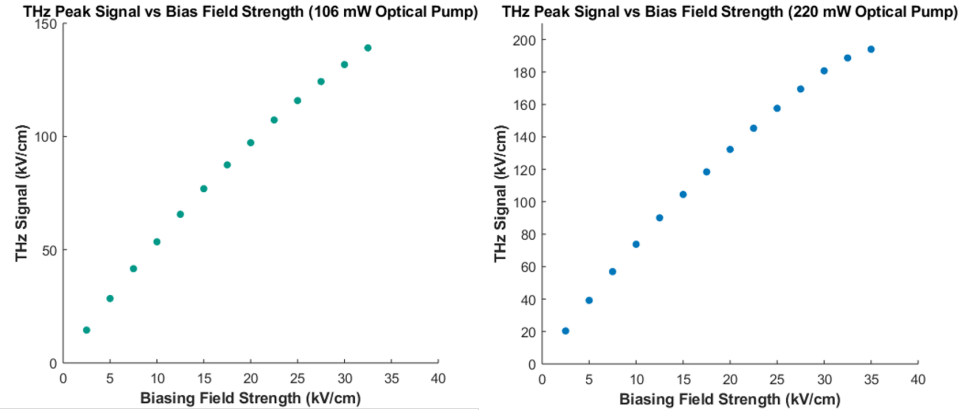

Figure 4.21: The peak THz field as a function of applied bias for the large area PCA, two different optical powers were used for excitation 106 mW (left) and 220mW (right).

A comparison of the THz field as a function of applied bias is shown in figure 4.22; the data is normalised to the small signal and plotted with a straight line showing the departure from a linear relationship. The THz signal generated by the device at the different optical pump powers can be seen to perform similarly. Both begin to generate a THz field strength that increased linearly with increasing bias field before showing increasing saturation at the highest biasing field strengths. The linear increase at smaller biasing fields is the expected behaviour the generation of THz radiation should have due to 3.2.2. The saturating trend observed at higher biasing strengths is not expected, and the reason for this was not initially understood. A similar trait can be seen from increasing optical excitation power and is attributed to optical saturation. However, this trend is seen with increasing bias strength at both optical excitation powers, so it can not be attributed to the same saturation mechanism. If it were saturation due to screening of the bias field, it would be less prevalent at lower optical powers as the number of carriers in the gap is reduced. Hence, this effect could be due to electrical saturation being reached in the device at higher biasing strengths. Higher electrical bias field strengths induce heating in the substrate, reducing the carrier mobility and consequently the strength of the emitted THz radiation. Although this provides a potential reason, it would be expected that the effect would be exaggerated at higher optical pump powers. However, it is clear to see this is not the case, with the same trend observed at both the higher and lower optical powers.

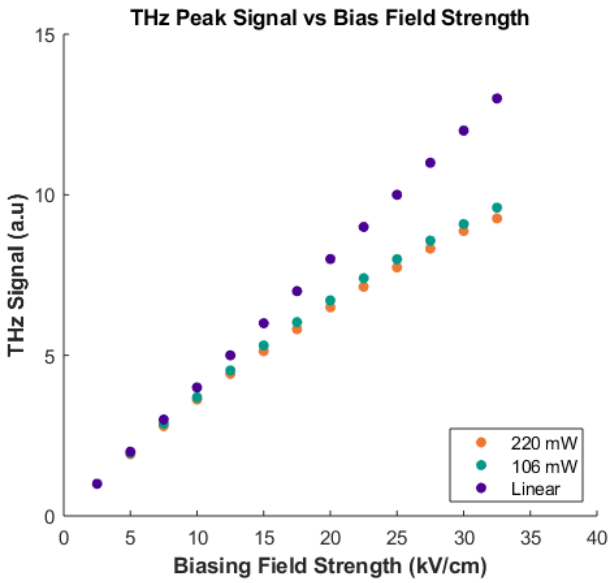

Figure 4.22: A comparison of the peak THz field as a function of applied bias for the large area device, with excitation optical pump powers of 106 mW and 220 mW. To compare linearity, the THz peak signals have been normalised and plotted with a straight line.

Investigating further, the results of this device were compared with a smaller area 50 μm gap device tested in 4.3. A comparison plot of the THz field strength as a function of applied bias is shown in 4.24. It can be seen that although not completely linear, the THz radiation produced by the smaller area device displays a stronger degree of linearity than that of the large area PCA and does not exhibit the same saturation at higher applied biases. This indicates that the issue is more likely to result from a fabrication issue rather than a device design issue. With the challenges during fabrication leading to a 'step' between the LT-GaAs material and the sapphire substrate, there is no longer an even BCB layer across the device; instead, it is isolated under the LT-GaAs bars. The reduced BCB could lead to a reduction in heat transfer to the substrate, which would lead to excess heating, but again, this does not seem likely as this mechanism is still seen at lower optical pump powers. As well with this created step, the continuity between the top of the electrode (situated on the sidewall of the LT-GaAs bar) and the bottom (which sits on the now exposed sapphire substrate) may not be good, introducing electrical issues. This could lead to excess heating in the substrate or non-uniform field if some of the sections are not connected properly.

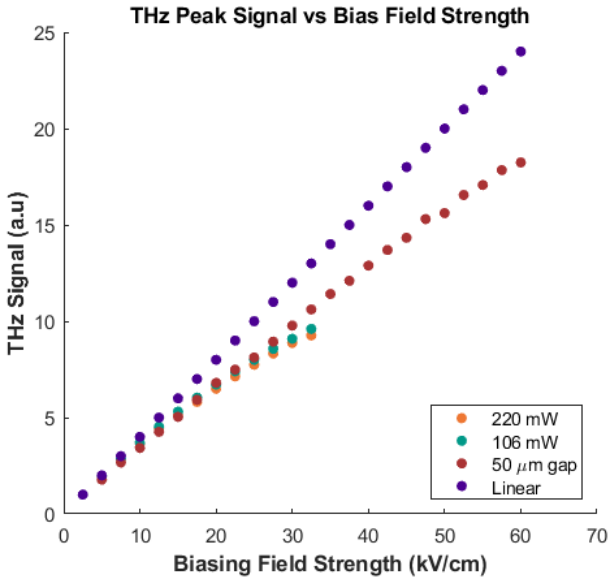

Figure 4.23: A comparison of the peak THz field as a function of applied bias for the large area device, operated optical pump powers of 106 mW and 220 mW, and for a smaller area 50 μm gap device from 4.3. The THz peak signals have been normalised and plotted with a straight line to compare linearity.

Figure 4.21 shows that under an optical excitation of 220 mW, a maximum THz field strength of 198 kV/cm was measured at an electric biasing field of 35 kV/cm. This field strength was measured via EO sampling using a 150 μm GaP crystal; the detected signal was processed through the method described in 1.9.2. Due to the earlier-than-expected breakdown of the device, no power measurement cross-reference was taken for this device. However, as the EOS accuracy has been demonstrated in 1.10.0.4, there is a high degree of confidence that these results are accurate. These results show that the device is capable of producing high field THz radiation and shows a significant improvement over the previous record achieved of 120kV/cm in [91] for a device fabricated on sapphire using the ELO technique. The previous record for an LT-GaAs device on sapphire was obtained using an 18x18 mm^2 active area with 200 μm wide gaps (discussed in 1.8.11). Comparing that device with the one fabricated here, they both have identical active areas of 324 mm^2 while the previous device has a better packing factor than the one demonstrated here of 52% to only 39% respectively, the reason discussed earlier. It can be seen that the maximum field strength achievable from the device here is almost 1.5 times higher from the same active area and with a lower packing factor. Another advantage of this design is that due to the gap size being a factor of 4 smaller than the older design, a smaller voltage can be used to achieve an equivalent biasing field strength.

Looking at the emitted THz pulse shape from the device in 4.24 (a), it can be seen that there is a large degree of asymmetry between the positive and negative sections. The quasi-half cycle pulse that is seen is believed to be a result of the structure of the array; this concept was discussed in the gap size section 4.3. As a consequence of the pulse shape, the bandwidth of the emitted THz pulse shape can be seen in figure 4.24 (b). The bandwidth extends up to 5.5 THz (limited by the bandwidth of the GaP crystal), with the majority of the spectral weight concentrated below 1 THz. The emitted pulse bandwidth displays lower spectral weight at higher frequencies, which is believed to be caused by the physical dimensions of the device array structure.

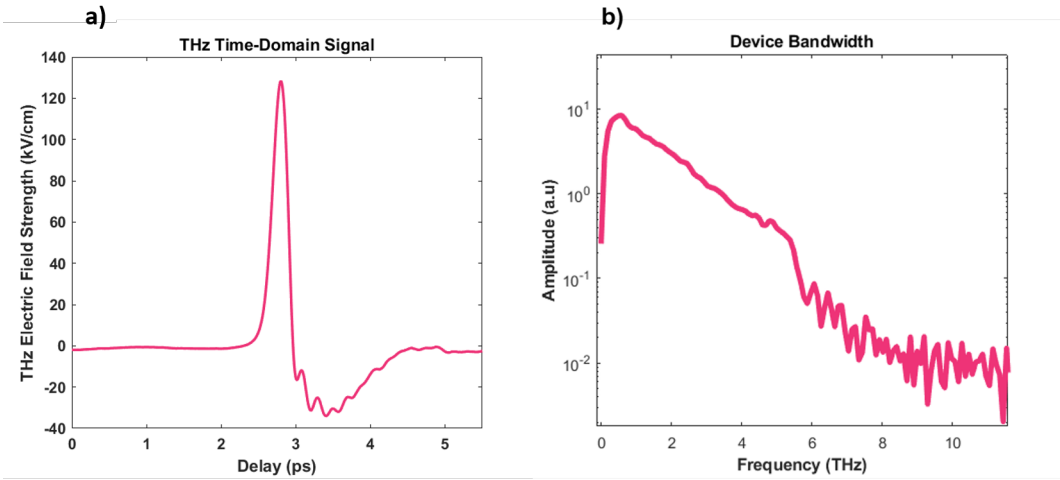

Figure 4.24: The figure shows the pulse of the emitted THz radiation (a) emitted under a bias field of 20 kV/cm and optical excitation of 220 mW. The resultant bandwidth of the pulse is shown in (b). A 150 μm thick GaP crystal was used for detection.

As mentioned in the previous section, the device experienced an earlier-than-expected breakdown. The device experienced complete failure as the bias was increased past the 35 kV/cm point, where the THz signal dropped to near zero. Under microscope inspection, it can be seen clearly that one of the emitting strip lines is completely destroyed. Figure 4.25 shows the microscope images of the damaged electrode pair; it can be seen that the discolouration of the LT-GaAs indicates significant surface roughness compared to the pairs either side which is due to the damage caused through a large discharge of current through this pair. The path of the discharge can be seen between two pairs through the 'dark gap'; this caused an effective shortfall across the entire device and rendered it no longer working. The reasons for the short happening could be due to several factors; firstly, the poor adhesion of the electrodes onto the device (due to removed BCB causing a 'step') discussed above would have caused issues with

the continuity of the gold effectively causing two paths of lower current carrying capabilities. When the current becomes too high, the electrode effectively blows from the lower part, creating a short across the gap. Secondly, as the 'dark gap' between conducting pairs is small, large enough pieces of debris can land on the device, effectively bridging the gap and providing a low resistance channel to ground for the current.

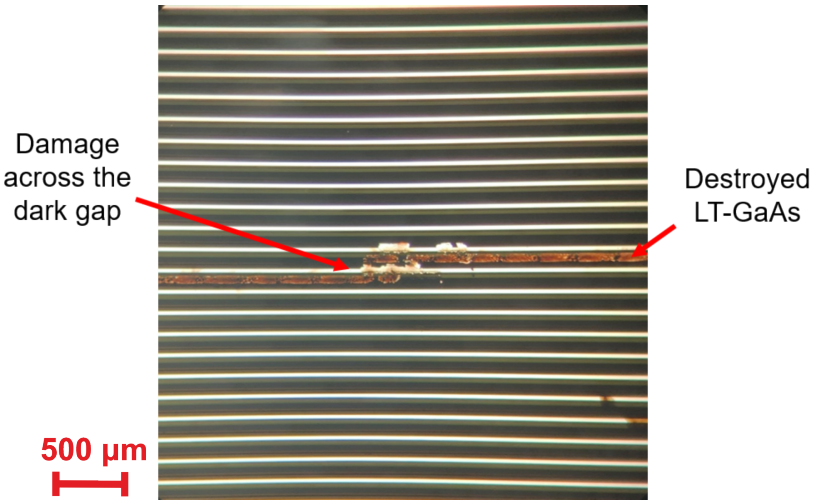

Figure 4.25: A microscope image of the device viewed in transmission. The damage to the device can be seen between two pairs, and the path that the current took can be clearly seen through the electrodes. The transmission view shows that the LT-GaAs material has been significantly damaged.

This is the highest field strength produced to date with a device fabricated on sapphire using the ELO technique. Also, it has been demonstrated that through the improvements of the electrode geometry and gap size spacing, it is possible to apply larger biases when compared to previous high field strength devices [91]. It can be seen from 4.3 that the 50 μm gap test device was able to operate at a much higher biasing field (60 kV/cm or 300 V) than the large device (30 kV/cm or 150V) here was capable of achieving, about 30 kV/cm smaller. This discrepancy between the two operating values was not expected but accounted for by the poor fabrication of the electrode structures, specifically the damaged point showed in figure 4.25, which prevented the device from being able to operate at a higher electrical biasing field strength. With an issue-free fabrication, achieving fields of over 300 kV/cm should be possible.

4.5 Small Gap Devices

The work in this chapter shows that moving to smaller gap sizes has yielded greater improvements and devices with higher efficiencies. A limiting factor with the fabrication process used for the previously described devices is that it is not possible to produce devices with gap widths smaller than 50 μm; hence, to move to even smaller gap sizes, a new process was developed (see 2.5.5).

The benefits of smaller gap sizes have been discussed previously in this chapter, and the desire to move to these even smaller gap sizes is to improve further on the results already seen. With gap sizes <50 μm, the need for larger DC power supplies is negated due to the smaller voltages needed for generating equivalent electric biasing fields, making it more accessible to operate.

4.5.1 Methodology

Three devices were designed to investigate the behaviour of the small gap devices. A 5, 10 and 20 μm gap was fabricated with the dimensions seen in 4.6. Here, the devices were fabricated separately on 3x3 mm pieces of LT-GaAs; due to the need for the biasing pads to sit on the LT-GaAs material, only a 3 x 1.5 mm area of the wafer is available as the active area. An important note for the designs is that all dark gaps were kept consistent; this decision was made to maximise the active area for each device. The dark gap was 8 um for each device, which is the minimum deemed achievable with this fabrication method.

Device Active area (mm)	Gap Size (μm)	Anode Width (μm)	Cathode Width (μm)	Number of Pairs
3 x 1.5	5	5	5	130
3 x 1.5	10	10	10	78
3 x 1.5	20	20	20	44

Table 4.6: Device dimensions for the three small gap designs. The gap sizes designed were 5, 10 and 20 μm. The dark gap for each was 8 um, hence the variation in pair numbers.

4.5.1.1 Fabrication Challenges

Working with such small devices, the tolerance of errors is understandably smaller than larger gap devices; for this reason, large area PCA devices are not fabricated with such small gaps. One of the main challenges with small gap fabrication is ensuring that all resist mask patterns are photo-aligned onto the devices accurately. Time must be taken to inspect the device under a microscope to make sure all photoresist clears in between channels and that none has delaminated from sidewalls, causing any gaps to become bridged, since the likelihood of such an occurrence is significantly increased due to the decreased distance between features. This also highlights the importance of plasma ashing

the devices after mask development to remove residue photoresist.

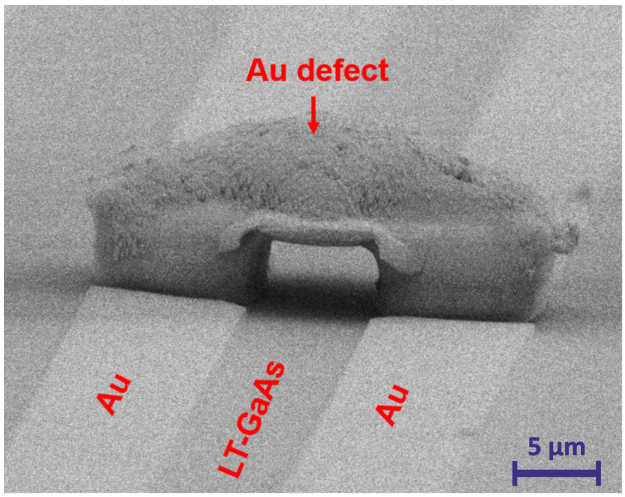

Figure 4.26: A SEM image showing a gold 'spit' that happened during the evaporation of the electrode metal. This defect can be seen to have bridged the gap causing an electrical short in the device.

A recurring issue throughout the fabrication process stemmed from the electrode deposition, particularly the spitting of the source material onto the surface of the device. When the source material, mainly gold, was evaporated from the heating crucible, it resulted in large metal deposits upon the device's surface. The image in figure 4.26 shows how the gold spits bridge device gaps, causing an electrical short; these are ~30 μm in height, making them near impossible to remove. To solve the deposition problem, the deposition was moved from a thermal evaporator to an E-beam evaporator. This switch allowed for a greater degree of control during the evaporation and provided a much cleaner film; the problem of spitting was no longer seen.

4.5.2 Results

The peak THz emission as a function of optical excitation power is shown in figure 4.27 for two different biasing field strengths. It can be seen from the graphs that the linear and saturation regimes are very distinctive. The first two optical excitation powers cause a larger increase in THz peak field before an abrupt beginning of the saturation regime.

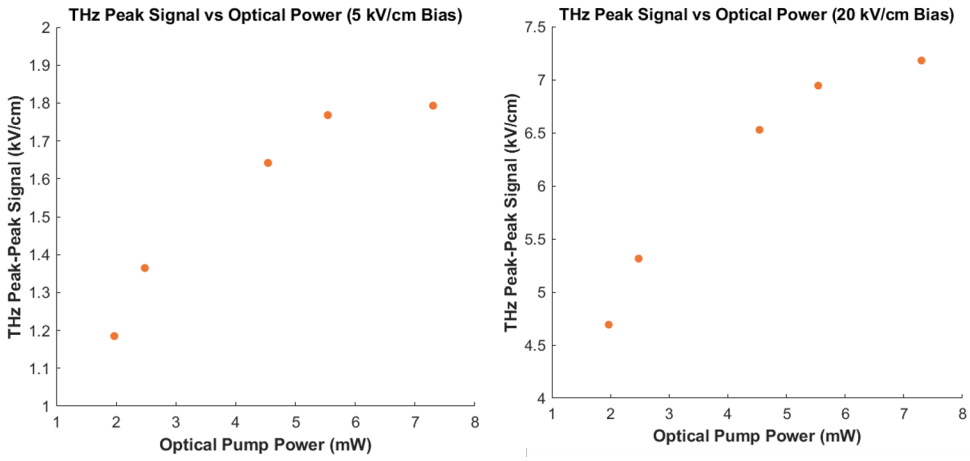

Figure 4.27: 5 μm gap device peak THz emission as a function of optical excitation power shown for two different applied bias field strengths; 5 kV/cm (left) and 20 kV/cm (right).

The abrupt jump from the linear regime to the saturation regime with 800 nm excitation is due to the limited variation of lower optical powers to choose from with the ND filters in the system; as the device is small, the fluence is much higher due to the focus through testing scheme. The saturation seen in smaller gaps can also be due to increased charge screening effects. At 7.3 mW of optical power on the device in a focus through testing regime, the fluence is 100 μJ/cm^2

An interesting trend in the devices is an asymmetrical scaling of the time domain pulse shape with both increasing optical excitation power and applied biasing field strength. Looking at the evolution of the time domain pulse for the device as the optical excitation power is increased, one can clearly see the change in asymmetry between the negative and positive peaks, shown in figure 4.28. As the pump power increases, the THz signal radiated increases; the growth in the positive peak at incremental powers is not equal to the growth of the negative peak at the same excitation power.

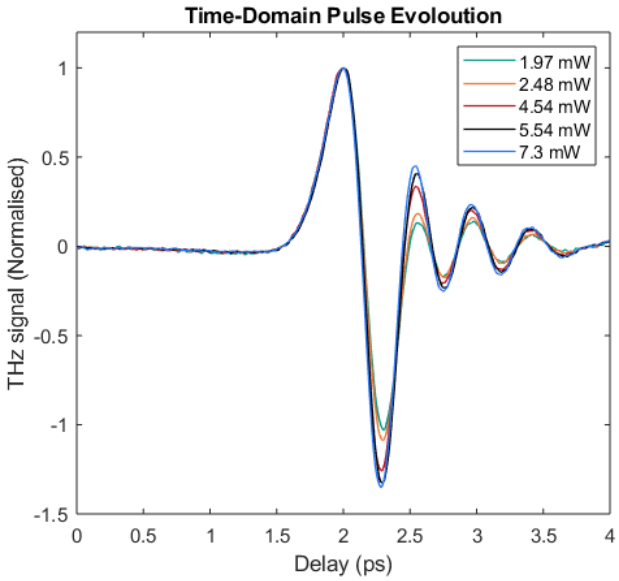

Figure 4.28: THz signal as a function of time for emitted pulses from the 5 μm small gap device for different optical excitation powers. The asymmetrical growth in the negative peak of the pulse with increasing excitation power can be seen. All pulses were normalised for comparison.

The THz emission as a function of applied bias can be seen in figure 4.29; the graphs show the data measured as both peak signal and also the peak-to-peak THz signal. In the first instance, looking at just the increase in peak signal, it does not show a complete linear trend; to begin with, the device appears to increase linearly between 2.5 and 17.5 kV/cm before a sublinear trend appears. Looking at the peak-to-peak case instead, it can be seen that the increase holds a greater degree of linearity. This is explained by a change in the emitted pulse shape discussed previously. It is important to note that a full electrical test was not performed during initial testing due to the availability of only a single device and the wish not to cause any damage; hence, only a safe operating bias of 30 kV/cm was applied. The linearity of the increased emitted THz field shows no electrical saturation up to the measured applied bias field.

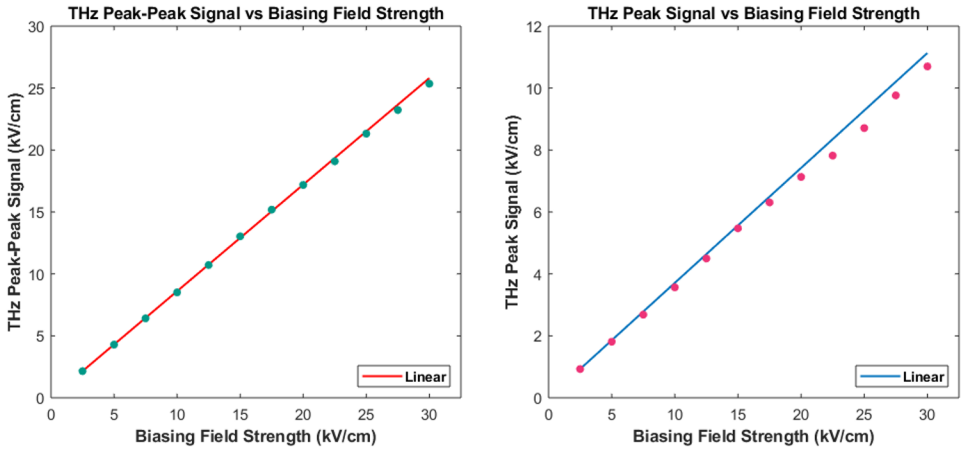

Figure 4.29: The peak-to-peak (left) and peak (right) THz emissions as a function of applied bias field. Both are plotted with straight line fits showing the degree of linearity.

As discussed within section 4.4, the array structure's increased period size distorts the pulse shape from large gap devices; this is reflected as a loss of amplitude at higher frequencies, as seen in the bandwidth plots of the devices. This behaviour is attributed to the grating effect caused by the large area array; this hypothesis is supported by the FFT bandwidth plot seen in 4.30.

When this bandwidth is compared to that of a large area device with 50 μm gaps, it is clear to see there is a significant improvement in the spectral weighting. For the large device, the highest spectral weight is at the lower frequencies, with the peak being below 1 THz before a steady decline as the frequency increases. The 5 μm gap device has roughly even spectral weighting between 1 and 4 THz before beginning to decline. The much-improved spectral weighting is desirable for spectroscopy, allowing for the probing of non-linear effects present at higher frequencies.

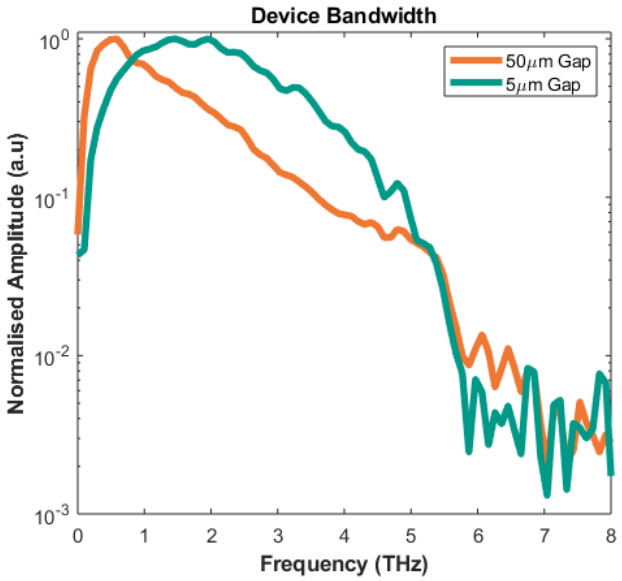

Figure 4.30: The 5 um gap device spectrum compared to that of a 50 um gap large area array device (from section 4.4). Both amplitudes have been normalised for a clear comparison to be drawn.

A simple simulation used to determine the effect the period of each device has on the diffraction of the emitted frequencies can be seen in figure 4.31. The diffraction of the THz beam from the array structure can be determined by thinking of each gap as an individual point source; the diffraction angle for each n^{th} order can be calculated:

$$\theta = sin^{-1}(\frac{n\lambda}{d}) \tag{4.1}$$

the grating separation, d, is taken as the period of the emitting pairs and λ is the radiation wavelength in free space.

The two graphs in figure 4.31 show the diffraction angles for the small 5 μm gap device, which has a small period spacing of 23 μm, and the larger 50 μm gap device, which has a larger period spacing of 370 μm. For the case of the larger device, there is less diffraction of the higher frequency components with complete suppression of the first five orders of diffraction only achievable up to $\sim$ 1 THz. The opposite can be seen for the 5 μm gap device; due to the smaller period spacing, the suppression of all orders of diffraction is obtained up until 13 THz. This supports the hypothesis that diffraction effects from the array structure of the device are responsible for the change in the emitted frequency spectrum of larger gap devices.

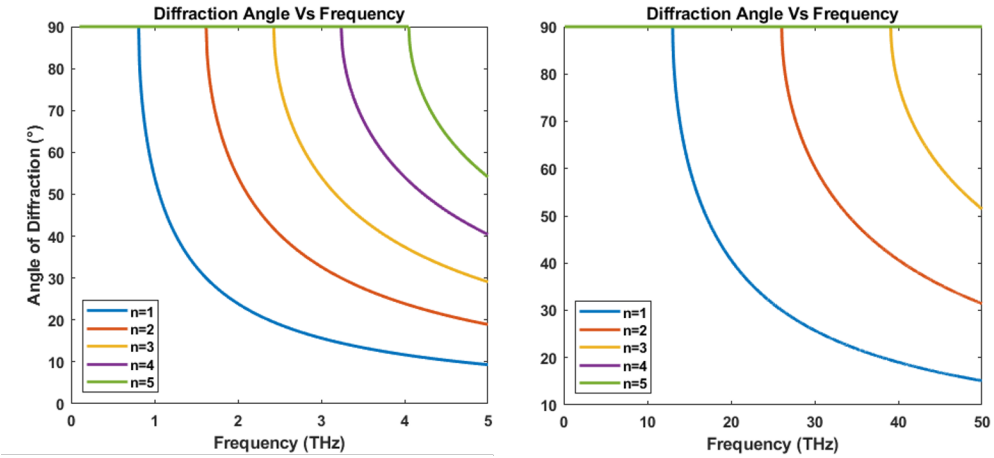

Figure 4.31: Diffraction angle vs Frequency for the two different devices. The large area 50 μm gap (left) with a 370 μm period, and 5 μm gap device (right) with a 23 μm period. It can be seen that the smaller period suppresses the higher orders of diffraction.

4.6 Conclusions

In conclusion, different electrode geometries were designed and tested, and the effects on the generation of THz emission were discussed. A study into a triangular electrode geometry was presented, this was done to investigate whether a triangular electrode was capable of supporting higher electrical biases. The results showed no advantage to using such an electrode design over a conventional rectangular electrode. However, this study did highlight how fabrication variations can impact the generated signal from a device, with two nominally identical devices fabricated separately having a ~ 20 % difference in peak signals.

An investigation of the enhancement of the generated THz signal through asymmetrical electrode widths was conducted. It was shown that increasing the anode width whilst keeping the cathode width constant enhanced the THz signal generated. In contrast, it was demonstrated that increasing the cathode width while keeping the anode width fixed did not produce the same enhancement. This enhancement effect was then compared against the enhancement arising from maximising the device's active area. It was shown that an increased packing factor showed a more significant enhancement of the THz signal.

Different gap sizes were studied to investigate whether smaller gap devices could support higher biasing fields. Three different gap sizes were produced; 200 μm,100 μm and 50 μm. It was found that the THz signal generated from each device was comparable at the same electrical bias and optical pump fluence. It

was also shown that the smallest gap device could support an electrical bias of twice that of the largest gap device.

An 18x18 mm large area PCA array was fabricated with 50 μm gaps. This device was shown to produce THz electrical fields of $\sim$ 200 kV/cm. This device showed a THz field enhancement of almost 1.5 times that of the previous high-power LT-GaAs on sapphire device fabricated by the group. The device, however, succumbed to earlier-than-expected device failure, with a complete electrical breakdown occurring at 35 kV/cm. The device failure was attributed to fabrication issues; it is believed that with issue-free fabrication, electric bias fields of up to 70 kV/cm could be applied.

Finally, a small 5 μm gap array was fabricated. This device was fabricated using the new small gap fabrication method presented in 2.5.5. It was shown that the small gap device produced a THz pulse with improved spectral weighting, with the emitted energy weighted fairly evenly between 1 and 4 THz. The reason that this was seen is explained by the smaller array geometry causing greater diffraction of the higher frequency orders.

Chapter 5

Large area LT-GaAs arrays pumped with a 1 μm Yb-fibre laser

The work discussed here was performed in collaboration with École Normale Supérieure Paris [6] with testing on a 1030 nm wavelength Ytterbium (Yb)-doped fibre laser system with a 200 kHz repetition rate. Investigations into the operation of LT-GaAs on sapphire PCA devices using high repetition rate lasers of this wavelength is limited, so this work is performed to understand the behaviour at this wavelength.

It was discussed in section 1.2 that the desire for intense THz pulses for spectroscopic investigations; currently, intense THz pulses have been achieved through a variation of different sources. These intense sources have commonly been driven by femtosecond pulses at 800 nm wavelengths, generated by relatively low repetition rate Ti:Sapphire amplified laser systems in the KHz range. LT-GaAs PCA devices are commonly excited at 800 nm to generate intense THz pulses due to the photon energy closely matching that of the LT-GaAs bandgap [128]. For some spectroscopy applications, a high signal-to-noise ratio is required, which in turn requires high repetition rate lasers. Yb-doped laser systems are capable of achieving fs pulse widths with optical powers reaching hundreds of μJ with high repetition rates of hundreds of kHz, as well these systems are cheaper than amplified ones. The ability to operate LT-GaAs PCA devices with high repetition rate lasers of this wavelength remains highly desirable due to the lack of photoconductive material available.

5.1 Heating Investigations

With the potential issues that device heating has on THz generation from PCA devices, it is important to garner a better understanding of the device heating and recovery time; the higher repetition rate is expected to increase heating. A major source of excess heating was removed during the ELO technique and helps to improve the device recovery time; this is discussed in 2.3. Another area of potential excess heating is expected to come from intense excitation pump laser pulses. These pulses have high peak energy values; thus, the absorbed pulse will cause a temperature rise within the LT-GaAs substrate. The compounding effect of repetitive high energy pulses heating a PCA device fabricated with the ELO has not been studied before. Here, a FE simulation software package (COMSOL Multiphysics) is used to analyse the thermal effects within the substrate, with particular interest in the heat dissipation away from the substrate and operating temperatures. Simulation of optical excitation is carried out for two different laser systems; firstly, an 800 nm Ti:Sapphire amplified laser system with a 1 kHz repetition rate and then secondly, a 1030 nm Ytterbium (Yb)-doped fibre laser system with a 200 kHz repetition rate.

5.1.1 Finite Element Analysis

The COMSOL Multiphysics FE package can analyse, simulate and model material behaviour. In essence, the FE analysis can be considered a discrete technique of solving partial differential equations, making it an indispensable tool for investigating many material properties such as fluid flow, magnetic fields and, importantly, for this work, heat transfer. As the name suggests, FE works based on splitting the modelled system into a set of discrete or finite elements connected by nodes. Separating the model into these finite elements allows the system to be represented by a set of finite equations. These equations are generally set from each other with independent variables that commonly depend on nodal distance. The independent set of solutions from each element allows a larger continuous picture to be formed, thus, the material behaviour to be modelled. [192]

5.1.2 Method

To analyse the heating effects, first, the device is modelled; figure 5.1 shows the composition of the model. The device consisted of a 2 μm thick, 5x5 mm LT-GaAs active area. The active layer was on a 650 μm thick, 1x1 cm sapphire substrate. Between the active layer and the substrate is a 500 nm thick BCB layer. The device is mounted on a PCB using a silver conductive paint; this was modelled as a pair of identical patches on top of the active area, the electrical connection between the active layer and the board. The gold electrode structure is omitted for the simplicity of modelling, and as it is assumed, the reflectivity of

gold is sufficiently high, and the gold film is thin enough to negate any heating through absorption, which is hence assumed negligible. Another key point to state is that any contribution to the heating from the induced photocurrent is not included because the average current is small enough to cause the temperature rise to be negligible compared to the laser heating. The PCB comprises a 1.5 mm thick aluminium board with a 0.1 mm top insulating FR4 board, to which the PCA is affixed. The cut out in the PCB is so that the device can be operated through both backside and front-side illumination.

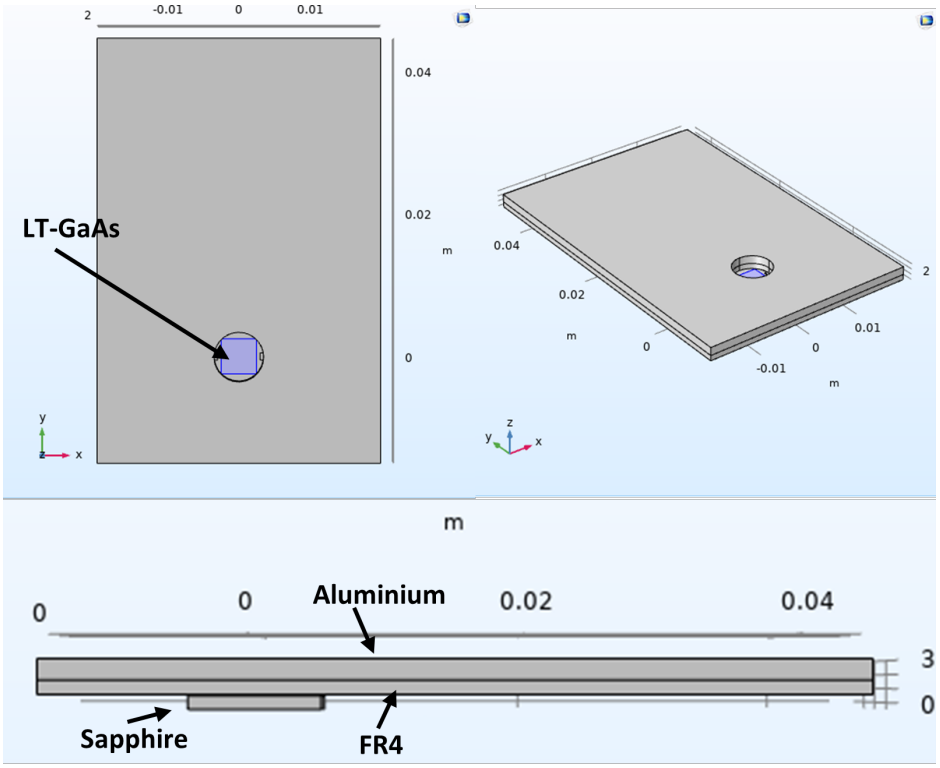

Figure 5.1: Comsol model of the LT-GaAs device on sapphire mounted to a PCB

The heat transfer model module of COMSOL handles the physics using thermal parameters input into the simulation. In order to obtain accurate simulations, it is important to use correct material values when setting up the model. The key thermal properties are specific heat capacity, thermal conductivity and material density. With COMSOL, these parameters are already programmed into the material catalogue and included in the thermal dynamic package. Before commencing the simulation, the thermal dynamic simulation requires set control variables and boundary conditions. The main value of note is that the bottom surface of the PCB, which is the aluminium part, is set as a boundary

condition to remain at 300 K, which is close to room temperature; this sets this surface as the heat sink of the model. This boundary condition was used because it is the only physical connection between the device and the optical table. Another important parameter was the initial heating from the laser source. The laser pulse heating was applied using a COMSOL function that simulates a deposited beam power. This function models a heat source based on a beam with a Gaussian-type distribution. The beam was set to have a 2.5mm radius to fill the active area fully and was centred on the active area. The temperature rise induced by this beam is calculated as:

$$\Delta T = \frac{E_{Beam}}{V \cdot \rho \cdot C_V} \tag{5.1}$$

Where E_{Beam} is the beam's energy, ρ, V and C_V are the density, volume and specific heat capacity of the LT-GaAs respectively. This assumes that all the beam energy incident on the active area is absorbed. The incident beam's power can be adjusted accordingly to simulate different absorption percentages. Solving the model allows for the localised heating to be analysed; by solving over a specific time period, the thermal dynamics of the device can also be found.

5.1.3 Results

The device heating effects due to optical pumping were modelled in two steps. First, the steady-state solution was calculated by applying the average incident beam power to the LT-GaAs film. This solution effectively assumes a constant (i.e. CW) laser power. In the second stage, outlined below, the effect of the time dependence of the laser pulses will be examined. The range of average laser powers simulated was based on the average laser powers that are obtainable across both the 800 nm and 1030 nm laser system; these powers can be seen in tables 5.1 and 5.2 with the corresponding substrate temperatures induced. It is important to note that the values used for the average laser power of the 1030 nm system (table 5.2) were adjusted to account for an absorption coefficient of 54 % (discussed further in 5.2.1) before performing the simulation.

Average laser power (W)	Sapphire Substrate Temperature (K)	LT-GaAs Temperature (K)
0.1	302.17	302.22
0.2	304.34	304.44
0.3	306.51	306.67
0.4	308.68	308.89
0.5	310.85	311.11

Table 5.1: Average laser powers used for optical excitement at 800 nm and the induced sapphire substrate and LT-GaAs temperature temperature at each.

Average laser power (W)	Sapphire Substrate Temperature (K)	LT-GaAs Temperature (K)
0.54	311.72	312
1.08	323.44	324
1.62	335.16	336
2.16	346.87	348
2.70	358.59	360
3.24	370.31	372
3.78	382.03	384
4.32	393.75	395.99
4.86	405.47	407.99

Table 5.2: Average laser powers used for optical excitement at 800 nm and the induced sapphire substrate and LT-GaAs temperature at each.

The graph in figure 5.2 shows the average sapphire substrate temperature as a function of the average laser power incident on the device. It can be seen that the substrate temperature has a linear increase with increasing average laser power. It can also be seen that the substrate temperature induced by the lower average laser powers used for optical excitement at 800 nm (0.1 W - 0.5 W) causes a much smaller temperature rise in the substrate. This trend is expected as the 800 nm system has a much lower average power. The temperature induced by the 1030 nm system is much higher, with a maximum substrate temperature of 405 K.

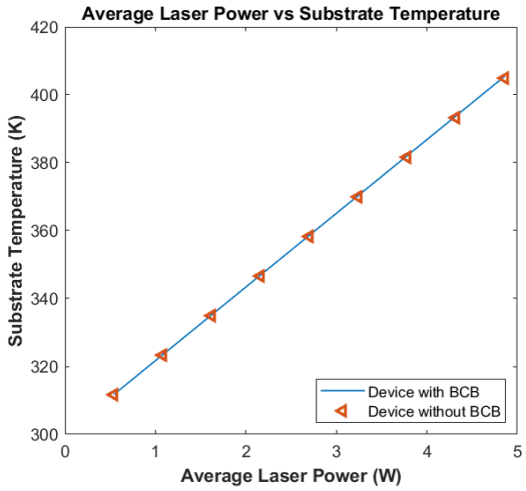

Figure 5.2: Substrate temperature induced as a function of average laser power. It can be seen that the substrate temperature increases linearly with increasing laser power. Also plotted is the same simulation, except the BCB layer has been removed; this shows that the BCB is thin enough not to have a major effect on the heat transfer between LT-GaAs and Sapphire layers

In the second step, to evaluate the device's thermal relaxation, the induced

substrate temperature can be set as the initial temperature, the deposited beam power is removed, and the temperature of the device is allowed to evolve towards the heat sink temperature. By allowing the model to be solved over a set time period corresponding to the repetition rate, the thermal evolution of the LT-GaAs and the sapphire substrate can be analysed between pulses. The graph in figure 5.3 shows the temperature variation for the sapphire and LT-GaAs layers over the 5 μs time interval between pulses when operated on the 200 KHz repetition rate system at 1030 nm wavelength. The LT-GaAs layer can be seen to quickly dissipate $\sim$ 40 % of the induced heat over the time period, but the layer will still be hot when the next pulse arrives. It can also be seen that the sapphire substrate does not dissipate any significant heat over the time period; this shows that the temperature of the sapphire substrate will stay nearly constant over each 5 μs period; this is because of the much larger thermal mass of the sapphire substrate. This finding gives confidence that the steady state model gives a reasonably accurate estimate of the sapphire temperature, despite the pulsed excitation. The LT-GaAs layer, with its much smaller thermal mass, will have a temperature that fluctuates between pulses. One would expect the temperature of this layer to increase above the sapphire bulk immediately after the optical excitation and decrease below it before the next pulse arrives, with a similar time scale and amplitude to that shown in figure 5.3.

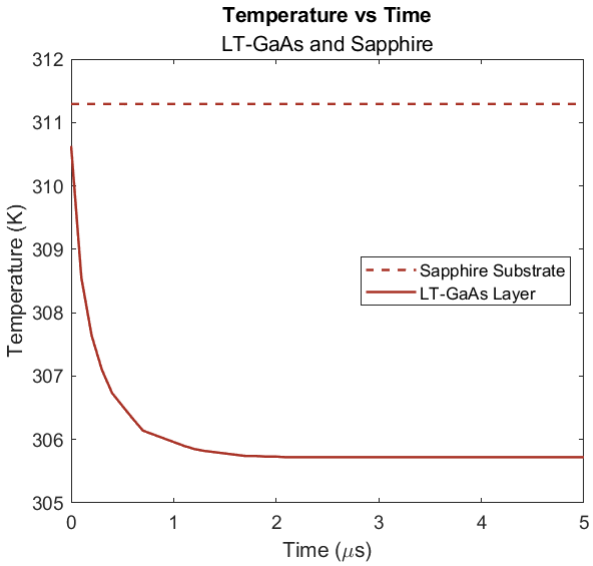

Figure 5.3: The time evolution of the sapphire substrate and the LT-GaAs layers. It can be seen that the sapphire substrate does not change over the 5 μs time period. The LT-GaAs layers' temperature relaxes between pulses. These results are obtained for an average laser power of 0.54 W when the device is operated on the 1030 nm 200 KHz rep rate system.

The graphs in figure 5.4 show the temperature of the LT-GaAs and sapphire layers of the device over a 1 ms time period; this is the time delay between pulses on the 1 KHz 800 nm system. This graph shows the LT-GaAs layer has an initial steep thermal relaxation as the heat dissipates into the PCB (the LT-GaAs layer is very close to the PCB) but then slowly begins to rise again as some of the heat from the sapphire flows back into the layer. The substrate temperature shows again that the temperature varies very little over the 1 ms time interval. Again, this finding gives confidence that the steady state model gives a reasonably accurate estimate of the sapphire temperature, despite the pulsed excitation, while the temperature of the LT-GaAs layer will fluctuate around the sapphire temperature as the pulses arrive.

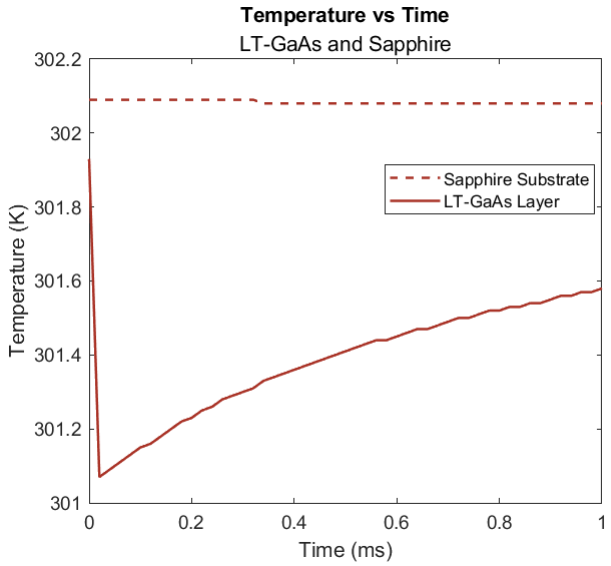

Figure 5.4: The time evolution of the sapphire substrate and the LT-GaAs layers. It can be seen that the sapphire substrate does not change substantially over the 1 ms time period. The temperature of the LT-GaAs layer relaxes between pulses initially and then begins to rise slowly again. These results are obtained for an average laser power of 0.1 mW when the device is operated on the 800 nm 1 KHz rep rate system.

The results from this modelling have shown that the operation of the LT-GaAs PCA device using the 800 nm 1 KHz repetition rate system is not likely to be affected by detrimental high-temperature effects [193]. At the highest modelled power of 0.5 W, the operating temperature will only be $\sim$ 11 K higher than the start temperature, with the temperature of the LT-GaAs fluctuating around this by 1-3 K. These thermal characteristics are greatly aided by a longer relaxation time and the fact that less power is applied to the devices than with the 1030 nm system. In the case of an LT-GaAs device operated using the 1030

nm 200 KHz system, it can be concluded that the operating temperatures will be much higher; at the highest average laser power that is applied, the device operating temperature would be $\sim$ 100 K higher than the start temperature. However, this temperature increase is not at a point that would lead to device thermal breakdown; it will still impact the device's performance. It is believed that carrier mobility will be somewhat reduced at higher optical powers, and hence THz emission would be affected.

5.2 1 μm Set-up

The device dimensions were designed to utilise the maximum beam diameter of the 1030 nm system to fill the device fully. The laser system diagram can be seen in 5.5, optical excitation was provided by a 1030 nm wavelength, 200 kHz repetition rate Yb-doped laser system (Tangerine laser system manufactured by Amplitude). To achieve pulses with durations of 30 fs yet still be spectrally broad, the pulse is manipulated using a krypton-filled capillary tube to spectrally broaden the pulse before using a compressor to achieve ultrashort pulse widths. The testing set-up shows this is a THz-TDS set-up similar to that mentioned in chapter 3. In this set-up, an EO detection scheme is used, with a 200 μm thick ZnTe crystal.

The device used in this experiment is the 1x3 mm active area, 5 μm gap device detailed in 4.5. To compare the results of the operation of the device at this wavelength, another device was fabricated. A 130 μm gap 2x2 mm PCA device, fabricated using LT-GaAs on a sapphire substrate.

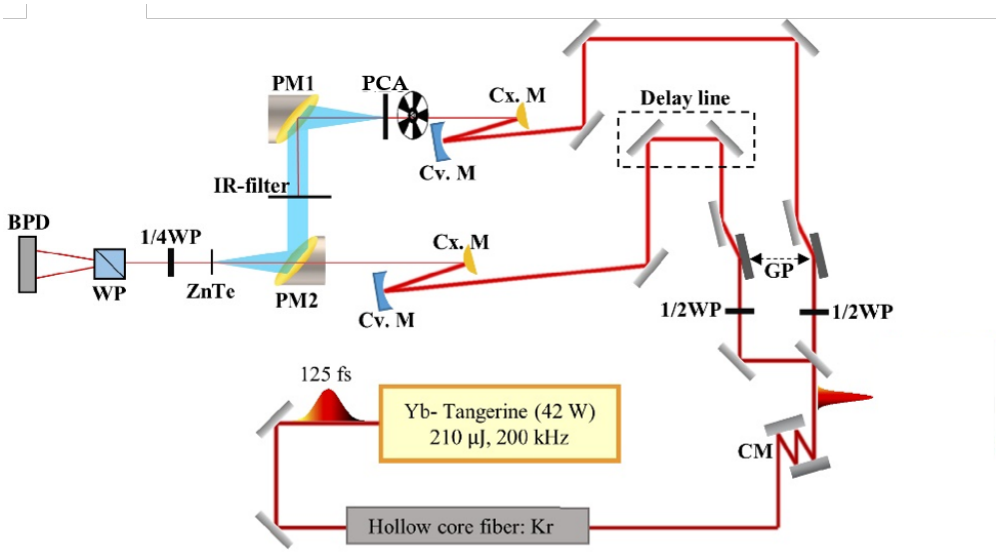

Figure 5.5: A system diagram of the 1030 nm system. The pulse originates as 120 fs pulse centred at 1030 nm from a 200 kHz repetition rate Tangerine laser system by Amplitude. The pulse is spectrally broadened and compressed to achieve a 30 fs pulse width. Diagram is taken from [5]

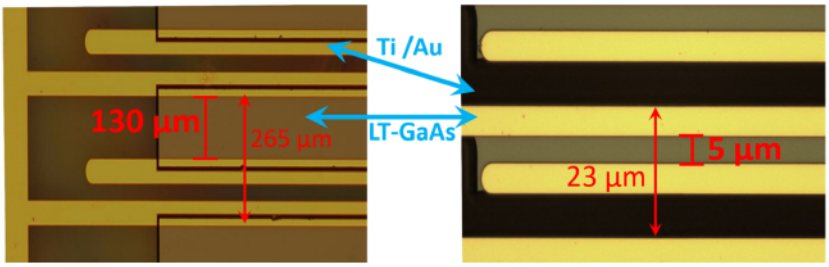

Figure 5.6: Microscope images of the two different LT-GaAs arrays tested on the 1030 nm system. The 130 μm gap array device (Left), and a 5 μm gap device (Right).

5.2.1 Absorption of 1030 nm wavelength pulses in LT-GaAs

As mentioned in the opening section of this chapter, the number of suitable photoconductive materials that can be excited at this wavelength is limited. Typically, SI-GaAs shows very little absorption of 1030 nm wavelength radiation due to the photon energy of 1.2 eV being smaller than the bandgap energy of the material (1.42 eV). It has been shown, however, that the absorption

characteristics of LT-GaAs differ considerably [113]. As discussed in chapter 2, during the growth of the semiconductor, an excess of arsenic is incorporated in the material as arsenic antisites and interstitial point defects. These points form a weakly-bound continuum of shallow defect around the bottom of the conduction band, which allows photons of energy lower than the material bandgap to be absorbed; this is an effect known as Urbach tail absorption. [194, 195]

To investigate the percentage of the excitation pulse absorbed at this wavelength, Fourier Transform Infrared (FTIR) spectroscopy was performed by the group at ENS Paris. The FTIR spectroscopy was carried out on the LT-GaAs layer of the device in a transmission geometry. Due to the broadening effects of the absorption tail, an absorption coefficient of 3900 cm^{-1} is obtained at a wavelength of 1030 nm (seen in figure 5.7. The percentage of the pulse absorbed can then be calculated:

$$A = 1 - e^{-\alpha x} \tag{5.2}$$

where α is the absorption coefficient and x is the thickness of the absorbing sample. Hence, in a 2 μm thick LT-GaAs layer, only 54% of the pulse energy is absorbed at a wavelength of 1030 nm. There will also be an enhancement of direct bandgap absorption in the material at increased temperatures due to a lowering of the bandgap energy (as discussed in 1.8.3.3). It has been simulated in section 5.1 that device operating temperatures can increase up to 100 K; this will play a role in the amount of direct bandgap absorption occurring as this can lower the bandgap by 0.1 meV [114]. The spectral broadening of the pump pulse was also considered. Using the obtained absorption data, the absorbed pulse was determined by applying the measured absorption to the spectrum of the input pulse; it can be seen in figure 5.8 that the broadening of the pump pulse does not change the absorption spectrum significantly.

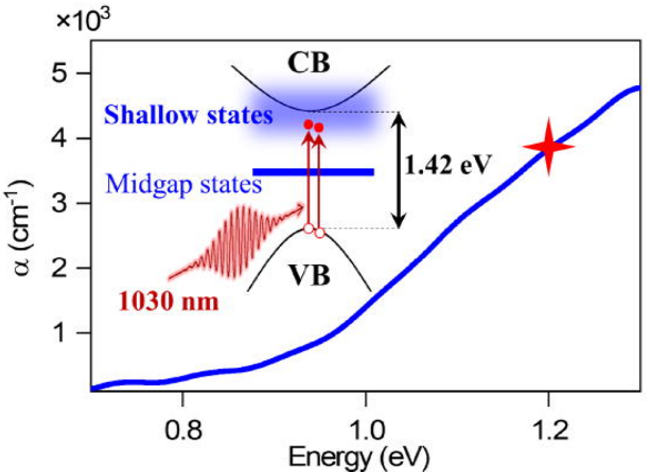

Figure 5.7: The absorption coefficient in the LT-GaAs layer as a function of excitation energy obtained from FTIR. The star denotes the 1030 nm wavelength, at which an absorption coefficient of 3900 cm^{-}1 can be seen. The inset diagram depicts the Urbach absorption of sub-bandgap energy photons into shallow defect states. Reproduced from [6]

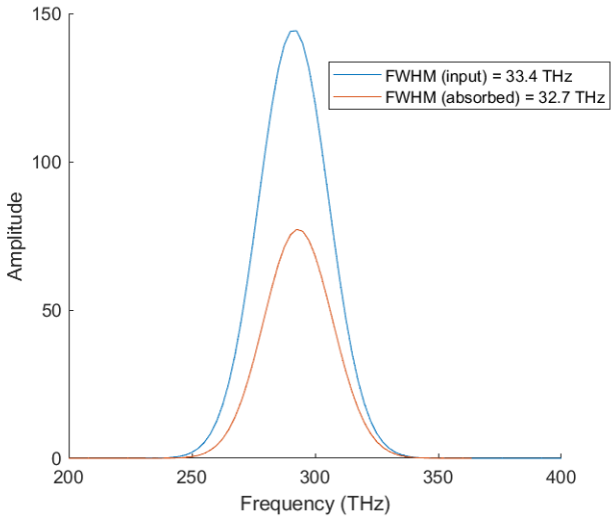

Figure 5.8: The Gaussian distribution of the absorbed pulse in the LT-GaAs, this is accounts for the spectral broadening of the pump pulse.

5.2.2 Results

The THz emission as a function of optical fluence for the device was first tested to see its behaviour at the longer wavelength. The THz electric field strength was measured through electric optic sampling using a 200 μm thick ZnTe crystal. The graph in figure 5.9 shows the radiated THz signal as a function of the optical pump power for the 130 μm gap array; it can be seen that, initially, a linear rise is seen up to 2W optical powers before entering the saturation regime from 2 W to 9 W. This behaviour follows the trend seen in devices characterised previously. However, the device never reaches a fully saturated state, limited by the maximum pump power of 9 W available from the laser system. The fluence produced is around 1.5 mJ/cm^2 at 9W average power; this is due to the 200 kHz repetition rate. Also, due to the percentage of the absorbed excitation pulse, the number of photogenerated carriers is reduced, further postponing optical saturation. The saturation seen in the device is due to the screening of the applied field via the induced field caused by the separation of charges.

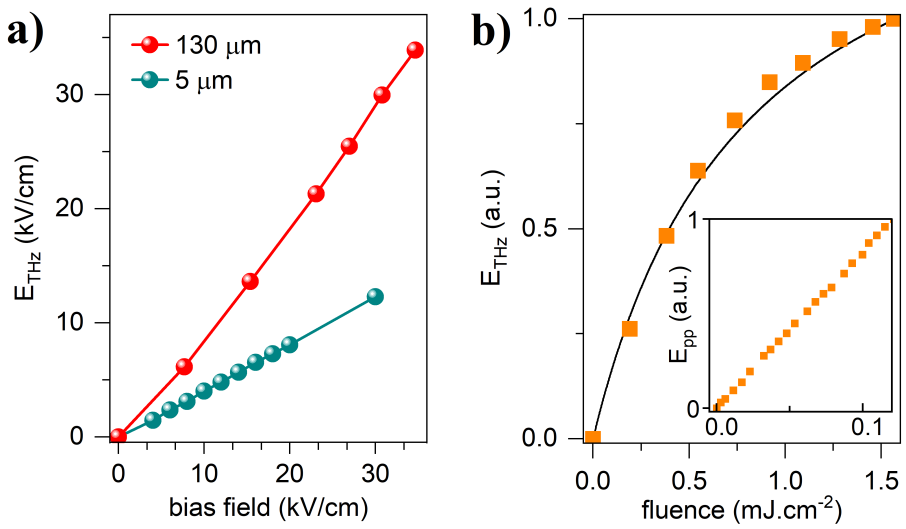

Figure 5.9: a) Comparison of the peak emitted THz field strength as a function of applied bias for the 130 μm and 5 μm gap array devices. b) The peak emitted THz field strength as a function of optical fluence of the 130 μ gap device. The inset shows the linear generation regime at low optical fluences. This figure was prepared by Dr Juliette Mangeney and Dr Niloufar Nilforoushan.

The effect of increasing electrical bias field strength can be seen in figure 5.9 (a). It shows that the peak-to-peak increase in THz radiation has a linear increase; this shows the good operation of the device following with the expected behaviour according to 3.2.2. The linear increase also demonstrates no electrical saturation occurring in the device. Comparing the device to the larger 130

μm gap array that was tested, it can be seen that it has a similar linear rise with increasing bias. Regarding maximum emitted field strengths, the 5 μm gap array has a peak field strength of 12 kV/cm, and the 130 μm gap array's peak emission is 34 kV/cm. The difference in maximum field obtained is due to the larger device area that can have the optical excitation pulse spread across and because of the larger fluence on the device. As the small gap device has a 1x3 mm active area, the beam spot size has to be a 1.5 mm radius to fill the entire array. In the case of the 130 μm gap array, the active area is 2x2 mm; thus, a small spot size can be used and, hence, a higher fluence than the small gap device.

The graph in figure 5.10 compares the emitted bandwidth from both gap size devices; the amplitude values normalised to the smaller device. The bandwidth of the radiation emitted by both devices can be seen to be similar. Both have the majority of the energy around 1 THz with quite a steep roll-off towards a maximum of 3.2 THz. The 5 μm gap array has slightly improved spectral weighting up until 3 THz. When looking at the time domain pulses emitted by both devices, shown in figure 5.11, the large gap has a pulse width of 487 fs, and the small gap is 458 fs. The slightly faster pulse emitted from the 5 μm gap array explains the slight improvement of the emission spectra (explained in 1.8.5).

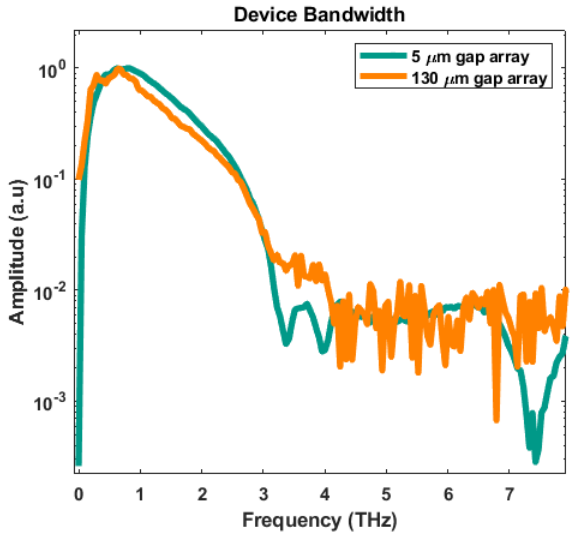

Figure 5.10: The spectrum of the emitted THz radiation from the 5 μm and 130 μm gap array devices, obtained through FFT of the time domain spectra. The bias fields and optical pump energy applied were 30 kV/cm (15V) and 0.4 mJcm^{-}2 for the 5 μm gap array, 34.6 kV/cm (450V) and 1.5 mJcm^{-}2 for the 130 μm gap device.

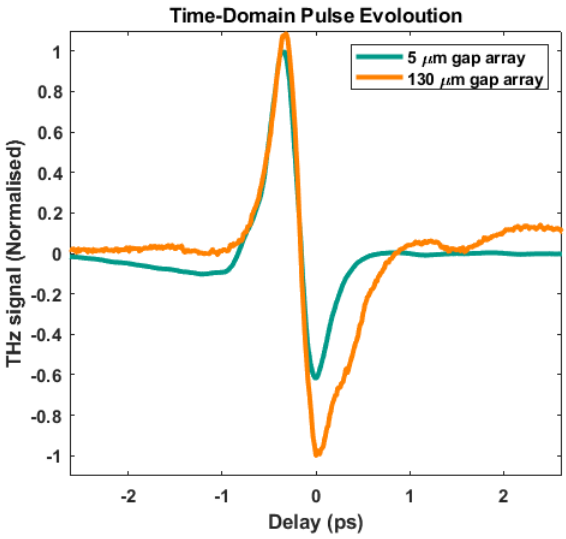

Figure 5.11: Evolution of the peak THz electric field with time for both 5 and 130 μm gap array devices.

5.2.3 Comparison of operation at 800 nm wavelength

To better understand the device's operational characteristics at the two different wavelengths, it can be compared with operation at 800 nm, presented in 4.5.

The difference in systems must be addressed to compare the THz radiation emitted as a function of optical excitation power. With the 800 nm system being a low repetition rate laser, the average power is lower. However, peak powers are much higher compared to the higher 200 kHz repetition rate at 1030 nm wavelength. In both cases, the pump spot size was adjusted to fill the array completely (ø=3 mm); the fluence obtainable at 800 nm is substantially higher than that at 1030 nm.

The THz radiation generated as a function of optical fluence can be seen in 5.12; this shows a saturation trend similar to all the other devices tested. From (a), it can be seen that the device became fully saturated at an optical fluence of 110 μJ/cm^2 when excited at 800 nm, unlike at 1030 nm, where full optical saturation was not observed until the fluence was at 400 μJ/cm^2.

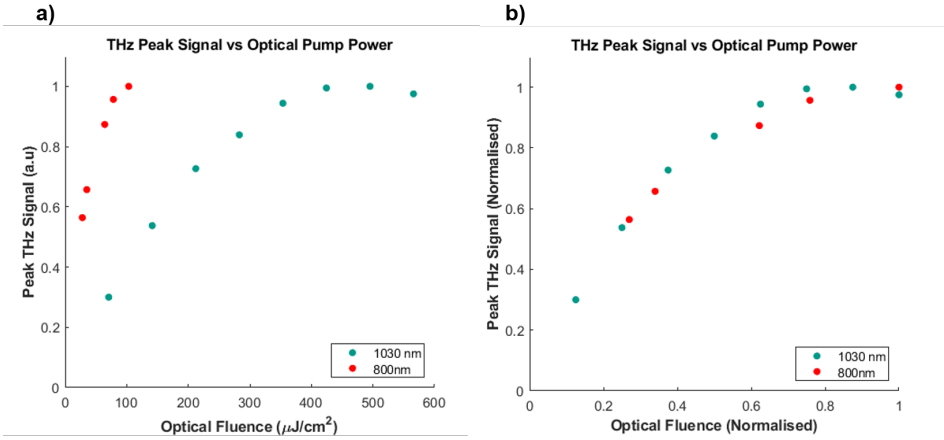

Figure 5.12: A comparison of the peak emitted THz signal as a function of optical fluence. A bias value of 20 kV/cm was used for both. a) Both devices plotted with normalised peak THz signal to show the difference in saturation fluences. b) Both devices plotted with normalised peak THz signal and normalised fluences to show the saturation trends are closely matched.

The higher saturation fluences are attributed to the lower absorption coefficient at that wavelength. Both devices exhibit the same trend as expected with increasing optical pump power, with optical saturation observed in both cases. Looking at b) the shape of the saturation trend for both devices is closely matched, suggesting that the mechanism for saturation is the same for both devices.

When looking at the peak THz emission characteristics as a function of applied electrical bias for the device at both wavelengths, it can be seen that the behaviour is similar for both (see figure 5.13). The devices exhibit a linear increase in peak-to-peak THz field strength at both wavelengths for increasing bias strengths. This shows that electrical saturation is not seen for both systems up to 30 kV/cm applied bias field. Again, it is important to note that the 30 kV/cm field was chosen as the maximum value applied so as not to damage the device. From the investigations in 4.3, it is believed that this value could be increased to 70 kV/cm applied field. It is also clear that the maximum peak-to-peak THz field strength obtainable is much higher using the device at 800 nm than at 1030 nm, with 26 kV/cm and 12 kV/cm achieved, respectively. Again, the difference in emitted field strengths is attributed to the lower optical fluences and significantly lower absorption at the longer wavelength.

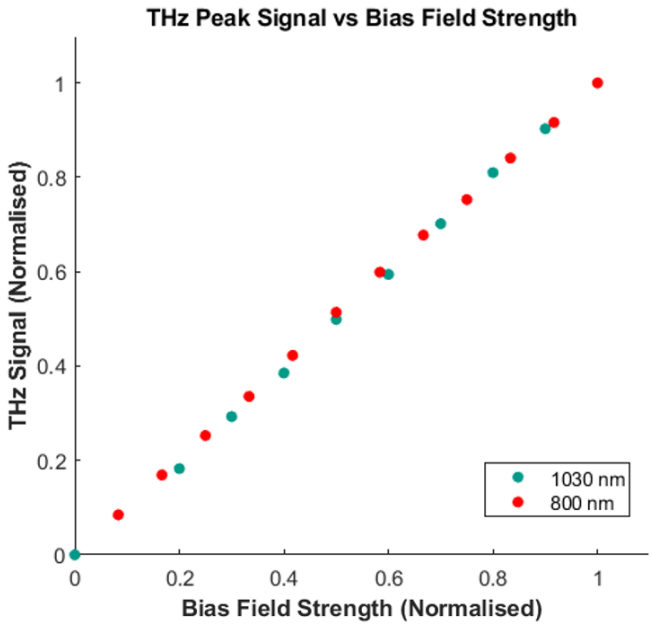

Figure 5.13: A comparison of the peak emitted THz signal as a function of the applied bias for the 5 μm gap array at the two different wavelengths with both operated with pump powers in the saturation regime. Both bias and peak emitted signal values have been normalised to compare clearly.

Comparing the bandwidths of the device at the two different wavelengths (see figure 5.14 (a)), it can be seen that they do not emit the same bandwidth. At 1030 nm, the bandwidth is limited to 3 THz with most of the energy concentrated below 1 THz. In contrast, at 800 nm, the device exhibits a bandwidth extending up to 6 THz with the energy more evenly spread between 1 and 3 THz before a gentler roll-off to 6 THz. It is essential to look at the detection method to compare the results. The measurements for both systems were obtained using EOS with a 200 μm ZnTe crystal to obtain results at 1030 nm, and a 150 μm GaP was used at 800 nm.

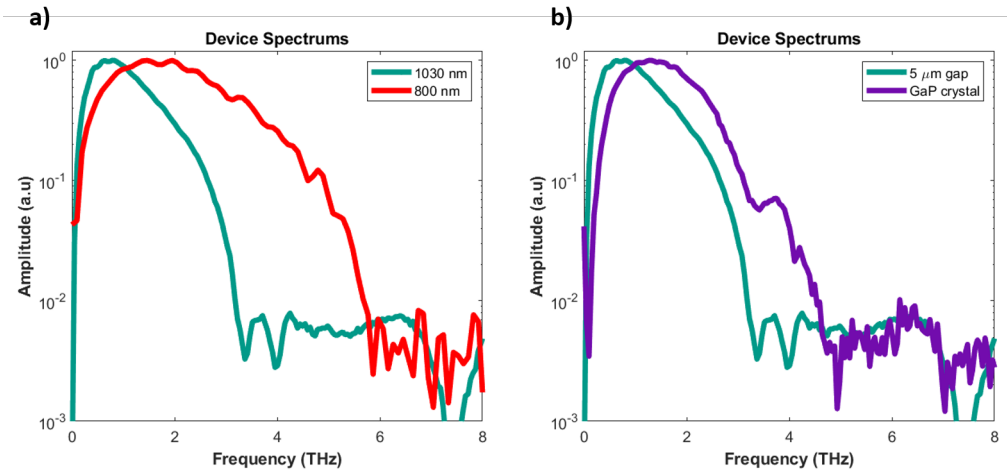

Figure 5.14: a) The FFT comparison shows the spectrum that the small 5 μm gap device emits when excited at 800 nm and 1030 nm wavelengths. b) The spectrum for the 5 μm gap array excited at 1030 nm compared to the spectrum emitted from a GaP crystal used for THz generation at 1030 nm using the same set-up. A 200 μm ZnTe crystal was used for EOS detection to obtain results at 1030 nm, and a 150 μm GaP was used at 800 nm. In both plots, the amplitude of both has been normalised for clear comparison.

As discussed in 1.8.5, the values contributing to the emitted bandwidth are carrier lifetimes and the pulse width of the exciting pulse. The material carrier lifetime will be the same for both, as the same device is used at both wavelengths. The pulse widths of the laser system are 40 fs and 30 fs at 800 nm and 1030nm respectively; again, these are very similar, so it would not explain the vast difference in bandwidths. Considering the detection bandwidth of the two different crystals used for EOS, The 150 μm thick GaP crystal used for detection on the 800 nm set-up does have a better detection bandwidth. However, it can be from the graph in figure 5.14 b) that the 200 μm ZnTe crystal is not limiting the bandwidth of the 5 μm gap device at 1030nm as the bandwidth produced by EO rectification from 1mm Thick GaP crystal exceeds that of the 5 μm gap device. Therefore, the reason for such a drastic difference must be the nature of the absorption of the exciting pulse. At 800 nm, the photon energy is closely matched to the bandgap of LT-GaAs, allowing for the direct promotion of an electron from the valence band into the conduction band; hence, the emission is determined by the pulse width of the excitation pulse. In the case of the 1030 nm wavelength system, the absorbed pulse promotes an electron from the valence band to the shallow defect states. The electron must reach the conduction band through scattering or hopping before being accelerated by the applied field and contributing to THz emission. It can be thought of now that the limiting factor is the time needed to reach the conduction band from the defect state and is no longer dependent on the pulse width of the excitation pulse. This

time is longer than the pulse duration, resulting in a reduced bandwidth.

5.3 Conclusion

This chapter presents investigations into the operation of PCA arrays at a longer wavelength of 1030 nm. These investigations form the basis of the work reported in [6]. A study into device heating was conducted using a FE modelling program, COMSOL Multiphysics. The heating effects due to optical pumping were simulated, and the thermal characteristics of the device were analysed. The thermal effects caused by laser heating in the device were simulated for powers obtainable from the 1030 nm and 800 nm laser systems. It was found that devices optically excited using the 1030 nm laser system were subjected to larger temperature changes, with the largest optical power obtainable from the system resulting in a 100 K temperature rise. The effects of device heating, when operated using the 800 nm system, were found to be much lower, with temperatures induced by the highest simulated laser power being only 11 K higher than at the start.

The absorption data was presented for the LT-GaAs device optically excited at 1030 nm. This showed below-bandgap absorption of the optical pump, resulting in an absorption coefficient of 3900 cm^{-1}. In the 2 μm thick LT-GaAs device, it was calculated that 54 % of the optical pump is absorbed.

A comparison was shown between a 5 μm gap array and a 130 μm gap array characterised at 1030 nm. It was seen that both devices displayed a linear increase in output THz signal with increasing electrical bias; this confirmed that no electrical saturation was present up to a bias field of 30 kV/cm for both. It was also shown that the emitted spectrum of both devices was very similar, with the bandwidth extending up to 3 THz and a slightly improved spectral weighting above 1 THz for the 5 μm gap array.

Finally, the emission characteristics of the 5 μm gap array device optically excited at 800 nm and 1030 nm were compared. At both wavelengths, the device displayed a linear increase with increasing electrical bias strengths. The device pumped at 1030 nm can be seen to optically saturate at a much larger fluence than when pumped at 800 nm; this was attributed to the lower absorption coefficient at the longer wavelength. The device pumped at 800 nm had a much larger bandwidth than when it was pumped at 1030 nm, which was explained by a difference in the absorption mechanism for the device when pumped at the two wavelengths. The Urbach tail absorption of carriers in the LT-GaAs, when pumped at 1030 nm, causes an increase in the transient photocurrent time and, thus, a reduction in the bandwidth.

Chapter 6

Conclusions And Further Work

6.1 Conclusions

In chapter 2, the improvements to the ELO fabrication process were presented. It was found that a ratio change of the constituent chemicals can be used to improve the sidewalls of the LT-GaAs bars of the device. By using a weaker etch (1000:8:1 of H_2O:H_2O_2:H_2So_4), the bars produced had better sidewalls with fewer defects; this method provided reproducible results.

A new method of protecting devices during the removal of the SI-GaAs carrier substrate was developed and demonstrated. A protective barrier was created using a negative photoresist and through-sapphire exposure that ensured the underlying LT-GaAs layer was not etched. This development allowed the yield of devices to be vastly improved over that seen in the initial method.

The ability to produce smaller electrode structures was shown through the use of a new electrode patterning and deposition method. Switching to a lift-off technique made it possible to create electrodes with widths smaller than 50 μm. This was an important step in enabling the design and realisation of smaller gap width devices, with electrode widths as small as 5 μm demonstrated.

A complete restructuring of devices post ELO and alternate etch chemistry was developed to create devices with gap widths smaller than 50 μm. By fabricating the electrode structures first and etching the LT-GaAs afterwards, it was possible to define smaller gaps whilst conserving higher packing factors. The improvements to the fabrication process and the development of the fabrication method for small gap devices have allowed for a greater versatility of device design. As well, all of the improvements have introduced more robustness into the process and improved the reproducibility of designs.

Chapter 3 discussed the techniques used for testing PCA antennas. The different optical set-ups used throughout this thesis were presented: a collimated generation and focus-through generation scheme. The instrument set-up was shown, which gave an overview of how the electrical equipment was interfaced and used to perform measurements of devices. A discussion of the different techniques employed for characterising PCA devices was presented. The theory of the characterisation methods was detailed, and how they can be used to determine a device's optical and bias performance. Finally, the experimental repeatability was evaluated; this included a discussion of the different factors that can introduce variation in the results of a device. One area where variation can arise is due to the laser system, which has both day-to-day and pulse-to-pulse power variations. The other factor that can introduce variations is device-to-device variation, resulting from the fabrication process.

In chapter 4, a systematic investigation was undertaken to determine the effects of differing device geometry, both gap sizes and electrode designs, had on the emitted THz emission. Changing the shape of electrodes from rectangular to triangular was investigated to increase the amount of current that could be supported in the device before electrical failure. Different triangular pitches were designed, tested, and compared with a rectangular electrode structure. It was found that although there were some slight improvements to the THz emission at higher optical powers, no significant improvements were seen in the ability to apply higher bias between the different electrode geometries. The maximum applied bias was also demonstrated, showing that both the triangular electrode design and rectangular design reached field strengths >60 kV/cm. This high-bias operation again showed no real enhancement between the two devices, and hence, the use of a conventional rectangular electrode design was continued.

The effects of asymmetrical electrode widths on THz emission were investigated. Both how anode width affects the generation and how important this effect is compared to the maximised packing factor were examined. This investigation involved changing the anode width for a fixed cathode width to enhance a plasmonic effect at the anode-semiconductor interface. It was seen that larger anode widths enhanced the generation significantly and that wider cathode widths did not contribute to any enhancement. However, an increased packing factor provided a better enhancement to the generation of THz signal compared to an enhancement from the anode widths at the cost of the device's packing factor.

For devices to be capable of supporting higher applied biasing field strengths, devices of different gap sizes were designed. It was clear that the smaller the gap size, the higher the applied biasing field could be applied before device failure. It was seen that the smallest (50 μm gap) device was able to support twice the amount that the largest (200 μm gap) device was able to, 30 kV/cm and 60 kV/cm, respectively.

A large area PCA device was fabricated using the knowledge obtained from the device geometry investigations. The device was designed with 50 μm gaps and an asymmetrical electrode design. Generation of high strength THz fields was demonstrated, with a maximum of 196 kV/cm achieved. This device showed an improvement over the previous record field obtained by an LT-GaAs device on a sapphire substrate reported in [91].

Lastly, the operation of a small 5 μm gap array was presented. The small gap device was fabricated to investigate whether further improvements could be obtained at even smaller gap sizes. A large improvement to the bandwidth of the emitted THz radiation was seen, with bandwidths extending beyond 5 THz.

One of the conclusions from this chapter of work is that a common theme of smaller gap sizes was generally seen to be more efficient; however, for high strength THz fields, the gap size can not be taken too small due to saturation mechanisms more prevalent at those gap sizes. Another important conclusion drawn was that the quality of the device fabrication played a crucial role in the device's performance and that it is important to ensure good device quality to support higher biasing fields and larger excitation powers.

Chapter 5 presented investigations of LT-GaAs PCA excited at 1030 nm wavelengths. Simulations of heating in the device were conducted to determine whether laser-induced heating would be detrimental to device operation. It was seen that the heating induced in the device excited at 1030 nm was higher than it would be when excited at 800 nm; the maximum operating temperature was found to be 100 K higher than the starting temperature at $\sim$ 5 W of optical power on the device.

Clear differences were observed when the device operation at 1030 nm wavelength was compared with the operation at 800 nm. At 1030 nm, the maximum emitted THz field strength was 12 kV/cm, which was half of the maximum observed at 800 nm, attributed to the lower absorption of the excitation pulse. Another significant difference is the bandwidth of the emitted pulses. A much smaller bandwidth is seen at 1030 nm compared to 800 nm; this was explained by the difference in absorption mechanisms in the material at the different wavelengths, causing a longer delay before the absorbed electrons can contribute to the current.

6.2 Further Work

The PCA devices fabricated in this thesis have given a better understanding of the effects of device geometry on the emission capabilities of a device. However, work is still required to investigate the effects further to improve the emission of THz radiation from PCA devices. Repeating the asymmetrical electrode width testing work on devices with even smaller gaps ($<$50 μm) would allow

the effects of the plasmonic enhancement to be studied further. It is thought that the dependence on the electrode widths will be greater at smaller gap sizes, which would also allow for an improvement of the packing factor for the smaller devices. Repeating the fabrication of the large area device, seen in section 4.4, to improve upon the fabrication of the larger area device, aiming to increase the maximum emitted field strength even further than the device reported. An investigation into fabricating the device using the method outlined in section 2.5.5 would allow an improvement of the packing factor as the longer sloped sidewalls would be removed.

These devices have shown the potential to be used as a source of THz radiation at this longer wavelength. Although the generation is not as efficient when compared to operation at 800 nm, there is much promise. Further work to increase the percentage of absorption in the material would allow for better utilisation of the energy available. Investigations into the annealing temperature of the LT-GaAs material would allow for an optimisation of the material structure to achieve higher absorption percentages. Plasmonic structures like that described in 1.8.10.3 could also enhance absorption at the 1030 nm wavelength. Increasing the amount of the optical power absorbed would allow for larger area devices to be used as the material would be saturated at lower optical fluences, which would allow for higher fields to be generated.

Chapter 7

References

[1] Sectra-Physics, "Spitfire ® ace™ user manual," 2011.

[2] J. R. Freeman, H. E. Beere, and D. A. Ritchie, *Generation and Detection of Terahertz Radiation*, pp. 1–28. Springer, Berlin, Heidelberg, 2012.

[3] C. Bull, S. M. Hewett, R. Ji, C.-H. Lin, T. Thomson, D. M. Graham, and P. W. Nutter, "Spintronic terahertz emitters: Status and prospects from a materials perspective," *APL Materials*, vol. 9, p. 090701, 9 2021.

[4] D. R. Bacon, A. D. Burnett, M. Swithenbank, C. Russell, L. Li, C. D. Wood, J. Cunningham, E. H. Linfield, A. G. Davies, P. Dean, and J. R. Freeman, "Free-space terahertz radiation from a lt-gaas-on-quartz large-area photoconductive emitter," *Optics Express*, vol. 24, p. 26986, 11 2016.

[5] N. Nilforoushan, T. Apretna, C. Song, T. Boulier, J. Tignon, S. Dhillon, M. Hanna, and J. Mangeney, "Ultra-broadband thz pulses with electric field amplitude exceeding 100 kv/cm at a 200 khz repetition rate," *Optics Express*, vol. 30, pp. 15556–15565, 2022.

[6] N. Nilforoushan, C. Kidd, A. Fournier, J. Palomo, J. Tignon, S. Dhillon, E. Lhuillier, L. Li, A. G. Davies, E. Linfield, L. Freeman, and J. Mangeney, "Efficient thz generation from low-temperature-grown gaas photoconductive antennas driven by yb-doped fiber amplifier at 200 khz repetition rate," *Applied Physics Letters [Accepted]*, 2023.

[7] R. A. Lewis, "A review of terahertz detectors," *Journal of Physics D: Applied Physics*, vol. 52, p. 433001, 2019.

[8] Y. S. Lee, "Principles of terahertz science and technology," *Principles of Terahertz Science and Technology*, pp. 1–340, 2009.

[9] E. Strepitov, E. Liakhov, N. Balbekin, M. Khodzitsky, O. Smolyanskaya, A. Trulyov, and M. Serebryakova, "Investigation of the optical properties of normal fibroblasts and fibroblasts cultured with cancer cells in terahertz

frequency range," *Medical Laser Applications and Laser-Tissue Interactions VII*, vol. 9542, 2015.

[10] M. Ney and I. A. II, "Modeling of reflectometric and ellipsometric spectra from the skin in the terahertz and submillimeter waves region," *Journal of Biomedical Optics*, vol. 16, 2011.

[11] M. Ney and I. Abdulhalim, "Does human skin truly behave as an array of helical antennae in the millimeter and terahertz wave ranges?," *Optics Letters, Vol. 35, Issue 19, pp. 3180-3182*, vol. 35, pp. 3180–3182, 10 2010.

[12] B. Yang, R. S. Donnan, M. Zhou, and A. A. Kingravi, "Reassessment of the electromagnetic reflection response of human skin at w-band," *Optics Letters, Vol. 36, Issue 21, pp. 4203-4205*, vol. 36, pp. 4203–4205, 11 2011.

[13] Z. D. Taylor, R. S. Singh, D. B. Bennett, P. Tewari, C. P. Kealey, N. Bajwa, M. O. Culjat, A. Stojadinovic, H. Lee, J. P. Hubschman, E. R. Brown, and W. S. Grundfest, "Thz medical imaging: In vivo hydration sensing," *IEEE Transactions on Terahertz Science and Technology*, vol. 1, pp. 201–219, 9 2011.

[14] T.-F. Tseng, S.-C. Yang, Y.-T. Shih, Y.-F. Tsai, T.-D. Wang, C.-K. Sun, O. P. Cherkasova, M. M. Nazarov, I. N. Smirnova, A. A. Angeluts, A. P. Shkurinov, H. Kim, Y. Park, J. h Son, S. J. Oh, J. s Suh, m Chiu, H. w Chen, Y. r Huang, Y. j Hwang, W. J. Lee, H. y Huang, C. k Sun, H. Chen, W. j Lee, C. m Chiu, Y. f Tsai, T. f Tseng, J. t Lu, W. l Lai, T. h Chen, C. c Kuo, S. c Fu, Y. y Huang, E. Y. Chuang, Y. J. Hwang, C. K. Sun, X. Wang, A. T. Ahuja, Y. t Zhang, E. Pickwell-Macpherson, E. Jung, H. j Choi, M. Lim, H. Kang, H. Park, H. Han, B. h Min, S. Kim, I. Park, H. Lim, P. C. Ashworth, E. Pickwell-MacPherson, E. Provenzano, S. E. Pinder, A. D. Purushotham, M. Pepper, and V. P. Wallace, "Near-field sub-thz transmission-type image system for vessel imaging in-vivo," *Optics Express, Vol. 23, Issue 19, pp. 25058-25071*, vol. 23, pp. 25058–25071, 9 2015.

[15] S. M. Kim, F. Hatami, J. S. Harris, A. W. Kurian, J. Ford, D. King, G. Scalari, M. Giovannini, N. Hoyler, J. Faist, and G. Harris, "Biomedical terahertz imaging with a quantum cascade laser," *Applied Physics Letters*, vol. 88, 4 2006.

[16] X. Yang, D. Wei, S. Yan, Y. Liu, S. Yu, M. Zhang, Z. Yang, X. Zhu, Q. Huang, H. L. Cui, and W. Fu, "Rapid and label-free detection and assessment of bacteria by terahertz time-domain spectroscopy," *Journal of Biophotonics*, vol. 9, pp. 1050–1058, 10 2016.

[17] N. Rothbart, O. Holz, R. Koczulla, K. Schmalz, and H. W. Hübers, "Analysis of human breath by millimeter-wave/terahertz spectroscopy," *Sensors 2019, Vol. 19, Page 2719*, vol. 19, p. 2719, 6 2019.

[18] V. Vaks, "High-precise spectrometry of the terahertz frequency range: The methods, approaches and applications," *Journal of Infrared, Millimeter, and Terahertz Waves*, vol. 33, pp. 43–53, 1 2012.

[19] P. Salén, M. Basini, S. Bonetti, J. Hebling, M. Krasilnikov, A. Y. Nikitin, G. Shamuilov, Z. Tibai, V. Zhaunerchyk, and V. Goryashko, "Matter manipulation with extreme terahertz light: Progress in the enabling thz technology," 12 2019.

[20] D. F. Swearer, S. Gottheim, J. G. Simmons, D. J. Phillips, M. J. Kale, M. J. McClain, P. Christopher, N. J. Halas, and H. O. Everitt, "Monitoring chemical reactions with terahertz rotational spectroscopy," *ACS Photonics*, vol. 5, pp. 3097–3106, 8 2018.

[21] H. Y. Hwang, S. Fleischer, N. C. Brandt, B. G. Perkins, M. Liu, K. Fan, A. Sternbach, X. Zhang, R. D. Averitt, and K. A. Nelson, "A review of non-linear terahertz spectroscopy with ultrashort tabletop-laser pulses," *Journal of Modern Optics*, vol. 62, pp. 1447–1479, 10 2015. doi: 10.1080/09500340.2014.918200.

[22] R. Ulbricht, E. Hendry, J. Shan, T. F. Heinz, and M. Bonn, "Carrier dynamics in semiconductors studied with time-resolved terahertz spectroscopy," *Reviews of Modern Physics*, vol. 83, pp. 543–586, 6 2011.

[23] S. Ašmontas, S. Bumelienė, J. Gradauskas, R. Raguotis, and A. Sužiedėlis, "Impact ionization and intervalley electron scattering in insb and inas induced by a single terahertz pulse," *Scientific Reports 2020 10:1*, vol. 10, pp. 1–7, 6 2020.

[24] I. C. Ho and X. C. Zhang, "Driving intervalley scattering and impact ionization in inas with intense terahertz pulses," *Applied Physics Letters*, vol. 98, p. 241908, 6 2011.

[25] F. H. Su, F. Blanchard, G. Sharma, L. Razzari, A. Ayesheshim, T. L. Cocker, L. V. Titova, T. Ozaki, J. c Kieffer, R. Morandotti, M. Reid, F. A. Hegmann, B. Nordstrom, K. Johnsen, S. J. Allen, A. p Jauho, B. Birnir, J. Kono, T. Noda, H. Akiyama, c Bandulet, H. F. Tiedje, H. K. Haugen, Y. Shen, G. L. Carr, J. B. Murphy, T. Y. Tsang, X. Wang, X. Yang, S. control, J. R. Danielson, Y. s Lee, J. P. Prineas, J. T. Steiner, M. Kira, and S. W. Koch, "Terahertz pulse induced intervalley scattering in photoexcited gaas," *Optics Express, Vol. 17, Issue 12, pp. 9620-9629*, vol. 17, pp. 9620–9629, 6 2009.

[26] T. Dekorsy, P. Leisching, C. Waschke, K. Kohler, K. Leo, H. G. Roskos, and H. Kurz, "Terahertz bloch oscillations in semiconductor superlattices," *Semiconductor Science and Technology*, vol. 9, p. 1959, 11 1994.

[27] O. Schubert, M. Hohenleutner, F. Langer, B. Urbanek, C. Lange, U. Huttner, D. Golde, T. Meier, M. Kira, S. W. Koch, and R. Huber, "Sub-cycle

control of terahertz high-harmonic generation by dynamical bloch oscillations," *Nature Photonics 2014 8:2*, vol. 8, pp. 119–123, 1 2014.

[28] S. D. Ganichev, W. Prettl, and P. G. Huggard, "Phonon assisted tunnel ionization of deep impurities in the electric field of far-infrared radiation," *Physical Review Letters*, vol. 71, p. 3882, 12 1993.

[29] S. D. Ganichev, I. N. Yassievich, W. Prettl, J. Diener, B. K. Meyer, and K. W. Benz, "Tunneling ionization of autolocalized dx centers in terahertz fields," *Physical Review Letters*, vol. 75, p. 1590, 8 1995.

[30] W. Kuehn, P. Gaal, K. Reimann, M. Woerner, T. Elsaesser, and R. Hey, "Terahertz-induced interband tunneling of electrons in gaas," *Phys. Rev. B*, vol. 82, 2010.

[31] Y. Sanari, T. Tachizaki, Y. Saito, K. Makino, P. Fons, A. V. Kolobov, J. Tominaga, K. Tanaka, Y. Kanemitsu, M. Hase, and H. Hirori, "Zener tunneling breakdown in phase-change materials revealed by intense terahertz pulses," *Physical Review Letters*, vol. 121, p. 165702, 10 2018.

[32] "Ieee xplore full-text pdf:."

[33] H. A. Hafez, X. Chai, A. Ibrahim, S. Mondal, D. Férachou, X. Ropagnol, and T. Ozaki, "Intense terahertz radiation and their applications," 2016.

[34] S. Li and R. R. Jones, "Ionization of excited atoms by intense single-cycle thz pulses," 2014.

[35] J. T. Steiner, M. Kira, and S. W. Koch, "Optical nonlinearities and rabi flopping of an exciton population in a semiconductor interacting with strong terahertz fields," *Phys. Rev. B*, vol. 77, 2008.

[36] B. E. Cole, J. B. Williams, B. T. King, M. S. Sherwin, and C. R. Stanley, "Coherent manipulation of semiconductor quantum bits with terahertz radiation," *Nature 2001 410:6824*, vol. 410, pp. 60–63, 3 2001.

[37] M. Rini, R. Tobey, N. Dean, J. Itatani, Y. Tomioka, Y. Tokura, R. W. Schoenlein, and A. Cavalleri, "Control of the electronic phase of a manganite by mode-selective vibrational excitation," *Nature 2007 449:7158*, vol. 449, pp. 72–74, 9 2007.

[38] X. Li, T. Qiu, J. Zhang, E. Baldini, J. Lu, A. M. Rappe, and K. A. Nelson, "Terahertz field–induced ferroelectricity in quantum paraelectric srtio3," *Science*, vol. 364, pp. 1079–1082, 6 2019.

[39] M. Nakajima, T. Kurihara, T. Shimizu, Y. Koike, and G. Isoyama, "Manipulation of ferromagnetic domain by the terahertz free electron laser excitation," *International Conference on Infrared, Millimeter, and Terahertz Waves, IRMMW-THz*, vol. 2020-November, pp. 496–497, 11 2020.

[40] O. Vänskä, I. Tittonen, S. W. Koch, and M. Kira, "Coherent terahertz control of vertical transport in semiconductor heterostructures," *Physical Review Letters*, vol. 114, p. 116802, 3 2015.

[41] S. Sato and A. Rubio, "Nonlinear electric conductivity and thz-induced charge transport in graphene," 2021.

[42] J. Hebling, K.-L. Yeh, M. C. Hoffmann, B. Bartal, and K. A. Nelson, "Generation of high-power terahertz pulses by tilted-pulse-front excitation and their application possibilities," *Journal of the Optical Society of America B*, vol. 25, p. B6, 7 2008.

[43] D. Strickland and G. Mourou, "Compression of amplified chirped optical pulses," *Optics Communications*, vol. 56, pp. 219–221, 12 1985.

[44] P. B. Bisht, *An Introduction to Photonics and Laser Physics with Applications*. IOP Publishing, 2022.

[45] S. O. Kasap, *Electrical and Thermal Conduction in Solids*. 2006.

[46] O. Svelto, *Principles of lasers*. Springer US, 2010.

[47] S. Wieneke and C. Gerhard, *Laser basics*. IOP Publishing, 9 2018.

[48] W. T. Silfvast, *Lasers*. Elsevier, 2003.

[49] T. H. Maiman, "Stimulated optical radiation in ruby," *Nature 1960 187:4736*, vol. 187, pp. 493–494, 1960.

[50] H. Abramczyk, "Lasers," *Introduction to Laser Spectroscopy*, pp. 59–106, 2005.

[51] J. Hecht, "A short history of laser development," *Applied Optics, Vol. 49, Issue 25, pp. F99-F122*, vol. 49, pp. F99–F122, 9 2010.

[52] O. G. Peterson, S. A. Tuccio, and B. B. Snavely, "Cw operation of an organic dye solution laser," *Applied Physics Letters*, vol. 17, p. 245, 10 2003.

[53] B. B. Snavely, O. G. Peterson, and R. F. Reithel, "Blue laser emission from a flashlamp-excited organic dye solution," *Appl. Phys. Lett*, vol. 11, p. 275, 1967.

[54] S. C. Singh, H. Zeng, C. Guo, and W. Cai, "Lasers: Fundamentals, types, and operations," 2012.

[55] D. J. Harter, M. A. Pessot, J. A. Squier, J. A. Nees, P. Bado, and G. A. Mourou, "Short pulse amplification in tunable solid state materials," *https://doi.org/10.1117/12.18653*, vol. 1229, pp. 19–28, 5 1990.

[56] K. F. Wall and A. Sanchez, "Titanium sapphire lasers," *Lincoln Laboratory Journal; (USA)*, vol. 3, 1 1990.

[57] A. E. A. E. Siegman, *Lasers*. University Science Books, 1986. Includes index.

[58] Q. Li, X. Liu, R. Zhou, M. S. A. Gandhi, and H. Y. Fu, "Recent advances and perspectives on pulsed fiber lasers," *Optical Fiber Technology and Applications*, 8 2021.

[59] P. W. Smith, M. A. Duguay, and E. P. Ippen, "Mode-locking of lasers," *Progress in Quantum Electronics*, vol. 3, pp. 107–229, 1 1974.

[60] F. Krausz, M. E. Fermann, T. Brabec, P. F. Curley, M. Hofer, M. H. Ober, C. Spielmann, E. Wintner, and A. J. Schmidt, "Femtosecond solid-state lasers," *IEEE Journal of Quantum Electronics*, vol. 28, pp. 2097–2122, 1992.

[61] A. Weiner, "Ultrafast optics," 2008.

[62] "Femtosecond laser pulses," 2005.

[63] A. K. Hamze, M. Reynaud, J. Geler-Kremer, and A. A. Demkov, "Design rules for strong electro-optic materials," *npj Computational Materials*, vol. 6, p. 130, 2020.

[64] A. Dunn, "Developing terahertz sources for characterising gan semiconductor structures," pp. 70–74, 2018.

[65] W. Sun, X. Wang, Y. Zhang, W. Sun, X. Wang, and Y. Zhang, "Terahertz generation from laser-induced plasma," *Opto-Electronic Science*, vol. 1, pp. 220003–1, 2022.

[66] B. Clough, J. Dai, and X. C. Zhang, "Laser air photonics: Beyond the terahertz gap," *Materials Today*, vol. 15, pp. 50–58, 1 2012.

[67] M. Kress, H. G. Roskos, T. Löffler, S. Eden, and M. Thomson, "Terahertz-pulse generation by photoionization of air with laser pulses composed of both fundamental and second-harmonic waves," *Optics Letters, Vol. 29, Issue 10, pp. 1120-1122*, vol. 29, pp. 1120–1122, 5 2004.

[68] X. Xie, J. Dai, and X. C. Zhang, "Coherent control of thz wave generation in ambient air," *Physical Review Letters*, vol. 96, p. 075005, 2 2006.

[69] A. D. Koulouklidis, C. Gollner, V. Shumakova, V. Y. Fedorov, A. Pugžlys, A. Baltuška, and S. Tzortzakis, "Observation of extremely efficient terahertz generation from mid-infrared two-color laser filaments," *Nature Communications 2020 11:1*, vol. 11, pp. 1–8, 1 2020.

[70] E. Matsubara, M. Nagai, and M. Ashida, "Ultrabroadband coherent electric field from far infrared to 200 thz using air plasma induced by 10 fs pulses," *Applied Physics Letters*, vol. 101, p. 011105, 7 2012.

[71] H. P. Freund and T. M. Antonsen, "Principles of free electron lasers," *Principles of Free Electron Lasers*, pp. 1–716, 4 2018.

[72] J. F. Ready, *Industrial applications of lasers*. Academic Press, 1997.

[73] E. A. Seddon, J. A. Clarke, D. J. Dunning, C. Masciovecchio, C. J. Milne, F. Parmigiani, D. Rugg, J. C. H. Spence, N. R. Thompson, K. Ueda, S. M. Vinko, J. S. Wark, and W. Wurth, "Short-wavelength free-electron laser sources and science: a review*," *Reports on Progress in Physics*, vol. 80, p. 115901, 10 2017.

[74] D. Saeedkia, *Optoelectronic techniques for the generation and detection of terahertz waves*, pp. 3–27. Elsevier Inc., 1 2013.

[75] Y. Zhang, K. Li, and H. Zhao, "Intense terahertz radiation: generation and application," *Frontiers of Optoelectronics*, vol. 14, pp. 4–36, 2021.

[76] J. A. Fülöp, G. Polónyi, B. Monoszlai, G. Andriukaitis, T. Balciunas, A. Pugzlys, G. Arthur, A. Baltuska, and J. Hebling, "Highly efficient scalable monolithic semiconductor terahertz pulse source," *Optica*, vol. 3, pp. 1075–1078, 10 2016.

[77] M. Shalaby and C. P. Hauri, "Demonstration of a low-frequency three-dimensional terahertz bullet with extreme brightness," *Nature Communications*, vol. 6, p. 5976, 2015.

[78] A. Singh, A. Pashkin, S. Winnerl, M. Welsch, C. Beckh, P. Sulzer, A. Leitenstorfer, M. Helm, and H. Schneider, "Up to 70 thz bandwidth from an implanted ge photoconductive antenna excited by a femtosecond er:fibre laser," *Official journal of the CIOMP*, vol. 9, pp. 2047–7538, 2020.

[79] A. G. Stepanov, J. Hebling, and J. Kuhl, "Efficient generation of subpicosecond terahertz radiation by phase-matched optical rectification using ultrashort laser pulses with tilted pulse fronts," *Applied Physics Letters*, vol. 83, pp. 3000–3002, 10 2003.

[80] H. Hirori, A. Doi, F. Blanchard, and K. Tanaka, "Erratum: "single-cycle terahertz pulses with amplitudes exceeding 1 mv/cm generated by optical rectification in linbo3" [appl. phys. lett. 98, 091106 (2011)]," *Applied Physics Letters*, vol. 103, p. 259901, 12 2013.

[81] X. Zhu, D. R. Bacon, J. Madéo, and K. M. Dani, "High field single- to few-cycle thz generation with lithium niobate," *Photonics*, vol. 8, 2021.

[82] W. Zhang, P. Maldonado, Z. Jin, T. S. Seifert, J. Arabski, G. Schmerber, E. Beaurepaire, M. Bonn, T. Kampfrath, P. M. Oppeneer, and D. Turchinovich, "Ultrafast terahertz magnetometry," *Nature Communications*, vol. 11, p. 4247, 2020.

[83] E. T. Papaioannou and R. Beigang, "Thz spintronic emitters: a review on achievements and future challenges," vol. 10, pp. 1243–1257, 2021.

[84] G. Torosyan, S. Keller, L. Scheuer, R. Beigang, and E. T. Papaioannou, "Optimized spintronic terahertz emitters based on epitaxial grown fe/pt layer structures," *Scientific Reports*, vol. 8, p. 1311, 2018.

[85] T. S. Seifert, N. M. Tran, O. Gueckstock, S. M. Rouzegar, L. Nadvornik, S. Jaiswal, G. Jakob, V. V. Temnov, M. Münzenberg, M. Wolf, M. Kläui, and T. Kampfrath, "Terahertz spectroscopy for all-optical spintronic characterization of the spin-hall-effect metals pt, w and cu80ir20," *Journal of Physics D: Applied Physics*, vol. 51, p. 364003, 2018.

[86] T. Seifert, S. Jaiswal, U. Martens, J. Hannegan, L. Braun, P. Maldonado, F. Freimuth, A. Kronenberg, J. Henrizi, I. Radu, E. Beaurepaire, Y. Mokrousov, P. M. Oppeneer, M. Jourdan, G. Jakob, D. Turchinovich, L. M. Hayden, M. Wolf, M. Münzenberg, M. Kläui, and T. Kampfrath, "Efficient metallic spintronic emitters of ultrabroadband terahertz radiation," *Nature Photonics*, vol. 10, pp. 483–488, 2016.

[87] Y. Wu, M. Elyasi, X. Qiu, M. Chen, Y. Liu, L. Ke, and H. Yang, "High-performance thz emitters based on ferromagnetic/nonmagnetic heterostructures," *Advanced Materials*, vol. 29, p. 1603031, 1 2017.

[88] D. M. Nenno, L. Scheuer, D. Sokoluk, S. Keller, G. Torosyan, A. Brodyanski, J. Lösch, M. Battiato, M. Rahm, R. H. Binder, H. C. Schneider, R. Beigang, and E. T. Papaioannou, "Modification of spintronic terahertz emitter performance through defect engineering," *Scientific Reports*, vol. 9, p. 13348, 2019.

[89] D. Yang, J. Liang, C. Zhou, L. Sun, R. Zheng, S. Luo, Y. Wu, and J. Qi, "Powerful and tunable thz emitters based on the fe/pt magnetic heterostructure," *Advanced Optical Materials*, vol. 4, pp. 1944–1949, 12 2016.

[90] R. Rouzegar, A. L. Chekhov, Y. Behovits, B. R. Serrano, M. A. Syskaki, C. H. Lambert, D. Engel, U. Martens, M. Münzenberg, M. Wolf, G. Jakob, M. Kläui, T. S. Seifert, and T. Kampfrath, "Broadband spintronic terahertz source with peak electric fields exceeding 1.5 mv/cm," *Physical Review Applied*, vol. 19, p. 34018, 3 2023.

[91] D. R. Bacon, T. B. Gill, M. Rosamond, A. D. Burnett, A. Dunn, L. Li, E. H. Linfield, A. G. Davies, P. Dean, and J. R. Freeman, "Photoconductive arrays on insulating substrates for high-field terahertz generation," *Optics Express*, vol. 28, p. 17219, 6 2020.

[92] N. M. Burford and M. O. El-Shenawee, "Review of terahertz photoconductive antenna technology," *Optical Engineering*, vol. 56, pp. 1–28, 1 2017.

[93] S. S. Dhillon, M. S. Vitiello, E. H. Linfield, A. G. Davies, M. C. Hoffmann, J. Booske, C. Paoloni, M. Gensch, P. Weightman, G. P. Williams, E. Castro-Camus, D. R. S. Cumming, F. Simoens, I. Escorcia-Carranza, J. Grant, S. Lucyszyn, M. Kuwata-Gonokami, K. Konishi, M. Koch, C. A. Schmuttenmaer, T. L. Cocker, R. Huber, A. G. Markelz, Z. D. Taylor, V. P. Wallace, J. A. Zeitler, J. Sibik, T. M. Korter, B. Ellison, S. Rea, P. Goldsmith, K. B. Cooper, R. Appleby, D. Pardo, P. G. Huggard, V. Krozer, H. Shams, M. Fice, C. Renaud, A. Seeds, A. Stöhr, M. Naftaly, N. Ridler, R. Clarke, J. E. Cunningham, and M. B. Johnston, "The 2017 terahertz science and technology roadmap," *Journal of Physics D: Applied Physics*, vol. 50, p. 043001, 1 2017.

[94] D. H. Auston, K. P. Cheung, and P. R. Smith, "Picosecond photoconducting hertzian dipoles," *Appl. Phys. Lett*, vol. 45, p. 284, 1984.

[95] P. R. Smith, D. H. Auston, and M. C. Nuss, "Subpicosecond photoconducting dipole antennas," *IEEE JOURNAL OF QUANTUM ELECTRONICS*, vol. 24, 1988.

[96] M. S. Kong, J. S. Kim, S. P. Han, N. Kim, K. Moon, K. H. Park, M. Y. Jeon, C. Li, G. Wang, T. Jiang, P. Li, A. Wang, Z. Zhang, P. Qin, Y. Song, H. Kim, J. Shin, D. Kwon, M. Hu, C. Wang, J. Kim, Z. Q. Luo, Y. Z. Huang, J. Z. Wang, H. H. Cheng, Z. P. Cai, and C. C. Ye, "Pulse shaping and evolution in normal-dispersion mode-locked fiber lasers," *IEEE J. Sel. Top. Quantum Electron*, vol. 19, pp. 28276–28283, 2011.

[97] I. Brener, D. Dykaar, A. Frommer, L. Pfeiffer, and K. West, "Terahertz emission from electric field singularities in biased semiconductors," *Optics Letters, Vol. 21, Issue 23, pp. 1924-1926*, vol. 21, pp. 1924–1926, 12 1996.

[98] M. Tani, S. Matsuura, K. Sakai, and M. Hangyo, "Multiple-frequency generation of sub-terahertz radiation by multimode ld excitation of photoconductive antenna," *IEEE MICROWAVE AND GUIDED WAVE LETTERS*, vol. 7, 1997.

[99] N. M. Froberg, B. B. Hu, X. C. Zhang, and D. H. Auston, "Terahertz radiation from a photoconducting antenna array," *IEEE Journal of Quantum Electronics*, vol. 28, pp. 2291–2301, 1992.

[100] J. T. Darrow, X. C. Zhang, D. H. Auston, and J. D. Morse, "Saturation properties of large-aperture photoconducting antennas," *IEEE Journal of Quantum Electronics*, vol. 28, pp. 1607–1616, 1992.

[101] R. H. BUBE, *9 - Electrical Properties*, pp. 171–213. Academic Press, 1992.

[102] M. Fox, *Optical Properties of Solids*. Oxford University Press, second edition ed., 3 2010.

[103] M. C. Beard, G. M. Turner, and C. A. Schmuttenmaer, "Subpicosecond carrier dynamics in low-temperature grown gaas as measured by time-resolved terahertz spectroscopy," *Journal of Applied Physics*, vol. 90, pp. 5915–5923, 12 2001.

[104] J. Mateos, S. Perez, D. Pardo, and T. Gonzalez, "Ultra fast gunn effect at thz frequencies in hemts," pp. 313–316, 2006.

[105] K. Ahi, "Review of gan-based devices for terahertz operation," *Optical Engineering*, vol. 56, p. 090901, 9 2017.

[106] R. Wang, L. Xie, S. Hameed, C. Wang, and Y. Ying, "Mechanisms and applications of carbon nanotubes in terahertz devices: A review," *Carbon*, vol. 132, pp. 42–58, 2018.

[107] P. Arifin, E. M. Goldys, and T. L. Tansley, "Electron mobility in low temperature grown gallium arsenide," *Materials Science and Engineering: B*, vol. 35, pp. 330–333, 1995.

[108] J. Qiu, Y. Li, and Y. Jia, "Characterization and simulation," *Persistent Phosphors*, pp. 93–125, 1 2021.

[109] L. Heijne, "Physical principles of photoconductivity," *Phillips Technical Review*, vol. 25, pp. 120–131, 1964.

[110] N. Vashistha, M. Kumar, R. K. Singh, D. Panda, L. Tyagi, and S. Chakrabarti, "A comprehensive study of ultrafast carrier dynamics of lt-gaas: Above and below bandgap regions," *Physica B: Condensed Matter*, vol. 602, p. 412441, 2021.

[111] V. Sa-Yakanit and H. Glyde, "Urbach tails and disorder," *Comments on Condensed Matter Physics*, vol. 13, pp. 35–48, 1987.

[112] B. Subedi, C. Li, C. Chen, D. Liu, M. M. Junda, Z. Song, Y. Yan, and N. J. Podraza, "Urbach energy and open-circuit voltage deficit for mixed anion–cation perovskite solar cells," *ACS Applied Materials Interfaces*, vol. 14, pp. 7796–7804, 2022. PMID: 35129320.

[113] S. U. Dankowski, D. Streb, M. Ruff, P. Kiesel, M. Kneissl, B. Knüpfer, G. H. Döhler, U. D. Keil, C. B. So/renson, and A. K. Verma, "Above band gap absorption spectra of the arsenic antisite defect in low temperature grown gaas and algaas," *Applied Physics Letters*, vol. 68, pp. 37–39, 1 1996.

[114] M. B. Panish and H. C. C. Jr., "Temperature dependence of the energy gap in gaas and gap," *Journal of Applied Physics*, vol. 40, pp. 163–167, 1 1969.

[115] Z. Piao, M. Tani, and K. Sakai, "Carrier dynamics and terahertz radiation in photoconductive antennas," *Japanese Journal of Applied Physics, Part 1: Regular Papers and Short Notes and Review Papers*, vol. 39, pp. 96–100, 1 2000.

[116] R. H. Jacobsen, P. U. Jepsen, and S. R. Keiding, "Generation and detection of terahertz pulses from biased semiconductor antennas," *JOSA B, Vol. 13, Issue 11, pp. 2424-2436*, vol. 13, pp. 2424–2436, 11 1996.

[117] E. Isgandarov, X. Ropagnol, M. Singh, and T. Ozaki, "Intense terahertz generation from photoconductive antennas," *Frontiers of Optoelectronics*, vol. 14, p. 64, 3 2021.

[118] D. R. Bacon, J. Madéo, and K. M. Dani, "Photoconductive emitters for pulsed terahertz generation," *Journal of Optics J. Opt*, vol. 23, p. 29, 2021.

[119] J. Prajapati, M. Bharadwaj, A. Chatterjee, and R. Bhattacharjee, "Magnetic field-assisted radiation enhancement from a large aperture photoconductive antenna," *IEEE Transactions on Microwave Theory and Techniques*, vol. 66, pp. 678–687, 2 2018.

[120] M. B. Johnston, D. M. Whittaker, A. Corchia, A. G. Davies, and E. H. Linfield, "Simulation of terahertz generation at semiconductor surfaces," *Physical Review B*, vol. 65, p. 165301, 3 2002.

[121] E. Castro-Camus, J. Lloyd-Hughes, and M. B. Johnston, "Three-dimensional carrier-dynamics simulation of terahertz emission from photoconductive switches," *Physical Review B*, vol. 71, p. 195301, 5 2005.

[122] Y. Huang, N. Khiabani, Y. Shen, and D. Li, "Terahertz photoconductive antenna efficiency," *Final Program and Book of Abstracts - iWAT 2011: 2011 IEEE International Workshop on Antenna Technology: Small Antennas, Novel Structures and Innovative Metamaterials*, pp. 152–156, 2011.

[123] E. Castro-Camus, J. Lloyd-Hughes, and M. B. Johnston, "Polarization-sensitive terahertz detection by multicontact photoconductive receivers," *Appl. Phys. Lett*, vol. 86, p. 254102, 2005.

[124] Y. Kamo, S. Kitazawa, S. Ohshima, and Y. Hosoda, "Highly efficient photoconductive antennas using optimum low-temperature-grown gaas layers and si substrates," *Japanese Journal of Applied Physics*, vol. 53, p. 032201, 2 2014.

[125] G. Rodriguez and A. J. Taylor, "Screening of the bias field in terahertz generation from photoconductors," *Optics Letters, Vol. 21, Issue 14, pp. 1046-1048*, vol. 21, pp. 1046–1048, 7 1996.

[126] A. Singh, S. Pal, and H. Surdi, "Highly efficient and electrically robust carbon irradiated semi-insulating gaas based photoconductive terahertz emitters," *Appl. Phys. Lett*, vol. 104, p. 63501, 2014.

[127] M. R. Melloch, N. Otsuka, K. Mahalingam, C. L. Chang, J. M. Woodall, G. D. Pettit, P. D. Kirchner, F. Cardone, A. C. Warren, and D. D. Nolte, "Arsenic cluster dynamics in doped gaas," *Journal of Applied Physics*, vol. 72, pp. 3509–3513, 10 1992.

[128] I. S. Gregory, C. Baker, W. R. Tribe, M. J. Evans, H. E. Beere, E. H. Linfield, A. G. Davies, and M. Missous, "High resistivity annealed low-temperature gaas with 100 fs lifetimes," *Applied Physics Letters*, vol. 83, pp. 4199–4201, 11 2003.

[129] N. Arora, "Prospective materials for photoconductive antennas for terahertz generation," *Journal of Innovation and Social Science Research*, vol. 9, 2022.

[130] G.-R. Lin and C.-L. Pan, "Picosecond responses of low-dosage arsenic-ion-implanted gaas photoconductors," *Applied Physics Letters*, vol. 71, pp. 2901–2903, 11 1997.

[131] G. Cao, L. Yang, and X. Yu, "Semiconductors for terahertz photonics applications you may also like applying deep learning method to data analysis of low voltage line carrier module," *Journal of Physics D: Applied Physics TOPICAL REVIEW Arnas Krotkus*, vol. 43, p. 273001, 2010.

[132] C. Baker, I. S. Gregory, W. R. Tribe, I. V. Bradley, M. J. Evans, E. H. Linfield, and M. Missous, "Highly resistive annealed low-temperature-grown ingaas with sub-500fs carrier lifetimes," *Applied Physics Letters*, vol. 85, p. 4965, 11 2004.

[133] F. E. Doany, D. Grischkowsky, and C.-C. Chi, "Carrier lifetime versus ion-implantation dose in silicon on sapphire," *Appl. Phys. Lett*, vol. 50, p. 460, 1987.

[134] K. Bertulis, A. Krotkus, and G. Aleksejenko, "Gabias: A material for optoelectronic terahertz devices," *Appl. Phys. Lett*, vol. 88, p. 201112, 2006.

[135] S. Kono, M. Tani, and K. Sakai, "Coherent detection of mid-infrared radiation up to 60 thz with an lt-gaas photoconductive antenna," *IEE Proceedings: Optoelectronics*, vol. 149, pp. 105–109, 6 2002.

[136] S. Matsuura, K. Sakai, M. Tani, and S. ichi Nakashima, "Emission characteristics of photoconductive antennas based on low-temperature-grown gaas and semi-insulating gaas," *Applied Optics, Vol. 36, Issue 30, pp. 7853-7859*, vol. 36, pp. 7853–7859, 10 1997.

[137] N. B. Alias and A. H. Awang, "Physical parametric analysis of terahertz photoconductive bow-tie dipole antenna on frequency and radiation pattern using electromagnetic simulation tools; physical parametric analysis of terahertz photoconductive bow-tie dipole antenna on frequency and radiation pattern using electromagnetic simulation tools," pp. 11–13, 2016.

[138] Y. Cai, I. Brener, and J. Lopata, "Design and performance of singular electric field terahertz photoconducting antennas," *Appl. Phys. Lett*, vol. 71, p. 2076, 1997.

[139] T. Furuya, K. Maeda, K. Yamamoto, T. Nakashima, T. Inoue, M. Hangyo, and M. Tani, "Broadband polarization properties of photoconductive spiral antenna; broadband polarization properties of photoconductive spiral antenna," *2009 34th International Conference on Infrared, Millimeter, and Terahertz Waves*, 2009.

[140] S. Park, K. Jin, J. Ye, and K. H. Jeong, "Nanoplasmonic photoconductive antenna for high power terahertz emission," *2011 16th International Solid-State Sensors, Actuators and Microsystems Conference, TRANSDUCERS'11*, pp. 2498–2501, 2011.

[141] C. W. Berry, N. Wang, M. R. Hashemi, M. Unlu, and M. Jarrahi, "Significant performance enhancement in photoconductive terahertz optoelectronics by incorporating plasmonic contact electrodes," *Nature Communications*, vol. 4, pp. 1–10, 3 2013.

[142] S.-H. Yang, G. S. Member, M. R. Hashemi, C. W. Berry, M. Jarrahi, and S. Member, "7.5photoconductive emitters with three-dimensional plasmonic contact electrodes," *IEEE Transactions on Terahertz Science and Technology*, vol. 4, p. 575, 2014.

[143] R. H. Jacobsen, K. Birkelund, T. Holst, P. U. Jepsen, and S. R. Keiding, "Interpretation of photocurrent correlation measurements used for ultrafast photoconductive switch characterization," *Journal of Applied Physics*, vol. 79, p. 2649, 6 1998.

[144] D. S. Kim and D. S. Citrin, "Coulomb and radiation screening in photoconductive terahertz sources," *Applied Physics Letters*, vol. 88, p. 161117, 4 2006.

[145] K. Fushinobu, A. Majumdar, and K. Hijikata, "Heat generation and transport in submicron semiconductor devices," *Journal of Heat Transfer*, vol. 117, pp. 25–31, 2 1995.

[146] V. M. Dwyer, A. J. Franklin, and D. S. Campbell, "Thermal failure in semiconductor devices," *Solid-State Electronics*, vol. 33, pp. 553–560, 5 1990.

[147] J. T. Darrow, X.-C. Zhang, and D. H. Auston, "Power scaling of large-aperture photoconducting antennas," *Appl. Phys. Lett*, vol. 58, p. 25, 1991.

[148] T. Hattori, K. Egawa, S. ichi Ookuma, and T. Itatani, "Intense terahertz pulses from large-aperture antenna with interdigitated electrodes," *Japanese Journal of Applied Physics*, vol. 45, p. L422, 2006.

[149] G. Matthäus, S. Nolte, R. Hohmuth, M. Voitsch, W. Richter, B. Pradarutti, S. Riehemann, G. Notni, and A. Tünnermann, "Microlens coupled interdigital photoconductive switch," *Applied Physics Letters*, vol. 93, p. 091110, 9 2008.

[150] A. Dreyhaupt, S. Winnerl, T. Dekorsy, and M. Helm, "High-intensity terahertz radiation from a microstructured large-area photoconductor," *Applied Physics Letters*, vol. 86, pp. 1–3, 3 2005.

[151] G. Matthäus, S. Nolte, R. Hohmuth, M. Voitsch, W. Richter, B. Pradarutti, S. Riehemann, G. Notni, and A. Tünnermann, "Large-area microlens emitters for powerful thz emission," *Applied Physics B: Lasers and Optics*, vol. 96, pp. 233–235, 8 2009.

[152] X. Ropagnol, R. Morandotti, T. Ozaki, and M. Reid, "Thz pulse shaping and improved optical-to-thz conversion efficiency using a binary phase mask," *OPTICS LETTERS*, vol. 36, 2011.

[153] A. Singh and S. S. Prabhu, "Microlensless interdigitated photoconductive terahertz emitters," *Optics Express*, vol. 23, pp. 1529–1535, 2015.

[154] N. T. Yardimci, S. Cakmakyapan, S. Hemmati, and M. Jarrahi, "A high-power broadband terahertz source enabled by three-dimensional light confinement in a plasmonic nanocavity," *Scientific Reports*, vol. 7, p. 4166, 2017.

[155] A. Singh, J. Li, A. Pashkin, R. Rana, S. Winnerl, M. Helm, and H. Schneider, "High-field thz pulses from a gaas photoconductive emitter for nonlinear thz studies," *Optics Express*, vol. 29, pp. 19920–19927, 2021.

[156] C. W. Berry, M. R. Hashemi, and M. Jarrahi, "Generation of high power pulsed terahertz radiation using a plasmonic photoconductive emitter array with logarithmic spiral antennas," *Applied Physics Letters*, vol. 104, p. 081122, 2 2014.

[157] P. Paufler, "P. n. butcher, d. cotter the elements of nonlinear optics. cambridge university press. cambridge 1990, xiv + 344p. preis £ 30.00, isbn 0-521-34183-3," *Crystal Research and Technology*, vol. 26, pp. 802–802, 1 1991.

[158] M. Hangyo, M. Tani, Y. Hirota, and R. Hattori, "Polarization modulation of terahertz electromagnetic radiation by four-contact photoconductive antenna," *Optics Express, Vol. 14, Issue 10, pp. 4486-4493*, vol. 14, pp. 4486–4493, 5 2006.

[159] C. D. Mosley, M. Failla, D. Prabhakaran, and J. Lloyd-Hughes, "Terahertz spectroscopy of anisotropic materials using beams with rotatable polarization," *Scientific reports*, vol. 7, 12 2017.

[160] C. D. Mosley, M. Staniforth, A. I. Serrano, E. Pickwell-Macpherson, and J. Lloyd-Hughes, "Scalable interdigitated photoconductive emitters for the electrical modulation of terahertz beams with arbitrary linear polarization," *AIP Advances*, vol. 9, p. 045323, 4 2019.

[161] B. Pradarutti, G. Matthäus, S. Riehemann, G. Notni, J. Limpert, S. Nolte, and A. Tünnermann, "Electro-optical sampling of ultrashort thz pulses by fs-laser pulses at 530 nm with batio3," *Journal of Applied Physics*, vol. 102, 2007.

[162] D. Bacon, "Time-resolved pump-probe investigation of the terahertz quantum cascade laser," pp. 35–36, 2017.

[163] S. G. Porter, "A brief guide to pyroelectric detectors," *Ferroelectrics*, vol. 33, pp. 193–206, 6 1981. doi: 10.1080/00150198108008086.

[164] T. B. Gill, "Non-linear terahertz spectroscopy of quantum materials," 2022.

[165] Y. Suzaki and A. Tachibana, "Measurement of the microm sized radius of gaussian laser beam using the scanning knife-edge.," *Applied optics*, vol. 14 12, pp. 2809–10, 1975.

[166] S. Verghese, K. A. Mcintosh, and E. R. Brown, "Optical and terahertz power limits in the low-temperature-grown gaas photomixers," *Appl. Phys. Lett*, vol. 71, p. 2743, 1997.

[167] H. Němec, A. Pashkin, and P. Kužel, "Carrier dynamics in low-temperature grown gaas studied by terahertz emission spectroscopy," *Journal of Applied Physics*, vol. 90, p. 1303, 2001.

[168] G. L. Witt, "Ltmbe gaas: present status and perspectives," *Materials Science and Engineering: B*, vol. 22, pp. 9–15, 1993.

[169] D. C. Look, D. C. Walters, G. D. Robinson, J. R. Sizelove, M. G. Mier, and C. E. Stutz, "Annealing dynamics of molecular-beam epitaxial gaas grown at 200°c," *Journal of Applied Physics*, vol. 74, pp. 306–310, 7 1993.

[170] M. R. Stone, M. Naftaly, N. N. Zinov'ev, and R. E. Miles, "Characteristics of large-aperture photoconductive terahertz antennas," pp. 125–128, 2002.

[171] M. O. Manasreh, D. C. Look, K. R. Evans, and C. E. Stutz, "Infrared absorption of deep defects in molecular-beam-epitaxial gaas layers grown at 200 °c: Observation of an el2-like defect," *Physical Review B*, vol. 41, p. 10272, 5 1990.

[172] J. K. Luo, H. Thomas, D. V. Morgan, and D. Westwood, "Transport properties of gaas layers grown by molecular beam epitaxy at low temperature and the effects of annealing," *Journal of Applied Physics*, vol. 79, pp. 3622–3629, 4 1996.

[173] A. J. Lochtefeld, M. R. Melloch, J. C. Chang, and E. S. Harmon, "The role of point defects and arsenic precipitates in carrier trapping and recombination in low-temperature grown gaas," *Applied Physics Letters*, vol. 69, p. 1465, 8 1998.

[174] E. Yablonovitch, D. M. Hwang, T. J. Gmitter, L. T. Florez, and J. P. Harbison, "Van der waals bonding of gaas epitaxial liftoff films onto arbitrary substrates," *Applied Physics Letters*, vol. 56, pp. 2419–2421, 6 1990.

[175] J. Cunningham, C. Wood, A. G. Davies, I. Hunter, E. H. Linfield, and H. E. Beere, "Terahertz frequency range band-stop filters," *Applied Physics Letters*, vol. 86, p. 213503, 5 2005.

[176] C. Wood, J. Cunningham, A. G. Davies, C. Hunter, P. Tosch, D. A. Evans, E. H. Linfield, and M. Missous, "Pulsed thz sensing of dielectric thin films using cascaded filter arrays," vol. 2, pp. 586–587 vol. 2, 2005.

[177] C. Russell, C. D. Wood, A. D. Burnett, L. Li, E. H. Linfield, A. G. Davies, and J. E. Cunningham, "Spectroscopy of polycrystalline materials using thinned-substrate planar goubau line at cryogenic temperatures," *Lab on a Chip*, vol. 13, pp. 4065–4070, 2013.

[178] J. S. Blakemore, "Semiconducting and other major properties of gallium arsenide," *Journal of Applied Physics*, vol. 53, pp. R123–R181, 10 1982.

[179] N. Chudpooti, N. Duangrit, A. D. Burnett, J. R. Freeman, T. B. Gill, C. Phongcharoenpanich, U. Imberg, D. Torrungrueng, P. Akkaraekthalin, I. D. Robertson, and N. Somjit, "Wideband dielectric properties of silicon and glass substrates for terahertz integrated circuits and microsystems," *Materials Research Express*, vol. 8, p. 056201, 2021.

[180] M. Schall and P. U. Jepsen, "Photoexcited gaas surfaces studied by transient terahertz time-domain spectroscopy," *Optics Letters*, vol. 25, pp. 13–15, 2000.

[181] E. R. Dobrovinskaya, L. A. Lytvynov, and V. Pishchik, *Properties of Sapphire*, pp. 55–176. Springer US, 2009.

[182] M. Leszczynski and J. F. Walker, "Thermal expansion of gallium arsenide layers grown by molecular beam epitaxy at low temperatures," *Applied Physics Letters*, vol. 62, pp. 1484–1486, 3 1993.

[183] R. Aggarwal and A. Ramdas, *Physical Properties of Diamond and Sapphire (1st ed.)*. CRC Press, 1st ed., 2019.

[184] J. Oishi and T. Kimura, "Thermal expansion of fused quartz," *Metrologia*, vol. 5, p. 50, 1969.

[185] D. M. Mattox, *Chapter 1 - Introduction*, pp. 1–24. William Andrew Publishing, 2010.

[186] I. I. S. Organization), "Test methods for laser beam parameters: Beam widths, divergence angle and beam propagation factor," 1997.

[187] A. Singh, S. Winnerl, J. C. König-Otto, D. R. Stephan, M. Helm, and H. Schneider, "Plasmonic efficiency enhancement at the anode of strip line photoconductive terahertz emitters," *Optics Express*, vol. 24, p. 22628, 10 2016.

[188] J. Wallauer, C. Grumber, and M. Walther, "Mapping the coupling between a photo-induced local dipole and the eigenmodes of a terahertz metamaterial," *Optics Letters*, vol. 39, pp. 6138–6141, 2014.

[189] U. D. Keil and D. R. Dykaar, "Ultrafast pulse generation in photoconductive switches," *IEEE Journal of Quantum Electronics*, vol. 32, pp. 1664–1671, 1996.

[190] X. Ropagnol, X. Chai, S. M. Raeis-Zadeh, S. Safavi-Naeini, M. Kirouac-Turmel, M. Bouvier, C. Y. Côté, M. Reid, M. A. Gauthier, and T. Ozaki, "Influence of gap size on intense thz generation from znse interdigitated large aperture photoconductive antennas (october 2016)," *IEEE Journal of Selected Topics in Quantum Electronics*, vol. 23, pp. 1–8, 2017.

[191] D. B. Go and D. A. Pohlman, "A mathematical model of the modified paschen's curve for breakdown in microscale gaps," *Journal of Applied Physics*, vol. 107, p. 103303, 5 2010.

[192] N. Knowles, "Finite element analysis," *Computer-Aided Design*, vol. 16, pp. 134–140, 1984.

[193] J. S. Blakemore, "Semiconducting and other major properties of gallium arsenide," *Journal of Applied Physics*, vol. 53, p. R123, 6 1998.

[194] F. Urbach, "The long-wavelength edge of photographic sensitivity and of the electronic absorption of solids," *Physical Review*, vol. 92, p. 1324, 12 1953.

[195] D. Webber, X. Liu, M. Dobrowolska, J. K. Furdyna, and K. C. Hall, "Control of the urbach band tail and interband dephasing time with post-growth annealing in low-temperature-grown gaas," *AIP Advances*, vol. 8, p. 045121, 4 2018.

Appendix A

Fabrication steps

The following subsections detail the fabrication process first presented by Bacon et al. [4].

A.0.1 Wafer Preparation

An important first step is to prepare the LT-GaAs and sapphire wafers for bonding. If this step is not adhered to it can lead to problems during the bonding stage. The LT-GaAs and sapphire wafers are bonding using a spin on polymer widely used in RF and micro-electromechanical systems, called BCB (discussed further in A.0.2), the layer thickness of which is comparatively small when compared to debris and organic contaminants typically present on the un-cleaned wafer surfaces. This can cause defect points in the BCB layer and cause bond failure. BCB is used as it is optically transparent at THz frequencies and exhibits low absorption at 800 nm.

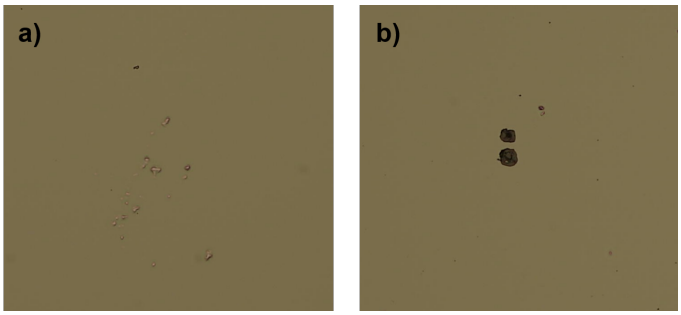

Figure A.1: Microscope images of the surface of an LT-GaAs layer after the ELO is complete. (a) Shows small areas of the surface raised where contaminants are between the sapphire and LT-GaAs layer preventing bonding. (b) shows an area where the substrate has come away from the layer completely due to the area not bonding.

Larger surface debris is first removed using alternating hand agitated rinses in Acetone (ACE) and Isopropyl alcohol (IPA). The wafers are then dried using nitrogen gas before a dehydration bake on a hotplate set to 180 °C for 5 minutes, this ensures the surface dries completely. For smaller contaminants ultrasonic agitation is required, again alternating between ACE and IPA solutions wafers are ultrasonicated for 5 minutes at varying levels of agitation power depending on the wafer. Sapphire can withstand higher levels of ultrasonic power so the highest level is used, whereas the LT-GaAs is somewhat brittle and therefore uses just 20 percent power. As above the wafers are dried and dehydrated before inspection. This process is repeated as required until the surface is clean. In some extreme cases in order to remove organic surface contaminants plasma ashing was used, this is a process in which an oxygen plasma created under a vacuum is utilised to remove surface contaminants through a reaction.

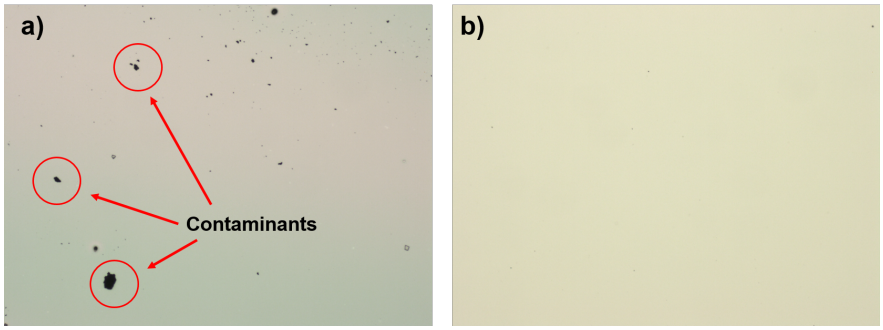

Figure A.2: Microscope images of an LT-GaAs surface before and after cleaning. (a) shows the surface before cleaning, with a large number of contaminants on the surface. (b) The surface after cleaning, the majority of large contaminants have been removed

A.0.2 Wafer Bonding

With clean wafers the next step is to prepare the wafers for the bond by applying the BCB which is pivotal for adhesion between the sapphire and LT-GaAs layer. First an adhesion promoter, AP300, is used. AP3000 is a organosilane coupling agent in an organic solvent that enhances the adhesion of the BCB to the wafers. The adhesion promoter is statically dispensed and spin coated onto both the sapphire and the LT-GaAs wafers. The promoter was span at a speed of 3000 rpm for 20 seconds. The adhesion promoter is baked at 100 °C for 30 seconds as this further enhances adhesion by removing the solvent.

The BCB solution is spin coated onto the sapphire wafer at 3000 rpm for 60 seconds (see section A.0.2.1), only the sapphire wafer is coated with the BCB solution as the sapphire surface is comparatively larger than the LT-GaAs wafer this in turn means that any edge bead that the BCB causes will not be an issue

when bonding. The BCB undergoes an initial soft baking to drive the remaining solvent from the layer, and provides stability and repeatability of the final film thickness. The soft bake is performed at 150 °C for 3 minutes.

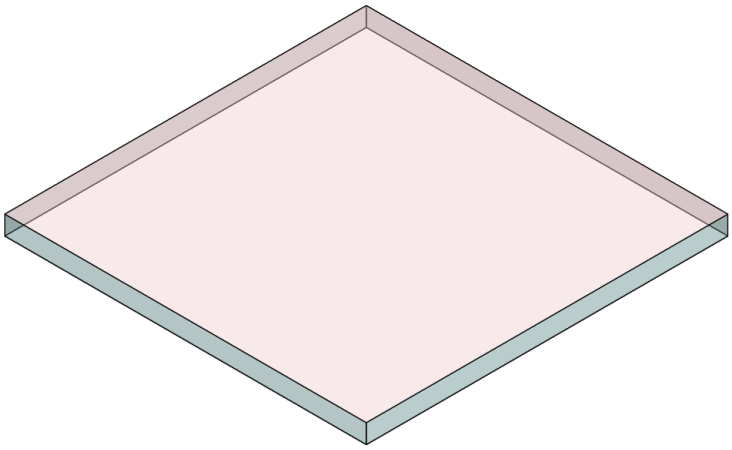

Figure A.3: Sapphire substrate with a BCB layer applied to the surface.

To bond the two wafers together the LT-GaAs wafer is inverted and placed in the center of the sapphire substrate so that the surface coated with adhesion promoter is in contact with the BCB covered sapphire wafer surface. To achieve the bond a wafer bonder is used, this machine is capable of providing both temperature and force control of the bond whilst providing a vacuumed atmosphere. The wafer bonder stage is pre-levelled as to ensure an even bond pressure across the device, this is a crucial step to achieving a strong bond. The device is transferred to the stage along with a graphite sheet which is placed on-top to account for any levelling inconsistencies between the two wafers, and ensures an even load across the surface. It is important to perform the bonding under a high vacuum (Cyclotene is susceptible to oxidation at high temperatures and therefore needs to be under an inert atmosphere) this ensure that the BCB is transmissive to the THz frequencies. At an atmospheric pressure of $\sim 2 \times 10^{-6}$ mBar pressure vacuum is considered reached and the temperature of the bonding plates can start to be increased. One of the aims of bonding is to hard cure the BCB layer as this provides maximum chemical resistance as well as stabilising the mechanical and electrical properties of the layer, the upper and lower bond plates are ramped at 5 °C/min until it reaches the target temperature of 250 °C. Whilst the temperature is ramping the pressure of the plates can be increased, a safe bonding force is considered to be 500 N/cm^2

(calculated from the area of the LT-GaAs wafer). When the desired temperature and bond force are reached the BCB takes 1 hour to hard cure, the plate heaters are then turned off and the device is left under the applied force to cool to room temperature. Once cooled the chamber can be vented, the pressure is released and the device removed.

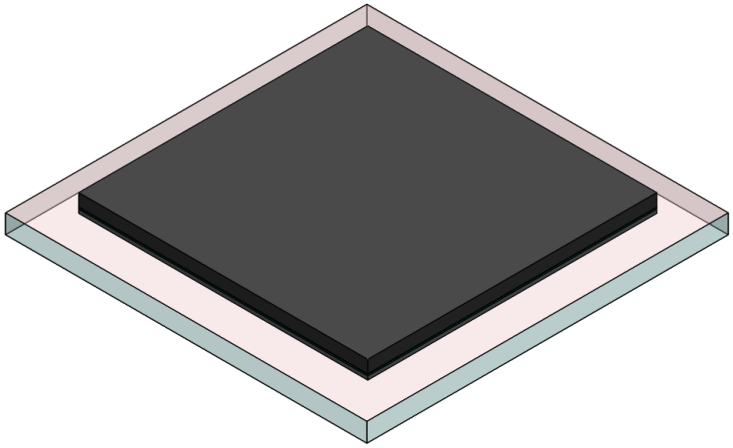

Figure A.4: The device after bonding showing the LT-GaAs face of the wafer bonded to the sapphire substrate.

A.0.2.1 BCB

Dow chemicals 'Cyclotene' is a polymer based resin derived from BCB that is designed for use in a variety of microelectronic applications. In this method of fabrication the BCB is utilised as the adhesive layer to ensure a reliable bond between the LT-GaAs and sapphire layers. Originally no adhesive was used during the bonding stage and Van der Waals forces were deemed a sufficient means [174], this lead to device reliability issues and as consequence BCB was chosen as it provides a more uniform and reliable bond than Van der Waals bonding.

In order for the layer of BCB to be thin enough to ensure as little interference with the THz as possible yet still yield a uniformly strong bond the layer thickness is chosen to be between 400-500 nm. Using Cyclotene 3022-57, the thinnest layer achievable is 5.55 μm, therefore a dilute BCB solution must be prepared. Mesitylene (1,3,5-trimethylbenzene) is a benzene derivative and solvent used to dilute Cyclotene. When mixed in various ratios, control of the layer thickness is achievable. In order to obtain the correct dilution ratio and spin speeds required

to achieve the desired layer thickness, spin curve tests were undertaken. Three different BCB:Mesitylene compositions mixed by weight were prepared; 1:1, 1:2 and 1:3. The BCB was statically dispensed and spun onto plain silicon samples (prepared with AP3000 applied in the aforementioned way) at three different spin speeds per BCB mixture 1000,2000 and 3000 rpm. After each spin coating the samples were soft baked at the data sheet recommended temperature and time, 150 °C for 3 minutes.

To measure the layer thickness first the refractive index,n, and extinction coefficient, k, must be determined. These values are obtained through optical ellipsometry, this technique exploits changes in polarisation of a reflected beam from the target film to measure the dielectric properties of a material. The measured results are compared to a model and the values can be extracted. The ellipsometry data from the BCB compositions are plotted in figure A.5, with a Sellmeier model fitting obtained from the model the n and k values can be extracted. For wavelengths above 350 nm k is zero as there is no absorption. The graph shows the values of n, there is a slight spread between the estimated values of n but this is fairly low.

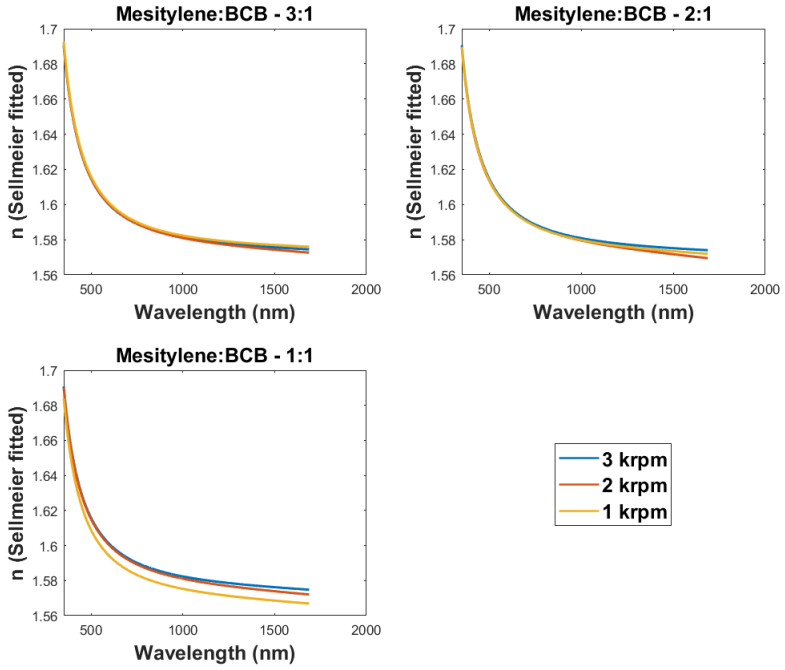

Figure A.5: The graphs show the different values of n obtained for three different compositions of BCB solutions each span at speeds of 1,2 and 3 krpm.

With the dielectric values obtained, measurements on a reflectometer were performed to measure the thickness of each of the BCB solution layers. The spin curves can be seen in figure A.6 and from this the desired thickness is can be seen to achieved with a dilution of 1:2 BCB:Mesitylene at a spin speed of 3000 rpm.

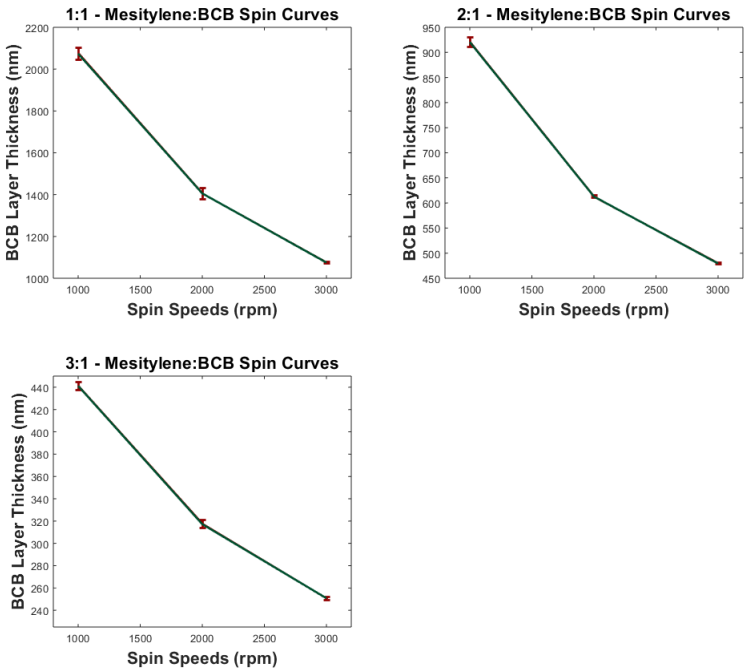

Figure A.6: The graphs show the variation of layer thickness with spin speeds for the three different BCB compositions, standard deviation errors bars are included.

A.0.3 Substrate Thinning and Removal

With the two wafers bonded the process of removing the bulk SI-GaAs begins. This thinning of the substrate is achieved through a combination of lapping and polishing. Preparing the bonded device for lapping involves mounting it onto a glass carrier disc, this disc is used to support the device during the thinning process. To mount the device a plasticised general bonding wax is applied to the glass disc on a hotplate set to 60 °C, the wax melts and the device is placed onto the melted wax with the sapphire wafer backside in contact. To ensure the mounting is level pressure is applied through a specially designed jig, the device is left under this applied pressure for 10 minutes and then left to cool. As the

levelling of the mounting is so crucial, careful measurements must be taken to acquire the levelling and the starting thickness of the wafer before thinning. If the device is not level on the glass disc then there is a serious risk of removing too much of the wafer which renders the device unusable. If the device is not level then it must be unmounted and the process repeated.

The lapping process works by rubbing the SI-GaAs surface against a rotating glass lapping plate with an abrasive between them. For the process here the abrasive used is a 3 μm grit calcined aluminium oxide powder suspended in water, this smaller grit allows for a more controlled removal of material. The carrier disc goes into a precision jig which keeps the device in contact with the lapping plate and applies the load to the device, the load used for device lapping is 250 g/cm^2. Devices are lapped at a plate speed of 20-30 rpm depending on the lapping rate, there is a micrometer attached to the precision jig that tracks the amount of material lapped from the device. Lapping is a faster substrate removal process than polishing but introduces higher levels of stress to the device, hence once the bulk of the SI-GaAs is removed the remaining bulk is removed via polishing. The aim of polishing is two fold, it allows for a higher level of removal precision and polishing leaves a uniform surface roughness. For polishing the plate is changed to a plate with a polishing cloth, the abrasive grit is replaced with a sodium hypochlorite polishing fluid which is suited for GaAs processing. The same level of force is applied from the jig and a similar plate speed is used to that whilst lapping. To avoid removing too much SI-GaAs, polishing is stopped with $\sim$30 μm of material left. The SI-GaAs surface must be cleaned thoroughly to ensure that any debris from removed material is not left on the surface as well as to stop the polishing fluid reacting with the surface, this is achieved through an in situ DI water rinse. The device is unmounted from the glass carrier disc by heating the wax again and sliding the device off. An important caveat here is to avoid contaminating the SI-GaAs surface with the melted wax as this will cause issues with the final removal in later steps. To remove the wax properly from the device it can be immersed in Tetrachloroethylene (TCE), this will dissolve the wax and remove it from the device.

To remove the remaining bulk SI-GaAs a wet etch is utilised, this is chosen to exploit the selectivity of the etch solution allowing a precision removal of SI-GaAs with out the risk of removing more material then needed and penetrating into the desired LT-GaAs layer, whilst this is slower than polishing it allows for a controlled removal of the remaining substrate. This methods preciseness is supported by the wafer composition seen in 2.1, the Aluminium Gallium Arsenide (AlGaAs) etch stop prevents the selective etch from removing the LT-GaAs material underneath. Although the etch stop will stop the etch from penetrating top down, due to the device geometry it does not protect the LT-GaAs layer from the etchant penetrating from the sides (see figure A.8). To account for this a protective photoresist layer is applied to the edges of the devices this stops the edges of the LT-GaAs layer from being exposed. It is

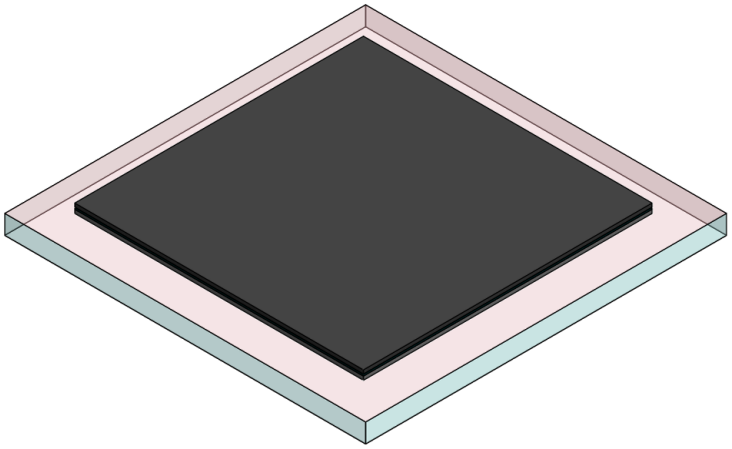

Figure A.7: The device after lapping and polishing, this removes the bulk of the SI-GaAs.

important that this photoresist does not get on the SI-GaAs surface as this will prevent it from etching.

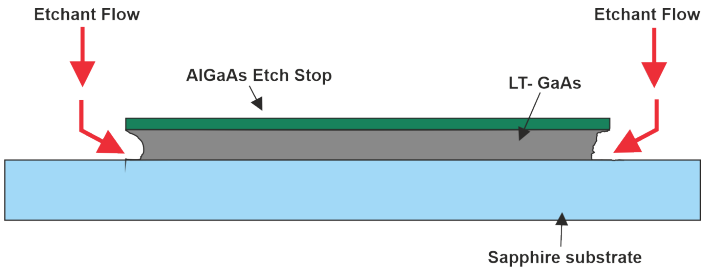

Figure A.8: Without a protective layer around the edges of the semiconductor wafer the etchant will attack the LT-GaAs layer

An etch solution comprising of citric acid and hydrogen peroxide having a solution concentration of 5:1-$C_6H_8O_7$:H_2O_2 is used. To provide stable etch conditions and reproducible results the set-up shown in figure A.9 is used, this consists of the etchant in a water bath kept at 30 °C on a hotplate with a resistive feedback thermometer, there is also a magnetic stirrer to mix the etchant solution and to provide agitation during etching. The solution is mixed in advance of use and left to reach the desired temperature. The device is placed into the etchant and the SI-GaAs begins to be removed, the rate is 1 μm/min,

there is a clear change in the surface colour of the device once the SI-GaAs is completely removed, the surface goes from grey to turquoise once the etch stop is revealed, this typically starts in one corner of the device before spreading across the entirety of the surface. Once this change is observed the device is left for another 10 minutes in the etchant solution to ensure that all of the bulk SI-GaAs is removed.

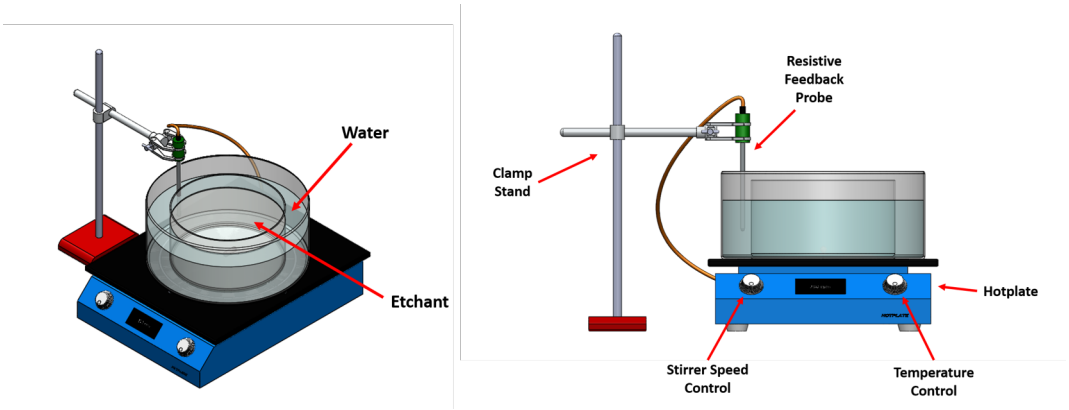

Figure A.9: The diagram shows the set up that is used for the etch, all components labelled. The water bath is kept at a constant temperature through the resistive feedback thermometer.

The final step to complete the ELO process is to remove the AlGaAs etch stop, this can be done in a buffered Hydrofluoric Acid (HF) solution. Buffered HF is selective so will only attack the etch stop and not the LT-GaAs underneath. The etch stop layer is visibly removed in 14 minutes, the colour reverts from turquoise back to grey, and then left for a further 6 minutes to ensure the etch stop is completely removed. Once this step is done the protective photoresist layer can be stripped.

A.0.4 Active Area Etching

With the ELO transfer complete the device geometries can be defined upon the surface. As seen in 1.8.9 the benefits of defining individual emitter strips from the larger piece of LT-GaAs over simply masking the alternating gaps were discussed. These features can be realised using another wet-etch, first an etch-mask must be patterned onto the device surface. A layer of S1813 photoresist is statically dispensed and spin coated onto the LT-GaAs at 3000 rpm before being baked for 90 seconds at 115 °C. A direct write laser system is used as the means of mask-less alignment for patterning, by not using a traditional mask aligned process it allows for design to be updated and adapted with having to remake masks. The pattern is exposed using a light energy of 130 mJ/cm^2 and a laser

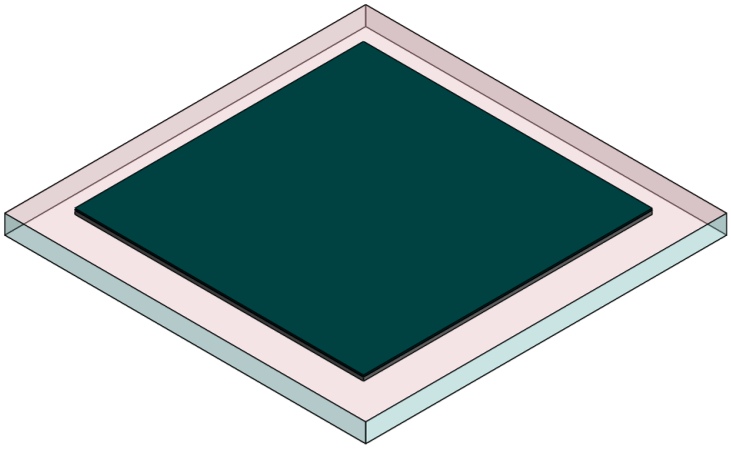

Figure A.10: Device with all SI-GaAs removed leaving the AlGaAs etch stop exposed.

defocus of -1, this provides a clear definition of features in the photoresist mask. Once patterned and consequently developed in S1813 developer, H_2O:MF319 4:1, the quality of the mask must be checked under a microscope as any defects will provide undesirable etch results.

The etch solution used is a weak piranha etch, H_2O:H_2O_2:H_2So_4 in a ratio 250:8:1. The reasoning as to using a weaker etch is produce sloped sidewalls on the bars, this allows for the gold contacts to be rolled up the sides of the LT-GaAs bars ensuring a good contact with the material and providing an even electric biasing field. As with the citric etch used for bulk SI-GaAs etching, a water bath set-up is utilised here to keep the temperature of the solution constant and to provide agitation. Once a solution temperature of 30 °C is obtained the device can be submerged in the solution, the etch rate is ∼125 nm/min which results in the LT-GaAs bars being defined fully in 16 minutes. It is clear to see this point visually due to the transparent sapphire substrate. When the bars are etched the device is rinsed in water to ensure etchant is fully removed preventing further etching.

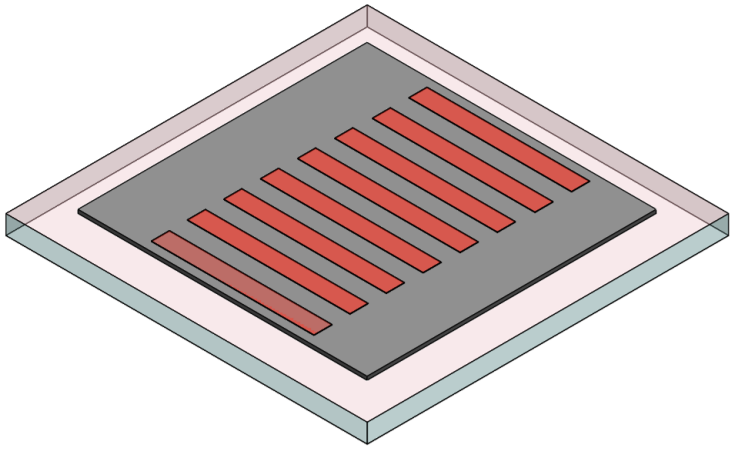

Figure A.11: The etch mask patterned onto the device will define the LT-GaAs bars.

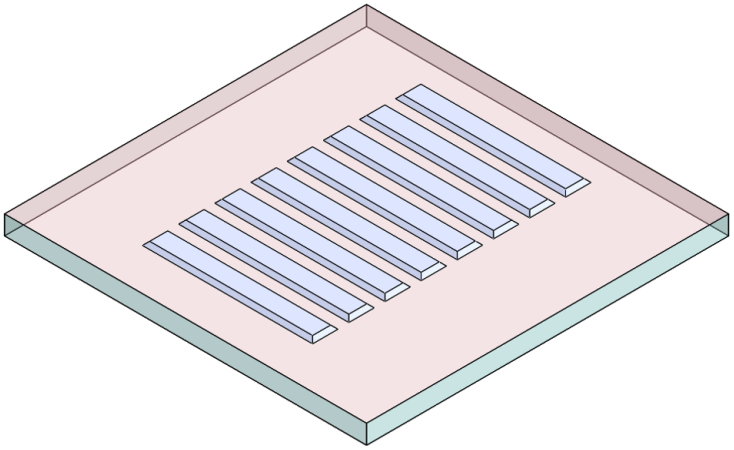

Figure A.12: The LT-GaAs bars defined fully from the larger active material, the etch mask is removed.

A.0.5 Electrode Patterning

The electrode structures are a key feature as they provide the means to bias the devices hence the fabrication procedure is carefully thought of. To ensure the electrodes cover the active material sidewalls well, a sputtering deposition technique is chosen. The method uses a blanket coverage of metal on the surface with the electrode structures defined after by means of etching down into the metal layer to remove unwanted material. The device is first cleaned in ACE and IPA solutions to remove the photoresist left from patterning and to remove any organic contaminants left on the surface. With a sufficiently clean surface the device can be secured to the sputtering deposition stage and placed into the chamber, the deposition is performed under vacuum so the chamber must be purged before proceeding. An initial 20 nm layer of titanium is sputtered onto the device, this has dual purpose, firstly it ensures good adhesion for the gold layer and secondly the gold etchant will attack the LT-GaAs so a thicker protection layer of Titanium is required. A thicker 200 nm layer of gold is then sputtered onto the device, this thicker layer ensures that at higher biases the current carrying ability of the electrodes is sufficiently high enough to avoid any electrical failures.

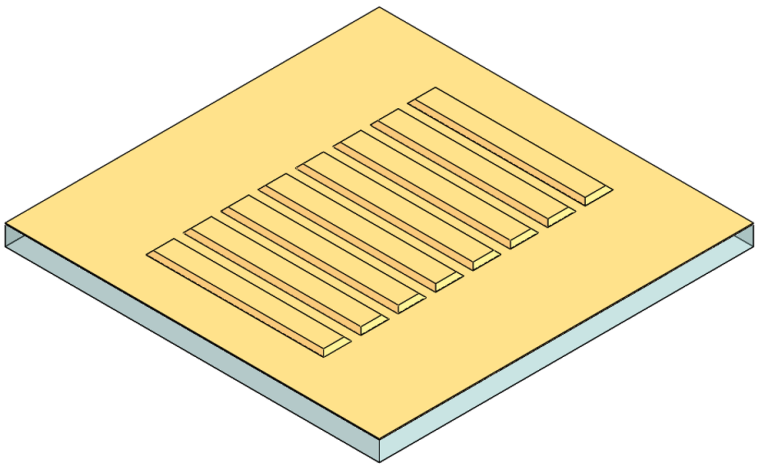

Figure A.13: The device covered with the Ti/Au layer.

In order for the electrode structures to be etched from the metallised layer an etch mask is again required. As in other steps, a layer of S1813 photoresist is spin coated onto the devices metal surface at a speed of 3000 rpm for 40 seconds and baked at 115 °C for 60 seconds on a hotplate. Similar to the etch mask for the LT-GaAs bar definition in A.0.4, the mask aligner is once again

used to realise the pattern. An example of an electrode mask design can be seen in figure (link), this is aligned to the reference alignment crosses defined previously. The alignment crosses ensure the electrodes are defined precisely on underlying LT-GaAs bars. The pattern is exposed with the same dose and defocus values used for defining the bars in A.0.4. The exposed mask pattern is developed in MF-319 photo-developer for 45 seconds, the pattern is checked under a microscope to ensure the features are sharp and not underexposure. It is crucial at this step to ensure that there is no photoresist remaining in undesired areas as this leads to electrical shorts after etching. To mitigate the risk of exposed and developed photoresist remaining across gaps the device is plasma ashed at 50 percent RF power for one and half minutes, this will ensure that only the unexposed photoresist pattern remains.

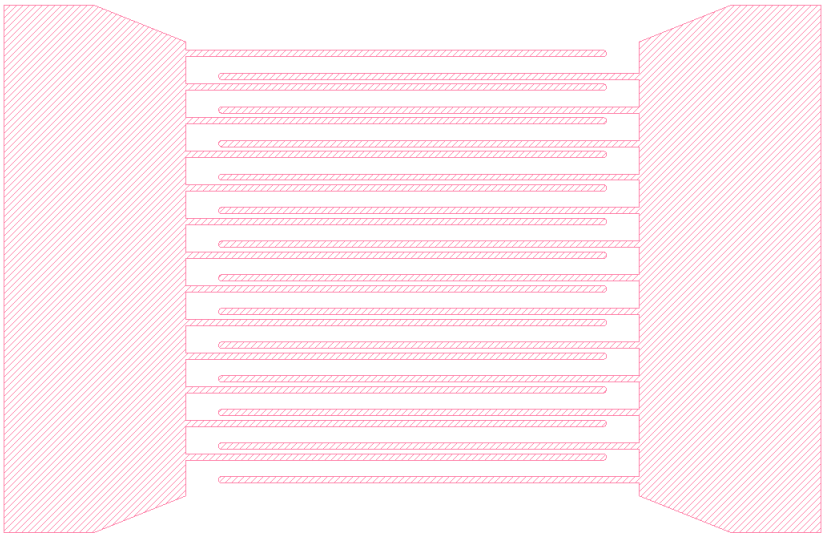

Figure A.14: The CAD 2D etch mask, this is patterned onto the gold layer.

To etch the gold a solution compromised of potassium iodide and iodine is chosen. The solution selectively etches the unmasked gold whilst not reacting with the photoresist mask. The etch rate is 150 nm/min, so for a 200 nm gold layer the total etch time needed is $\approx$ 1 minute 22 seconds. Due to the nature of the chemistry, over-etching can occur relatively fast causing large undercuts of the electrode structures which can cause complete removal of electrodes depending on their width. The titanium layer can be removed in 1 minute using a buffered HF solution, as the HF is highly selective it will not attack the rest of the device. It is important to ensure complete removal of unwanted metal, an example of a device without the titanium layer completely removed is seen in figure A.16, this causes an electrical short.

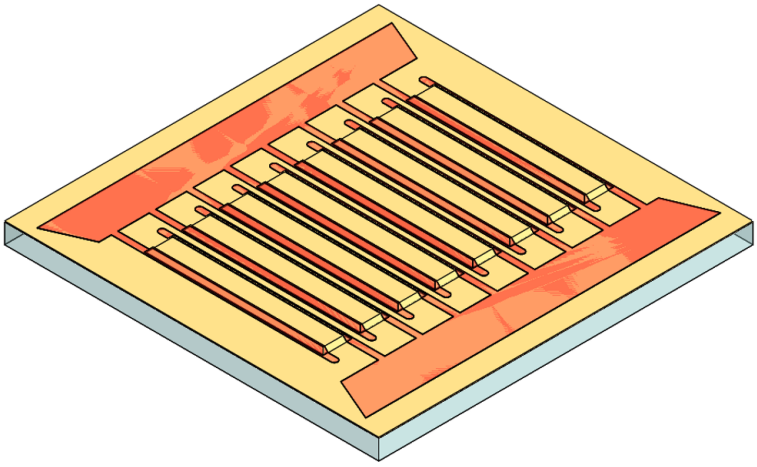

Figure A.15: The etch mask used for realising the gold electrodes from the metallic over layer patterned onto the device.

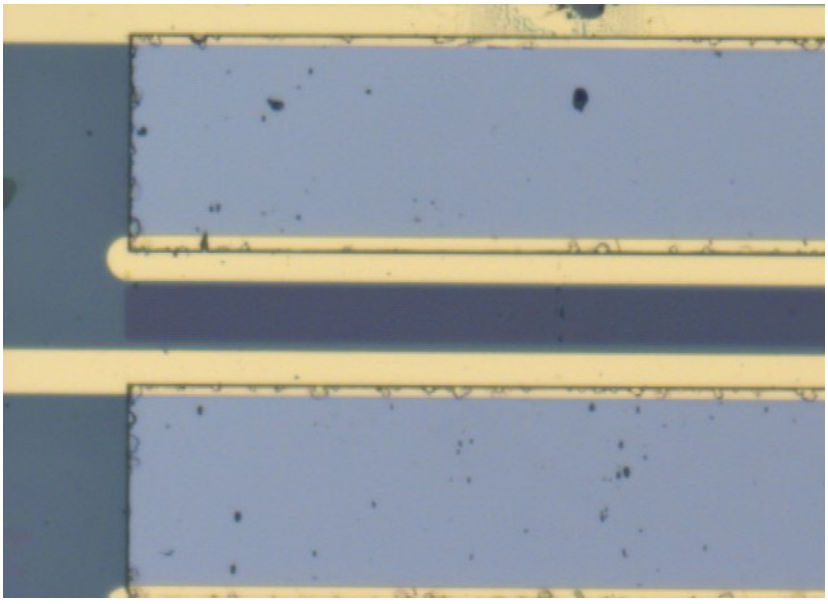

Figure A.16: The darker colour seen between the gold bars indicates all the metal was removed, the lighter colour is remaining Ti which causes a short between electrodes